eman ta zabal zazu
Universidad del País Vasco
Euskal Herriko Unibertsitatea

INGENIARITZA MEKANIKOA SAILA
DEPARTAMENTO DE INGENIERÍA MECÁNICA

Ph.D. Thesis

Mechanical analysis and design of dental restorations: fatigue, microgap and screw loosening

Presented by:

Mikel Armentia Sánchez

Thesis Advisors:

Dr. Mikel Abasolo Bilbao
Dr. Ibai Coria Martínez

Bilbao, January 2023

Más vale un diente que un pariente

Agradecimientos

Una vez terminado un trabajo tan extenso como una Tesis Doctoral, con la de horas de dedicación y esfuerzo que conlleva, es momento de echar la vista atrás y pensar en aquellas personas con las que he compartido estos últimos cuatro años.

Mi primer agradecimiento va dirigido a mis directores de Tesis, Mikel Abasolo e Ibai Coria, que siempre han mostrado una disponibilidad completa, una dedicación que pocos demuestran y una pasión inagotable por lo que hacen. Me habéis acompañado durante toda esta etapa, guiándome y aconsejándome en las distintas investigaciones, empujándome cuando veíais que bajaba el ritmo y dándome ánimos y consejos cuando los he necesitado. También quiero extender este agradecimiento a Josu Aguirrebeitia e Iker Heras, que tanto me han ayudado a lo largo de todo este tiempo. De todos vosotros he aprendido mucho tanto a nivel profesional como personal.

Continuando con el Departamento de Ingeniería Mecánica, quiero mencionar a los profesores Rafael Avilés y Joseba Albizuri, porque gracias a ellos empezó mi interés por la fatiga de los materiales y la investigación. A los compañeros de la sala de doctorandos, por haber compartido tantos momentos y por habernos apoyado y ayudado mutuamente. En especial, Rakel, con la que he tomado tantos cafés desde el TFM, Laura, con la que he compartido tantos viajes a la uni y tantas conversaciones, e Íñigo Martín, compañero de máster, grupo de investigación y de alguna que otra juerga. Sin olvidarme de la estimable ayuda de los compañeros Raúl Cosgaya e Isaac Casas en los ensayos experimentales y de Mari Jose Maestu, María Fernández y Pilar Furones en los temas administrativos.

Sin duda, este trabajo no se podría haber realizado sin la generosa colaboración de BTI y, en especial, de Eduardo Anitua, a quien debo agradecer haber confiado en mi para realizar esta tarea y formar parte del equipo de I+D. Hago extensible el agradecimiento a mis compañeros de I+D: Naiara, Iker, Gloria,

Odei, Andoni, Unai, Luis y Ricardo. La generosidad y compañerismo de este equipo hace que trabajar con vosotros sea un auténtico lujo. Cómo no, quiero mencionar también a Jose Ramón, que ha ejercicio como nexo entre la universidad y BTI y como tutor a nivel profesional y personal.

Ich möchte auch Professor Simon Zabler und seinem Team dafür danken, dass sie mich aufgenommen haben und mit mir an einem der Forschungsprojekte dieser Doktorarbeit zusammengearbeitet haben. Mein Aufenthalt in Würtzburg war wunderbar.

Je tiens également à remercier le professeur Nicolas Saintier et son équipe pour m'avoir accueilli pendant près de deux mois à Bordeaux et avoir collaboré avec moi sur une partie de cette thèse de doctorat.

Mis últimas palabras no pueden ser sino para la gente que más lo merece. A mis padres, Ramón y Merche, a mis hermanos, Asier y Gorka, y a mis tías y mi primo, Ana, Mamen, Sol y Aratz. Gracias a vuestra ayuda, cuidados y apoyo incondicional he conseguido llegar hasta aquí. A mis amigos, por tantos buenos momentos. Y en especial a ti, Paula, por haber compartido la carga, por tu apoyo y por estar a mi lado. A todos vosotros, lamento haberos dedicado menos tiempo del que me habría gustado y espero disfrutar más de todos vosotros ahora que termina esta etapa.

Mikel

Abstract

Dental implants are a widely used option to replace a single tooth as well as several teeth. The simplest screw-retained dental restoration consists of a dental implant, that is inserted into the bone, and a crown, that is cemented on an abutment, and all together is assembled on the implant by means of a prosthetic screw. The screw is properly tightened so that the structural integrity of the dental restoration is achieved.

Even though the use of dental implants is a highly predictable treatment with a high success rate, any case could result in either biological or mechanical complications. The most common mechanical problems are the fatigue failure of either the prosthetic screw or the dental implant, microgap formation in implant-abutment connection, leading to bacterial colonization and possible implant loss, and self-loosening of the prosthetic screw.

A dental restoration is, indeed, a screwed joint, that is, a mechanical element that has been widely studied over the years in the field of mechanical engineering. In fact, the aforementioned three mechanical faults that may be found on dental restorations are also common in screwed joints used for more general purposes. Consequently, many studies analyze these phenomena in screwed joints attempting to predict the mechanical behavior in order to eliminate, or at least reduce, the problems caused by these phenomena.

This PhD Thesis brings together a significant part of the expertise acquired over the years by the industry regarding screwed joints and transfers it to the field of dental implantology, creating predictive methodologies and in-depth studies that help provide better understanding of these phenomena and to be able to predict and avoid them in future dental implant designs. As a result, the fatigue behavior of dental restorations has been studied, distinguishing between, on the one hand, those in which the critical component is the prosthetic screw and, on the other hand, those in which the critical component is the dental implant. For both cases, fatigue life prediction methodologies have

been developed, providing very accurate predictions in the experimental verification tests carried out. Moreover, some changes in the machining process of the prosthetic screw have been proposed after experimentally proving its benefits in terms of fatigue behavior. In addition, the microgap formation in the implant-abutment connection has been studied experimentally and some of the parameters which had the most significant effects were analyzed. Finally, the loosening phenomenon of the prosthetic screw has been studied and a methodology to predict screw loosening on dental restorations has been developed and experimentally validated.

Resumen

Las restauraciones dentales son una opción muy utilizada para sustituir tanto una como varias piezas dentales. La restauración dental atornillada más sencilla está compuesta por un implante dental, que se inserta en el hueso, y una corona, que se cementa sobre un pilar, y juntos se colocan sobre el implante. Finalmente se inserta un tornillo protésico, que apretado al par de apriete adecuado, aporta una integridad estructural a la restauración dental.

Aunque el uso de restauraciones dentales es un tratamiento muy predecible y con una alta tasa de éxito, cualquier caso es susceptible de sufrir complicaciones biológicas o mecánicas. Los problemas mecánicos más comunes son el fallo por fatiga del tornillo protésico o del implante dental, la formación de microgaps en la conexión poste-implante, que pueden conducir a la colonización bacteriana y a una posible pérdida del implante, y el aflojamiento del tornillo protésico.

Una restauración dental es, en efecto, una unión atornillada, es decir, un elemento mecánico ampliamente estudiado a lo largo de los años en el campo de la ingeniería mecánica. De hecho, los tres fallos mecánicos ya mencionados que pueden encontrarse en las restauraciones dentales son también comunes en las uniones atornilladas utilizadas para fines más generales. En consecuencia, son muchos los estudios que analizan estos fenómenos en las uniones atornilladas intentando predecir el comportamiento mecánico, y eliminar, o al menos reducir, los problemas causados por estos fenómenos.

Esta Tesis Doctoral recoge gran parte del conocimiento adquirido a lo largo de los años sobre las uniones atornilladas por la industria y lo traslada a la industria de la implantología dental, creando metodologías predictivas y estudios en profundidad que ayudan a comprender mejor estos fenómenos para poder predecirlos y evitarlos en los futuros diseños de restauraciones dentales. Como resultado, se ha estudiado el comportamiento a fatiga de las restauraciones dentales, diferenciando, por un lado, aquellas en las que el componente crítico es el tornillo protésico y, por otro, aquellas en las que el componente crítico es

el implante dental. Para ambos casos, se han desarrollado metodologías de predicción de la vida a fatiga, proporcionando predicciones muy precisas en los ensayos de verificación experimentales realizados. También, se han propuesto ciertos cambios en el proceso de mecanizado del tornillo protésico después de comprobar experimentalmente sus beneficios en el comportamiento a la fatiga. Además, se ha estudiado la formación de microgap en la conexión poste-implante y se han analizado algunos de los parámetros que más afectan. Por último, se ha estudiado el fenómeno de aflojamiento del tornillo protésico y se ha desarrollado y validado experimentalmente una metodología para predecir el aflojamiento del tornillo en restauraciones dentales.

Contents

List of Figures **xi**

List of Tables **xxv**

Acronyms **xxvii**

Context, objectives, and document structure **1**

Context and motivation 1
Aim and scope 2
Document structure 3

1 Introduction and background **7**

1.1 Dental restorations: an overview 7
1.2 Mechanical behavior of screwed joints 13
1.2.1 Screw preload 13
1.2.2 External axial loading 15
1.2.3 External shear loading 17
1.2.4 Tightening torque-preload relationship 19
1.2.5 Screwed joint faults 24
1.3 Fatigue analysis 25
1.3.1 Uniaxial fatigue analysis 27
1.3.2 Multiaxial fatigue analysis 52
1.4 Screw loosening analysis 64
1.4.1 Analysis of the screw head contact 67
1.4.2 Analysis of the screw thread contact 70
1.4.3 Equilibrium condition of the screw 78
1.5 Microgap in screwed joints 80

1.6 Mechanical of dental implants: a literature review 81
1.6.1 Fatigue behavior on dental restorations 81
1.6.2 Self-loosening of the prosthetic screw 85
1.6.3 Microgap formation at implant-abutment connection .. 86

2 Tools used for simulations and experimental tests 89

2.1 Geometries, materials, and coefficients of friction of dental restorations 90
2.1.1 Geometries and materials 90
2.1.2 Coefficients of friction 91
2.2 Finite Element models of dental restorations 93
2.2.1 Geometry and materials 93
2.2.2 Contacts 95
2.2.3 Mesh 95
2.2.4 Boundary conditions 99
2.2.5 Screw preload and external loads 99
2.2.6 Specific Features of the Finite Element models used in Chapter 5 101
2.3 Finite Element model of standardized specimens 102
2.3.1 Geometry and materials 103
2.3.2 Mesh 103
2.3.3 Boundary conditions and external load 104
2.4 Test Benches 105
2.4.1 INSTRON E3000 Electropuls for fatigue tests 105
2.4.2 INSTRON 8801 for screw loosening and standardized specimens fatigue tests 106
2.5 Development of an innovative fatigue test bench prototype . 111
2.5.1 Mechanism description 112
2.5.2 Mechanical considerations 114
2.5.3 Overall description of the test bench 115
2.5.4 Validation of the new test bench 118

3 Fatigue behavior of the prosthetic screw: life prediction methodology 121

3.1 Development of a fatigue life prediction methodology 123
3.1.1 Experimental Fatigue Tests 123
3.1.2 Finite Element Analysis 126

3.1.3 Model fitting 132
3.1.4 Use of the methodology 132
3.2 Validation of the methodology on different dental restorations 133
3.2.1 Implant-supported restorations 134
3.2.2 Transepithelial-supported restorations 144
3.3 Conclusions 151
3.4 Clinical implications derived from experimental fatigue tests 153
3.4.1 Effect of the tightening torque of the prosthetic screw 153
3.4.2 Effect of different implant geometry parameters on fatigue behavior 153
3.4.3 Influence of the transepithelial component 157

4 Fatigue behavior of the prosthetic screw: improvement of the manufacturing process 161

4.1 Screw head socket 161
4.2 Screw thread: rolling versus cutting 164
4.2.1 Sample preparation 164
4.2.2 Thread profile, surface roughness, and residual compressive stresses 165
4.2.3 Mechanical behavior 169
4.3 Conclusions 171

5 Fatigue behavior of the dental implant: life prediction methodology 173

5.1 Determination of the notch effect on fatigue behavior 174
5.2 Determination of critical distances via Finite Element Analyses 176
5.3 Fatigue life prediction methodology for dental implants 183
5.4 Validation of the methodology 185
5.4.1 Experimental validation 185
5.4.2 Methodology prediction 189
5.5 Conclusions 197

6 Microgap at the Implant-Abutment Connection 199

6.1 Introduction 199
6.2 Experimental tests 201
6.3 Conclusions 207

7 Self- loosening of the prosthetic screw 209

7.1 Simplified model for loosening torque determination under external loading 211
7.2 Methodology to predict self-loosening of prosthetic screws on dental restorations 213
7.3 Validation of the methodology 215
7.4 Conclusions and clinical implications 220

8 Conclusions 223

8.1 Conclusions and further research 223
8.2 Research work dissemination 225

References 227

List of Figures

Figure 1. Implant-supported restoration inserted in mandibular bone. 1

Figure 2. Different bone densities due to proportions of cortical and trabecular bone. Denser bone in the left side and less dense in the right side.[2] 8

Figure 3. Step by step drilling process and implant positioning. A, Incision. B, Initial drill. C, Pilot drill. D, Further drilling after pilot drilling. E, Example of a complete drilling procedure for a specific implant. F, Implant insertion.[2] 9

Figure 4. A, Inserted implant with a healing abutment and sutured mucosa around it. B, Inserted implant with a healing cap and sutured mucosa over it. C, Inserted implant with a transepithelial element and sutured mucosa around it.[2] 10

Figure 5. A, Implant-supported restoration. B, Transepithelial-supported restoration. C, One-stage surgery using a transepithelial component.[2] 11

Figure 6. Most common IACs. A, External butt-joint. B, Internal butt-joint. C, Internal conical. D, External conical. Contact surfaces marked in red. 12

Figure 7. Two sheets joined by a preloaded screwed joint.[3] 14

Figure 8. Representation of the stiffnesses of the screw and elements to be joined in the screwed joint in Figure 7.[3] 14

Figure 9. Joint diagram of the screwed joint in Figure 7. 15

Figure 10. Preloaded joint under external axial load.[3] 15

Figure 11. Joint diagram of the screwed joint in Figure 10. 17

Figure 12. Screwed joint subjected to shear loading. 17

Figure 13. Screwed joint working as a 'friction type' joint. 18

Figure 14. Stress transmission lines on a friction type screwed joint. 18

Figure 15. Screwed joint working as 'bearing type' joint. 19

Figure 16. Screw preload and the analogy with a block over an inclined plane. 20
Figure 17. Free body diagram of a tightened screw. A, Tightening process. B, Untightening process. 20
Figure 18. Geometrical parameters of a screwed joint..... 22
Figure 19. Energy consumed by the resistance torques under the screw head T_h, the resistance torque in the thread T_t, and the pitch torque T_p. A, Torque versus turn diagram.[3] B, Pie chart of the consumed energy during the tightening process. 23
Figure 20. Initial preloads obtained for a large number of specimens tightened at the same torque.[3] 23
Figure 21. Relaxation process over time.[3]..... 24
Figure 22. Failure section of a bolt due to fatigue.[54] 26
Figure 23. Zwick/Roell rotating bending fatigue machine..... 28
Figure 24. Schematic of the Zwick/Roell rotating bending fatigue machine..... 28
Figure 25. A, Instron 8801 servo-hydraulic direct stress fatigue machine. Image courtesy of Instron. B, Grips used for cylindrical specimens..... 29
Figure 26. S-N chart with the three duration ranges: LCF, HCF and VHCF. 30
Figure 27. Staircase method (or the up-and-down method). 32
Figure 28. S-N curve for material (specimens) and S-N curve for mechanical part (end product) obtained by using modification factors. 34
Figure 29. Effect of mean stress in S-N curve. 36
Figure 30. Different stress cycles corresponding to different stress ratios. A, $R = -1$. B, $R = 0$. C, $0 < R < 1$. D, $0 > R > -1$.[53] 37
Figure 31. Different stress ratios in the Haigh diagram. 38
Figure 32. S-N curve and Haigh diagram correlated. 39
Figure 33. Most used criteria for tensile mean stress consideration.[81] 39
Figure 34. Fatigue behaviors of different ductile materials and their most suitable criteria in the Haigh diagram. A, Fatigue behavior of different steels.[53] B, Fatigue behavior of different ductile materials.[85] 41
Figure 35. Criteria for compressive mean stress. 42

Figure 36. Normalized Haigh diagram showing the experimental results on 11 ferritic materials together with the Smith line for brittle materials and the Elliptical relationship for ductile materials.[86] 43
Figure 37. Notched sheet subjected to axial loading. 44
Figure 38. Nominal stress shape extrapolation from nearby sections.[53] 45
Figure 39. Notch sensitivity q versus notch radius r.[90] 45
Figure 40. Parts with the same notch factor k_t but different notch sensitivity q 46
Figure 41. a^*value versus material strength.[52,55] 46
Figure 42. A value versus material strength.[52,88] 47
Figure 43. High diagrams of different materials (notched and unnotched). A, aluminum. B, ductile steel.[63] 48
Figure 44. Approach proposed by Fatemi for considering mean stresses with stress concentration.[52] 48
Figure 45. Point method applied on a notched specimen. 50
Figure 46. Methods based on the TCD A, Point Method. B, Line Method. C, Area Method. D, Volume Method. 50
Figure 47. Example of a meshed part (nodes numbered) and the critical distance Δs considered.[69] 51
Figure 48. k_t/k_f versus the normailzed stress gradient χ and material properties.[69] 52
Figure 49. Multiaxial fatigue testing of cruciform specimens. A, Biaxial force fatigue test bench.[95] B, Specimen with fillets and thickness reduction.[96] 53
Figure 50. A, Axal-torsion fatigue test bench.[97] B, Specimen for axial-torsion test.[98] C, Torsion-bending fatigue test bench.[99] D, Specimen for torsion-bending test.[99] 54
Figure 51. Tubular specimen for multiaxial fatigue (axial loading and internal pressure cycling).[53] 54
Figure 52. Multiaxial stress cycles. A) Proportional, B) Non-proportional. 55
Figure 53. Proportional multiaxial stress cycles. A) Constant amplitude, B) Variable amplitude. 55
Figure 54. Stresses at a point P according to plane Π.[53] 59
Figure 55. Normal and shear stress components for a plane Π.[53] 60

Figure 56. Mean and alternating components of shear stress calculations. A) Minimum Circumscribed Circumference method (MCC), B) Minimum Circumscribed Ellipse method (MCE).[53] 61
Figure 57. Junker test machine.[3] 64
Figure 58. Transverse relative displacement among the elements of a screwed joint that may cause self-loosening.[3] 65
Figure 59. Force balance on the contact surface of the screw head (seen from below)..... 67
Figure 60. Force balance on the contact surface of the screw thread (seen from below)..... 70
Figure 61. Pressure on the screw thread surface and the resulting loosening force dF_{Tp} (seen from above)..... 71
Figure 62. Vertical component of pressure. 72
Figure 63. Friction force on the screw thread surface (seen from above)..... 72
Figure 64. Vector on horizontal plane (u, v) (screw seen from below). 73
Figure 65. $cos\lambda$ determination. 73
Figure 66. Torque versus transverse load: slip limit curves. 79
Figure 67. Bolted joint in a pipeline.[135] 80
Figure 68. Schematic of the test set-up for non-angulated dental restorations according to ISO 14801 standard.[141] 85
Figure 69. Main elements of a screw-retained dental restoration. A, Implant-supported restoration. B, Transepithelial-supported restoration. 91
Figure 70. Pin-on-disk test. A, pin-on-disk tribometer MicroTest SMT-A/0200. B, Detail view of the test. 92
Figure 71. FE models of dental restorations. A, Implant-supported restoration. B, transepithelial-supported restoration. 95
Figure 72. Mesh of a FE model of an implant-supported restoration. 96
Figure 73. Mesh of a FE model of a transepithelial-supported restoration. 97
Figure 74. Close views of meshes of the FE models. A, Implant-supported restoration. B, Transepithelial-supported restoration. 98
Figure 75. Boundary conditions of the model. 99

Figure 76. Load application. A, Fatigue load case. B, Screw loosening load case. 100
Figure 77. Model of an implant-supported restoration with a sphere refinement. A, section view. B, Detail of the progressive spherical refinement. 102
Figure 78. FE model of quarter of the specimen geometry. 103
Figure 79. Mesh of a notched specimen FE model. A, Complete model. B, Closer view of the notch. C, Detail of the progressive sphere refinement. 104
Figure 80. Boundary conditions of the model and external load application. 104
Figure 81. INSTRON E3000 Electropuls. A, General view with a generic set-up. Image courtesy of Instron B, Set-up for dental implant testing according to ISO 14801.[141] 106
Figure 82. A, Assembly of the fixture tooling designed for self-loosening tests. B, Drawing of the fixture tooling. C, Section view. 107
Figure 83. Hourglass shaped specimens made of CP4 Titanium. A, Whole specimen. B, View of the notch. 108
Figure 84. Test bench set-up for specimen fatigue tests. A, General view. B, View of the specimen and grips. 109
Figure 85. Specimen failures. A, Specimen with a non-negligible misalingment. B, Aligned specimen. 110
Figure 86. Designed tooling to limit the rotation of the lower head (actuator). A, General view. B, Close up view. 110
Figure 87. A, Schematic of a cam-follower mechanism. B, Schematic of a radial engine used in aviation. 112
Figure 88. Detail of the mechanism of one arm of the test bench... 113
Figure 89. A, Loading block with the removable plate in contact with the specimen. B, Detailed view of the removable plate and the rollers. 113
Figure 90. Rigid body dynamics of the mechanism of one arm of the test bench. A, Diagram. B, Schematic with force directions. 115
Figure 91. Top view of the test bench. 116
Figure 92. Software interface of the test bench. 117
Figure 93. Example of testing to obtain 16 experimental results. 117

Figure 94. Notched pins for test bench validation. A, General view. B, Notch view. 118
Figure 95. Fatigue data points and linear regression models of all tests benches compared. 119
Figure 96. IN-I4.5-P4.1 dental restoration used for experimental tests. 124
Figure 97. Fatigue failure sections on the prosthetic screws of IN-I4.5-P4.1. A, Screw head. B, First thread in contact. 125
Figure 98. Fatigue results of all fatigue tests performed on the IN-I4.5-P4.1 dental restoration. 125
Figure 99. F-N linear models of the IN-I4.5-P4.1 dental restoration at each of the three tightening torques (lines) along with the experimental fatigue results (markers). 126
Figure 100. A, FE model of IN-I4.5-P4.1 dental restoration. B, Contact reactions on the screw head contact surface (section A) and fatigue failure section (section B). 127
Figure 101. Force reactions under the screw head (section A in Figure 100B). A, Axial force F_a. B, Transverse force F_t. C, Bending moment M. 128
Figure 102. Forces in the failure section (section B in Figure 100B). A, Axial force F_a. B, Bending moment M 129
Figure 103. FEA performed to asses the parameters in equations (134) and (135). A, Axial case to calculate the effective area A. B) Bending case to calculate the inertia I. 130
Figure 104. Nominal normal stress (with axial and bending components) in the screw thread according to equation (133). 131
Figure 105. Mean and alternating components of the nominal stress in the screw thread versus the external load F. 131
Figure 106. Haigh diagram and Walker fitting curves. 132
Figure 107. Steps of the methodology proposed to predict the fatigue life of dental restorations in which the critical component is the prosthetic screw. 133
Figure 108. Dental restorations under study. 135
Figure 109. F-N curves of the dental restorations under study: experimental tests (markers) and linear model (lines). Data points with rhombus markers were obtained in the previous test campain (section 3.1.1). 136

Figure 110. FE models. A, IN-I5.5-P5.5 (2,365,587 DoF). B, IN-I5.5-P4.1 (2,202,267 DoF). C, EX-I4.5-P4.1 (1,671,387 DoF). 138
Figure 111. Experimental fatigue data points (markers), F-N linear regression (solid blue line), confidence bands (dotted lines), prediction intervals (dashed lines) and the F-N obtained using the prediction methodology (solid red line) for IN-I4.5-P4.1. Data points with rhombus markers were obtained in a previous test campaign (section 3.1.1). 138
Figure 112. Experimental fatigue data points (markers), F-N linear regression (solid blue line), confidence bands (dotted lines), prediction intervals (dashed lines) and the F-N obtained using the prediction methodology (solid red line) for IN-I5.5-P4.1. 139
Figure 113. Experimental fatigue data points (markers), F-N linear regression (solid blue line), confidence bands (dotted lines), prediction intervals (dashed lines) and the F-N obtained using the prediction methodology (solid red line) for IN-I5.5-P5.5. 139
Figure 114. Experimental fatigue data points (markers), F-N linear regression (solid blue line), confidence bands (dotted lines), prediction intervals (dashed lines) and the F-N obtained using the prediction methodology (solid red line) for EX-I4.5-P4.1. 139
Figure 115. Experimental results versus methodology life prediction (all tests). 140
Figure 116. Experimental results versus methodology life prediction (using average life values). 141
Figure 117. Experimental fatigue data points (markers), F-N linear regression (solid blue line), confidence bands (dotted lines), prediction intervals (dashed lines) and the F-N obtained using the theoretical prediction methodology with the new fitting parameters (solid red line) for IN-I4.5-P4.1..... 142
Figure 118. Experimental fatigue data points (markers), F-N linear regression (solid blue line), confidence bands (dotted lines), prediction intervals (dashed lines) and the F-N obtained using the theoretical prediction methodology with the new fitting parametres (solid red line) for IN-I5.5-P4.1..... 142

Figure 119. Experimental fatigue data points (markers), F-N linear regression (solid blue line), confidence bands (dotted lines), prediction intervals (dashed lines) and the F-N obtained using the theoretical prediction methodology with the new fitting parametres (solid red line) for IN-I5.5-P5.5..... 142
Figure 120. Experimental fatigue data points (markers), F-N linear regression (solid blue line), confidence bands (dotted lines), prediction intervals (dashed lines) and the F-N obtained using the theoretical prediction methodology with the new fitting parametres (solid red line) for EX-I4.5-P4.1..... 143
Figure 121. Experimental results versus life prediction with the new fitting parameters (average values)..... 143
Figure 122. Transepithelial-supported restorations under study: UNIT-H2, UNIT-H4, and MULTI-IM-H2..... 145
Figure 123. Experimental tests performed on the restorations in Figure 122..... 146
Figure 124. FE models of the transepithelial-supported restorations under study. A, UNIT-H2. B, UNIT-H4. C, MULTI-IM-H2..... 146
Figure 125. Experimental results versus life prediction for transepithelial-supported restorations (all tests)..... 147
Figure 126. Surfaces at the valley of the first engaged thread of the screw. A, Screw used in one of the transepithelial-supported restorations studied. B, Screw used in one of the implant-supported restorations studied. 148
Figure 127. Experimental results versus theoretical life prediction for transepithelial-supported restorations with the new fitting parameters (all tests)..... 149
Figure 128. Experimental results versus theoretical life prediction for transepithelial-supported restorations with the new fitting parameters (using average life values)..... 149
Figure 129. Experimental fatigue data points (markers), F-N linear regression (solid blue line), confidence bands (dotted lines), prediction intervals (dashed lines) and the F-N obtained using the prediction methodology with the new fitting parameters in equation (138) (solid red line) for UNIT-H2. 150

Figure 130. Experimental fatigue data points (markers), F-N linear regression (solid blue line), confidence bands (dotted lines), prediction intervals (dashed lines) and the F-N obtained using the prediction methodology with the new fitting parameters in equation(138) (solid red line) for UNIT H4. 151
Figure 131. Experimental fatigue data points (markers), F-N linear regression (solid blue line), confidence bands (dotted lines), prediction intervals (dashed lines) and the F-N obtained using the prediction methodology with the new fitting parameters in equation (138) (solid red line) for MULTI-IM H2..... 151
Figure 132. All implant-supported restorations coupled isolating one variable in each case. 154
Figure 133. IN-I4.5-P4.1 versus IN-I5.5-P4.1: effect of increasing implant body diameter by 1mm. 155
Figure 134. IN-I5.5-P4.1 versus IN-I5.5-P5.5: effect of increasing implant platform diameter by 1.4mm. 156
Figure 135. IN-I4.5-P4.1 versus EX-I4.5-P4.1: effect of using an external instead of an internal butt-joint connection..... 157
Figure 136. Transepithelial-supported restorations under study: UNIT-H2, UNIT-H4, and MULTI-IM-H2..... 158
Figure 137. IN-I4.5-P4.1 versus UNIT-H2: effect of using a transepithelial-supported restoration instead of an implant-supported restoration..... 159
Figure 138. UNIT-H2 versus MULTI-IM-H2: effect of using a non-rotational or rotational connection on fatigue behavior of transepithelial-supported dental restorations..... 159
Figure 139. UNIT-H2 versus UNIT-H4: effect of transepithelial heigh on fatigue behavior of dental restorations. 160
Figure 140. Screw head socket. A, Shape obtained by broaching. B, Shape obtained by milling. 162
Figure 141. Cylinders with the socket compatible with milling process used in maximum torque tests. 162
Figure 142. A, Original prosthetic screw (INTTUH). B, Proposed screw design with a milling compatible head socket. 163
Figure 143. Fatigue failure of the new design of the screw at the first engaged thread. 163

Figure 144. Thread profile. A, Cut thread. B, Rolled thread. 165
Figure 145. Surface roughness measurements. A, Cut thread. B, Rolled thread. 166
Figure 146. Diffractometer: general view and detail of the specimen. 168
Figure 147. Fatigue data, linear models (F-N curves), and 95% confidence bands for IN-I-4.5P-4.1 dental implants assemblies mounting cut- and roll-threaded screws. In the case of cut-threaded screws, data with rhombus markers were obtained in section 3.1.1 while those marked with points were obtained in section 3.2.1. 170
Figure 148. Fatigue failure of the prosthetic screw. A, First engaged thread in cut-threaded screw. B, Head-shank transition in roll-threaded screw. 170
Figure 149. A, Unnotched hourglass specimens used for fatigue characterization of CP4 Titanium. B, Detail of R0.137 notched specimen. C, Detail of R0.164 notched specimen. D, Detail of R0.650 notched specimen. 175
Figure 150. Fatigue data (markers) and linear regression models (lines) of all tested specimens. 175
Figure 151. Nominal stresses corresponding to 50,000 cycles for each specimen under study. 178
Figure 152. EF model of the R0.137mm notched specimen. A, Complete model. B, Closer view of the notch. C, Detail of the progressive sphere refinement. 179
Figure 153. Findley and Dang Van effective stresses versus the sphere radius (critical distance) and the critical distances corresponding to effective stress at 50,000 cycles. A, R0.137mm notched specimen. B, R0.164mm notched specimen. C, R0.650mm notched specimen. 180
Figure 154. Findley and Dang Van effective stresses versus the sphere radius (critical distance) and their corresponding stress gradients at the root of the notch. A, R0.137mm notched specimen. B, R0.164mm notched specimen. C, R0.650mm notched specimen. 182
Figure 155. Critical distance (sphere radius) versus normalized stress gradient for the three notched specimens, along with the linear models proposed. 183

Figure 156. Steps of the methodology proposed to predict fatigue life of dental restorations whose critical component is the dental implant. 185
Figure 157. Dental restorations under study. A, IN-I3.3-P4.1. B, IN-I3.0-P3.0. C, EX-I2.5-P3.5. 187
Figure 158. Experimental fatigue results of each dental implant tested along with their normal distribution function, and the mean value. A, IN-I3.3-P4.1 tested at 220N. B, IN-I3.0-P3.0 tested at 140N. C, EX-I2.5-P3.5 tested at 130N. 188
Figure 159. Crack initiation section located at the thread notch immediately below the limit of the embedment of the implant with the specimen holder (IN-I3.0-P3.0)..... 188
Figure 160. FE models and details of the mesh of the crack initiation point. A, IN-I3.3-P4.1 model section. B, IN-I3.0-P3.0 FE model section. C, EX-I2.5-P3.5 model section. D, Crack initiation point mesh refinement of IN-I3.3-P4.1. E, Crack initiation point mesh refinement of IN-I3.0-P3.0. F, Crack initiation point mesh refinement of EX-I2.5-P3.5..... 190
Figure 161. Findley and Dang Van effective stress versus the sphere radius (critical distance) and the stress gradients at the root of the notch. A, IN-I3.3-P4.1. B, IN-I3.0-P3.0. C, EX-I2.5-P3.5. 191
Figure 162. Critical distance (sphere radius) versus normalized stress gradient for the dental restorations under study with the linear models proposed. 192
Figure 163. Findley and Dang Van effective stress values obtained for fatigue calculations. A, IN-I3.3-P4.1. B, IN-I3.0-P3.0. C, EX-I2.5-P3.5. 193
Figure 164. Experimental fatigue results of each dental implant tested and the fatigue life prediction by using the proposed methodology and Findley effective stresses..... 194
Figure 165. Experimental fatigue results of each dental implant tested and the fatigue life prediction by using the proposed methodology and Dang Van effective stresses..... 195
Figure 166. Experimental results versus methodology life prediction (Findley)..... 196
Figure 167. Experimental results versus methodology life prediction (Dang Van)..... 196

Figure 168. All dental restorations under study coupled isolating one variable in each case: Platform diameter, implant body diameter, and the use of a transepithelial-supported restorion versus an implant-supported restoration. 201
Figure 169. Portable device able to perform a static load meeting the requirements in ISO 14801.[141] 203
Figure 170. Experimental setup in the Micro-CT cabin. 203
Figure 171. Radiograph of loaded implant at 4μm/pixel sampling. Gap measurement. A, General view. B, Detail of the IAC microgap. Measurements were taken manually using ImageJ2 software. 204
Figure 172. IAC microgap measurements versus applied load and the power regression model for IN-I4.5-P4.1. Each marker corresponds to a different sample. 205
Figure 173. IAC microgap measurements versus applied load and the power regression model for IN-I5.5-P4.1. Each marker corresponds to a different sample. 205
Figure 174. IAC microgap measurements versus applied load and the power regression model for IN-I5.5-P5.5. Each marker corresponds to a different sample. 205
Figure 175. IAC microgap measurements versus applied load and the power regression model for MULTI-IM-H2. Each marker corresponds to a different sample. 206
Figure 176. Power regression models of microgap value versus external applied load for each dental restoration under study. Solid lines correspond to the tested load range. Dashed lines correspond to model extrapolation 206
Figure 177. Torque versus transverse load: slip limit curves. Nassar model[125,126] and new equations approximated by parabolic curves. 212
Figure 178. Steps of the methodology proposed. 214
Figure 179. IN-I3.3-P4.1 dental restoration. A, Original tetralobular connection. B, Modification on abutment tetralobular connection to bring about self loosening. 215
Figure 180. FE model of IN-I3.3-P4.1. 216
Figure 181. Box and whisker plot of all untightening operations performed before cyclic loading. 218

Figure 182. External load values that cause self-loosening obtained by using the staircase method at three tightening torques. A, 10Ncm. B, 15Ncm. C, 20Ncm. 219

List of Tables

Table 1. Percent of replication depending on the type of test.[62] 31
Table 2. Number of specimens for finite life determination depending on o the type of test.[62] 31
Table 3. Values of α_S and β_S depending on the equation used for the Sines method.[53] 58
Table 4. Chemical composition of materials used in implant and prosthetic component manufacturing process. 91
Table 5. Coefficients of friction values measured in the pin-on-disk test. 93
Table 6. Stiffness and maximum working loads of the springs used on the test bench. 114
Table 7. All the implant-supported restorations under study, including the previously studied IN-I4.5-P4.1. 135
Table 8. All the transepithelial-supported restorations under study, all of them mounting a different transepithelial component on the IIPSCA4513 dental implant. 144
Table 9. Surface roughness average R_a and mean roughness depth R_z in the different paths shown in Figure 126 of two screws used in: transepithelial-supported restoration and implant-supported restoration..... 148
Table 10. Maximum torque test results for both socket designs: original design (can only be produced by broaching) and new design (compatible with milling). 163
Table 11. Dimensions of thread profile..... 166
Table 12. Surface roughness parameters. 166
Table 13. Mean values and standard errors of compressive residual stresses in threaded area. 168
Table 14. Maximum loads measured in static tests. 171
Table 15. $(\sigma_{nom})_{unnotched}/(\sigma_{nom})_{notched}$ ratio versus the number of cycles. 176

Table 16. Nominal stresses (at 50,000 cycles) and their corresponding axial loads. 178
Table 17. Findley and Dang Van critical distances for the three notched specimens under study. 181
Table 18. Normalized stress gradients for Findley and Dang Van methods for the three notched specimens under study. . 183
Table 19. All the narrow implant-supported restorations under study. 186
Table 20. Findley and Dang Van stress gradient values at the root of the notch for all dental restorations under study. 192
Table 21. Findley and Dang Van critical distance values for all dental restorations under study. 192
Table 22. Findley and Dang Van effective stress values for all dental restorations under study. 194
Table 23. Predicted external load values that cause self-loosening in the dental implant under study at each tightening torque: 10, 15, and 20 Ncm. 217
Table 24. External load values that cause self-loosening in the dental implant under study: methodology prediction versus experimental results..... 220

Acronyms

ASME: American Society of Mechanical Engineers

BTI: Biotechnology Institute

CP: Commercially Pure

CP4: Commercially Pure Grade 4

DuMAS: Département de Durabilité Matériaux des Assemblages et des Structures

ELI: Extra Low Interstitial

ENSAM: Ecole Nationale Supérieure d'Arts et Métiers

FE: Finite Element

FEA: Finite Element Analysis

FEM: Finite Element Method

GCF: Giga-Cycle Fatigue

GR5: Grade 5

HCF: High Cycle Fatigue

IAC: Implant-Abutment Connection

LCF: Low Cycle Fatigue

MCC: Minimum Circumscribed Circumference

MCE: Minimum Circumscribed Ellipse

MD: Maximum Damage

MSSR: Maximum Shear Stress Range

SEM: Scanning Electron Microscope

TCD: Theory of Critical Distances

UPV/EHU: University of the Basque Country

VHCF: Very High Cycle Fatigue

WCC: Tungsten Carbide Carbon

Context, objectives, and document structure

Context and motivation

Dental restorations are a widely used option to replace a single tooth as well as several teeth.[1] The simplest screw-retained dental restoration (see Figure 1) consists of a dental implant, that is inserted into the bone, and a crown, that is cemented on an abutment, and all together is assembled on the implant by means of a prosthetic screw. The screw is properly tightened so that the structural integrity of the dental restoration is achieved.

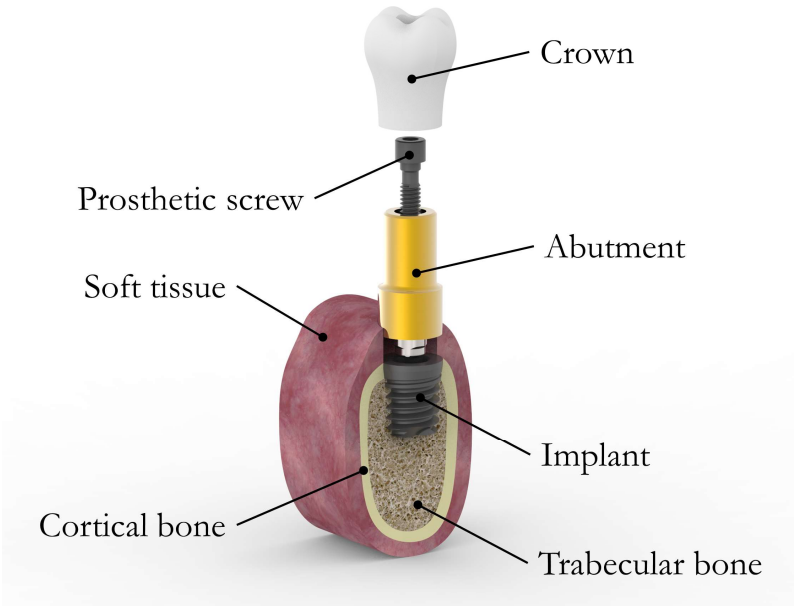

Figure 1. Implant-supported restoration inserted in mandibular bone.

Even though the use of dental implants for teeth replacement is a highly predictable treatment with a high success rate, any case could result in either biological or mechanical complications. The most common mechanical problems, in which this PhD Thesis is focused on, are self-loosening of the

prosthetic screw, fatigue failure of some of its components, and microgap formation in implant-abutment connection (IAC). There is a large amount of works that analyze the behavior of the restoration in patients' mouths (in-vivo) by means of retrospective studies. In those studies, success ratios of different dental restorations and clinical cases may be found. Besides this, there are other studies that analyze the mechanical behavior of dental restorations through experimental tests in laboratories (in-vitro) or by simulations by means of Finite Element Analysis (FEA). Nevertheless, these studies are usually focused on making comparisons among various cases (implant geometries, connection types, implant arrangement in the mouth, and so on) and obtaining direct clinical conclusions, without more extensive investigation into the phenomena or aiming to predict or avoid them. This may be explained by the fact that most of these works are published in journals whose target readers are clinicians, with works scarcely published in journals aimed to engineers or, at least, with an engineering approach.

It must be kept in mind that a dental restoration is, in fact, a screwed joint, that is, a mechanical element that has been extensively studied over the years in the field of mechanical engineering. Moreover, the aforementioned three mechanical faults that may be found on dental restorations are also common in screwed joints used for more general purposes.

Therefore, this PhD Thesis aims to bring together all the expertise acquired over the years by the industry regarding screwed joints and transfer it to the industry of dental implantology, creating predictive methodologies and in-depth studies that help provide better understanding of these phenomena and to be able to predict and avoid them in future dental implant designs.

Aim and scope

Based on the aforementioned, the main objective of this PhD Thesis is, first, to explain the phenomena that cause the most common mechanical failures in dental restorations (fatigue, screw loosening and microgap formation) from a theoretical point of view, based on relevant literature.

Once understood the phenomena, experimental tests are carried out to see how these phenomena affect the behavior of dental restorations. After observing and understanding the mechanical behavior of dental restorations in depth, those with the biggest impact are identified and the keys by which to reduce such failures are provided. Furthermore, in the case of fatigue failure and

prosthetic screw loosening, theoretical methodologies, based on simple expressions fed by FEA, capable of predicting the occurrence of such faults are developed. These methodologies will allow R&D engineers to compare different designs without the need for extensive experimental test campaigns to optimize the design. In addition, the methodologies presented in this PhD Thesis have a didactic component as they allow for the understanding of the performance of dental restorations and to identify the key parameters to delay or even avoid the restoration fault.

Therefore, the target audience for this PhD Thesis are mechanical engineers and R&D teams, unlike the majority of publications in the field of implant dentistry, focused on clinicians.

In addition to the benefit of the in-depth study of the various mechanical phenomena and methodologies mentioned, clinical conclusions derived from the various studies performed will also be presented in this PhD Thesis. These conclusions may be of interest to engineers or R&D teams as well as to clinicians.

Document structure

As explained throughout the chapter, this PhD Thesis studies the mechanical behavior of different dental restorations and develops various prediction methodologies that allow for the optimization of the design of a dental implant and its prosthetic components against different types of mechanical faults. In particular, it is focused on the study of the three most common mechanical problems suffered by dental implants: fatigue fracture of some of its components, the gradual loss of preload (loosening) suffered by the prosthetic screw due to masticatory loads, and the opening of small cavities called microgaps in the IAC that, over time, can cause infections due to bacterial colonization. In order to develop all the content in a structured way, this PhD Thesis document has been divided into 8 chapters which are briefly described as follows.

Chapter 1 explains what a dental restoration is, presents the elements that it consists of and explains that, in essence, it behaves like a screw-retained joint. Next, the necessary theoretical foundations concerning screw connections, microgap (or leakage), fatigue phenomena, and screw loosening are explained for the correct understanding of the methodologies and tools used and

developed in this PhD Thesis. Finally, a state of the art of fatigue, loosening and microgap phenomena in dental restorations is presented.

For the study of the mechanical behavior of dental restorations, different numerical models and experimental tests have been performed in this PhD Thesis. Chapter 2 initially describes the types of dental restorations studied. Then, the Finite Element (FE) models used are explained. The simplifications assumed in the geometry, meshing, boundary conditions, and so on, are defined. Although each model will undergo small variations depending on the particular case being analyzed (geometry, prosthetic screw preload and load application), the basis of the FE models will always be the same. In addition to this, this chapter presents the test benches used for the various experimental tests. Finally, an innovative fatigue test bench prototype developed within the scope of this PhD Thesis is presented, which is capable of testing up to 8 dental restorations simultaneously.

Chapter 3 presents a methodology for predicting the fatigue life of dental restorations where the critical component is the prosthetic screw. First, the methodology is defined, and the theoretical analyses and experimental tests performed for the fitting of the methodology parameters are detailed. Then, the accuracy of the methodology is tested for a wide range of dental restorations apart from the one used to create the methodology. Finally, taking advantage of the numerous experimental tests carried out to validate the fatigue life prediction methodology in different dental restorations, the effect on fatigue behavior of different parameters is determined. These parameters are the tightening torque of the prosthetic screw, different geometric parameters of the dental implant (diameter of the implant body, diameter of the platform and connection type) and the use of transepithelial-supported restorations instead of the use of classic implant-supported restorations. In conclusion, a methodology that allows for the estimation of the fatigue life of dental restorations in which the critical component is the prosthetic screw is presented, giving rise to a powerful design tool that allows for the study of the effect of different parameters on the restoration life in a versatile and efficient way.

Continuing with the fatigue analysis of the prosthetic screw, Chapter 4 explores improvements that are beyond the scope of the fatigue life prediction methodology presented in Chapter 3, such as manufacturing methods. On the one hand, the option of milling the screw head socket where the torque wrench tip is inserted is studied, in order to avoid broaching, a much more aggressive

manufacturing process. On the other hand, the alternative of manufacturing the threads of the prosthetic screw by rolling instead of cutting has been studied, considerably improving the fatigue behavior of the screw and, therefore, of the whole dental restoration.

Chapter 5 is focused on the fatigue behavior of the implant, setting aside the prosthetic screw. First, the effect of stress concentration on the fatigue behavior of the material the implants are made of is studied. Then, in order to apply the Theory of Critical Distances (TCD), a linear model that relates the normalized stress gradient at the root of the notch versus the critical distance is defined. After this research, a fatigue life prediction methodology is presented for dental restorations in which the critical component is the dental implant. The accuracy of the methodology is then tested for various dental restorations.

In Chapter 6 the microgap formation in IAC is experimentally analyzed on different dental restorations under in-situ loading. To carry out the experimental measurements, a portable tooling capable of applying static loads on any dental restoration has been developed. Due to its portability, the tooling can be inserted into a Micro-CT cabin so that X-ray images can be obtained while a load is applied to the implant in-situ. From these tests, the effect on the microgap of varying the diameter of the implant body, the diameter of the platform and the use of a transepithelial-supported restoration instead of the classical implant-supported restoration has been quantified.

Chapter 7 studies the loosening phenomenon of the prosthetic screw. A methodology is presented to predict whether or not loosening will occur in a dental restoration under certain loading conditions. This methodology combines FEA, to determine the forces acting on the screw when an external load is applied, with a mathematical formula to estimate if screw loosening will occur. The methodology is then validated by experimental testing on dental restorations under alternating transverse loading.

Finally, Chapter 8 provides the final conclusions of this PhD Thesis as well as the proposed future work. In addition, the publications and congress presentations derived from this work carried out are shown.

1 Introduction and background

The objective of this PhD Thesis, as explained in the 'Context, objectives, and document structure' section, is to study the phenomena that cause the most common mechanical faults in dental restorations. In order to carry out this work rigorously, this chapter aims to explain the theoretical principles on which the studies and methodologies developed throughout this PhD Thesis are based.

First, in section 1.1 it is explained what a dental implant is, the main components that form a dental restoration are identified and the basic surgical concepts are explained.

Since, from a mechanical point of view, a dental restoration is, to all intents and purposes, a screwed joint, it has the advantage that the most common faults in dental restorations have already been the subject of studies on screwed joints for decades. Accordingly, in section 1.2, the fundamentals of screwed joints are explained: the screwed joint preload concept, why preload is a critical aspect of the screwed joint, and its relationship to screw torque. Based on this, it is explained how a screwed joint works under axial and transverse loads. The most frequent faults in screwed joints are also explained: fatigue failure, self-loosening of the screw and microgap formation or leakage.

Having understood how screwed joints work and having presented the most frequent faults, sections 1.3, 1.4, and 1.5 provide in-depth explanations of each of the three phenomena and their existing theories and analysis models.

Finally, a literature review of how fatigue, screw loosening and microgap affect dental restorations is provided in section 1.6.

1.1 Dental restorations: an overview

Dental implants are a widely used option to replace a single tooth as well as several teeth.[1] The simplest screw-retained dental restoration consists of a dental implant, that is inserted into the bone, and a crown, that is cemented on

an abutment, and all together is assembled on the implant by means of a prosthetic screw (see Figure 1). The screw is properly tightened so that the structural integrity of the dental restoration is achieved.

Before further explanation of prosthetic components, it must be briefly explained how a dental implant is applied. Figure 1 shows a mandibular bone; that is, the restoration shown is replacing a lower tooth. Upper teeth, instead, are found in the maxilla.

Both the maxillary and mandibular bones are composed by an inner less dense bone called the trabecular bone and covered by a shell of a denser bone known as the cortical bone as can be seen in Figure 2. Depending on the combinations of these two bones, the maxilla or the mandible of the patient may be harder to drill, likely providing better stability to the implant (left, in Figure 2), or may be easier to drill, likely providing poor stability (right, in Figure 2).[2]

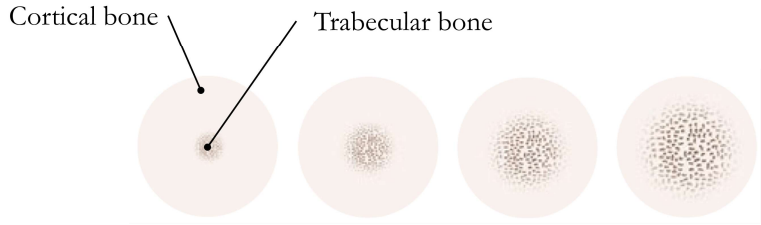

Figure 2. Different bone densities due to proportions of cortical and trabecular bone. Denser bone in the left side and less dense in the right side.[2]

The surgery starts with a crestal incision in the keratinized mucosa (Figure 3A). Then, the drilling process begins with an initial drill that will establish the direction for the rest of the drilling performed afterwards (Figure 3B). The location for the implant is, then, prepared with a pilot drill (Figure 3C). Depending on the bone density and the implant size, further drills may be performed after these two mentioned ones (Figure 3D). Figure 3E shows an example of a complete drilling procedure for a specific implant and bone density. Next, the implant is inserted by means of a surgical motor, completing the insertion to the desired level manually by means of a surgical torque wrench (Figure 3F). Finally, the implant mount (blue part in Figure 3F) is removed.

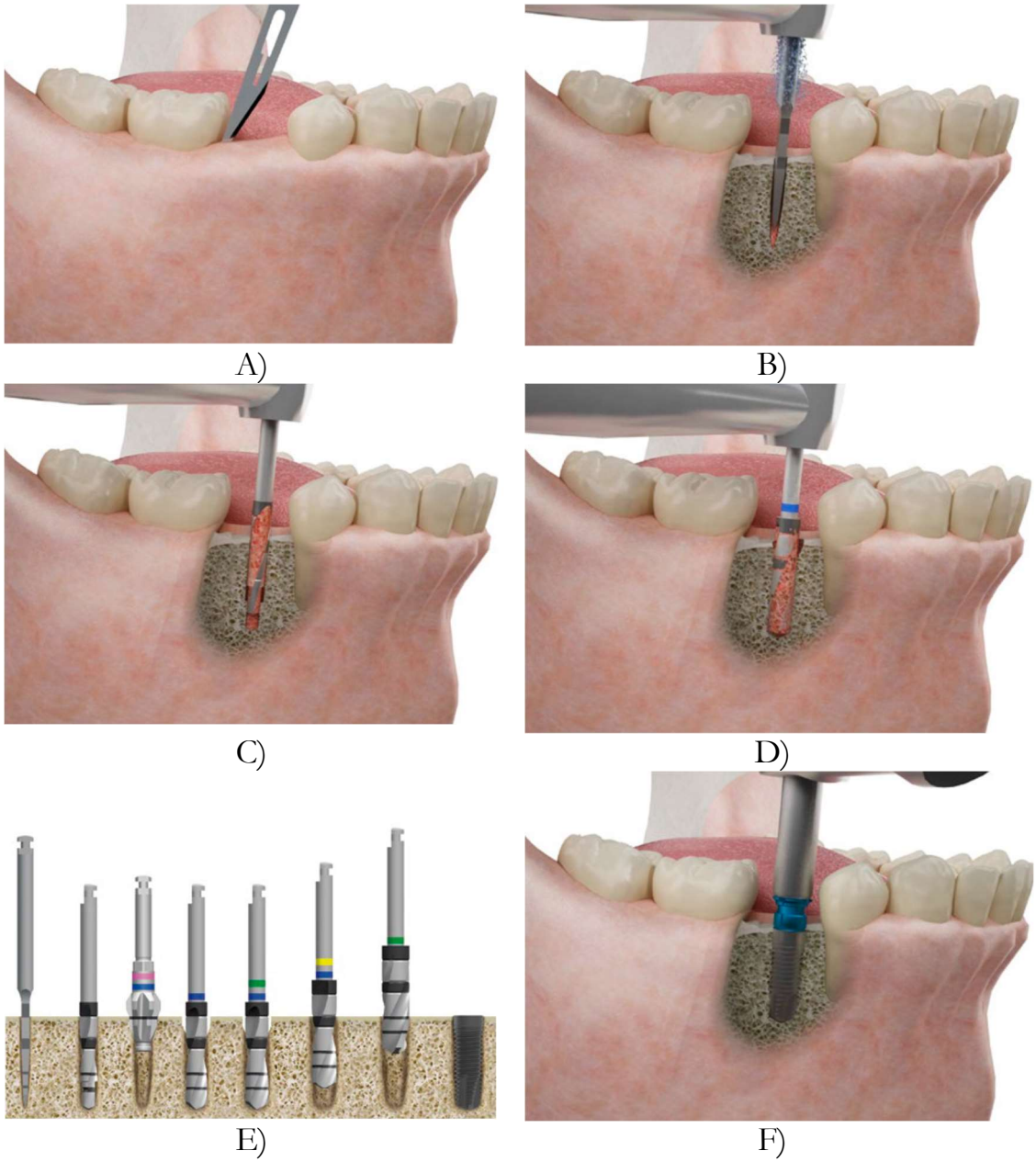

Figure 3. Step by step drilling process and implant positioning. A, Incision. B, Initial drill. C, Pilot drill. D, Further drilling after pilot drilling. E, Example of a complete drilling procedure for a specific implant. F, Implant insertion.[2]

Once the implant is inserted, 3 different techniques may be used, as long as the patient has no pathological parafunctional habits.[2]

In one-stage surgery, as soon as the implant is placed, a healing abutment is assembled on the implant and the mucosa is sutured around the healing abutment (see Figure 4A). No complementary surgical techniques are performed. Once the implant is osseointegrated and the implant stability is ensured, the rest of prosthetic components are assembled on the implant.

In case correct primary stability of the implant is not achieved and/or additional surgeries are required, two-stage surgery must be performed. In the first stage, the implant is inserted, a healing cap is positioned on the implant, and the flap is sutured over it (see Figure 4B). It shall be reopened (second stage) after a healing period of 3-5 months depending on the bone quality, and either a healing abutment (see Figure 4A) or the rest of the prosthetic components (see Figure 4C) are applied, depending on the case.

If sufficient primary stability is achieved in the implant directly after the insertion, immediate loading is allowed, i.e., the prosthetic elements can be assembled on the implant after the insertion (or within the first week after insertion) as can be seen in Figure 4C.

A) B) C)

Figure 4. A, Inserted implant with a healing abutment and sutured mucosa around it. B, Inserted implant with a healing cap and sutured mucosa over it. C, Inserted implant with a transepithelial element and sutured mucosa around it.[2]

There are also monobloc or monotype implants that are composed of a single element and the crown is cemented on it. Nevertheless, once shown how complex surgeries are, it may be understood why screw-retained dental restorations are more versatile. They are able to adapt to each one of the three surgeries presented, they allow the clinician to remove the prosthetic components to make any correction or for cleaning purposes and, finally, in the event of further dental loss, they allow for new planning of the mouth restoration, taking advantage of the implant already fitted and changing only the prosthetic components.

Following with the screw-retained dental restorations, in the beginning of this section a simple restoration consisting of an implant, an abutment and a prosthetic screw was presented. This restoration is known as an implant-supported restoration, directly attached restoration or direct-to-implant

restoration (Figure 5A). Besides this, a transepithelial element can also be added to the restoration between the implant and the abutment as can be seen in Figure 5B. The main advantage of a transepithelial element is that it may be placed (between the implant and the healing abutment) in one-stage surgery immediately after placing the implant, allowing for further restoration steps to be performed at tissue level rather than at bone level, considerably reducing clinical complications (see Figure 5C).

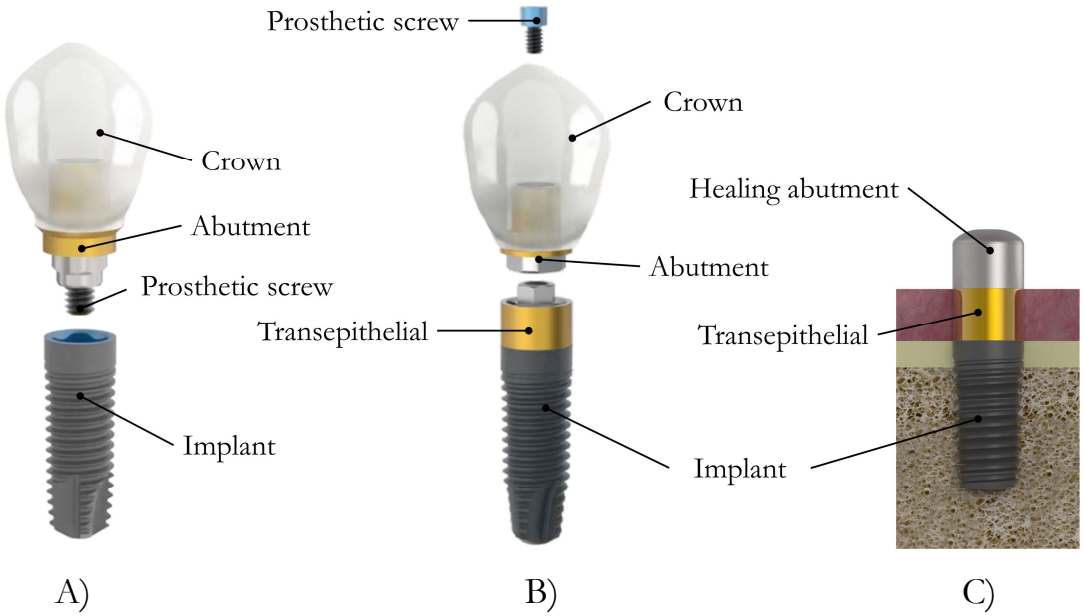

Figure 5. A, Implant-supported restoration. B, Transepithelial-supported restoration. C, One-stage surgery using a transepithelial component.[2]

After explaining the most common basic components that form a dental restoration, the most important geometric parameters - not only from a mechanical but also from a clinical point of view - must be presented.

IAC is one of the most important parameters of a dental restoration since, along with the screw, it determines the structural integrity of the assembly.[3–6] Besides this, the connection must ensure correct sealing so that bone health is not compromised by possible bacterial colonization in connection with cavities or mismatches.[7–11] The most common connections are the external and internal butt-joint, and the external and internal conical ones (see Figure 6). There are other connections derived from them or even combining some of them.

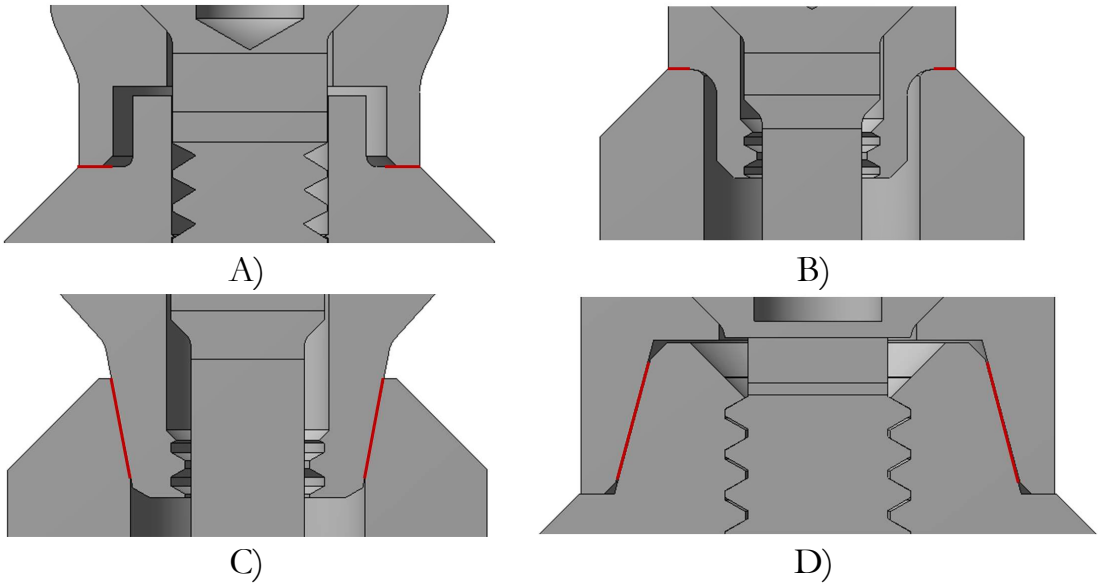

Figure 6. Most common IACs. A, External butt-joint. B, Internal butt-joint. C, Internal conical. D, External conical. Contact surfaces marked in red.

Implant body diameter also plays an important role[12] because, evidently, the thicker an implant is, the better mechanical performance it will have. The same occurs with implant platform diameter: the larger the platform diameter the more robust connection.[13] Nevertheless, the size of the implant is often limited by the bone dimensions of the patient. Implant length is assumed to be a negligible parameter from a mechanical point of view as long as the stability of the implant in the bone is ensured. From a clinical point of view, instead, implant length may have a slight influence.[14,15] However, the use of short and extra-short implants has increased in recent years due to their high success rate shown in several retrospective studies.[16–20] Some other parameters such as surface treatments, implant external thread geometry or material biocompatibility were not included this PhD Thesis since they are not related to the mechanical behavior of the restorations.

Even though the use of dental implants for teeth replacement is a highly predictable treatment with a high success rate, all cases are prone to either biological or mechanical complications. The most common mechanical problems, that this PhD Thesis is focused on, are briefly presented hereafter.

Microgaps may appear at the IAC,[21] being a proper environment for bacterial colonization.[7–11] The bacteria may spread to peri-implant tissues, leading to chronic inflammation[22–24] and crestal bone resorption.[8,25–29] This is the prelude of peri-implantitis,[30] the main cause of implant loss.[31–33]

Moreover, implants and prosthetic components are subjected to variable loading during their life span.[34,35] This cyclic loading may lead to structural failure in two different ways: on the one hand, fatigue failure of either the implant or the prosthetic screw (with abutment failure very uncommon);[36] on the other hand, preload loss (loosening) of the screwed joint between the implant and the prosthetic components.[4,37–40]

As mentioned before, a dental implant can be considered a screwed joint. For this reason, the basic theory of screwed joints, the concept of preload and its importance in mechanical behavior, its relation to the tightening torque of the screw, and how a screwed joint works under axial and transverse loads are explained in the following section.

1.2 Mechanical behavior of screwed joints

A screwed joint is used to join two or more parts reversibly, unlike welded joints that are permanent. The main function of the assembly process of a screwed joint is to apply a tensile load on the screw, generating a clamping force (preload) between the joined elements and, therefore, ensuring the structural integrity of the assembly.[41–43] The screw preload therefore plays an important role in the mechanical behavior of the assembly.

1.2.1 Screw preload

In the screwed joint shown in Figure 7, the screw is subjected to a preload related to the applied tightening torque. The joined elements are subjected to a compression load while the screw is subjected to a tensile load. Since the joint is statically balanced, the magnitudes of the tensile load (screw) and the compression load (joined elements) are the same. In fact, the joint can be studied as an assembly where the screw and the joined elements are springs (as shown in Figure 8), the first loaded under tension and the second under compression, in equilibrium.

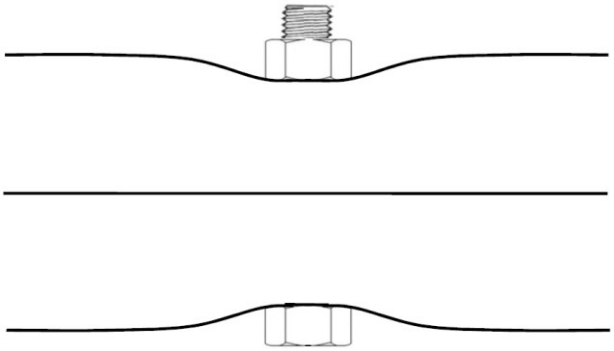

Figure 7. Two sheets joined by a preloaded screwed joint.[3]

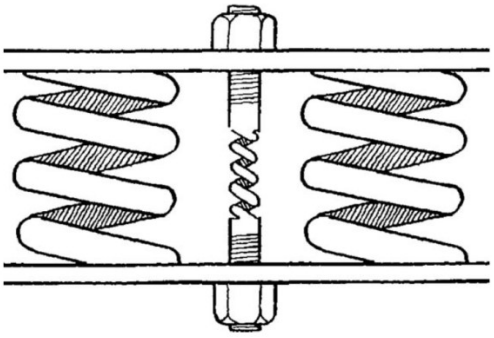

Figure 8. Representation of the stiffnesses of the screw and elements to be joined in the screwed joint in Figure 7.[3]

The stiffness of the joined elements is usually greater than the stiffness of the screw. Hence, since the forces are balanced, the tensile deformation suffered by the screw must be larger than the compressive deformation suffered by the joined elements. Nevertheless, this difference is not always that notable. For example, in dental restorations shown in Figure 6, the resistant sections of the prosthetic screws are closer to the ones of the joined elements, and this is the same for stiffness.

The next equation establishes the balance condition for a screwed joint in the absence of external loads.[44]

$$F_p = F_e = F_s = k_e \cdot \delta_e = k_s \cdot \delta_s \quad (1)$$

Where F_p is the preload force on the screwed joint, F_e is the compression load on the joined elements, F_s is the tensile load on the screw, k_e is the compression stiffness of the joined elements, δ_e is the deformation of the joined elements, k_s is the tensile stiffness of the screw, and δ_s is the deformation of the screw.
The balance status is often represented by a so-called joint diagram, shown in Figure 9. In the diagram, force magnitude is represented on the vertical axis

(always upwards, regardless of whether the force is tensile or compressive) while deformation is represented on the horizontal axis (to the left, compressive, δ_e, and to the right, tensile, δ_s). By means of this joint diagram it can be seen how the force is the same for both the screw and the joined elements and, since the stiffnesses are different, so are the deformations.

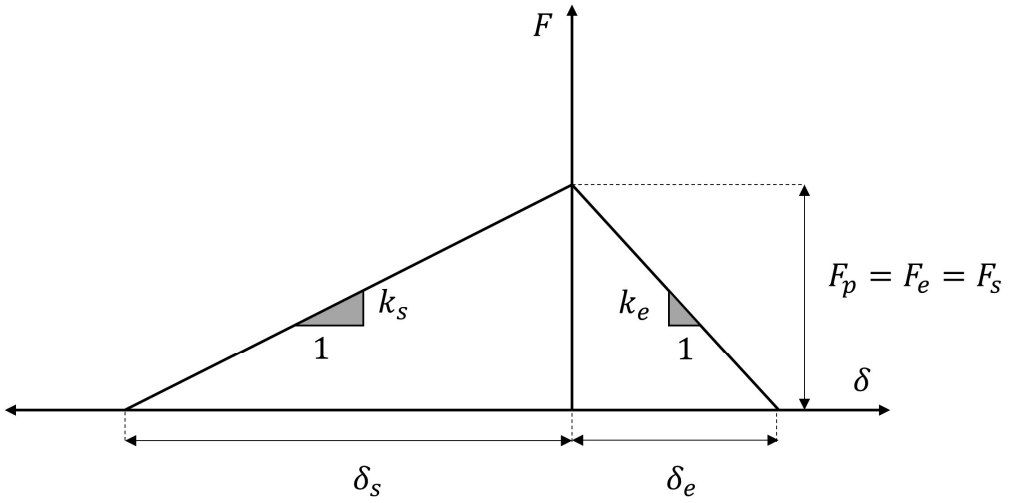

Figure 9. Joint diagram of the screwed joint in Figure 7.

1.2.2 External axial loading

Once understood the behavior of a balanced screwed joint in absence of external loading, in Figure 10 an external axial load is applied to the screw of the joint.

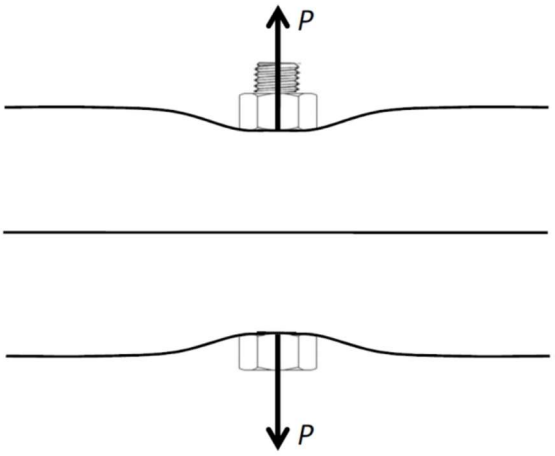

Figure 10. Preloaded joint under external axial load.[3]

When the axial load P is applied, it is split between the screw and the joined elements. The percentage of the P load withstood by the screw and the joined elements is determined by their stiffnesses. Assuming that the P load does not generate a contact loss between the screw and the joined elements, the

deformation increase $\Delta\delta$ suffered by the screw (increasing the initial tension) must be equal to deformation detriment suffered by the joined elements (releasing part of the initial compressive load). Hence, the P load may be defined as the deformation $\Delta\delta$ multiplied by the total stiffness of the joint:

$$P = (k_s + k_e) \cdot \Delta\delta \tag{2}$$

Thus, the total forces assumed by both the screw and the joined elements in the presence of an external axial load are:

$$F_e = F_p - k_e \cdot \Delta\delta = k_e \cdot \delta_e - k_e \cdot \Delta\delta = k_e \cdot (\delta_e - \Delta\delta) \tag{3}$$

$$F_s = F_p + k_s \cdot \Delta\delta = k_s \cdot \delta_s - k_s \cdot \Delta\delta = k_s \cdot (\delta_s - \Delta\delta) \tag{4}$$

The load factor C of the screwed joint is defined by:

$$C = \frac{k_s}{k_s + k_e} \tag{5}$$

Substituting in (3) and (4):

$$F_e = F_p - (1 - C) \cdot P \tag{6}$$

$$F_s = F_p + C \cdot P \tag{7}$$

The joint diagram in Figure 11, shows that starting from the initial preload F_p, the screw axial load increases up to $F_p + C \cdot P$ (upwards, in the diagram), while the force assumed by the joined elements decreases down to $F_p - (1 - C) \cdot P$ (downwards, in the diagram). It must be noted that, in the diagram, the amount of the external load assumed by the joined elements is higher than the amount of load assumed by the screw, because commonly the joined elements are stiffer than the screw. In other words, the screw only withstands the C-th part of the axial load P, rather than the total amount. This is beneficial for mechanical behavior since the screw is usually the critical component of the joint. If the axial load P is high enough to generate contact loss among joined elements (when $F_e = 0$; that is, when $P > F_p/(1 - C)$), the total amount of the external load P will be assumed by the screw, with the axial load withstood by the screw equal to P. This occurs either when the axial load P is very high or when the preload is very low. At this point, the importance of the preload arises. The preload should be high enough so that the contact among the screw and elements joined is guaranteed but not too high such that the screw does not have enough margin to withstand the C-th part of the axial load P without collapsing.

Regarding deformations, the joint diagram shows that the screw deformation increases by the same amount as the amount by which joined elements deformation decreases, $\Delta\delta$. To sum up, in absence of external loads, the common variable is the preload F_p with the deformations δ_e and δ_s being

different. When an axial external load is applied, the common variable is the deformation increment $\Delta\delta$ with the load assumed by each component proportional to their stiffnesses.

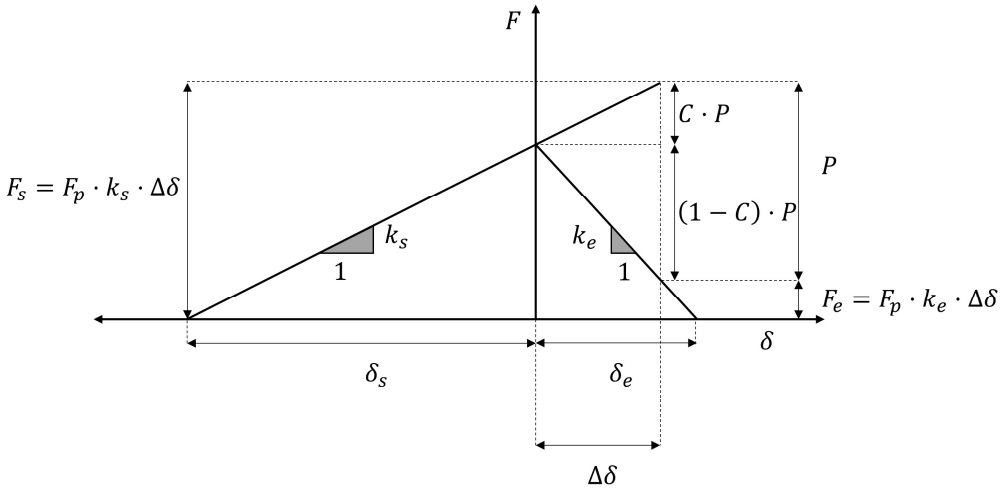

Figure 11. Joint diagram of the screwed joint in Figure 10.

1.2.3 External shear loading

When a screwed joint is subjected to shear or transverse loading (see Figure 12), it may be classified as 'friction type' or 'bearing type', depending on its behavior.[3] The screwed joint will operate as 'friction type' when the transverse load P_t does not overcome the friction force generated between the joined elements (see Figure 13) as established in equation (8). If this condition is fulfilled, the friction force does not allow the joined elements to slip between themselves, whereby the screw is not affected by the transverse load P_t and the screwed joint has structural integrity (see Figure 14).

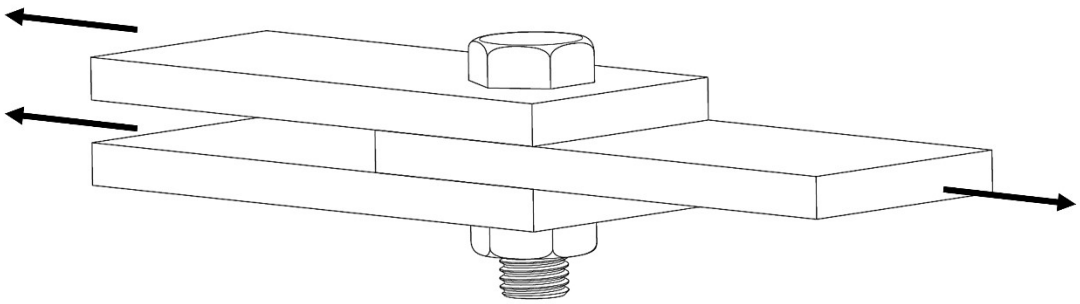

Figure 12. Screwed joint subjected to shear loading.

$$P_t < \mu \cdot F_e \cdot m \tag{8}$$

Where P_t is the transverse load applied, μ is the coefficient of friction between the joined elements, F_e is the axial force assumed by the elements joined, and m is the number of element surfaces in contact.

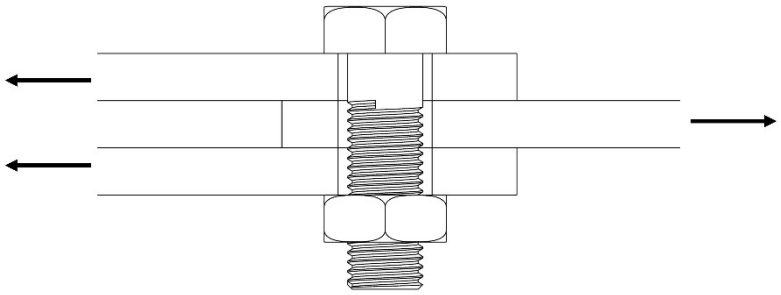

Figure 13. Screwed joint working as a 'friction type' joint.

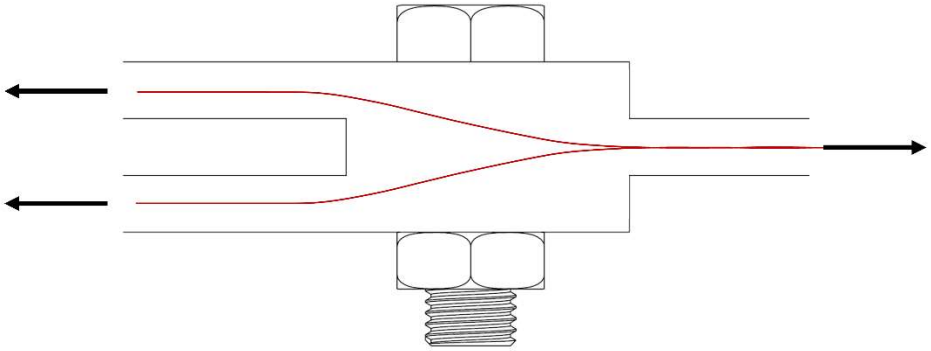

Figure 14. Stress transmission lines on a friction type screwed joint.

By contrast, the screwed joint will operate as 'bearing type' when the transverse load applied P_t exceeds the friction generated between the joined elements, that is:

$$P_t > \mu \cdot F_e \cdot m \tag{9}$$

Hence, the joined elements will suffer slippage between them and the screw will suffer shearing as shown in Figure 15. Nevertheless, bearing type operating conditions is not desirable and can be considered a malfunction due to relative displacements between the screw and the joined elements.

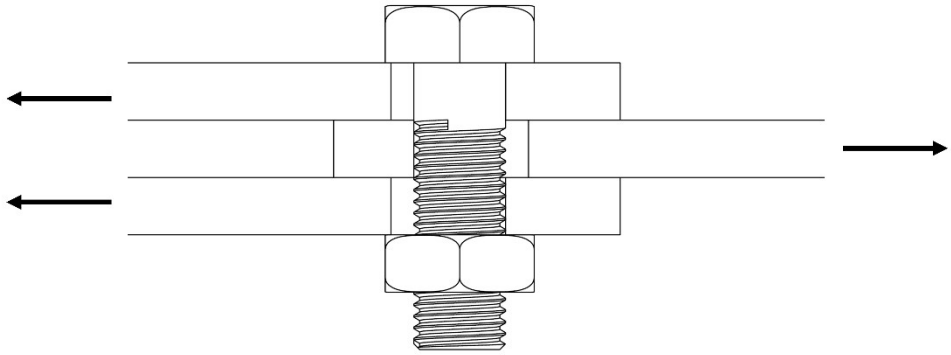

Figure 15. Screwed joint working as 'bearing type' joint.

Once understood how a screwed joint behaves under an external force and once observed the importance of the preload, it is necessary to understand the relationship between the preload and the tightening torque applied on the screw.

1.2.4 Tightening torque-preload relationship

Even though the importance of the preload on mechanical behavior of a screwed joint has been highlighted in sections 1.2.2 and 1.2.3, how the preload is achieved in the screwed joint has not been explained yet. Commonly, also on dental implants, the preload is exerted by applying a tightening torque on the screw. The relationship between the applied screw tightening torque and the obtained preload can be explained by using the analogy of a block on an inclined plane, as illustrated in Figure 16. The block represents the moving threads that try to climb the inclined plane, that represents the fixed thread, when a force F_T caused by a tightening torque is applied. The angle of the inclined plane represents the helix angle of the thread β (directly related to the thread pitch, p), and α is the half angle of the thread section. The force F_T should overcome the existing preload (if so) $F \cdot \sin(\beta)$ (always against tightening) and the friction force $\mu \cdot N$ (always against the movement). When the tightening torque ceases, F_T disappears and the friction force $\mu \cdot N$ changes its direction to avoid the block going downwards; i.e., to avoid loosening of the joint. If the coefficient of friction was null, the screwed joint would loosen as soon as the tightening torque ceases.[41–43]

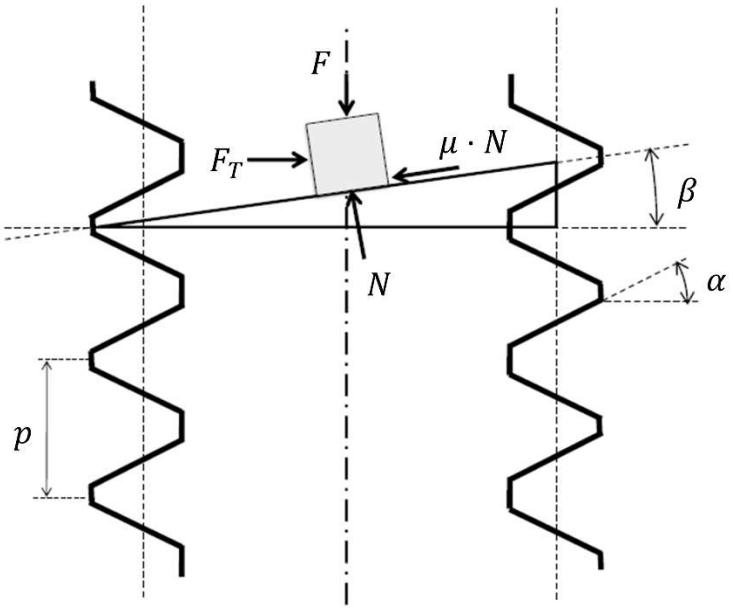

Figure 16. Screw preload and the analogy with a block over an inclined plane.

The analogy of the block on an inclined plane is useful for understanding the forces generated by the preload and the friction forces on thread contact. Nevertheless, there is another friction not considered hitherto, the friction generated on screw head contact. Figure 17 shows the free body diagrams of a screw during both tightening and untightening processes.

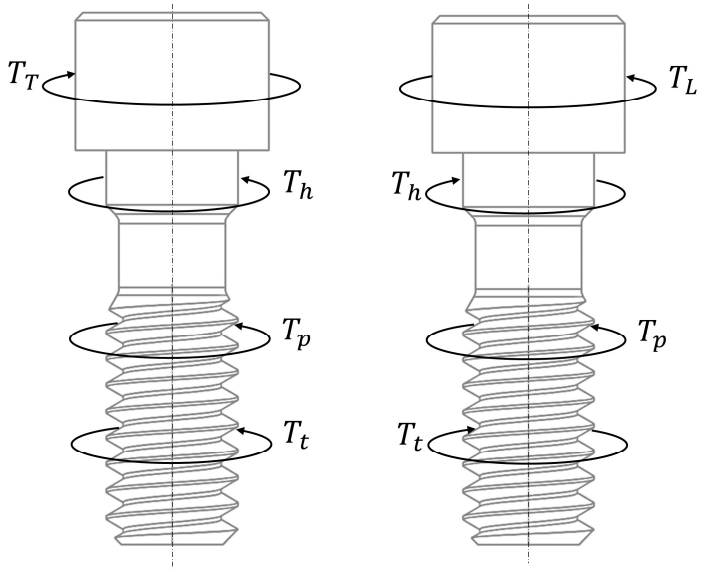

Figure 17. Free body diagram of a tightened screw. A, Tightening process. B, Untightening process.

Where T_h is the resistant moment due to friction under the screw head, T_t is the resistant moment due to friction between thread surfaces and T_p is the pitch torque generated by the preload F_p acting on the helix surface of the threads.

Both T_h and T_t act against movement, since they are friction moments; i.e., they will change the direction depending on whether the screw is being tightened or untightened. By contrast, T_p always acts in the loosening direction. Equations (10) and (11) show the balance conditions for tightening and untightening processes, respectively.[45]

$$T_T = T_h + T_t + T_p \tag{10}$$

$$T_L = T_h + T_t - T_p \tag{11}$$

Based on the equilibrium condition established in equation (10), equation (12) relates the tightening torque T_T with the preload F_p.[41]

$$T_T = F_p \cdot \mu_h \cdot r_h + F_p \cdot \frac{\mu_t \cdot r_t}{(cos\alpha - \mu \cdot tan\beta)} + F_p \cdot \frac{tan\beta \cdot cos\alpha \cdot r_t}{(cos\alpha - \mu \cdot tan\beta)} \tag{12}$$

Where μ_h and μ_t are respectively the coefficients of friction of the screw head and thread contacts and r_h and r_t are respectively the screw head and thread effective contact radii obtained by considering the preload to be uniformly distributed under the screw head and on the thread surface:

$$r_h = \frac{2}{3} \cdot \frac{r_{hmax}^3 - r_{hmin}^3}{r_{hmax}^2 - r_{hmin}^2} \approx \frac{r_{hmax} + r_{hmin}}{2} \tag{13}$$

$$r_t = \frac{2}{3} \cdot \frac{r_{tmax}^3 - r_{tmin}^3}{r_{tmax}^2 - r_{tmin}^2} \approx \frac{r_{tmax} + r_{tmin}}{2} \tag{14}$$

Where r_{hmax} and r_{hmin} are, respectively, the maximum and minimum radii of the screw head contact surface, and r_{tmax} and r_{tmin} are the maximum and minimum radii of the screw thread contact surface, respectively, as shown in Figure 18.

Motosh simplified equation (12) by assuming $cos\alpha \gg \mu \cdot tan\beta$, obtaining equation (15).[41,46] In the same way, equation (16) can be shown as a simplification of equation (12) for the untightening process.

$$T_T = F_p \cdot \mu_h \cdot r_h + F_p \cdot \mu_t \cdot \frac{r_t}{cos\alpha} + F_p \cdot tan\beta \cdot r_t \tag{15}$$

$$T_L = F_p \cdot \mu_h \cdot r_h + F_p \cdot \mu_t \cdot \frac{r_t}{cos\alpha} - F_p \cdot tan\beta \cdot r_t \tag{16}$$

Moreover, equations (15) and (16) are particularized for a flat screw head contact with equations (17) and (18) being the general expressions that can be used for the case of countersunk head screws, where ρ is the angle of the screw head contact surface.

$$T_T = F_p \cdot \frac{\mu_h \cdot r_h}{\cos\rho} + F_p \cdot \mu_t \cdot \frac{r_t}{cos\alpha} + F_p \cdot tan\beta \cdot r_t \quad (17)$$

$$T_L = F_p \cdot \frac{\mu_h \cdot r_h}{\cos\rho} + F_p \cdot \mu_t \cdot \frac{r_t}{cos\alpha} - F_p \cdot tan\beta \cdot r_t \quad (18)$$

Surprisingly, the main part of the energy provided when tightening a screw contributes to overcome friction (the first two summands in equations (10), (15), and (17)). T_h consumes approximately 50% of the energy, T_t consumes another 40% and T_p receives only 10% of the applied torque T_T as shown in Figure 19.[3]

Besides this, the coefficient of friction is the factor that has more influence in preload scatter, with its value virtually impossible to predict and leading to a discrepancy between the theoretical value of the preload and the real one. There are several variables that affect the coefficient of friction. The most important ones are surface hardness, surface finishes, type of material, lubricant (if used), tightening speed, thread fit, hole clearance, surface pressures, presence or absence of washers, cut versus rolled threads, and so on.[3]

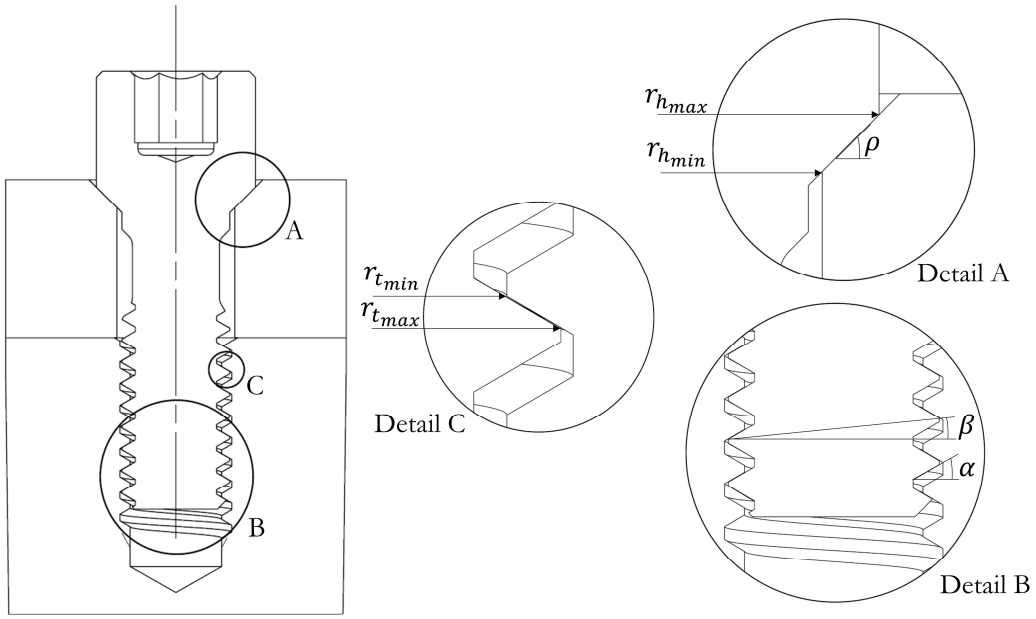

Figure 18. Geometrical parameters of a screwed joint.

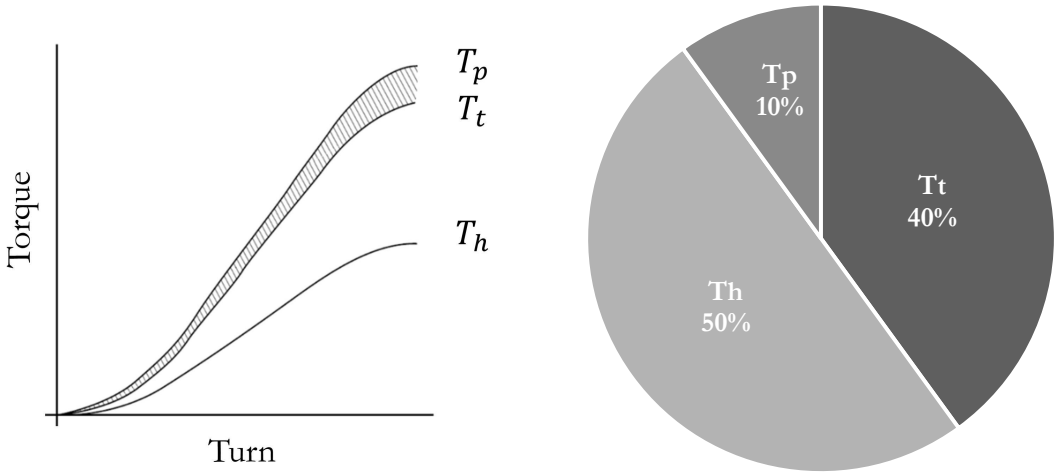

A) B)

Figure 19. Energy consumed by the resistance torques under the screw head T_h, the resistance torque in the thread T_t, and the pitch torque T_p. A, Torque versus turn diagram.[3] B, Pie chart of the consumed energy during the tightening process.

Hence, for the same tightening torque there is an unavoidable scatter on the obtained preload that may be distributed as in the example in Figure 20. As can be seen, that distribution is not Gaussian or normal but skewed to the right.[47] Nevertheless, this is a specific case, whilst as a guide value, a scatter of ±30% in preload can be assumed for a specific tightening torque.[3]

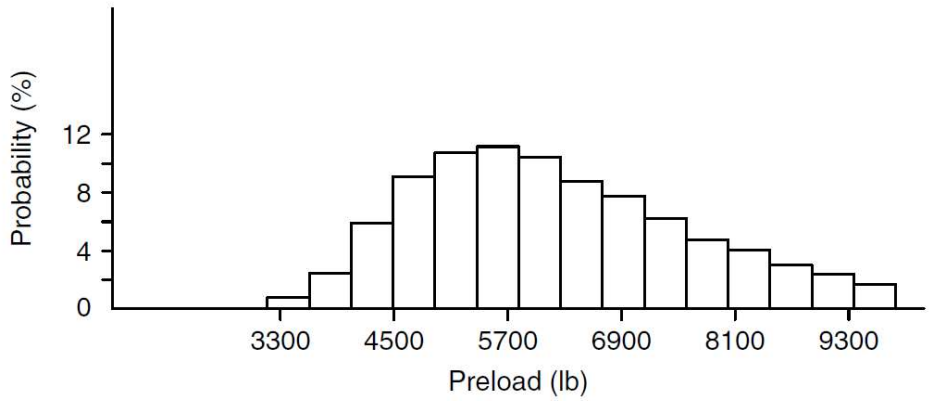

Figure 20. Initial preloads obtained for a large number of specimens tightened at the same torque.[3]

Apart from coefficient of friction scatter, variables such as thread pitch p, half-angle α, or effective contact radii r_h and r_t between parts are not constant in real life. Small variations, even within the tolerances imposed, may alter the preload obtained.

Finally, unlike coefficient of friction or geometric variables that are at least visible in the torque-preload equation (see equations (15)(16)(17)(18)), there are

some sources of error that the torque-preload equation is oblivious to. On the one hand, interferences among threads or between the screw and the hole require energy from the tightening torque to be overcome but this torque does not contribute to screw preload. On the other hand, the torque-preload equation assumes the screw and the elements to be joined as rigid solids (apart from the evident elastic deformation on the screw shank). Nevertheless, when preloaded, some parts of the screw or joined elements may suffer high stresses, leading to yield and material flow until the equilibrium is reached. This phenomenon is known as relaxation and causes preload loss due to joint embedment. Figure 21 provides an illustrative example, where it can be seen that a significant part of relaxation occurs immediately after the tightening process ends. Subsequently, relaxation continues with a much lower ratio to a third stage where the relaxation may be considered negligible.[48] For this reason, a retightening torque is generally recommended after various weeks.[3]

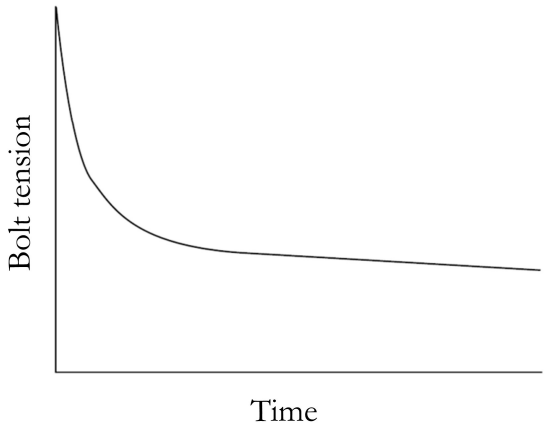

Figure 21. Relaxation process over time.[3]

1.2.5 Screwed joint faults

In section 1.1, it was explained that dental restorations are liable to suffer microgap formation in IAC, loosening of the prosthetic screw, or fatigue failure of some of their elements. These phenomena have been widely studied in screwed joints in the industrial sector.

Regarding microgap, this phenomenon can make the joint operate incorrectly. This phenomenon allows any liquid to pass through the screwed joint, causing, for example, leakage in a pipe or allowing bacterial penetration in a dental restoration. This problem is caused either by an excessive external load and/or an insufficient tightening torque[49,50] or in absence of loads if there is a mismatch

among the joined elements.[22] Further information regarding microgap phenomenon will be provided in section 1.5.

An excessive static load may cause the collapse of the screw, leading to a mechanical failure of the joint. Besides this, lower loads but repeated through time, may lead to a failure of the screwed joint as well,[34,35] in this case, due to fatigue.[36] The fatigue phenomenon is complex and will be explained in detail in section 1.3. There, the theoretical principles will be detailed in order to manage the fatigue failure of the screw as well as on the joined elements (the dental implant, in this PhD Thesis).

External loads (especially transverse loads) may cause displacement among the elements joined and the screw in such a way that the friction is overcome, and the screw may loosen, considerably reducing the preload of the joint.[4,37–40] Screw self-loosening will be explained extensively in section 1.4. Besides this, it should also be noted that the preload reduction due to self-loosening may stimulate either of the two phenomena that have already been presented: fatigue failure or microgap formation.

1.3 Fatigue analysis

According to ASTM E-1823,[51] 'fatigue is the process of progressive localized permanent structural change occurring in a material subjected to conditions that produce fluctuating stresses and strains at some point or points that may culminate in cracks or a complete fracture after a sufficient number of fluctuations'. Thus, any mechanical component subjected to variable loads is liable to fail after a certain amount of load cycles.

Fatigue phenomenon starts as a result of the initiation of one or more cracks and their subsequent propagation until they cross most of the resistant section of the component, leading to the collapse of the part. Figure 22 shows the 3 stages that can be observed in a failure section due to fatigue.

Stage I is the initiation of microcracks due to the cyclic plastic deformation followed by crystallographic propagation extending from 2 to 5 grains around the origin. This stage cannot be seen by the naked eye. Stage II progresses from microcracks to macrocracks forming parallel plateau-like fracture surfaces separated by longitudinal ridges. These plateaus are normally smooth and normal to the direction of maximum tensile stress. These surfaces are also known as 'beach marks'. Finally, stage III occurs during the final stress cycle

when the remaining material cannot support the load, resulting in a sudden and fast fracture.[43]

Fatigue is the cause of most of the operating machine failures. There are studies confirming that 50-90% of the mechanical failures are caused by fatigue.[52] These failures are, generally, caused by stresses much lower than the ultimate stress level and even lower than the yield strength. These relatively low stresses, combined with a stress concentration factor such as a pore or a notch, will lead to crack initiation and gradual propagation until the effective section cannot resist the load and collapses statically, as explained before.[53]

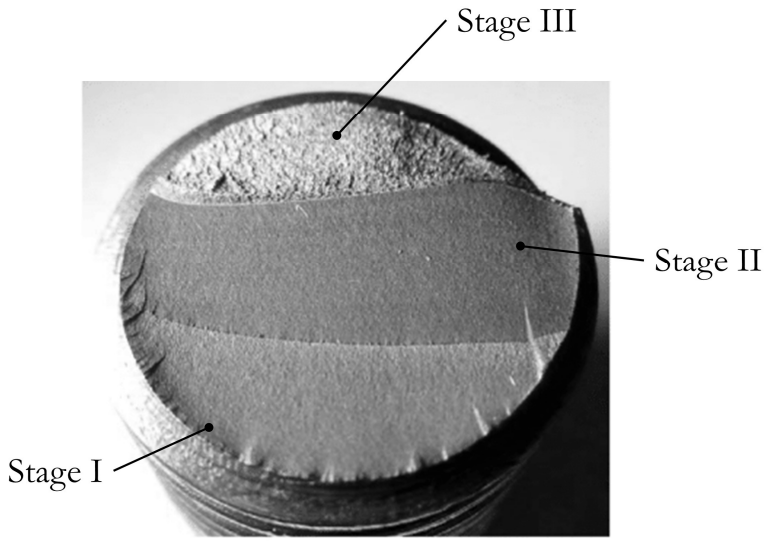

Figure 22. Failure section of a bolt due to fatigue.[54]

Fatigue analysis methods aim to estimate the life span of a component suffering variable stresses/deformations. Nevertheless, statistical dispersion inherent to fatigue[55] and the lack of accurate analytical models reproducing fatigue phenomenon makes fatigue analysis valid only for the early stages of the design process, whereby experimental validation is required.

In the following sections, the background on these analysis procedures will be outlined. First, uniaxial fatigue analysis will be described, including the effect of mean stress and stress concentration effects (due to fillets, notches, or grooves), and the most common uniaxial experimental fatigue tests. This background will be used to analyze the fatigue behavior of the prosthetic screw in Chapter 3, since it works under uniaxial stress conditions. Then multiaxial fatigue analysis will be described, with an explanation of the most used methods (classic method, invariant-based methods, and critical plane methods), the effect of

stress concentration, and the most common multiaxial experimental fatigue tests. This will be used for the analysis of the fatigue behavior of the dental implant in Chapter 5, since it works under multiaxial stress conditions.

1.3.1 Uniaxial fatigue analysis

A component can be affirmed to work uniaxially when only one principal stress can be considered non-negligible. There are components such as screws that are assumed to work uniaxially in real working conditions. The simplicity of this approach enables engineers to make calculations very easily.

1.3.1.1 S-N curve for the pure-alternating stress case

As mentioned, fatigue analysis methods aim to estimate the life span of a component subjected to a variable load. The simplest working case is the uniaxial pure-alternating stress case, in which the estimation of the number of life cycles before fracturing is related to the amplitude of the alternating stress. This association between stress amplitude and duration is normally presented in a chart known as the S-N chart/curve, also known as the Wohler curve, which is based on experimental fatigue tests performed on standardized specimens.

Figure 23 shows a Zwick/Roell UBM 200tC rotating bending fatigue machine. On this type of fatigue test benches, the specimen is subjected to a constant bending moment. The specimen is clamped by 2 grips. On the right side, the specimen is clamped by a fixed support 'C' where no displacement is allowed but the rotation on the longitudinal axis of the specimen is by means of a bearing. On the left side, the free support 'B' allows for free movement along the plane of the bench as well as the rotation of the specimen by means of another bearing. Moreover, the rotating movement is generated by an electric motor and transmitted to the support on the right side 'C' by means of a belt. The dimensions of the specimens are determined by DIN 50113,[56] ISO 1143,[57] and ASTM E2948-16a.[58]

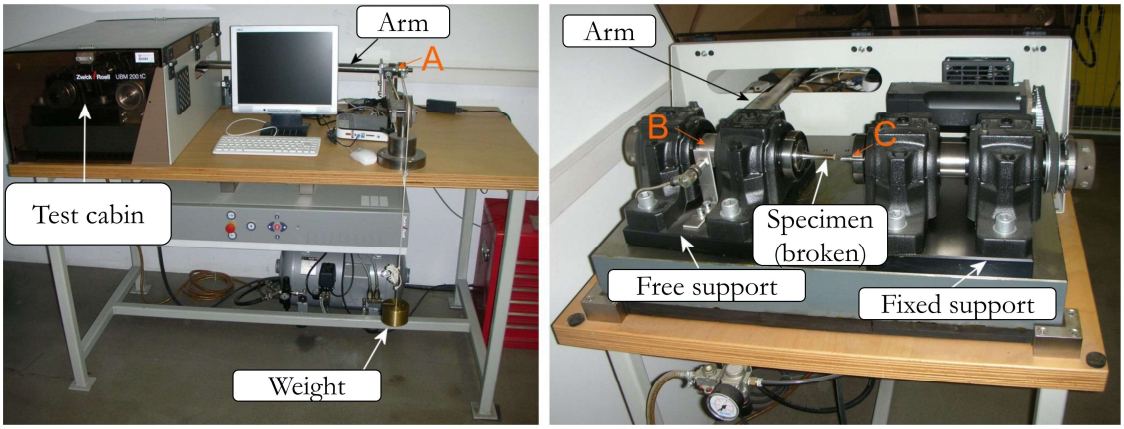

Figure 23. Zwick/Roell rotating bending fatigue machine.

Figure 24 shows the force and bending moment in the specimen rotating bending fatigue test. In addition to a constant bending moment, an axial force is also applied on the specimen. Nevertheless, the stresses caused by this axial force are negligible since:

$$\sigma_W = \frac{4W}{\pi d^2} \ll \sigma_M = 32\frac{WL}{\pi d^3} \tag{19}$$

Where σ_W is the stress caused by the axial force W, σ_M is the stress caused by the bending moment M, d is the diameter of the specimen neck (failure section), and L is the arm that causes the bending moment M. As a result, the specimen is mainly subjected to an alternating axial peak stress caused by the constant bending moment along with the rotating movement, leading to pure-alternating stress cycles. This is why it is known as the rotating bending fatigue test.

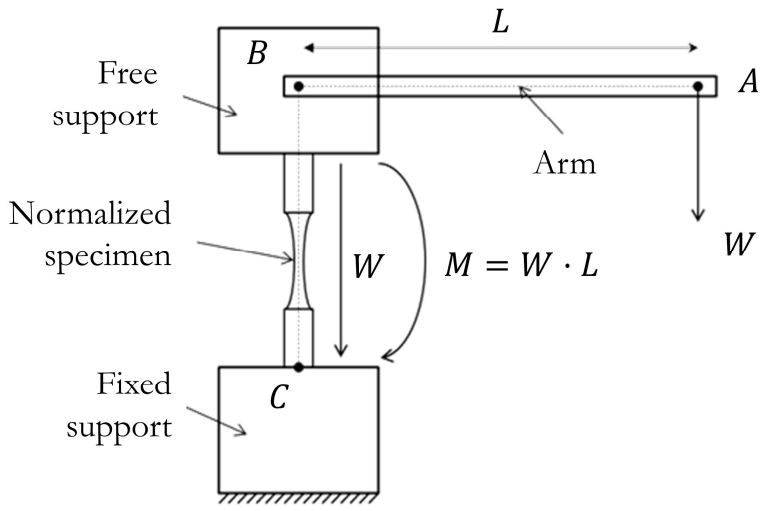

Figure 24. Schematic of the Zwick/Roell rotating bending fatigue machine.

Apart from the rotating bending fatigue machine, there are direct stress fatigue machines where a non-rotating specimen is subjected to axial stress. These machines are more versatile for two main reasons. First, since the axial load is generated by a linear actuator, loads can vary in such a way that mean components of the load can be applied (the effect of the mean stress will be discussed in section 1.3.1.2) or even load cases with variable amplitude can be applied. Second, the fact that the specimen is not rotating, allows the machine to be used for fatigue test of specimens with other geometries rather than the axisymmetric ones tested in rotating bending tests (i.e. flat-sheet specimens). Moreover, real components may also be tested as long as proper tooling is used and the dimensions fit the test bench. Figure 25A shows an Instron 8801 servo-hydraulic direct stress fatigue machine. This machine has two grips that hold the specimen (Figure 25B) from each end, whereby the desired force function can be transmitted. Female threads instead of grips can be used to hold the specimen. The specimen dimensions are determined by ASTM E466,[59] ISO 1099,[60] and DIN 50100,[61] being similar to the ones used for rotating bending machine.

A) B)

Figure 25. A, Instron 8801 servo-hydraulic direct stress fatigue machine. Image courtesy of Instron. B, Grips used for cylindrical specimens.

In this way, a certain number of specimens may be tested, either in the rotating bending fatigue machine or in the direct stress fatigue machine, at different

alternating load magnitudes obtaining their corresponding durations. This data is usually shown by using the S-N chart, where duration N (horizontal axis) of each test versus the alternating stress applied σ_a (vertical axis) is plotted. Figure 26 shows an S-N chart with three clearly distinguished zones: low cycle fatigue (LCF), high cycle fatigue (HCF) and very high cycle fatigue (VHCF) or giga-cycle fatigue (GCF). LCF normally refers to fatigue tests where the maximum applied force causes a stress higher than the cyclic yield strength. Thus, the specimens will show not only elastic but also plastic deformations. Hence, the best approach is a strain-life method that uses the local deformation rather than the stress level, setting aside the S-N chart and using the ε-N (strain-life) chart. In HCF the stresses lie in the elastic stress-range and the fatigue analysis is performed by considering the stresses (stress-cycles approach). VHCF also uses the stress-cycles approach but including (for some materials such as Titanium and Titanium alloys) the fatigue limit concept, i.e., a stress value below which the specimen is assumed to survive (infinite life). In this PhD Thesis the stress-cycles approach for HCF is used.[3]

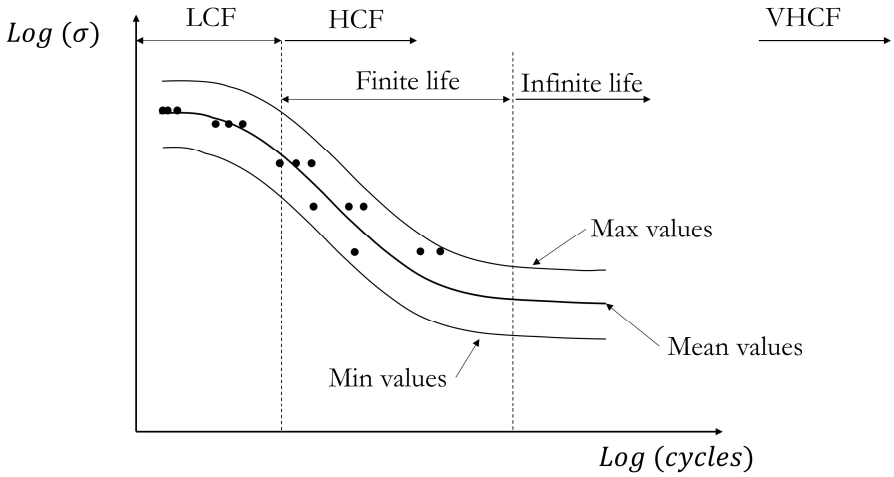

Figure 26. S-N chart with the three duration ranges: LCF, HCF and VHCF.

The characterization of fatigue behavior of a material in HCF can be divided in two parts. First, the finite life is determined by performing fatigue tests on different specimens at different load levels aiming at failure of the specimens. Then, the fatigue limit is obtained by performing fatigue tests at lower load levels pursuing the survival of the specimens. For a proper fatigue campaign planning, an ASTM manual[62] determines the number of specimens and the number of different load levels needed for finite life part determination depending on the test type. Table 1 presents the percent replication for each

test purpose, with the percent replication determined by equation (22), and the minimum number of specimens provided in Table 2.

Table 1. Percent of replication depending on the type of test.[62]

Type of test	Percent replication
Preliminary and exploratory	17-33%
Research and development testing of components and specimens	33-50%
Design allowable data	50-75%
Reliability data	75-88%

$$\%\, replication = 100\left[1 - \frac{\begin{matrix}total\ number\ of\ different \\ stress\ levels\ used\ in\ testing\end{matrix}}{\begin{matrix}total\ number\ of \\ specimens\ tested\end{matrix}}\right] \quad (20)$$

Table 2. Number of specimens for finite life determination depending on o the type of test.[62]

Type of test	Number of specimens
Preliminary and exploratory	6-12
Research and development testing of components and specimens	6-12
Design allowable data	12-24
Reliability data	12-24

As mentioned before, Titanium and Titanium alloys have a fatigue limit[63] that is usually obtained by calculating the average value of the points obtained through the well-known staircase method (also known as the up-and-down method).[62] Using this method, the specimens are tested sequentially. The first specimen shall be tested at a load based on preliminary data. If this specimen survives a specified number of cycles (run-out) the next specimen is tested at a higher stress level. Otherwise, it is tested at a lower stress level. The run-out is a value assumed as the boundary of infinite life. If the tested specimen reaches that number of cycles, it is assumed that it will never brake regardless of the number of cycles the test would last. Run-out value is normally set as 10^6 or $2{\cdot}10^6$ but it may vary for each case. Note that the first values must be neglected, with the first considered test being the first change from either survival to failure or failure to survival. The same manual recommends the use of 30 specimens for fatigue limit determination even though an expert in experimental fatigue should know that this value may be conservative, and 7-15 specimens should be enough.[62]

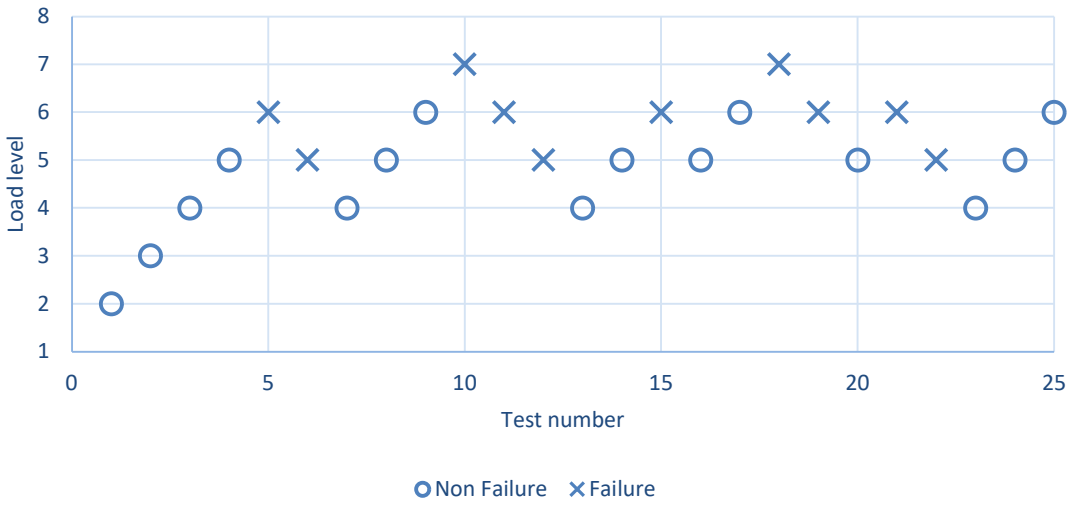

Figure 27. Staircase method (or the up-and-down method).

Once the test campaign is completed, the results can be plotted in an S-N chart that relates the stress level with number of cycles obtained in each test. According to ASTM E-739[64] the results corresponding to the finite-life region are modelled by a straight line in $\log\sigma$-$\log N$ scale (or less commonly in σ-$\log N$ scale). $\log N$ is used as the dependent variable in analysis and is called Y. The stress level σ or $\log\sigma$ is the independent variable and is called X.

$$Y = A + B \cdot X \begin{cases} \log N = A + B \cdot \log\sigma \\ \log N = A + B \cdot \sigma \end{cases} \tag{21}$$

The maximum likelihood estimators of A and B are:

$$\left.\begin{matrix} \hat{A} = \bar{Y} - \hat{B} \cdot \bar{X} \\ \hat{B} = \dfrac{\sum_{i=1}^{k}(X_i - \bar{X}) \cdot (Y_i - \bar{Y})}{\sum_{i=1}^{k}(X_i - \bar{X})^2} \end{matrix}\right\} where \begin{cases} \bar{X} = \dfrac{\sum_{i=1}^{k} X_i}{k} = \dfrac{\sum_{i=1}^{k}\log(\sigma_i)}{k} \\ \bar{Y} = \dfrac{\sum_{i=1}^{k} Y_i}{k} = \dfrac{\sum_{i=1}^{k}\log(N)}{k} \end{cases} \tag{22}$$

Where the 'caret' symbol (^) denotes estimation and the 'overbar' symbol denotes average. k is the total number of specimens tested and included in the curve fitting process. The recommended equation for estimating the variance of the normal distribution for $\log N$ is:

$$\hat{\sigma}^2 = \frac{\sum_{i=1}^{k}\left(Y_i - \hat{Y}_i\right)^2}{k-2} \tag{23}$$

And the standard deviation:

$$\hat{\sigma} = \sqrt{\frac{\sum_{i=1}^{k}\left(Y_i - \hat{Y}_i\right)^2}{k-2}} \tag{24}$$

Hence, the linear model for the finite-life region of the S-N curve is defined as:

$$\widehat{Y}_i = \hat{A} + \hat{B} \cdot X_i \tag{25}$$

Regarding the staircase method, Dixon and Mood[65] proposed statistical analysis to obtain the fatigue limit σ_{fm} and the standard deviation S_f.

$$A = \sum_{i=0}^{i_M} m_i\,; \quad B = \sum_{i=0}^{i_M} i \cdot m_i\,; \quad C = \sum_{i=0}^{i_M} i^2 \cdot m_i \tag{26}$$

$$\begin{gathered} \sigma_{fm} = \sigma_{f0} + \Delta s \cdot \left(\frac{B}{A} \pm 0.5\right) \\ if\ \frac{A \cdot C - B^2}{A^2} \geq 0.3 \rightarrow S_f = 1.62 \Delta s \cdot \left(\frac{A \cdot C - B^2}{A^2} + 0.029\right) \\ if\ \frac{A \cdot C - B^2}{A^2} < 0.3 \rightarrow S_f = 0.53 \Delta s \end{gathered} \tag{27}$$

Where i is a counter from 0 to i_M that is the number of stress levels used -1. If the majority of specimens in the staircase method fail, then the lowest stress level at which one or more specimens survived corresponds to $i = 0$ and m_i will represent the number of specimens that survive at each stress level i. Otherwise, if the majority of the specimens in the staircase method survive, the lowest stress level at which one or more failures occurred will be $i = 0$ and m_i will correspond to the number of specimens that fail at each stress level i.

In fatigue, surface finish, specimen size, and working conditions, among other factors, have significant effects on both finite life and the fatigue limit. The S-N curve obtained corresponds to fatigue tests performed on specimens prepared carefully and tested under closely controlled conditions while the end product has a rougher surface finish and more unfavorable working conditions. Hence, if the fatigue behavior of the mechanical component (end product) is pursued, the S-N curve must be modified. Marin identified factors that quantified the effects of surface condition, specimen size, working conditions (load case), temperature, etc.[53] Figure 28 shows the S-N curve obtained through fatigue testing of standardized specimens, the modified ones obtained through some of Marin's modification factors and the S-N of the end product.

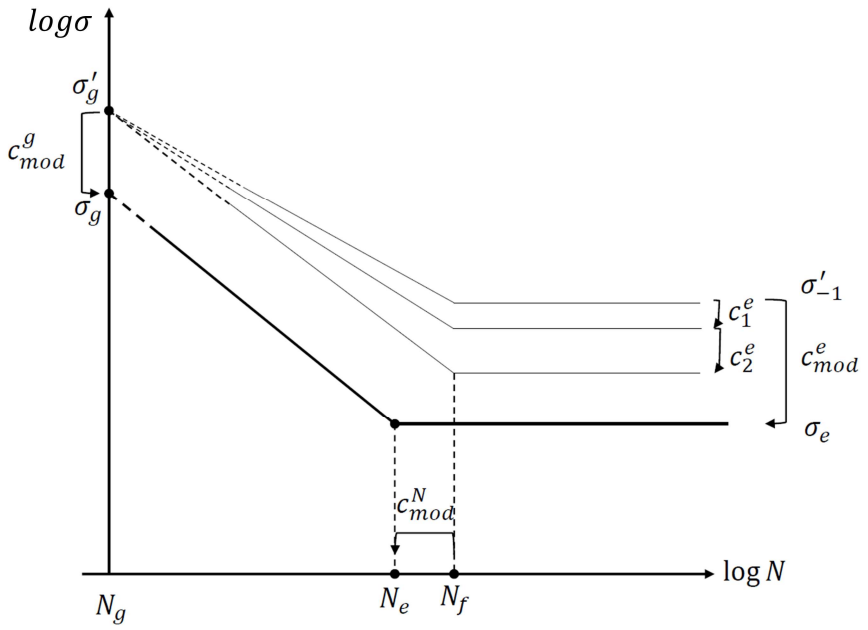

Figure 28. S-N curve for material (specimens) and S-N curve for mechanical part (end product) obtained by using modification factors.

Where σ_e is the fatigue limit (or endurance limit) of the end product, σ_g is the stress value at N_g cycles (generally 10^3 cycles), and N_e is the number of cycles at which the slope part and the fatigue limit intersect. c_{mod}^g and c_{mod}^e are the result of the multiplication of all the modification factors in N_g and N_e cycles. Note that the changes in fatigue limit due to Marin's modification factors may change the value of N_e.

As mentioned, Marin identified factors that quantified the effects of surface condition, size, loading, temperature, and miscellaneous items. Hence, the fatigue limit of the end product can be calculated as:

$$\sigma_e = c_s^e \cdot c_L^e \cdot c_S^e \cdot c_R^e \cdot c_m^e \cdot \sigma'_{-1} \tag{28}$$

Where c_s^e is the surface modification factor, c_L^e is the load modification factor, c_S^e is the size modification factor, c_R^e is the reliability modification factor, and c_m^e is the mechanical treatment modification factor; all of them for infinite life. For a certain number of cycles N in the finite-life region of the S-N:

$$\sigma_N = c_s^N \cdot c_L^N \cdot c_S^N \cdot c_R^N \cdot c_m^N \cdot \sigma'_N \tag{29}$$

Regarding the factors considered above, surface roughness plays an important role in crack propagation. The rougher the surface, the higher probability of crack initiation due to small stress concentrations. Average roughness R_a and mean roughness depth R_z are the most used parameters for determining surface roughness, and they can be determined by ISO 4287[66] and ASME B46.1.[67] Many

studies can be found providing values of surface condition modification factors obtained experimentally.[41–43,68,69] Even though most of these values may be reliable, the surface roughness obtained through each manufacturing process is unique and, to properly determine this factor, experimental fatigue tests of specimens under same conditions must be performed. Negligible effects of the surface modification factor may be assumed for low cycles range since stress concentration does not affect ductile materials under static loads. Fatigue limit, though, has to be modified by this factor since its effect is not negligible.

The load case also affects the fatigue behavior of specimens and mechanical components. For same maximum axial stress level applied, a specimen subjected to axial loading (direct stress fatigue machine) will present a poorer fatigue behavior than the same specimen subjected to a bending moment (rotating bending fatigue machine). Regarding crack initiation, if it occurs at the surface the stress status will be the same for both cases. Nevertheless, if it occurs inside the parts, i.e., due to a pore, in the axial load case failure it is more likely to occur and occur faster than in the bending load case. Regarding crack propagation, nominal stress decreases as the crack propagates in the bending load case while it remains constant in the axial load case.

Under static loading, size has a negligible effect. Hence, for low cycles $c_S^g = 1$ can be assumed. Nevertheless, for higher fatigue cycle range, size effect must be considered due to the following reasons. A large-sized part is more likely to have defects, notches, pores, and inclusions. A big part may have more high stress points (critical sections) for the same applied load level. Manufacturing processes for big parts are more complicated and usually less precise.

Besides this, the S-N curve obtained directly from the specimens assumes a reliability of 50%. If another reliability curve is pursued, the S-N curve must be modified by the reliability modification factor c_R^N.

Finally, with regards to fatigue analysis, mechanical treatments that create compression stresses on surfaces are the most interesting ones such as shot peening,[70,71] laser shock-peening,[72] low plasticity burnishing,[73–76] and others[73,77–79] since they hinder crack initiation. Unlike the other factors, whose modification factors may be between 0 and 1, i.e., they reduce fatigue life, these factors may considerably enhance fatigue life. Hence, these factors are usually higher than 1.

There are other factors such as impacts, working temperature, or fretting that also affect fatigue behavior but are not included within the scope of this PhD

Thesis. Even for the factors mentioned in this section, and therefore considered in this PhD Thesis, which have been briefly described, no specific values of the factors are given since they will not be used in this PhD Thesis.

1.3.1.2 Effect of the mean stress

Thus far, only pure alternating stresses have been considered. Nevertheless, withstanding non-null mean stresses is quite common for mechanical components. If the mean stress is tensile, the fatigue life of the component against alternating stresses will be reduced. If the mean stress is compressive instead, the fatigue life against alternating stresses may be generally enhanced, but in some cases it may be even worsened or remain equal (depending on the material). Figure 29 shows how the S-N curve is affected by the effect of the mean stresses.

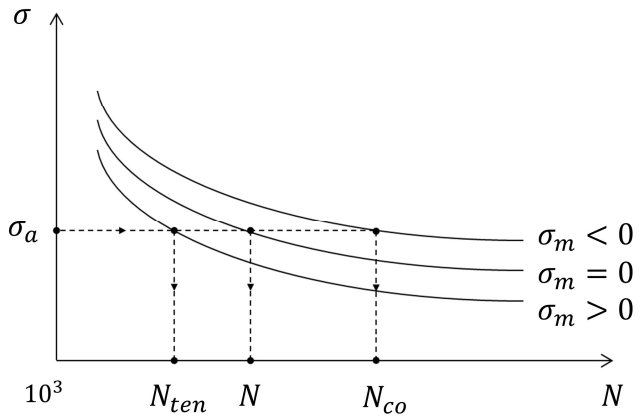

Figure 29. Effect of mean stress in S-N curve.

Where N_{co} is the estimated life of a component subjected to a mean stress of compression, N_{ten} is the estimated life of the same component subjected to a mean tensile stress and, N is the estimated life of the component subjected only to pure alternating stresses. Stress cycles in fatigue are determined by the mean and alternating components as follows:

$$\sigma_m = \frac{1}{2}(\sigma_{max} + \sigma_{min})$$
$$\sigma_a = \frac{1}{2}(\sigma_{max} - \sigma_{min}) \quad (30)$$

Where σ_{max} is the maximum stress, σ_{min} is the minimum stress, σ_m is the mean component of the stress, and σ_a is the alternating component of the stress. The shape of variation between the stress peaks and valleys as well as the frequency have no effect on fatigue behavior below 200Hz in metals.[52] The type of fatigue test regarding the load case is defined by the stress ratio, R:

$$R = \frac{\sigma_{min}}{\sigma_{max}} \tag{31}$$

Figure 30 shows different cases of stress ratios R.

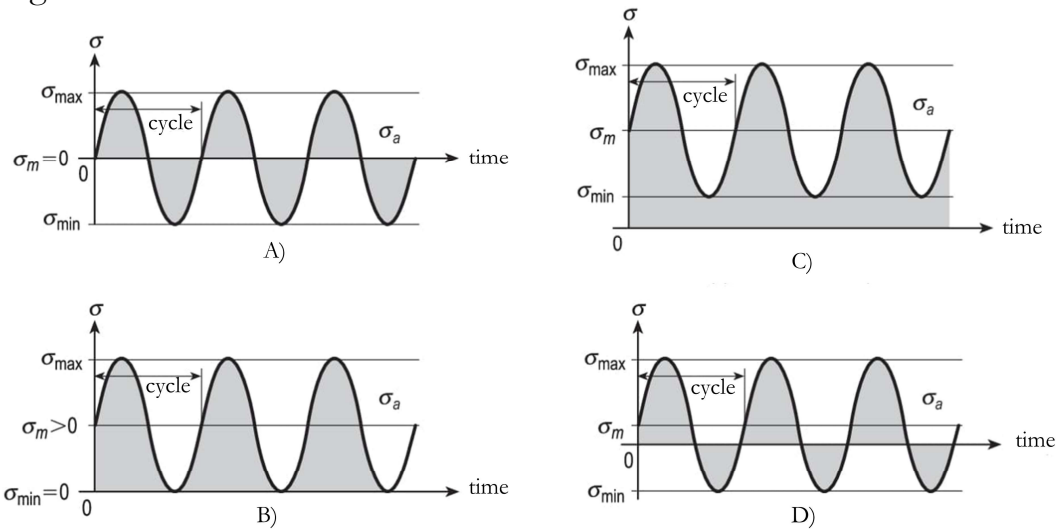

Figure 30. Different stress cycles corresponding to different stress ratios. A, $R = -1$. B, $R = 0$. C, $0 < R < 1$. D, $0 > R > -1$.[53]

In Figure 31, the diagram proposed by Haigh[80] is shown, where the effect of mean stress is considered. The diagram is divided into 4 zones depending on the sign (positive for tension and negative for compression) of both maximum and minimum stresses. A zone corresponds to positive stresses, i.e., both maximum and minimum stresses are tensile stresses. B and C zones represent positive maximum stress and negative minimum stress, but different signs for the mean value (tension in B and compression in C). In zone D zone, finally, both the maximum and minimum stresses are compressive (negative). In this zone no fatigue failure is expected to occur because the stress is compressive all the time.

To sum up:

$$A\begin{cases}\sigma_{max} > 0\\ \sigma_{min} > 0\\ \sigma_m > 0\end{cases} \quad B\begin{cases}\sigma_{max} > 0\\ \sigma_{min} < 0\\ \sigma_m > 0\end{cases} \quad C\begin{cases}\sigma_{max} > 0\\ \sigma_{min} < 0\\ \sigma_m < 0\end{cases} \quad D\begin{cases}\sigma_{max} < 0\\ \sigma_{min} < 0\\ \sigma_m < 0\end{cases} \tag{32}$$

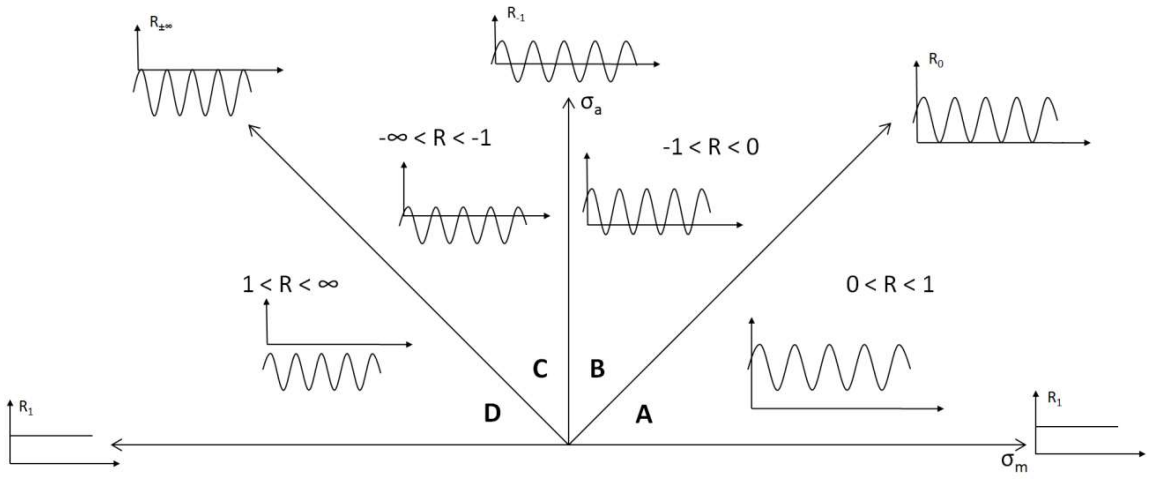

Figure 31. Different stress ratios in the Haigh diagram.

1.3.1.2.1 Criteria for the tensile region of the Haigh diagram

Both the S-N chart and the Haigh diagram can be easily related as shown in Figure 32. As previously shown in Figure 29, the different curves in the S-N chart show the effect of the mean stress on fatigue life. That is, each line corresponds to a certain value of the mean component of the stress. In the same way, each curve in the Haigh diagram shows a certain number of cycles that the specimen or the component will last (or infinite life in the case of the fatigue limit). This fatigue life can be achieved using different combinations of mean and alternating stresses.

In the same way the S-N curve is determined using experimental data obtained from pure-alternating stress fatigue tests, each iso-duration line in the Haigh diagram is obtained by performing fatigue tests at different stress ratios R. Once fatigue behavior under different combinations of alternating and mean stresses has been observed, the most suitable criteria is determined. These suitable criteria may be a straight line, a parabola or other curves. In Figure 33 and equations (33)-(39), the most used criteria in the Haigh diagram for the mean tensile region are shown, even though some other criteria may be found.[53]

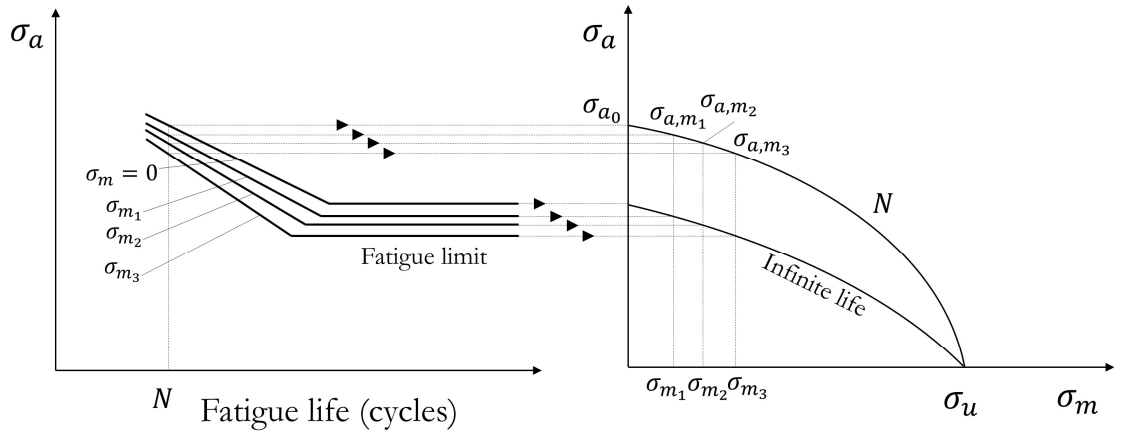

Figure 32. S-N curve and Haigh diagram correlated.

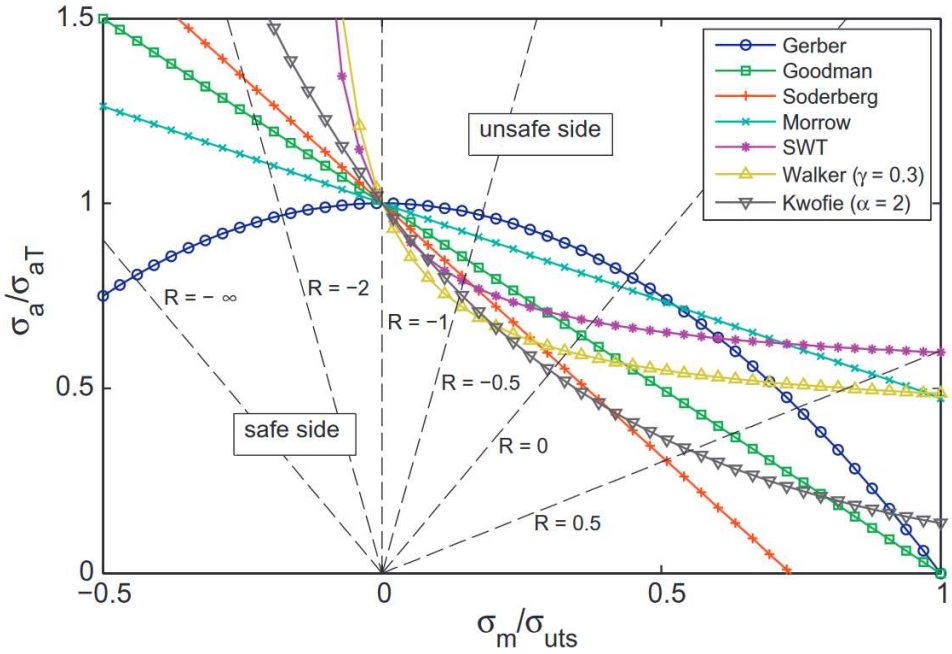

Figure 33. Most used criteria for tensile mean stress consideration.[81]

The Gerber method consists of a symmetric (ordinate-axis, alternating stress) parabola that considers the tensile strength σ_{ut} as the static failure:

$$\frac{\sigma_a}{\sigma_e} + \left(\frac{\sigma_m}{\sigma_{ut}}\right)^2 = 1 \tag{33}$$

Goodman proposed a straight line that also considers tensile strength σ_{ut}. It is widely used (especially in the automotive industry) even though the criterion is quite conservative:

$$\frac{\sigma_a}{\sigma_e} + \frac{\sigma_m}{\sigma_{ut}} = 1 \tag{34}$$

There is a more conservative version known as the modified Goodman version that considers the yield strength σ_{yp} and it consists of the original Goodman criterion combined with a line that connects the yield strength of the mean stress axis and the alternating stress axis.

The Soderberg criterion considers the yield strength σ_{yp} as a failure and its criterion is formed by a line that connects the yield strength with the fatigue limit. This criterion is conservative in most cases and will lead to part over-dimensioning.

$$\frac{\sigma_a}{\sigma_e} + \frac{\sigma_m}{\sigma_{yp}} = 1 \tag{35}$$

The Dietmann criterion is formed by a parabola like Gerber but, in this case, the symmetric axis is the abscissa-axis (mean stress) rather than the ordinate-axis.

$$\left(\frac{\sigma_a}{\sigma_e}\right)^2 + \frac{\sigma_m}{\sigma_{ut}} = 1 \tag{36}$$

Morrow is a widely used criterion (especially in the aeronautic industry) also formed by a straight line like Goodman but, in this case, considering the true fracture strength σ_{ur}.

$$\frac{\sigma_a}{\sigma_e} + \frac{\sigma_m}{\sigma_{ur}} = 1 \tag{37}$$

Walker is a well-known criterion specially used for high resistance steels. Unlike the other criteria, the Walker[82] equation has an adjustable fitting parameter γ that calls for the fatigue behavior of the material to be known to calculate its value.[83]

$$\sigma_e = \sigma_{max}\left(\frac{1-R}{2}\right)^{\gamma} \tag{38}$$

SWT[84] is a particular case of the Walker criterion where $\gamma = 0.5$, resulting in:

$$\sigma_e = \sigma_{max}\sqrt{\frac{1-R}{2}} \tag{39}$$

Finally, Smith is a more suitable criterion for brittle materials, similar to SWT:

$$\frac{\sigma_a}{\sigma_e} = \frac{\left(1-\frac{\sigma_m}{\sigma_{ut}}\right)}{\left(1+\frac{\sigma_m}{\sigma_{ut}}\right)} \tag{40}$$

As an illustrative example, Figure 34A shows the fatigue behavior of different steels, where it can be seen how Goodman is suitable for steels 1 and 2 (AISI 1045) while Dietmann or Morrow are more suitable for steel 3 (S45C with hardening and tempering). Figure 34B shows different performances for ductile materials suitable for Goodman, Dietmann, and Gerber criteria (among others).

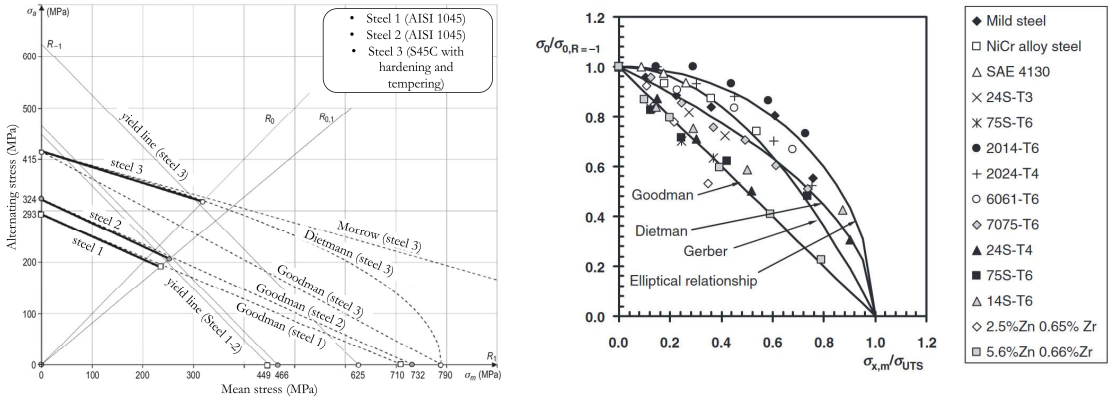

A) B)

Figure 34. Fatigue behaviors of different ductile materials and their most suitable criteria in the Haigh diagram. A, Fatigue behavior of different steels.[53] **B, Fatigue behavior of different ductile materials.**[85]

1.3.1.2.2 Criteria for the compressive region of the Haigh diagram

As mentioned above, compressive mean stresses are less restrictive since they usually have a positive effect on fatigue behavior. In Figure 35, the criteria for the compressive region of the Haigh diagram are shown. The JK line corresponds to static failure by compression, and it is formed by connecting the ultimate compression strength σ_{uc} with its equivalent on the pure alternating stress axis (vertical axis). In the same way, the yield line (EF line) is obtained by connecting the compressive yield strength σ_{yp} with its equivalent on the pure alternating stress axis (vertical axis). The OJ line is determined by the $R_{\pm\infty}$ line. The criterion shown in blue in Figure 35, for simplification purposes, assumes that the compressive mean stress does not affect fatigue life. This criterion is represented by a horizontal line from fatigue limit σ_e (or from σ_N in the case of a certain finite duration). The line is extended up to the yield line, with the criterion continued by the yield line up to E. Other less conservative criterion is shown in green in Figure 35 too. It assumes that the purely compressive zone (D zone in Figure 31) is completely secure. In this way, the $\widehat{CFD}$ triangle and EFJK zone are considered secure.

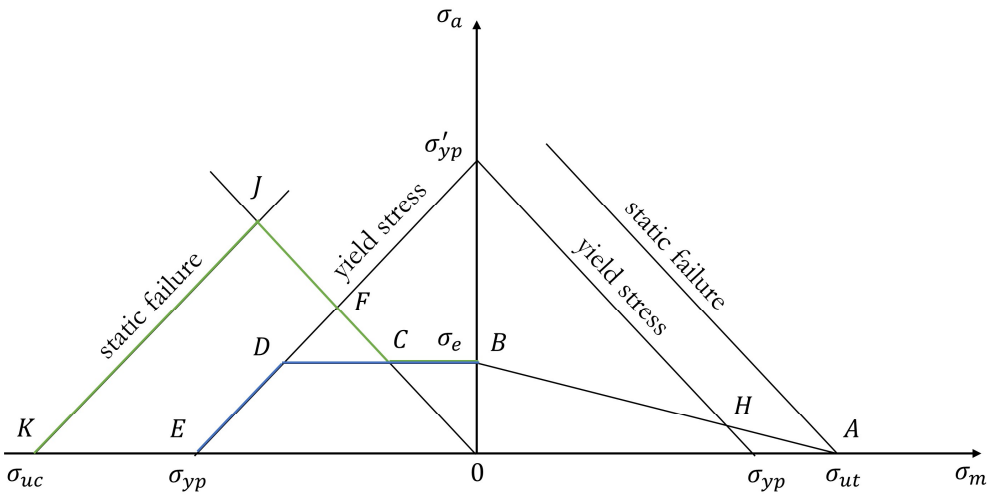

Figure 35. Criteria for compressive mean stress.

To conclude the analysis of the effect of mean stresses on fatigue behavior, Pallarés et al.[86] compiled the results of different work obtaining the following conclusions (see Figure 36). All the fatigue results fell in between the ellipse and Smith criterion. The fatigue behavior of ductile materials follows a concave curve while brittle materials follow a convex curve. For most treated structural steels and non-treated aluminum, performance in the Haigh diagram is not symmetric; i.e., compressive mean stresses have a positive effect on fatigue behavior up to a mean stress value where it starts to have a negative effect. Most ductile steels fall above the Goodman criterion and more than half of them fall in between the Goodman and the Gerber criteria. Extra-ductile materials showed an elliptical relationship, demonstrating symmetric performance; i.e., tensile mean stress has the same effect as compressive mean stress. Finally, brittle materials follow the Smith criterion (convex curve), indicating non-symmetric material; i.e., compressive mean stress has a positive effect on fatigue behavior.

It should be mentioned that the effect of compressive mean stresses on fatigue behavior is not explained more deeply since the prosthetic screw always operates under tensile mean stresses and, therefore, it falls outside the scope of this PhD Thesis.

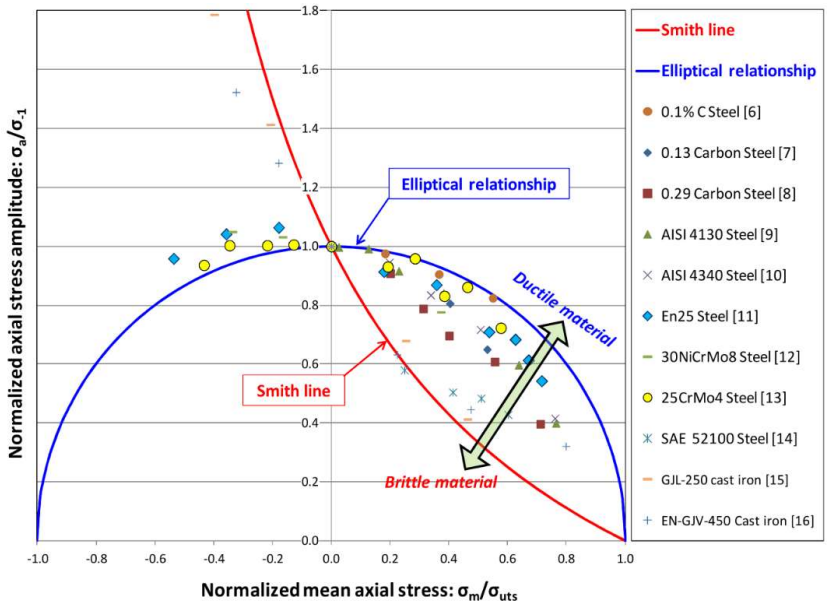

Figure 36. Normalized Haigh diagram showing the experimental results on 11 ferritic materials together with the Smith line for brittle materials and the Elliptical relationship for ductile materials.[86]

1.3.1.3 The effect of stress concentration on fatigue life

The existence of geometrical irregularities or discontinuities such as holes, grooves, or notches increases stresses significantly in the immediate vicinity of the discontinuity. Under variable loads, in both ductile and brittle materials the effect of stress concentration must be considered for to estimate fatigue life.[87]

Figure 37 represents a notched component subjected to an axial load. The nominal stress status can be easily calculated by dividing the applied lateral load by the transversal section ($\sigma = F/A$) in both IJ and EF sections. Higher nominal stress may be expected in EF since lower area remains. Nevertheless, the real shape of the stress status along the transverse section EF will be different than the constant value obtained use classical formulae from the Theory of Elasticity ($\sigma = F/A$), suffering a peak stress in the stress concentration point and having a lower stress value than the nominal stress in points sufficiently far away from the stress concentration point. Hence, the peak stress can be calculated using the following equation:

$$\sigma_{pk} = k_t \cdot \sigma_{nom} \tag{41}$$

Where σ_{pk} is the peak value of the stress, σ_{nom} is the nominal stress, i.e. the value of the stress not taking account of the effect of the stress concentration (but considering the reduction of the area after the notch/groove), and k_t is known as the notch factor.

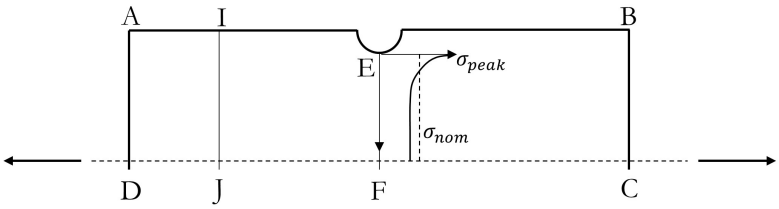

Figure 37. Notched sheet subjected to axial loading.

Under cyclic loading, the use of the peak stress σ_{pk} for the calculation to calculate the fatigue life in the S-N curve will lead to conservative results, while the use of the nominal stress σ_{nom} will lead to an overestimated life. Hence, the need for another factor for fatigue calculations resulted in the definition of the fatigue notch factor k_f, that can be calculated by using the following expression:

$$k_f = 1 + q(k_t - 1) \tag{42}$$

Where q is the notch sensitivity factor, with $q = 0$ being a non-notch-sensitive material and $q = 1$ a high notch-sensitive material. Hence, the effective stress used for fatigue calculation purposes is obtained as:

$$\sigma_{eff} = k_f \cdot \sigma_{nom} < \sigma_e \tag{43}$$

To sum up, in order to obtain the value of the fatigue notch factor k_f, the notch factor k_t and notch sensitivity q must be calculated.

1.3.1.3.1 Notch factor calculation, k_t

Even though there are a number of works[88,89] that provide tabulated values of the notch factor k_t for typical structural details, generally there will be no such table for the specific case under study due to complex geometry and/or the load case. Thus, if the value of k_t for a specific case is to be calculated, equation (44) (derived from equation (41)) must be used.

$$k_t = \frac{\sigma_{pk}}{\sigma_{nom}} \tag{44}$$

Peak stress σ_{pk} can be obtained by performing an FEA and obtaining the stress value known as 'pseudo-stress'; that is, the maximum stress considering linear-elastic material and thus neglecting eventual local plastic deformations. Besides this, the nominal stress σ_{nom}, i.e. the stress that would exist if there was no effect of the stress concentration but considering the section reduction (net section), can be calculated in some cases by using classic formulae from the Theory of Elasticity. Otherwise, the nominal stress may be calculated by extrapolating the stresses from stress status in zones nearby. Then, P_1 and P_2 points in Figure 38

are calculated representing the stress status assuming no stress concentration; i.e., nominal stress. This may not be very thorough unless performed according to a standard or with a well-known procedure.[53]

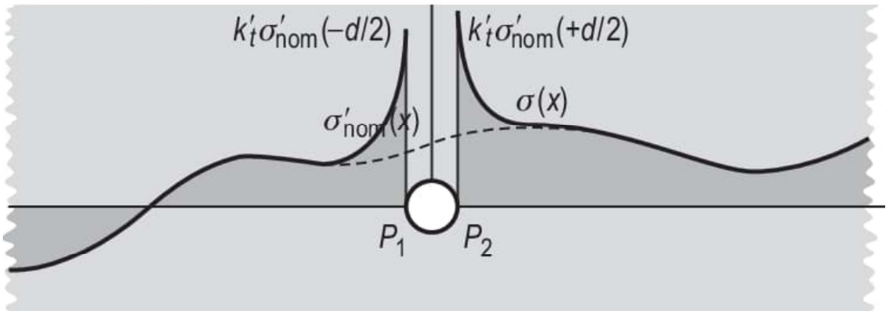

Figure 38. Nominal stress shape extrapolation from nearby sections.[53]

1.3.1.3.2 Notch sensitivity calculation, q

Once the notch factor k_t is known, notch sensitivity q must be obtained in order to calculate k_f according to equation (42). In the previous section, it could be deducted that notch sensitivity q depends only on material, however, it also depends on notch geometry (stress gradient). There are several approaches by which to obtain notch sensitivity q. Figure 39 shows Neuber curves[90] for steels, that relate notch radius r, material strength σ_{ut} and notch sensitivity q. This means that notch sensitivity q does not depend on notch factor k_t but on notch radius r. Consequently, the small part in Figure 40 will have the same notch factor k_t than the large one since both sizes are proportional, but notch sensitivity q of each part will be different.

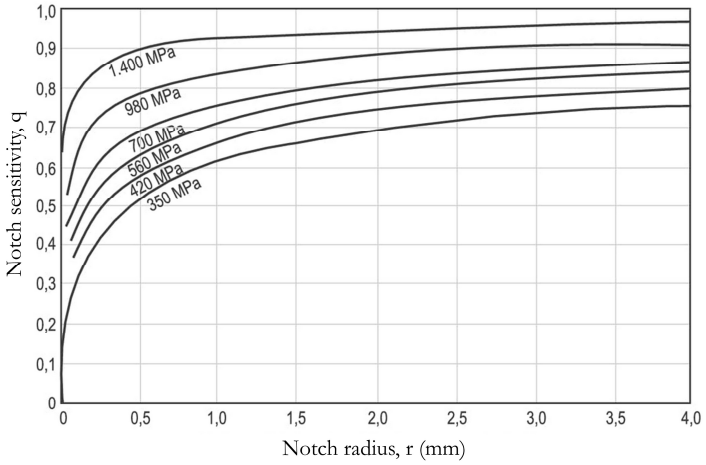

Figure 39. Notch sensitivity q versus notch radius r.[90]

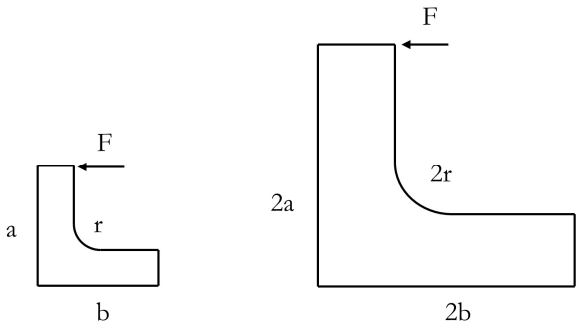

Figure 40. Parts with the same notch factor k_t but different notch sensitivity q.

Peterson[88] proposed a formula to obtain the notch sensitivity q based on R_{-1} fatigue tests performed on notched specimens.

$$q = \frac{1}{1 + a^*/r} \tag{45}$$

Where a^* depends on material strength and is obtained from the chart in Figure 41.[52,55]

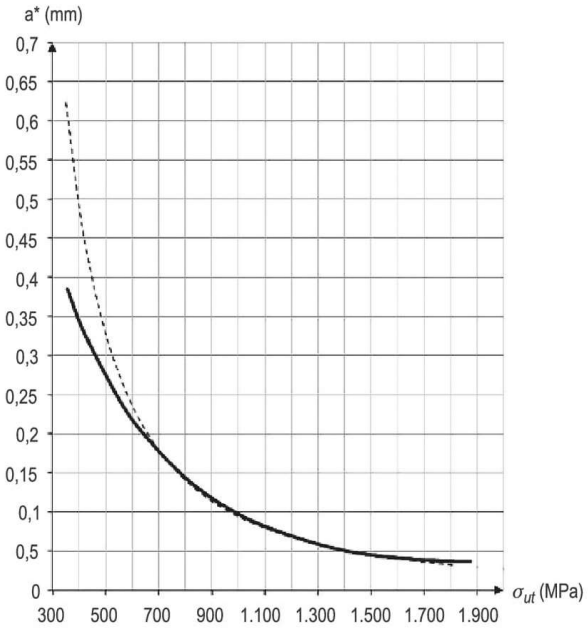

Figure 41. a^*value versus material strength.[52,55]

Neuber,[91] Kuhn and Hardrath[92] proposed the following formula based on empirical results.

$$q = \frac{1}{1 + \sqrt{A/r}} \tag{46}$$

Where $\sqrt{A}$ is obtained from the chart in Figure 42.

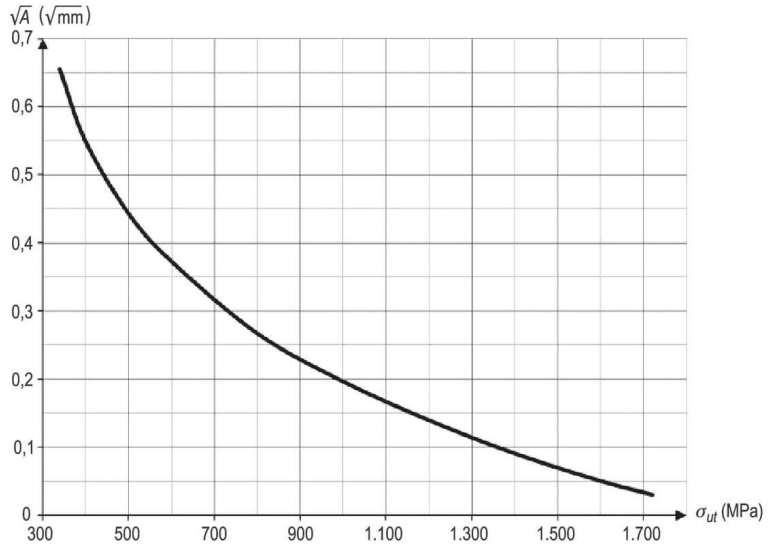

Figure 42. $\sqrt{A}$ value versus material strength.[52,88]

Nevertheless, pure alternating stresses have only been considered, thus far. In order to take account of the effect of mean stresses, several methods may be used. In (47)-(49), three methods are presented, which consider the Goodman criterion and the positive (tensile) mean stress component.[53] These expressions may be considered as a generalization of equation (43).

Ductile material, mean nominal stress method→ $\frac{k_f\sigma_a}{\sigma_e}+\frac{\sigma_m}{\sigma_{ut}}<1$ (47)

Ductile material, residual stress method→ $\frac{k_f\sigma_a}{\sigma_e}+\frac{k_f\sigma_m}{\sigma_{ut}}<1$ (48)

Brittle material→ $\frac{k_f\sigma_a}{\sigma_e}+\frac{k_t\sigma_m}{\sigma_{ut}}<1$ (49)

For ductile materials, the mean nominal stress method is generally used. It is less conservative because it does not increase the mean stress. Nevertheless, its use is not recommended with less conservative criteria, such as Morrow or Dietmann, since it would lead to double non-conservativeness. For the same reason, using the residual stress method with Goodman leads to double conservativeness.

In Figure 43 Haigh diagrams for both unnotched and notched specimens made out of different materials can be seen, showing different behavior depending on the material (aluminum in Figure 43A and ductile steel in Figure 43B).

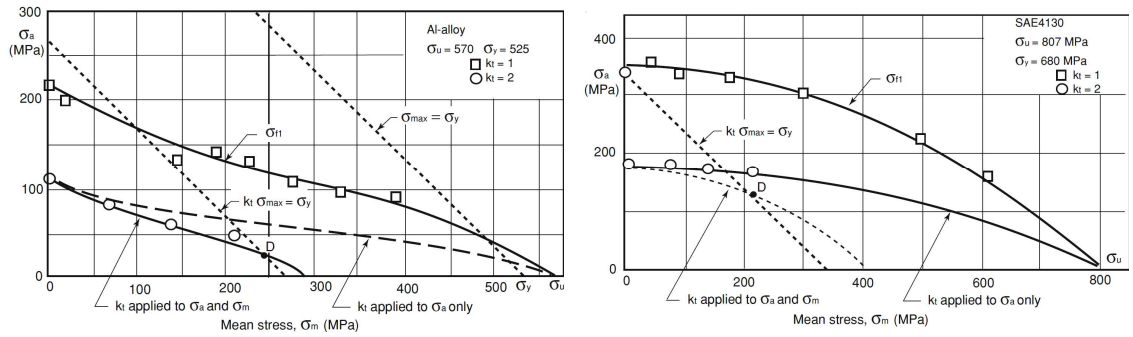

Figure 43. High diagrams of different materials (notched and unnotched). A, aluminum. B, ductile steel.[63]

Finally, there are other criteria such as the one proposed by Fatemi in Figure 44 using a line parallel to Morrow's criterion starting from a D point determined by material properties (S_{cat}).[52]

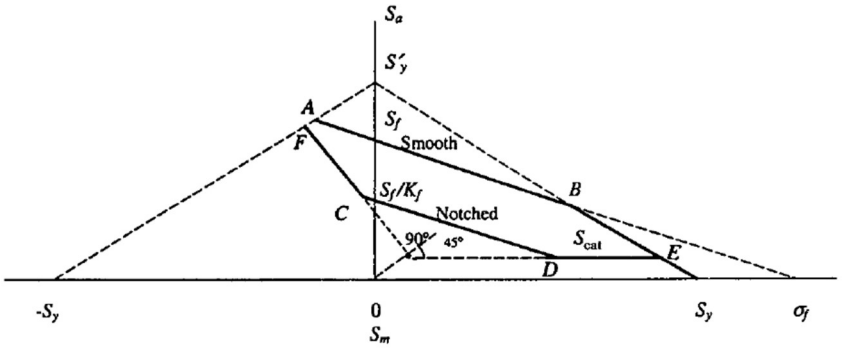

Figure 44. Approach proposed by Fatemi for considering mean stresses with stress concentration.[52]

So far, only infinite life has been considered for the calculation of fatigue behavior of parts with stress concentrations. For finite life, the notch factor k_f varies in relation to cycles. Therefore, it will be necessary to calculate this value experimentally by performing fatigue tests on notched and unnotched specimens. Then, to perform a fatigue calculation to estimate the cycles that a part will withstand, the following steps shall be followed:

1. First, the expected number of cycles must be assumed.
2. Then, the corresponding notch factor k_f must be calculated.
3. Next, the number of cycles must be calculated by entering the S-N curve.
4. Finally, if the number of cycles obtained in the result does not coincide with the assumed one, this calculation shall be repeated iteratively using as an assumption the number of cycles of the last result. The problem will be solved when both number of cycles match.

1.3.1.3.3 The Theory of Critical Distances

As mentioned, when there is stress concentration, neither the peak stress nor the nominal stress can be used for fatigue calculations. The previous approach consisted of calculating a fatigue notch factor k_f so that the nominal stress σ_{nom} is multiplied by it, obtaining an effective stress σ_{eff} (see equation (43)) for fatigue calculations for the pure alternating load case. By contrast, the Theory of Critical Distances (TCD) focuses on directly obtaining an effective stress σ_{eff} to be used for fatigue calculations without the need to calculate either the fatigue notch factor k_f or the nominal stress σ_{nom}.[93,94] This effective stress σ_{eff} is obtained at a certain distance (critical distance) from the notch root and its value is equivalent to the effective stress obtained by the previous approach (Figure 45). Starting with the easiest method, the Point Method uses the stress value of a point located at a certain distance, known as the critical distance d_{PM} (Figure 46A) and compares it with the fatigue limit (equation (50)).

$$\text{Peterson} \rightarrow \sigma_{eff} = \sigma(d_{PM}) < \sigma_{eR} \tag{50}$$

Where the critical distance d_{PM}, in the case of infinite life, depends on the stress ratio R and the material, and therefore so does the effective stress σ_{eff}. It must be pointed out that the effect of the mean stress is not neglected since the fatigue limit used in equation (50) σ_{eR} must be the one at the same stress ratio R as the critical section of the part under study. The critical distance (d_{PM}) can be obtained by using equation (51).

$$L_R = \frac{1}{\pi}\left(\frac{\Delta K_{IthR}}{\Delta \sigma_{eR}}\right)^2 \tag{51}$$

Where ΔK_{IthR} is the threshold stress intensity factor for a certain stress ratio R and $\Delta\sigma_{eR}$ is the fatigue limit range at the same stress ratio R. In the case of the Point Method, the critical distance will be $L_R/2$.

Once the critical distance d_{PM} is calculated, the value of the effective stress σ_{eff} can be easily obtained at this distance by performing a linear elastic FEA of the part under study and considering only the alternating component of the stress.

In addition to the Point Method, there are other methods based on the TCD such as the Line Method, that uses the elastic stress average through a line, the Area Method, that uses the stress average through a half circle centered in the notch root, and the Volume Method, that uses a spherical volume also centered in the notch root. Figure 46 shows each method and their corresponding critical distance using equation (51).

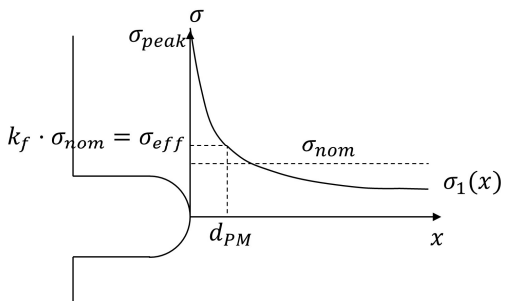

Figure 45. Point method applied on a notched specimen.

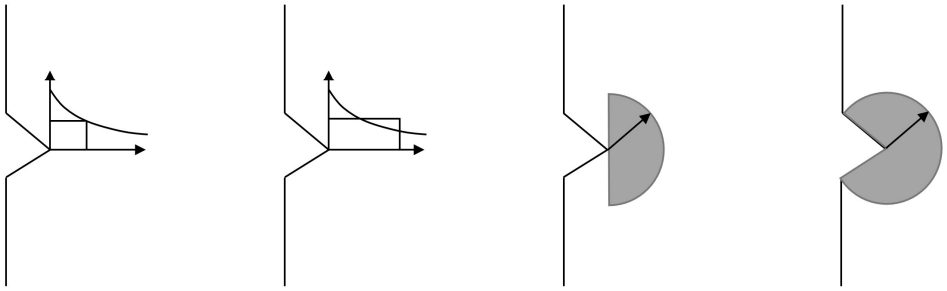

$d_{PM} = L_R/2$ A) $d_{LM} = 2L_R$ B) $d_{AM} = L_R$ C) $d_{VM} = 1.54L_R$ D)

Figure 46. Methods based on the TCD A, Point Method. B, Line Method. C, Area Method. D, Volume Method.

Even though, thus far, the TCD has been developed for infinite life (see equation (50)), Susmel[94] suggested its use also for finite life. Hence, the critical distance would follow a straight line (in log-log scale):

$$L(N) = A \cdot N^B \tag{52}$$

With A and B being material parameters. These parameters are said to also be dependent of the stress ratio R. Nevertheless, Susmel[94] suggests considering them only as material properties (regardless of R) so that the values of A and B can be obtained from R_{-1} fatigue tests whatever the load case of the mechanical part is. The finite life estimation may be solved iteratively.

1. First, a certain fatigue life (number of cycles *N*) is assumed.
2. The effective stress σ_{eff} is obtained at the critical distance determined by $L(N) = A \cdot N^B$.
3. The number of cycles *N* are obtained by entering the S-N curve with the effective stress σ_{eff}.
4. Finally, the number of cycles obtained in the third step is compared with the number of cycles assumed in the first step. If both number of cycles match, the iterative process can be stopped. Otherwise, it must continue

from the first step assuming a number of cycles equal to the estimation obtained in the third step.

1.3.1.3.4 FKM Method

Another way of considering the stress concentration effect is by using the methodology followed in FKM Guideline[69] on a section where the fatigue life is assessed by considering local stresses. The methodology that is valid for steel, cast steel, cast iron, aluminum alloys and cast aluminum alloys, uses FEA assuming fully reversed loading. The local stress is recorded at the critical point (Figure 47) as well as at a neighboring point (Δs) so that the normalized stress gradient $\overline{G_\sigma}$ is obtained as shown in equation (53).

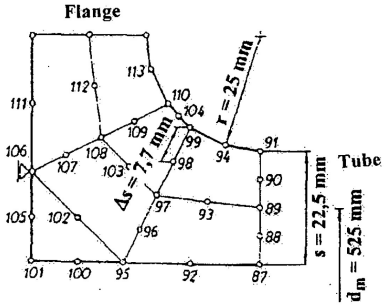

Figure 47. Example of a meshed part (nodes numbered) and the critical distance Δs considered.[69]

$$\overline{G_\sigma} = \frac{1}{\sigma_1} \cdot \frac{\Delta\sigma_a}{\Delta s} \tag{53}$$

Where σ_1 is the local or peak stress (maximum principal stress) at the critical point, Δs is the distance at which the second stress is recorded and $\Delta\sigma_a$ is the stress gradient. Then, the k_t/k_f ratio (that depends on both the normalized stress gradient $\overline{G_\sigma}$ and the tensile strength σ_{ut} is obtained from the chart in Figure 48 and used to modify the fatigue limit of the unnotched specimens.

$$\sigma_{eff} = \sigma_{pk} < \sigma_e \cdot \frac{k_t}{k_f} \tag{54}$$

If the component under study is subjected to mean stresses, the procedure remains the same; that is, the stress gradient $\overline{G_\sigma}$ and the k_t/k_f ratio are also obtained from a fully reversed FEA. In order to take account of the effect of mean stresses, the same methods from equations (47)-(49) are used. In this case, k_f shall be found from Figure 48.

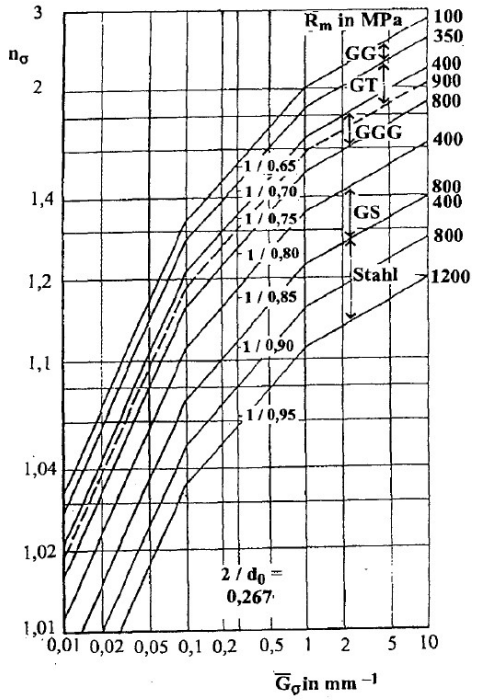

Figure 48. k_t/k_f versus the normailzed stress gradient χ and material properties.[69]

Finally, in the case of finite life, FKM assumes a slope $-1/k$, with k being a parameter that depends on the material and is provided by the guideline.

It must be pointed out that dividing the peak stress σ_{pk} by the k_t/k_f ratio is equivalent to multiplying the nominal stress σ_{nom} by the fatigue notch factor k_f. In other words, the effective stress obtained for fatigue calculations will be the same regardless of the three approaches used.

Everything mentioned so far corresponds to uniaxial fatigue, which will be used in Chapter 3 to analyze the mechanical behavior of the prosthetic screw.

1.3.2 Multiaxial fatigue analysis

In previous section, uniaxial stress was only considered, as is the case with the prosthetic screw. Nevertheless, crack initiation points can instead be subjected to multiaxial (biaxial or more rarely, triaxial) stress conditions. This is the case with dental implants, that cannot be assumed to operate uniaxially and, therefore, a multiaxial fatigue approach is needed.

Multiaxial fatigue analysis is more difficult to perform since, generally, there are 6 stress components (equation (55)) that can vary independently, which complicates experimental testing, results interpretation, and the development of methodologies for fatigue life estimation compared to uniaxial fatigue:

$$[\sigma(t)] = \begin{bmatrix} \sigma_{xx}(t) & \tau_{xy}(t) & \tau_{xz}(t) \\ \tau_{xy}(t) & \sigma_{yy}(t) & \tau_{yz}(t) \\ \tau_{xz}(t) & \tau_{yz}(t) & \sigma_{zz}(t) \end{bmatrix} \quad (55)$$

1.3.2.1 Experimental testing

Multiaxial fatigue testing is more challenging than uniaxial fatigue testing (where an axial load or a bending moment is enough) since more complex and expensive fatigue test benches are needed to introduce controlled multiaxial stresses. The most typical multiaxial tests are the ones performed on cruciform and cylindrical specimens.

Cruciform specimens are subjected to biaxial force by means of two linear actuators (Figure 49A). The problem with stress concentration in the center may be avoided by a large fillet radius and applying an hourglass-like thickness reduction (Figure 49B). As a drawback, the stress status must be calculated using an FEA since, for example, a force applied in one direction does not generate a uniaxial stress status on the specimen.

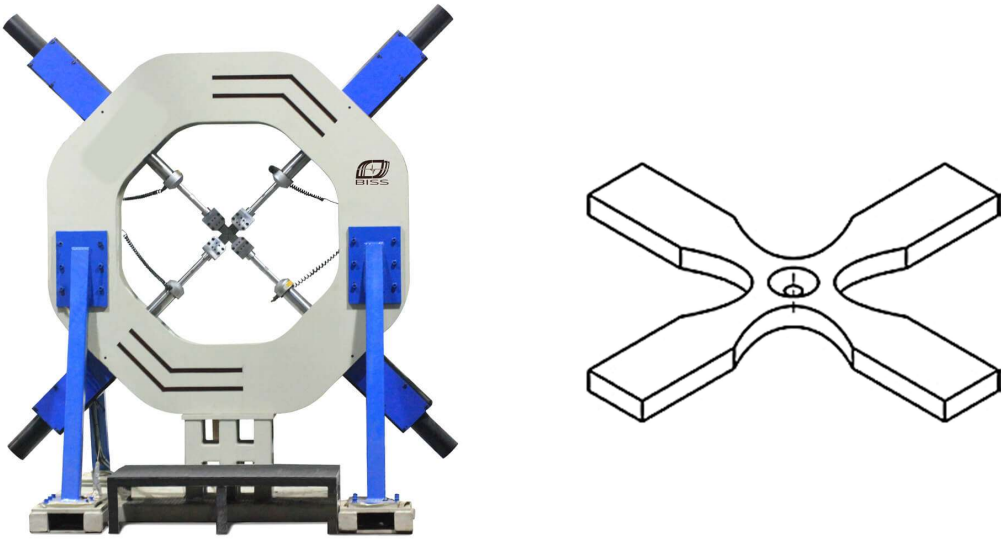

A) B)

Figure 49. Multiaxial fatigue testing of cruciform specimens. A, Biaxial force fatigue test bench.[95] **B, Specimen with fillets and thickness reduction.**[96]

Cylindrical specimens can be subjected by axial-torsion loading by a typical direct stress fatigue test bench equipped with a rotational actuator (Figure 50A and B) or by a torsion-bending gripping system (see Figure 50C and D).

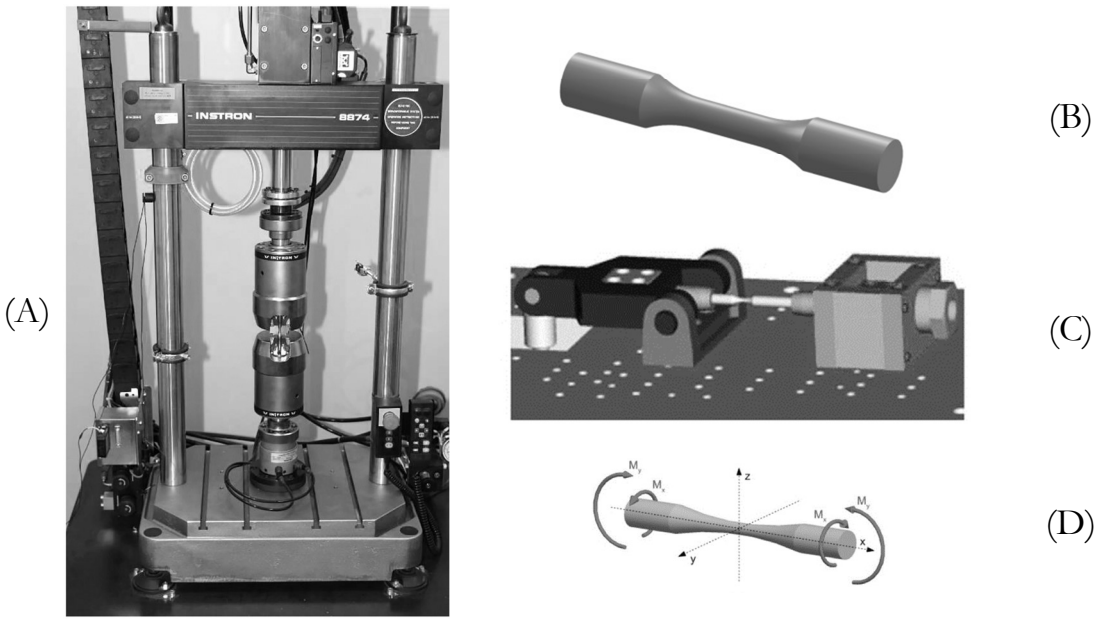

Figure 50. A, Axal-torsion fatigue test bench.[97] **B, Specimen for axial-torsion test.**[98] **C, Torsion-bending fatigue test bench.**[99] **D, Specimen for torsion-bending test.**[99]

Another way to apply multiaxial stresses is by subjecting tubular specimens to axial loading (or bending moment) and internal or external pressures (Figure 51).

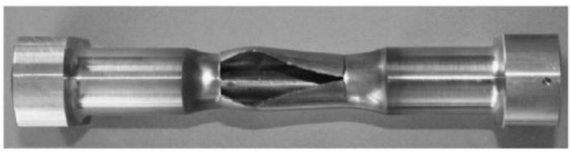

Figure 51. Tubular specimen for multiaxial fatigue (axial loading and internal pressure cycling).[53]

1.3.2.2 The effect of mean shear stress

The effect of the mean shear stress component is controversial. According to some authors, the mean shear stress does not affect the fatigue limit when the maximum shear stress is lower than the yield strength.[100–102] However, there are also numerous studies documenting a non-negligible effect of the mean shear stress,[103,104] even though, some other studies affirm that the effect of mean torsional stress is always lower than that of mean axial stress. There are also authors that state that mean shear stress does not affect standardized specimens but does affect components due to some factors such as surface finish, stress concentrations, among others.[42] More recently, Pallarés et al. compiled the results from other studies concluding that the effect of the shear mean stress is lower than the axial mean stress for ductile materials, with the effect of both axial and shear mean stresses being stronger for brittle materials such as cast irons.[86] Consequently, the most advanced multiaxial fatigue methods study

mean shear stress separately, so that some of them consider it in the calculation and others do not.

1.3.2.3 Stress proportionality

A multiaxial stress status is said to be proportional when all the components of the stress tensor have proportional relationships with each other, and these proportions remain invariant over time. This happens, for example, when all stresses are caused by the application of a single force (a rather common case). As a consequence, the principal stresses ($\sigma_1, \sigma_2, \sigma_3$) will also vary proportionally, any equivalent stresses (e.g., von mises) will also be proportional and, finally, the principal directions will remain fixed.

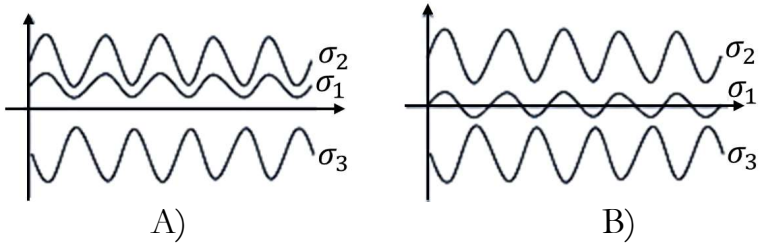

Figure 52. Multiaxial stress cycles. A) Proportional, B) Non-proportional.

In addition to this, cycles can be defined as constant amplitude cycles if they vary only between a maximum and a minimum (in other words, they can be defined by a mean and alternating stress components). Otherwise, cycles should be defined as variable amplitude cycles.

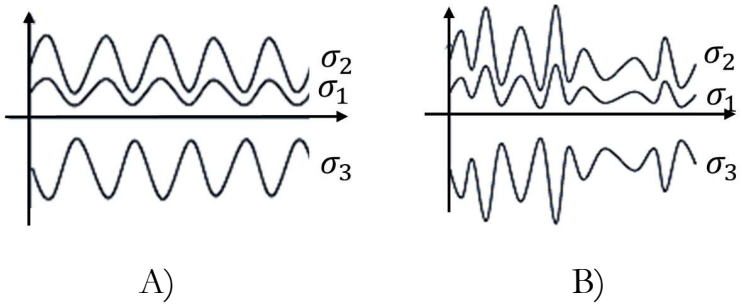

Figure 53. Proportional multiaxial stress cycles. A) Constant amplitude, B) Variable amplitude.

1.3.2.4 Multiaxial fatigue methods

1.3.2.4.1 Classic method

The classic method establishes an equivalence between a multiaxial stress status and a uniaxial status by means of static failure theories such as Von Mises for ductile materials. In the case of a proportional multiaxial stress status with constant amplitude ($\sigma(t)$), separating the mean components ($\sigma_{m_1}, \sigma_{m_2}, \sigma_{m_3}$)

from the alternating ones ($\sigma_{a_1}, \sigma_{a_2}, \sigma_{a_3}$) is proposed, so that the mean (σ_{VM_m}) and alternating (σ_{VM_a}) Von Mises uniaxial equivalent stresses are obtained. Thus, the Haigh diagram may be easily used as if it was a simple uniaxial case ($\sigma_{VM_m}, \sigma_{VM_a}$), as explained previously.

$$\sigma_{VM_m} = \sqrt{\frac{1}{2} \cdot \left[\left(\sigma_{1_m} - \sigma_{2_m}\right)^2 + \left(\sigma_{2_m} - \sigma_{3_m}\right)^2 + \left(\sigma_{1_m} - \sigma_{3_m}\right)^2 \right]} \quad (56)$$

$$\sigma_{VM_a} = \sqrt{\frac{1}{2} \cdot \left[\left(\sigma_{1_a} - \sigma_{2_a}\right)^2 + \left(\sigma_{2_a} - \sigma_{3_a}\right)^2 + \left(\sigma_{1_a} - \sigma_{3_a}\right)^2 \right]} \quad (57)$$

Where σ_{VM_m} may be positive (if $\sigma_{1_m} + \sigma_{2_m} + \sigma_{3_m} > 0$) or negative (if $\sigma_{1_m} + \sigma_{2_m} + \sigma_{3_m} < 0$).[53]

By contrast, for a variable amplitude stress status, the analysis becomes more complicated, and it is necessary to use cycle counting methods (such as Rainflow)[105] and cumulative damage rules (such as Miner)[106]. However, these procedures will not be explained in depth since they will not be used in this PhD Thesis.

To conclude, it should be mentioned that this method does not consider mean shear stress separately. In addition, it should be noted that this method uses static failure theories for fatigue, which, in theory, does not seem reasonable. In practice, however, the method has been found to work reasonably well for fatigue calculations, since a lot of components have been designed by means of this method, showing proper performance.

1.3.2.4.2 Invariant-based methods

Invariant-based methods use an equivalent stress based on stress tensor invariants. They are suitable for a proportional stress status of constant amplitude, and, unlike the classical method (Von Mises), they separately study the effect of mean shear stresses and are suitable for quasi-hydrostatic stress status. Generally, they are simple to apply, but they include material-dependent parameters. These parameters are usually estimated by means of various simple failure tests such as torsional, pulsating or alternating stress tests. The most common global approach methods are Sines and Crossland methods.

The Sines method uses the amplitude of the octahedral shear stress and the mean value of the hydrostatic stress at the point under study. This criterion, therefore, considers that the mean shear stress can be neglected and that only the mean component of the normal stresses has influence. Since it is based on

the octahedral stress, this method, to some extent, takes over the Von Mises criterion, but in contrast to the von Mises criterion, quasi-hydrostatic stress statuses are now detected, due to the effect of the corresponding hydrostatic stress.

The mean hydrostatic stress is defined as:

$$\sigma_{h_m}(t) = \frac{\sigma_{1_m}(t) + \sigma_{2_m}(t) + \sigma_{3_m}(t)}{3} \tag{58}$$

While the alternating octahedral stress is defined as:

$$\tau_{oct_a}(t) = \frac{1}{3}\left[\left(\sigma_{1_a}(t) - \sigma_{2_a}(t)\right)^2 + \left(\sigma_{1_a}(t) - \sigma_{3_a}(t)\right)^2 + \left(\sigma_{2_a}(t) - \sigma_{3_a}(t)\right)^2\right]^{0.5} \tag{59}$$

As mentioned above, this method is only useful for constant amplitude proportional stress status, where the mean and alternating components can be defined separately. Thus, the equivalent Sines alternating stress is expressed as follows and proposes that the specimen will survive if it is verified that:

$$\sigma_{eq_S} = \tau_{oct_a} + \alpha_S \cdot \sigma_{h_m} < \beta_S \tag{60}$$

Where α_S and β_S are material-dependent parameters. Since octahedral shear stress and equivalent Von Mises stress are very similar (they differ only in the value that multiplies the square root as shown in equation (61)) the Sines criterion is usually also expressed as a function of the Von Mises stress, as shown in equation (62).

$$\sigma_{VM} = \frac{3}{\sqrt{2}}\tau_{oct} \tag{61}$$

$$\sigma_{eq_S} = \frac{\sqrt{2}}{3}\sigma_{eq_a} + \alpha_S \cdot \sigma_{h_m} > \beta_S \tag{62}$$

The Sines criterion is also frequently expressed by using the square root of the second invariant of the stress tensor, obtaining the expression shown in equation (63).

$$\sigma_{eq_S} = \sqrt{J_{2_a}} + \alpha'_S \cdot \sigma_{h_m} > \beta'_S \tag{63}$$

Being:

$$\sqrt{J_2(t)} = \frac{1}{\sqrt{2}}\left[\left(\sigma_1(t) - \sigma_2(t)\right)^2 + \left(\sigma_1(t) - \sigma_3(t)\right)^2 + \left(\sigma_2(t) - \sigma_3(t)\right)^2\right]^{0.5} \tag{64}$$

Where α_S and β_S parameters are obtained from 2 experimental tests performed on specimens. β_S is obtained either from an alternating rotating bending test or from an alternating torsional test while α_S may be obtained either from a

pulsating axial test or from a static tensile test. Table 3 shows the values of α_S and β_S depending on the equation used for the Sines method.

Table 3. Values of α_S and β_S depending on the equation used for the Sines method.[53]

Octahedral stresses (equation (60))	Von Mises stresses (equation (62))	Second invariant square root (equation (63))
$\alpha_S = \sqrt{6} \cdot \frac{\tau_e}{\sigma_{R_0}} - \sqrt{2}$	$\alpha_S^M = \frac{3}{\sqrt{2}} \cdot \alpha_S$	$\alpha_S' = \frac{3}{\sqrt{6}} \cdot \alpha_S$
$\beta_S = \sqrt{\frac{2}{3}} \cdot \tau_e$	$\beta_S^M = \frac{3}{\sqrt{2}} \cdot \beta_S$	$\beta_S' = \frac{3}{\sqrt{6}} \cdot \beta_S$

The Crossland method procedure is similar to the Sines one (with the only difference being that it uses the maximum hydrostatic stress instead of the mean one) and it can also be expressed in the 3 aforementioned forms: octahedral stresses, second stress invariant square root, and Von Mises stress.

The octahedral stress-form may be expressed as:

$$\sigma_{eq_C} = \tau_{oct_a} + \alpha_C \cdot \sigma_{h_{max}} = \tau_{oct_a} + \alpha_C \cdot \left(\sigma_{h_m} + \sigma_{h_a}\right) > \beta_C \quad (65)$$

The square root of the second stress tensor invariant-form is expressed as follows:

$$\sigma_{eq_C} = \sqrt{J_{2_a}} + \alpha_C' \cdot \sigma_{h_{max}} = \sqrt{J_{2_a}} + \alpha_C' \cdot \left(\sigma_{h_m} + \sigma_{h_a}\right) > \beta_C' \quad (66)$$

Finally, the Von Mises stress-form is expressed as:

$$\sigma_{eq_C} = \sigma_{eq_a} + \alpha_C^M \cdot \sigma_{h_{max}} = \sigma_{eq_a} + \alpha_C^M \cdot \left(\sigma_{h_m} + \sigma_{h_a}\right) > \beta_C^M \quad (67)$$

Where α_C and β_C parameters are different from the ones used for the Sines method (α_S and β_S). Unlike for the Sines criterion, α_C and β_C parameters are different depending on the tests performed to determine them. The following values are the ones for the expression in equations (65) and (66):

$$\alpha_C' = 3\frac{\tau_e}{\sigma_e} - \sqrt{3} \quad (68)$$

$$\beta_C' = \tau_e \quad (69)$$

1.3.2.4.3 The critical plane methods

The classical and invariant-based methods explained in previous sections are based on principal stresses and they do not consider possible variations of principal directions along time. Critical plane methods, by contrast, are based on the hypothesis that fatigue behavior of a certain point is defined by the most affected plane of that point (critical plane). Hence, possible variations of principal directions are considered in these methods. The damage is usually

calculated as a linear combination of normal and shear stresses on the critical plane, establishing whether that stress status will lead to a fatigue failure at this point.

Since these methods study the stress status on a certain plane, the first step consists of determining the stress components on a certain plane Π determined by its normal vector $\{n\}$ as shown in Figure 54 and determined as:

$$\{\sigma(t)\} = [\sigma(t)]\{n\} \tag{70}$$

While the vectors of the normal and shear components are:

$$\{\sigma(n,t)\} = (\{n\}^T[\sigma(t)])\{n\} \tag{71}$$

$$\{\tau(n,t)\} = \{\sigma(t)\} - \{\sigma(n,t)\} \tag{72}$$

The modules of the normal and shear components are defined by:

$$\sigma(n,t) = \{n\}^T[\sigma(t)] \tag{73}$$

$$\tau_u(n,t) = \{\sigma(t)\}^T\{u\} \tag{74}$$

$$\tau_v(n,t) = \{\sigma(t)\}^T\{v\} \tag{75}$$

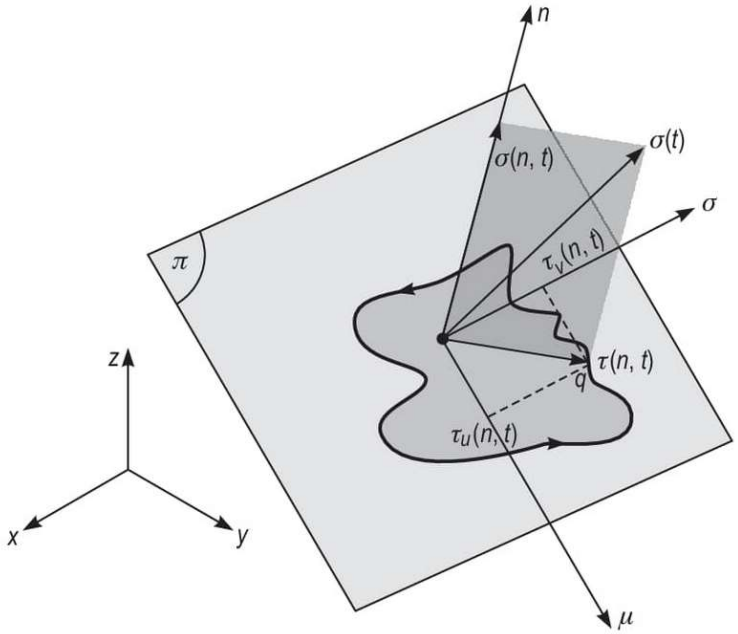

Figure 54. Stresses at a point *P* according to plane *Π*.[53]

Over time, the stress vector of plane Π, $\{\sigma(t)\}$, will trace a trajectory Ψ_n such as the one marked with a thick line in Figure 55. Accordingly, a multiaxial stress cycle is defined by a closed trajectory Ψ_n, where the period T is the time it takes to complete the cycle. For any moment, the stress vector $\{\sigma(t)\}$ can be decomposed into a normal stress contained on the n-axis $\{\sigma(n,t)\}$ and a shear

stress contained on the plane itself, whose components on two arbitrary axes u and v will be $\{\tau_u(n,t)\}$ and $\{\tau_v(n,t)\}$ respectively.

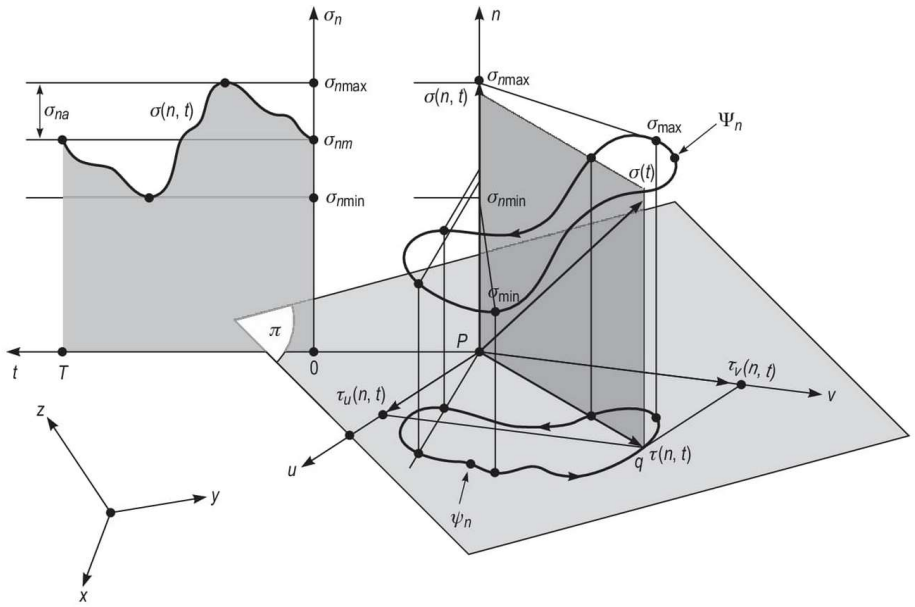

Figure 55. Normal and shear stress components for a plane Π.[53]

If, during this multiaxial cycle (or closed trajectory Ψ_n), there is only one maximum and minimum of the 3 components $\{\sigma(n,t)\}$, $\{\tau_u(n,t)\}$, and $\{\tau_v(n,t)\}$, the definition of multiaxial cycle and fatigue cycle will match and, therefore, it is possible to work with the mean and alternating components of the stress. If, by contrast, there is more than one maximum or minimum in any of the 3 components, the definition of the multiaxial cycle and fatigue cycle will not match, and the problem must be treated from a cumulative damage approach since average and alternating stress components cannot be defined. This approach will not be explained in this section since it falls outside the scope of this PhD Thesis.

Therefore, in cases where multiaxial cycle and fatigue cycle match, the mean and the alternate of the normal component of the in-plane stress is defined as:

$$\sigma_{n_m} = \frac{1}{2}(\sigma_{n_{max}} + \sigma_{n_{min}})$$
$$\sigma_{n_a} = \frac{1}{2}(\sigma_{n_{max}} - \sigma_{n_{min}}) \quad (76)$$

As the normal stress always maintains the same direction, defined by the vector $\{n\}$, the definition of its mean and alternating components is straightforward, using the same expressions as for the uniaxial case (equation (30)). However, calculating the mean and alternating components of the shear stress is more complex, since the shear stress does not maintain a constant direction over time,

but rather traces a trajectory Ψ_Π, which is the projection of Ψ_n onto plane Π (see Figure 55). Therefore, the definition of the mean and alternating shear stress is performed using methods such as the Minimum Circumscribed Circumference (MCC) method, the Minimum Circumscribed Ellipse (MCE) method, the maximum variance method, the longest chord method, etc.[94]

The MCC method uses the circumference of the minimum radius circumscribed to the trajectory Ψ_Π. The mean component of the shear stress τ_m is defined as the modulus of the vector that joins points P and Q (Figure 56) while the alternating component τ_a is defined by the value of the circumference radius.[94] The MCE method does the same with an ellipse instead of a circumference, with the mean components of the shear stress τ_m again defined by the modulus of the vector that joins points P and Q while the alternating component τ_a is defined by the square root of the sum of the squares of semi-axes (the hypotenuse of the triangle whose sides are the semi-axes of the ellipse).

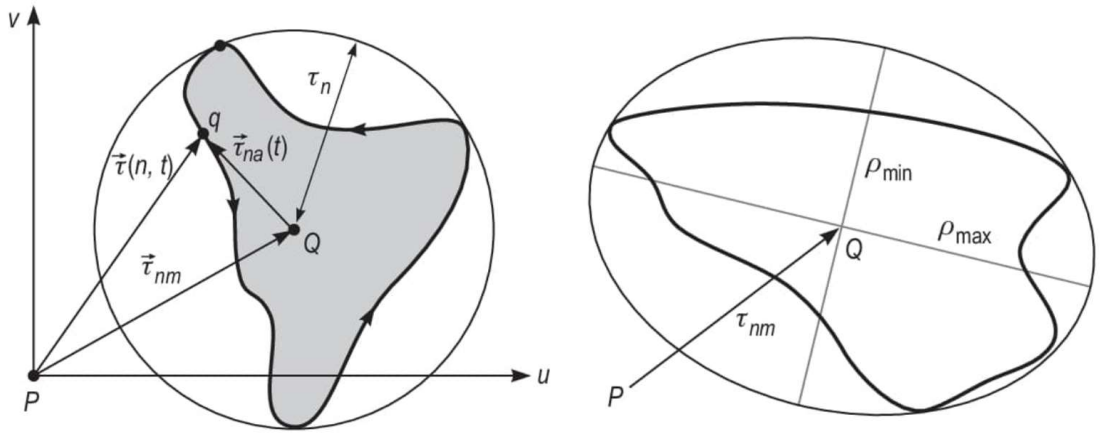

Figure 56. Mean and alternating components of shear stress calculations. A) Minimum Circumscribed Circumference method (MCC), B) Minimum Circumscribed Ellipse method (MCE).[53]

Once known how to calculate the mean and alternating components of normal and shear stresses, the critical plane methods are based on calculating these components on various planes, finding the most unfavorable plane (critical plane) and calculating the damage on that plane with a damage function. This damage function uses an equivalent stress function of the mean and alternating components of the normal and shear stresses. Critical plane methods can be basically divided into two types, depending on whether or not they use the same function to find the critical plane and to calculate damage. On the one hand, Maximum Shear Stress Range (MSSR) methods identify the critical plane as the one with the maximum alternating shear stress and calculate the damage

function on that plane. On the other hand, Maximum Damage (MD) methods identify the critical plane with the damage function itself by searching for the plane for which the damage function is at a maximum.

The steps to follow, whichever critical plane method is selected, are:

1. Obtain the stress status $\sigma(t)$ at the critical points of the part
2. Choose p planes for each point
3. Calculate the mean and alternating components of the normal and shear stresses ($\sigma_m, \sigma_a, \tau_m, \tau_a$)
4. Find the critical plane and calculate the damage
5. Calculation of fatigue behavior (finite or infinite life) of the point and plane with the most damage

There are many critical plane methods, each with its own damage function.[107] In this PhD Thesis, two methods will be used, the Findley and Dang Van methods, which are explained below.

The Findley method (MD) is one of the most cited in literature and identifies the critical plane as the one that meets:

$$max_{n=1}^{p}(\tau_a + \alpha(\sigma_m + \sigma_a)) \tag{77}$$

It uses the following damage function:

$$\tau_{a_{eq}=}\tau_a + \alpha(\sigma_m + \sigma_a) < \beta \tag{78}$$

The parameters are obtained from the cases of alternating axial stress and alternating torsion tests:[53]

$$\alpha = \frac{2 - \frac{\sigma_{-1}}{\tau_{-1}}}{2\sqrt{\frac{\sigma_{-1}}{\tau_{-1}} - 1}} \tag{79}$$

$$\beta = \frac{\sigma_{-1}}{2\sqrt{\frac{\sigma_{-1}}{\tau_{-1}} - 1}} \tag{80}$$

This method will only be valid if $\frac{\tau_{-1}}{\sigma_1} > 0.5$.

The Dang Van method (MD) is based on the study of stresses at the microscopic level of crystals, relating microscopic stresses to macroscopic stresses by means of the Lin-Taylor hypothesis.[108,109] It is usually used directly with macroscopic stresses, although in theory one should transform the macroscopic stresses into their microscopic equivalents and use the method with the latter. Unlike previous methods, Dang Van does not rely on calculating

the mean and alternating components of normal and shear stresses but evaluates the stress status at each moment to find the critical plane and calculate the damage, so that it can be used for cases of cumulative damage in infinite life calculations. The cost of this method is an order of magnitude higher than the previous one, since as well as studying several critical points with their various critical planes, it also studies them for several moments. The critical plane in the Dang Van method is identified as:

$$max_{n=1}^{p}(\tau_a(t) + \alpha \cdot \sigma_h(t)) \tag{81}$$

Being, evidently, the damage function:

$$\tau_{a_{eq}} = \tau_a(t) + \alpha \cdot \sigma_h(t) < \beta \tag{82}$$

Where:

$$\alpha = 3\left(\frac{\tau_{-1}}{\sigma_{-1}} - 0.5\right) \tag{83}$$

$$\beta = \tau_{-1} \tag{84}$$

In this method, the alternating components of the shear stress $\tau_a(t)$ is calculated for each moment t (see Figure 56) by means of MCC or MCE methods as the distance that joins the center of the circumference or the ellipse and the point of the trajectory at moment t. That is that $\tau_a(t)$ will always have a positive value while $\sigma_h(t)$ may be either positive or negative.

The methods explained so far are useful, as they have been explained, to determine whether or not infinite life will exist. For finite life, Socie proposes using the equivalent alternating stress calculated with any of the multiaxial fatigue methods presented and, with that, enter the S-N curve to estimate the fatigue life. In particular, Socie proposes using the equivalent alternating shear stress $\tau_{a_{eq}}$ which is calculated by using the Findley damage function (see equation (78)) and entering the S-N curve corresponding to the alternating torsion test.[110]

Regarding stress concentrations, Susmel proposes to use the TCD (Point Method), hence, using the alternating equivalent stress at an $L/2$ distance from the notch root to calculate fatigue life. Note that, according to Susmel, the critical distance depends on the number of cycles (see equation (52)). Hence, this problem shall be used by iteration as explained in section 1.3.1.3.3.[94]

The methods explained throughout this section will be used for fatigue analysis of the dental implant that will be discussed in Chapter 5.

1.4 Screw loosening analysis

As seen in section 1.2, when a screwed joint is preloaded, the screw is tensioned while the elements to be joined are compressed, so the system stores energy. As long as the friction of the screw head plus the friction of the threads can maintain this energy, the preload will not be lost.

The loosening torque-preload relationship (16), shows the value of the loosening torque T_L required to loosen the screw. However, this equation does not consider the effect of external actions (beyond the untightening torque) on the screw preload. This is a limitation, since it is known that external static or, especially, dynamic loads can alter this equilibrium, leading to loosening of the screw.[3,111] In effect, an external load may overcome the friction forces in the screw thread and head, causing slippage and, therefore, loss of preload, i.e., screw loosening. Therefore, other theories or approaches that include the effect of an external action (apart from the tightening or untightening torque) are needed.

Junker[112] developed the first machine to test the ability of screws to resist loosening under cyclic lateral loading. This machine became very popular and was widely used in research work.[113–116] The test consists of an eccentric cam that transforms the rotating movement provided by an electric motor into a linear alternating transverse displacement of one of the two plates that the screwed joint is connecting. The other plate as well as the nut (or female thread) is fixed. As can be seen in Figure 57, there are rollers between the movable plate and the fixed plate. Due to the nature of the machine, the test is controlled by an imposed movement, rather than force, even though the force is measured by load cells. As a consequence of the transverse alternating displacements of the upper plate, the screw may rotate and lose preload.

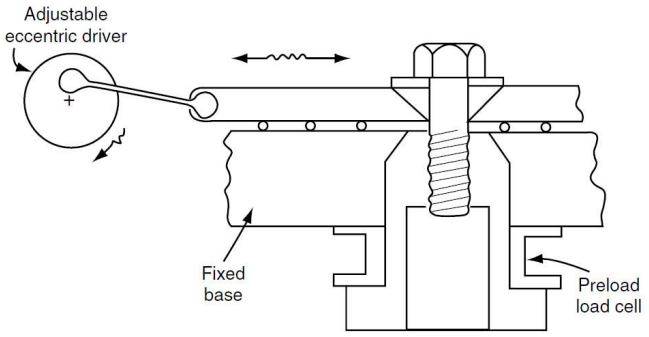

Figure 57. Junker test machine.[3]

In this sense, Junker[112] mentions that transverse dynamic loads cause greater loosening than axial loads, since they produce an oscillating movement between threads and among joined elements, which favors relative movement, while axial dynamic loads produce a much smaller and less critical relative movement. Figure 58 shows the sliding process between the screw and the fasteners under this transverse loading.

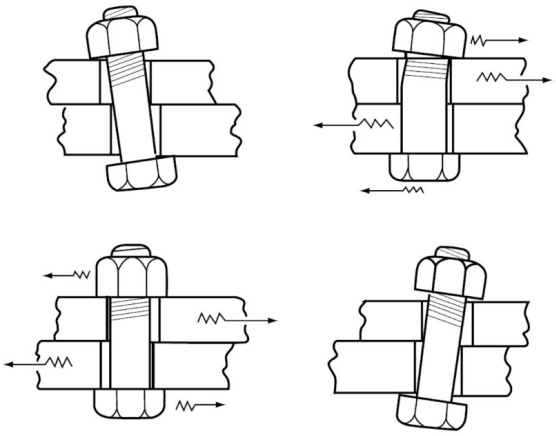

Figure 58. Transverse relative displacement among the elements of a screwed joint that may cause self-loosening.[3]

There are many theories that study the screw loosening phenomenon, and they all agree that a screwed joint subjected to dynamic loads does not lose all its preload immediately, but gradually over the external load cycles. However, although this phenomenon has been extensively studied, today there are still various theories that attempt to predict this gradual loss of preload due to the great complexity and dispersion of the phenomenon itself.

According to Junker,[112] if there is relative movement between the threads and on the joined element contact faces due to an external load, the screwed joint will lose part of its preload because the external load together with the normal force of the threads that favor loosening exceeds the frictional forces that maintain the screw preload. Nichols et al.[117] proposed an approach for detecting non-linearities, amongst them loosening of bolted structures. Sakai[118] proposed a theoretical model that considers the slippage between screw contact surfaces. Haviland[119] stated that loosening takes place due to the ratcheting action of the nut, even though no mathematical model or experimental data were provided to support this theory. Yamamoto et al.[120] assumed screw loosening to be the result of the accumulation and the release of elastic energy due to torsional screw deformation. In their FE study, Tanaka et al.[121] adopted the same loosening process as Yamamoto et al.[120] Vinogradov et al.[122] presented a

dynamic model that simulates the self-loosening of screwed joints under very high frequencies, skipping the operation range of most screwed joints. Zadoks et al.[123,124] also presented a dynamic model that simulates the self-loosening of the screw, but, in this case, in a tapped hole. Finally, Nassar et al.[125,126] proposed an experimentally validated mathematical model and experimental procedure to study the threaded fastener loosening phenomena under cyclic transverse loads. They used a linear model that resulted in a linear correlation between the clamp load loss and the number of cycles. Nevertheless, subsequently Nassar et al. developed a more accurate nonlinear model that is based on the relative slippage between friction surfaces. In these studies, the elastic beam theory is applied to the bolt bending under transverse load with certain hypotheses, such as uniform or linear varying contact pressure distributions under the bolt head, under the nut and in the threads. Fort et al.[127] found some limitations in these mathematical models such as the difficulty to analytically obtain the bending stiffness under the bolt head and nut, and further developed a model that includes the effect of plate thickness on self-loosening.

In any case, both Nassar et al.[125,126] and Fort et al.[127] aim to calculate the value of external force and moment needed in both the head and the threads of the screw for friction to be overcome, and therefore to initiate the screw loosening process. The differences between their models lie in the way they deal with the deformation of the screw and in how they model the process of progressive preload loss. In any case, this PhD Thesis is going to be based precisely on the common points; that is, on the analysis of the external forces acting to overcome the friction on the screw head and threads, since what is sought is to avoid the conditions that initiate the loosening process, not to calculate the loosening speed once the phenomenon has already started. The following section explains this previous approach on which this PhD Thesis is based, as it will be later explained in Chapter 7 where the self-loosening phenomenon of the prosthetic screw is analyzed.

As mentioned, the loosening torque-preload relationship shown in equation (16) does not consider the effect of external loads affecting the screwed joint other than the loosening torque itself. In this equation T_L is the external loosening torque that must be applied in order to overcome the friction torques in the screw head and thread contact surfaces (first and second terms in equation (16), respectively), while the pitch torque (third term in equation (16)) favors loosening. In the absence of external loading, the friction torques will be larger than the pitch torque, so T_L in equation (16) will be greater than 0,

indicating that a loosening torque will be needed to loosen the screw, whereby, under this condition no self-loosening will take place.

As mentioned, Nassar et al.[125,126] included the effect of transverse loads in the loosening torque of screwed joints. An external transverse load F_t acting on the screw will help to overcome the friction forces, thus reducing the value of T_L needed to loosen the screw. Consequently, for a given critical value of F_t, T_L may become null and, therefore, the screw will loosen without the need for an external loosening torque, i.e., the screw will self-loosen. This model will next be explained in detail.

1.4.1 Analysis of the screw head contact

Figure 59 shows the screw head seen from below (from the shank). The torque T_h (acting in the direction of rotation of the screw loosening) is the torque required to overcome the friction of the screw head when a transverse load F_{t_h} is acting. This torque produces a differential force dF_{T_h} on a contact area differential. Additionally, the transverse force F_{t_h}, produces a differential force $dF_{F_{t_h}}$ on the same contact area differential. These forces are opposed by a frictional differential force $dF_{f_h} = \mu p \cdot dA$. For the screw to loosen in this contact zone of the screw head, the entire contact surface must slide. This condition implies that the surface must rotate with respect to point c_h in Figure 59, which is at a distance of r_{c_h} from the screw axis.

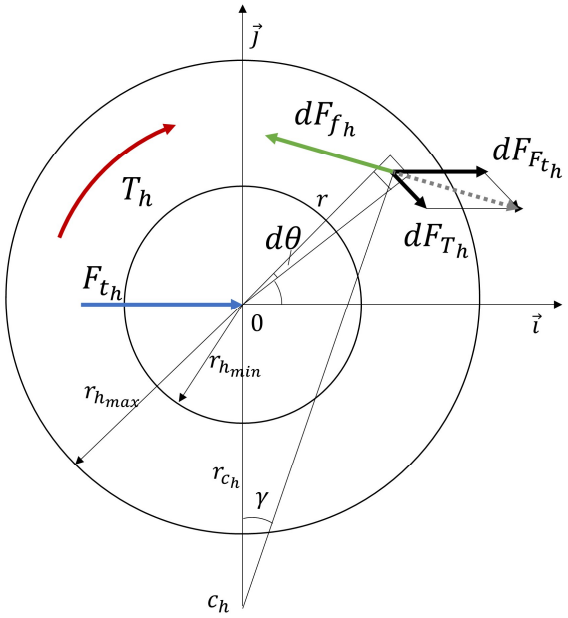

Figure 59. Force balance on the contact surface of the screw head (seen from below).

Angle γ is defined by the angle formed by the $\vec{j}$ axis and the center of the differential area under study review in Figure 59, being:

$$cos\gamma = \frac{r_{c_h} + rsin\theta}{\sqrt{\left(r_{c_h} + rsin\theta\right)^2 + (rcos\theta)^2}} = \frac{r_{c_h} + rsin\theta}{\sqrt{{r_{c_h}}^2 + r^2 + 2r_{c_h}rsin\theta}} \tag{85}$$

$$sin\gamma = \frac{rcos\theta}{\sqrt{{r_{c_h}}^2 + r^2 + 2r_{c_h}rsin\theta}} \tag{86}$$

Considering the torque balance with respect to the point c_h:

$$T_{f_h} = T_h + F_{t_h}r_{c_h} \tag{87}$$

Where T_{f_h} is the torque generated by the fractional forces dF_{f_h} with respect to c_h:

$$T_{f_h} = \int r \cdot \, dF_{f_h} = \int \mu p \sqrt{\left(r_{c_h} + rsin\theta\right)^2 + (rcos\theta)^2}\, dA \tag{88}$$

Assuming constant pressure and with the differential area being:

$$dA = r \cdot dr \cdot d\theta \tag{89}$$

Equation (88) can be expressed as:

$$T_{f_h} = \mu p \iint \sqrt{\left(r_{c_h} + rsin\theta\right)^2 + (rcos\theta)^2} r dr d\theta = \mu p \iint \sqrt{{r_{c_h}}^2 + r^2 + 2r_{c_h}rsin\theta}\, r dr d\theta \tag{90}$$

Moreover, considering the equilibrium of forces in the $\vec{\imath}$ direction:

$$\begin{aligned} F_{t_h} = \int dF_{f_h} \cdot cos\gamma = \mu p \iint \frac{r_{c_h} + rsin\theta}{\sqrt{\left(r_{c_h} + rsin\theta\right)^2 + (rcos\theta)^2}} r dr d\theta = \\ = \mu p \iint \frac{r_{c_h} + rsin\theta}{\sqrt{{r_{c_h}}^2 + r^2 + 2r_{c_h}rsin\theta}} r dr d\theta \end{aligned} \tag{91}$$

Equations (89) and (90) must be integrated numerically between $r_{h_{min}} < r < r_{h_{max}}$ (maximum and minimum screw head contact radii) and $0 < \theta < 2\pi$. Substituting equations (90) and (91) inequation (87) the value of T_h as a function of r_{c_h}:

$$T_h = T_{f_h} - F_{t_h}r_{c_h} = \mu p \iint \frac{r + r_{c_h}sin\theta}{\sqrt{{r_{c_h}}^2 + r^2 + 2r_{c_h}rsin\theta}} r^2 dr d\theta \tag{92}$$

Where p is the axial pressure generated by the axial load F_a acting on the screw:

$$p = \frac{F_a}{\pi \cdot \left({r_{h_{max}}}^2 - {r_{h_{min}}}^2\right)} \tag{93}$$

It is to be noted that equations (91) and (92) coincide with expressions 20 and 18 of the study of Nassar et al.[125]

Substituting equation (93) in equations (91) and (92):

$$F_{t_h} = \frac{\mu F_a}{\pi \cdot \left({r_{h_{max}}}^2 - {r_{h_{min}}}^2\right)} \int_{r_{h_{min}}}^{r_{h_{max}}} \int_0^{2\pi} \frac{r_{c_h} + r sin\theta}{\sqrt{{r_{c_h}}^2 + r^2 + 2 r_{c_h} r sin\theta}} r dr d\theta \tag{94}$$

$$T_h = \frac{\mu F_a}{\pi \cdot \left({r_{h_{max}}}^2 - {r_{h_{min}}}^2\right)} \int_{r_{h_{min}}}^{r_{h_{max}}} \int_0^{2\pi} \frac{r + r_{c_h} sin\theta}{\sqrt{{r_{c_h}}^2 + r^2 + 2 r_{c_h} r sin\theta}} r^2 dr d\theta \tag{95}$$

From equation (94), the value of r_{c_h} corresponding to a given external F_{t_h} force can be obtained and, entering this r_{ch}value in equation (95), the value of T_h needed to generate slippage in this contact is calculated.

To provide a specific case, when the transverse force F_{t_h} is null, r_{c_h} is zero and T_h is calculated by:

$$T_h\left(F_{t_h} = 0\right) = \mu F_a \cdot \frac{2}{3} \cdot \frac{{r_{h_{max}}}^3 - {r_{h_{min}}}^3}{{r_{h_{max}}}^2 - {r_{h_{min}}}^2} \tag{96}$$

Equation (96) coincides with expression 10 from the work of Nassar et al.[126]

For relatively small ratios of $r_{h_{max}}/r_{h_{min}}$, it can be assumed that:

$$\frac{2}{3} \cdot \frac{{r_{h_{max}}}^3 - {r_{h_{min}}}^3}{{r_{h_{max}}}^2 - {r_{h_{min}}}^2} \approx \frac{r_{h_{max}} + r_{h_{min}}}{2} \tag{97}$$

Hence, equation (96) can be expressed as:

$$T_h\left(F_{t_h} = 0\right) = \mu F_a \cdot \frac{r_{h_{max}} + r_{h_{min}}}{2} \tag{98}$$

This expression obviously coincides with the first term of equation (16) and with expression 1 from the work of Nassar et al.[126]

Another specific case is when no untightening torque is applied; that is, $T_h = 0$ and $r_{c_h} = \infty$. In this case, equations (94) and (95) leads to equation (99) showing that, in the absence of torque, a transverse force F_{t_h} equal to μF_a is needed to cause slippage of the screw head.

$$F_{t_h}(T_h = 0) = \mu F_a \tag{99}$$

These expressions are valid even when there is a bending moment on the contact surface, since the pressure variation due to a bending moment is linear and, therefore, the pressure increase of one half of the surface is compensated by the pressure decrease of the other half, giving the same results as there would be in the absence of bending moment (uniform pressure). This is valid if, as is the usual case, there is no contact loss at any point on the surface.

1.4.2 Analysis of the screw thread contact

Figure 60 shows the screw thread seen from below. A local coordinate system $(\vec{u}, \vec{v}, \vec{w})$ is defined. The $\vec{u}$ and $\vec{v}$ axes are contained on the horizontal plane (in true magnitude in Figure 60) formed by the global $\vec{\imath}$ and $\vec{\jmath}$ axes so that local axis $\vec{w}$ coincides with global axis $\vec{k}$. The plane of the thread surface is not horizontal, but has a double incline, α in the radial direction (negative slope as the radius increases) and β in the tangential direction, as shown in Figure 61 (screw seen from above).

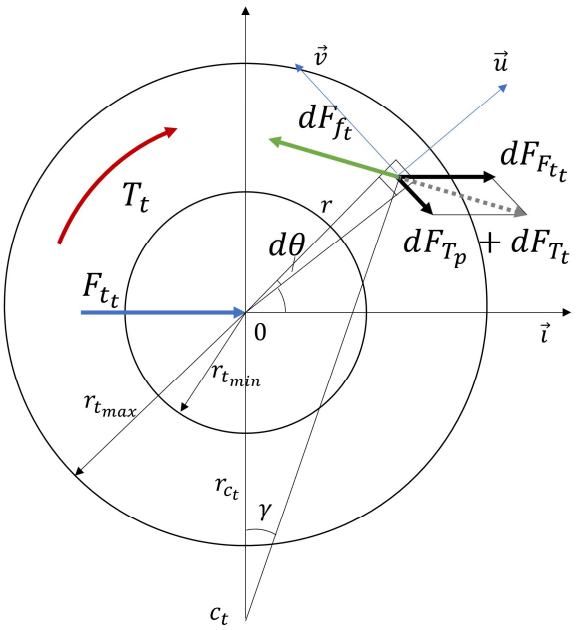

Figure 60. Force balance on the contact surface of the screw thread (seen from below).

For this reason, a local coordinate system $(\vec{u}_r, \vec{v_t}, \vec{w_1})$ is also defined which shares its origin with the system $(\vec{u}, \vec{v}, \vec{w})$ but with a double rotation: α with respect to the $\vec{v}$ axis, and $-\beta$ with respect to the $\vec{u}$ axis (see Figure 61). Hence, $\vec{u_r}$ axis forms an α angle with respect to the $\vec{u}$ axis, and the $\vec{v_t}$ axis forms an β angle with respect to the $\vec{v}$ axis. Thus, the $\vec{u_r}$ and $\vec{v_t}$ axes are contained in the plane

of the thread surface, with $\overrightarrow{w_1}$ being normal with it, i.e., the direction in which the contact pressure acts.

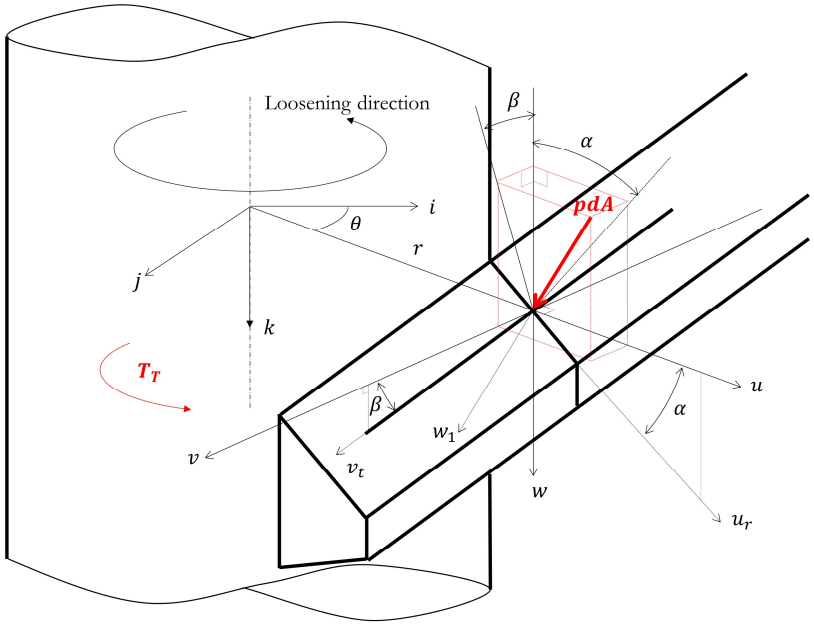

Figure 61. Pressure on the screw thread surface and the resulting loosening force dF_{T_p} (seen from above).

According to Figure 62, extracted from Figure 61, the pressure forms an ψ angle with the vertical axis, whereby:

$$cos\psi = \frac{1}{\sqrt{1 + tg^2\alpha + tg^2\beta}} = \frac{1}{\sqrt{sec^2\alpha + tg^2\beta}} \tag{100}$$

Different torques and forces act on the screw thread contact. Torque T_t is the torque necessary to overcome the friction on the screw threads (torque towards the screw loosening rotation direction) through a differential force dF_{T_t} when a transverse force F_{t_t} is applied. Additionally, the contact pressure due to the axial load F_a of the screw generated due to the inclination of the thread generates a differential force dF_{T_p} that causes a torque of T_p, also towards the screw loosening rotation direction. Moreover, there is a transverse force of F_{t_t}, which generates a differential force of $dF_{F_{t_t}}$ in Figure 60. These differential forces are opposed by the frictional differential force dF_{f_t}. This force develops on the plane of the thread, i.e., on the plane $(\overrightarrow{u_r}, \overrightarrow{v_t})$ in Figure 62, following vector $\overrightarrow{u_f}$. That is, in Figure 60 the differential force dF_{f_t} is not being viewed in true magnitude, but rather its projection on the horizontal plane $(\vec{u}, \vec{v})$ of value $dF_{f_t} \cdot cos\lambda$ in $\vec{u}_{f_p}$ direction in Figure 63.

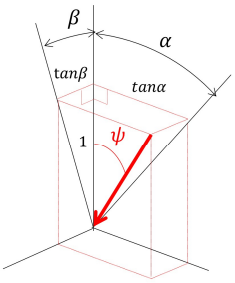

Figure 62. Vertical component of pressure.

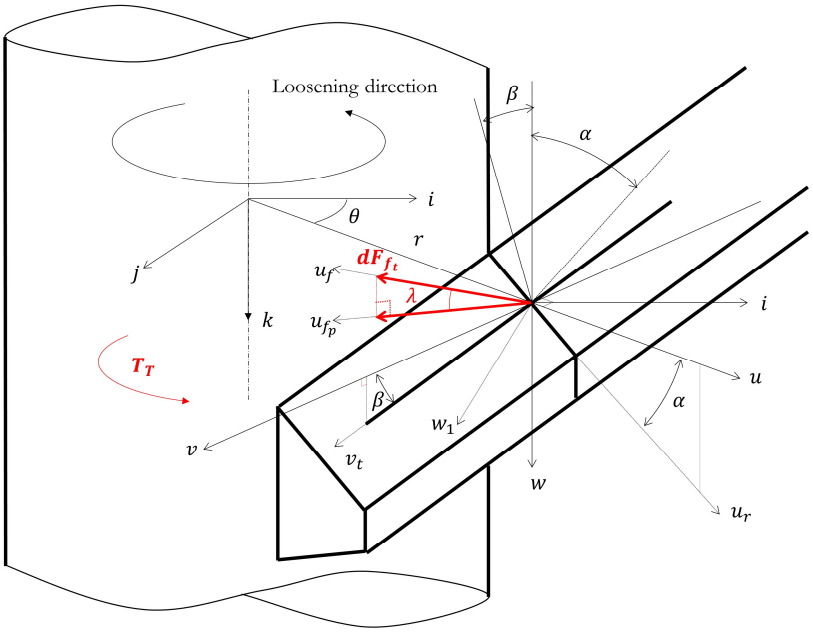

Figure 63. Friction force on the screw thread surface (seen from above).

According to Figure 64(screw viewed from below), where all axes and vectors are contained on the horizontal plane and are, therefore, seen in their true magnitude, the unit vector $\vec{u}_{f_p}$ is:

$$u_{f_p} = -cos\gamma\ i + sin\gamma\ j = (sin\gamma sin\theta - cos\gamma cos\theta)u + (sin\gamma cos\theta + cos\gamma sin\theta)v = \\ = -cos(\gamma + \theta)\ u + sin(\gamma + \theta)\ \ v \tag{101}$$

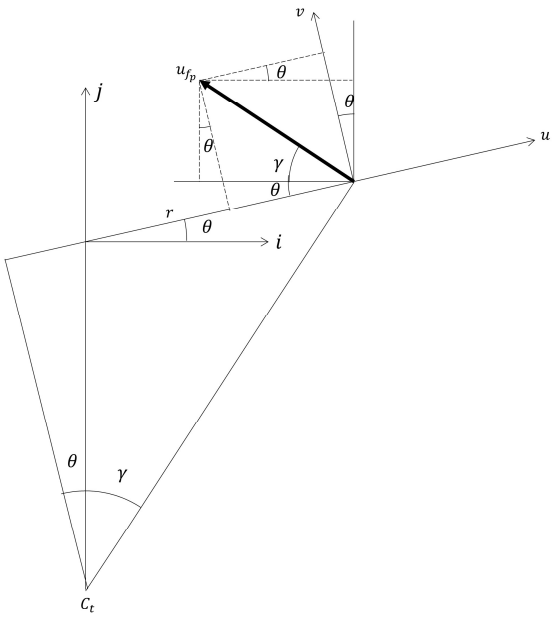

Figure 64. Vector on horizontal plane $(\vec{u}, \vec{v})$ (screw seen from below).

The vector $\vec{u}_f$ contained on the plane $(\overrightarrow{u_r}, \overrightarrow{v_t})$ of the thread surface is obtained in Figure 65 from the projected vector $\vec{u}_{f_p}$. Considering that as seen in equation (96) the vector $\vec{u}_{f_p}$ is unitary, its modulus $|u_f|$ is:

$$|u_f| = \sqrt{1 + (cos(\gamma + \theta)tg\alpha - sin(\gamma + \theta)tg\beta)^2} \tag{102}$$

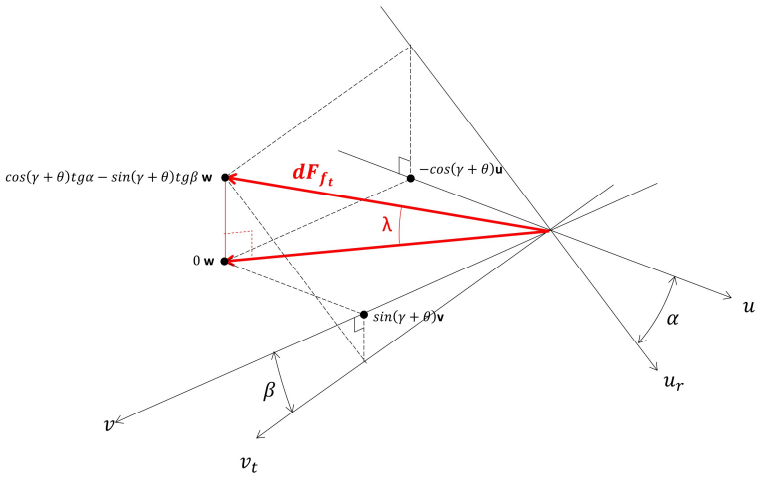

Figure 65. $cos\lambda$ determination.

Thus:

$$cos\lambda = \frac{1}{\sqrt{1 + (cos(\gamma + \theta) \cdot tg\alpha + sin(\gamma + \theta) \cdot tg\beta)^2}} \tag{103}$$

In addition, according to Figure 64:

$$cos(\gamma+\theta)=\frac{r_{c_t}cos\theta}{\sqrt{{r_{c_t}}^2+r^2+2r_{c_t}rsin\theta}} \tag{104}$$

$$sin(\gamma+\theta)=\frac{r+r_{c_t}sin\theta}{\sqrt{{r_{c_t}}^2+r^2+2r_{c_t}rsin\theta}} \tag{105}$$

So, substituting equations (104) and (105) in (103):

$$cos\lambda=\frac{1}{\sqrt{1+\frac{\left(rtg\beta+\ _{c_t}(cos\theta tg\alpha+sin\theta tg\beta)\right)^2}{{r_{c_t}}^2+r^2+2r_{c_t}rsin\theta}}} \tag{106}$$

Assuming $cos\theta\cdot tg\alpha \gg sin\theta\cdot tg\beta$ and $sin\theta \gg tg\beta\cdot cos\theta\cdot tg\alpha$:

$$cos\lambda=\frac{\sqrt{{r_{c_t}}^2+r^2+2r_{c_t}rsin\theta}}{\sqrt{{r_{c_t}}^2\cdot(1+tg^2\alpha cos^2\theta)+r^2\cdot(1+tg^2\beta)+2r_{c_t}r\cdot sin\theta}} \tag{107}$$

For the screw to loosen in this thread contact zone, the entire contact surface must slide. Therefore, all frictional differential forces $dF_{f_t}=\mu pdA$ are in the opposite direction to the sliding motion. This implies that in this condition the surface must rotate with respect to point c_t in Figure 60. Proposing the balance of torques with respect to c_t:

$$T_{f_t}=T_t+T_p+F_{t_t}r_{c_t} \tag{108}$$

Where T_{f_t} is the torque corresponding to the frictional differential forces dF_{f_t} with respect to c_t, according to Figure 60 and Figure 62, where $dF_{f_t}=\mu pdA$. Therefore:

$$T_{f_t}=\int \mu pcos\lambda\cdot\sqrt{{r_{c_t}}^2+r^2+2r_{c_t}rsin\theta}\,dA \tag{109}$$

In this case, the area differential is, as can be obtained from Figure 65:

$$dA=\sqrt{1+tg^2\alpha+tg^2\beta}\cdot rdrd\theta=\sqrt{sec^2\alpha+tg^2\beta}\cdot rdrd\theta \tag{110}$$

So, substituting equation (110) in (109):

$$T_{f_t}=\mu p\sqrt{sec^2\alpha+tg^2\beta}\cdot\iint cos\lambda\cdot\sqrt{{r_{c_t}}^2+r^2+2r_{c_t}rsin\theta}rdrd\theta \tag{111}$$

In addition, considering the equilibrium of forces in the $\vec{\imath}$ direction:

$$F_{t_t} = \int dF_{f_t} cos\lambda cos\gamma = \mu p \sqrt{sec^2\alpha + tg^2\beta} \cdot \iint cos\lambda \cdot \frac{r_{c_t} + rsin\theta}{\sqrt{{r_{c_t}}^2 + r^2 + 2r_{c_t} rsin\theta}} r dr d\theta \tag{112}$$

Substituting equation (107) into equation (112) matches expression 32 of the work of Nassar et al.[125]

Thus, the value of $T_t = T_{f_t} - F_{t_t} r c_t$ from equation(108) is:

$$\begin{gathered} T_t = T_{f_t} - F_{t_t} r_{c_t} = \\ = \mu p \sqrt{sec^2\alpha + tg^2\beta} \cdot \iint cos\lambda \left(\sqrt{{r_{c_t}}^2 + r^2 + 2r_{c_t} rsin\theta} - r_{c_t} \cdot \frac{r_{c_t} + rsin\theta}{\sqrt{{r_{c_t}}^2 + r^2 + 2r_{c_t} rsin\theta}} \right) r dr d\theta = \\ = \mu p \sqrt{sec^2\alpha + tg^2\beta} \cdot \iint cos\lambda \cdot \frac{r^2 + r_{c_t} rsin\theta}{\sqrt{{r_{c_t}}^2 + r^2 + 2r_{c_t} rsin\theta}} r dr d\theta \end{gathered} \tag{113}$$

Substituting equation (107) in (113):

$$T_t = \mu p \sqrt{sec^2\alpha + tg^2\beta} \cdot \iint \frac{(r + r_{c_t} sin\theta) r^2 dr d\theta}{\sqrt{{r_{c_t}}^2 \cdot (1 + tg^2\alpha cos^2\theta) + r^2 \cdot (1 + tg^2\beta) + 2r_{c_t} r \cdot sin\theta}} \tag{114}$$

Equation (114) coincides with expression 34 from the work of Nassar et al.[125]

Moreover, the torque T_p (acting towards loosening) caused by the circumferential component of the pressure $p \cdot cos\psi \cdot tg\beta$ (see Figure 61 and Figure 62) is:

$$T_p = \int r \, x \, dF_{Tp} = \int r p cos\psi tg\beta \, dA \tag{115}$$

Substituting equation (102) and (110) in (115), operating and integrating between $r_{t_{min}} < r < r_{t_{max}}$ (maximum and minimum screw thread contact radii) and $0 < \theta < 2\pi n$ (n is the number of thread coils in engaged):

$$T_p = p tg\beta \int r^2 dr d\theta = p \mathrm{n} tg\beta \cdot \frac{2\pi}{3} ({r_{tmax}}^3 - {r_{tmin}}^3) \tag{116}$$

Finally, the pressure p is obtained as a function of the axial load of the screw F_a. By proposing the balance of forces in the vertical direction (k axis), the axial load F_a is balanced by the vertical components of the contact pressure and the friction force. Proposing the balance of forces and substituting equations (100) and (110):

$$\begin{gathered} F_a = \int (p cos\psi - \mu p sin\lambda) \, dA = p \iint \left(1 - \mu sin\lambda \sqrt{sec^2\alpha + tg^2\beta}\right) r dr d\theta = \\ = p \cdot \left(n\pi ({r_{tmax}}^2 - {r_{tmin}}^2) - \mu \sqrt{sec^2\alpha + tg^2\beta} \iint sin\lambda r dr d\theta \right) \end{gathered} \tag{117}$$

Assuming $cos\theta tg\alpha \gg sin\theta tg\beta$:

$$sin\lambda = \frac{rtg\beta + r_{ct}cos\theta tg\alpha}{\sqrt{{r_{ct}}^2 + r^2 + 2r_{ct}rsin\theta}} \cdot cos\lambda = \\ = \frac{rtg\beta + r_{ct}cos\theta tg\alpha}{\sqrt{{r_{ct}}^2 \cdot (1 + tg^2\alpha cos^2\theta) + r^2 \cdot (1 + tg^2\beta) + 2r_{ct}r \cdot sin\theta}} \quad (118)$$

Substituting equation (118) in (117):

$$F_a = p \cdot \left(n\pi({r_{tmax}}^2 - {r_{tmin}}^2) - \mu\sqrt{sec^2\alpha + tg^2\beta} \right. \\ \left. \cdot \iint \frac{rtg\beta + r_{ct}cos\theta tg\alpha}{\sqrt{{r_{ct}}^2 \cdot (1 + tg^2\alpha cos^2\theta) + r^2 \cdot (1 + tg^2\beta) + 2r_{ct}r \cdot sin\theta}} rdrd\theta \right) \quad (119)$$

Finally, substituting equation (107) in (112):

$$F_{t_t} = \mu p\sqrt{sec^2\alpha + tg^2\beta} \\ \cdot \iint \frac{r_{ct} + rsin\theta}{\sqrt{{r_{ct}}^2 \cdot (1 + tg^2\alpha cos^2\theta) + r^2 \cdot (1 + tg^2\beta) + 2r_{ct}r \cdot sin\theta}} rdrd\theta \quad (120)$$

From these expressions, equation (108) can be used to calculate the torque T_t required to cause slippage at the thread contact, and thereby promote loosening of the screw, as a function of the transverse force F_{t_t} and the axial force F_a.

As a specific case, when the transverse force F_{t_t} is null, according to equation (32), r_{c_t} is also null. Then, according to equation (119):

$$F_a = p \cdot \left(n\pi({r_{tmax}}^2 - {r_{tmin}}^2) - \mu\sqrt{sec^2\alpha + tg^2\beta} \iint \frac{tg\beta}{\sqrt{1 + tg^2\beta}} rdrd\theta \right) \\ = pn\pi({r_{tmax}}^2 - {r_{tmin}}^2) \cdot \left(1 - \mu sin\beta\sqrt{sec^2\alpha + tg^2\beta}\right) \quad (121)$$

Equation (121) coincides with expression 19 from the work of Nassar et al.[126]

Now, the value of T_t can be expressed as a function of the axial load F_a by isolating p from equation (121) and substituting it in (114), obtaining:

$$T_t = \frac{\mu F_a\sqrt{sec^2\alpha + tg^2\beta} \cdot \iint \frac{(r + r_{c_t}sin\theta)r^2 drd\theta}{\sqrt{{r_{c_t}}^2 \cdot (1 + tg^2\alpha cos^2\theta) + r^2 \cdot (1 + tg^2\beta) + 2r_{c_t}r \cdot sin\theta}}}{n\pi({r_{tmax}}^2 - {r_{tmin}}^2) \cdot \left(1 - \mu sin\beta\sqrt{sec^2\alpha + tg^2\beta}\right)} \quad (122)$$

And equation (120) can be expressed as:

$$F_{t_t} = \frac{\mu F_a\sqrt{sec^2\alpha + tg^2\beta} \cdot \iint \frac{r_{ct} + rsin\theta}{\sqrt{{r_{ct}}^2 \cdot (1 + tg^2\alpha cos^2\theta) + r^2 \cdot (1 + tg^2\beta) + 2r_{ct}r \cdot sin\theta}} rdrd\theta}{n\pi({r_{tmax}}^2 - {r_{tmin}}^2) \cdot \left(1 - \mu sin\beta\sqrt{sec^2\alpha + tg^2\beta}\right)} \quad (123)$$

Doing the same and isolating p from equation (121) and substituting it in equation(116):

$$T_p = \frac{F_a}{\left(1 - \mu sin\beta\sqrt{sec^2\alpha + tg^2\beta}\right)} tg\beta \cdot \frac{2}{3}\frac{\left({r_{t_{max}}}^3 - {r_{t_{min}}}^3\right)}{\left({r_{t_{max}}}^2 - {r_{t_{min}}}^2\right)} \quad (124)$$

Equation (124) coincides with expression 21 from the work of Nassar et al.[126]

If in equations (124) it is assumed that $1 \gg \mu sin\beta\sqrt{sec^2\alpha + tg^2\beta}$ and $sec^2\alpha \gg tg^2\beta$, and considering equation (97):

$$T_p = F_a tg\beta \cdot \frac{r_{tmax} + r_{tmin}}{2} \quad (125)$$

Equation (125) coincides with the third term of equation (16) and with expression 1 from the work of Nassar et al.[126]

Continuing with the particular case of null F_{t_t}, and therefore also null r_{c_t}, T_t from equation (114) can now be expressed as:

$$\begin{aligned} T_t &= \mu p\sqrt{sec^2\alpha + tg^2\beta} \cdot \frac{1}{\sqrt{1 + tg^2\beta}} \cdot \iint r^2 dr d\theta = \\ &= \mu p cos\beta\sqrt{sec^2\alpha + tg^2\beta}\frac{2\pi n}{3}({r_{tmax}}^3 - {r_{tmin}}^3) \end{aligned} \quad (126)$$

Substituting p from equation (121) in (126):

$$T_t = \frac{F_a \mu cos\beta\sqrt{sec^2\alpha + tg^2\beta}}{\left(1 - \mu sin\beta\sqrt{sec^2\alpha + tg^2\beta}\right)}\frac{2}{3}\frac{({r_{tmax}}^3 - {r_{tmin}}^3)}{({r_{tmax}}^2 - {r_{tmin}}^2)} \quad (127)$$

Equation (127) coincides with expression 25 from the work of Nassar et al.[126]

If in equation (127)it is assumed that $1 \gg \mu sin\beta\sqrt{sec^2\alpha + tg^2\beta}$, $sec^2\alpha \gg tg^2\beta$ and $cos\beta \approx 1$, and considering equation (97):

$$T_t = \frac{\mu F_a}{cos\alpha}\frac{r_{tmax} + r_{tmin}}{2} \quad (128)$$

Equation(128) coincides with the second term of equation (16) and with expression 1 from the work of Nassar et al.[126]

Another particular case is when torque T_t is null; that is, r_{c_t} is ∞. In this case, according to equations (114), (116), (120) and (121):

$$F_{t_t} = \frac{\mu F_a \sqrt{sec^2\alpha + tg^2\beta}}{2n\pi \cdot \left(1 - \mu sin\beta \sqrt{sec^2\alpha + tg^2\beta}\right)} \cdot \int \frac{1}{\sqrt{1 + tg^2\alpha cos^2\theta}} d\theta$$
$$\approx \frac{\mu F}{2n\pi \cdot \left(1 - \mu sin\beta \sqrt{sec^2\alpha + tg^2\beta}\right)} \cdot \frac{1}{cos\alpha} \cdot \int \frac{1}{\sqrt{(1 + tg^2\alpha cos^2\theta)}} d\theta \quad (129)$$
$$= \frac{2\mu F}{\left(1 - \mu sin\beta \sqrt{sec^2\alpha + tg^2\beta}\right)(1 + cos\alpha)}$$

The integral of F_{t_t} of equation (129) must be solved numerically. From which it is deducted that the pure transverse force (with $T_t = 0$) to cause loosening in the threads is always greater than μF (because $cos\alpha < 1$).

As in the case of the screw head, these expressions are valid even when there is a bending moment on the contact surface, since the pressure variation due to a bending moment is linear, and therefore the pressure increase on one half of the surface is compensated by the pressure decrease on the other half, giving the same results as when there is no bending moment (uniform pressure). This is valid as long as there is no loss of contact at any point on the surface.

1.4.3 Equilibrium condition of the screw

Therefore, the loosening torque T_L can be calculated by adding the three calculated torques (T_h from equation (95), T_t from equation (122), and T_p from equation (125)), following the same structure as the torque-preload relationship (in its loosening version) of equation (11), except that, in this case, the effect of the transverse loads reaching the screw is considered.

$$T_L = T_h + T_t - T_p =$$
$$= \left(\frac{\mu F_a}{\pi \cdot \left({r_{h_{max}}}^2 - {r_{h_{min}}}^2\right)} \iint \frac{r + r_{c_h} sin\theta}{\sqrt{{r_{c_h}}^2 + r^2 + 2 r_{c_h} r sin\theta}} r^2 dr d\theta \right) +$$
$$+ \frac{\mu F_a \sqrt{sec^2\alpha + tg^2\beta} \cdot \iint \frac{(r + r_{c_t} sin\theta) r^2 dr d\theta}{\sqrt{{r_{c_t}}^2 \cdot (1 + tg^2\alpha cos^2\theta) + r^2 \cdot (1 + tg^2\beta) + 2 r_{c_t} r \cdot sin\theta}}}{n\pi ({r_{tmax}}^2 - {r_{tmin}}^2) \cdot \left(1 - \mu sin\beta \sqrt{sec^2\alpha + tg^2\beta}\right)} \quad (130)$$
$$+ F_a tg\beta \cdot \frac{r_{tmax} + r_{tmin}}{2}$$

Where r_{c_h} and r_{c_t} values shall be obtained from equations (94) and (123), respectively. This equation can be graphically represented by means of the normalized graph in Figure 66 which relates the torque and transverse force, both normalized with respect to the axial force. The graph shows the three terms of equation (127), with resisting torques T_h and T_t being non-constant and pitch torque T_p constant. In short, the combinations of transverse force F_t and loosening torque T_L that fall above the T_L/F_a curve will cause relative

displacement between the screw and the elements joined and, therefore, will cause self-loosening. The trend shift of the T_L/F_a curve for high values of F_t/F_a should be mentioned. Note that this occurs when T_h/F_a drops to zero, and only T_t and T_p are affecting T_L/F_a.

The markers in the graph show points where the curves intersect the axes, corresponding to the values of the specific cases in which the resisting torque is overcome only with a transverse force or only with a torsional moment.

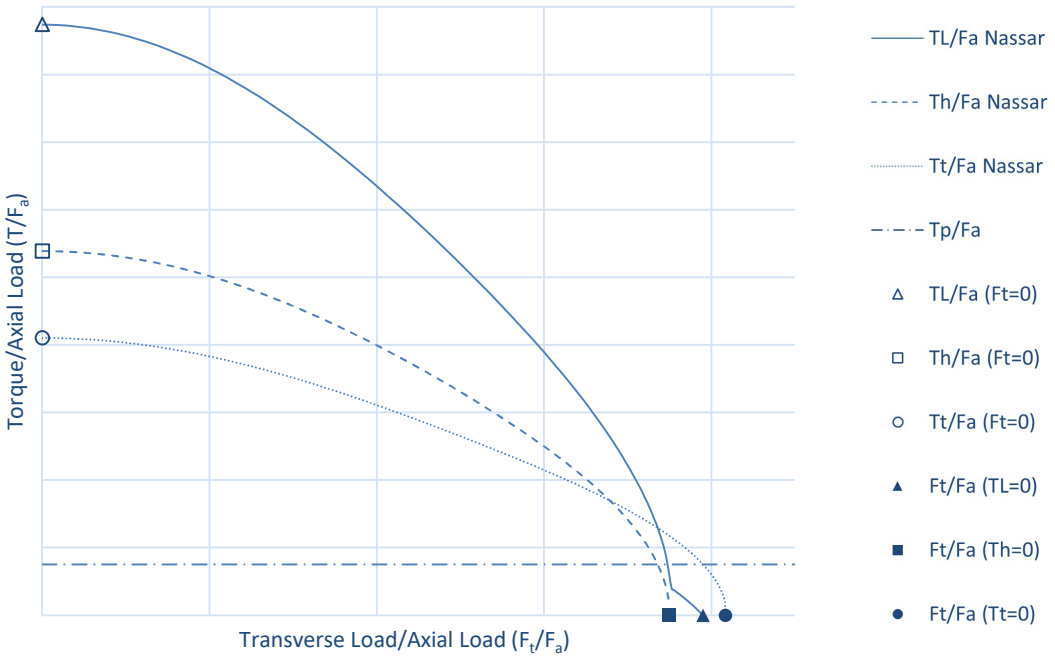

Figure 66. Torque versus transverse load: slip limit curves.

This model to predict self-loosening in screwed joints under transverse cyclic loading was validated experimentally for the case of two sliding plates, similar to the Junker test described at the beginning of section 1.4. This model forms the basis of the mechanical foundations of the self-loosening phenomenon and quantifies the effect of the different design, manufacturing and operational variables involved, thus enabling the designer to select the appropriate screw head and thread geometry, coefficient of friction, tightening torque, and other relevant parameters. One drawback is the fact that its applicability is not straightforward because the equations must be solved by means of numerical integration.

The methodology explained in this section is used in Chapter 7, where the loosening phenomenon of the prosthetic screw mounted on a dental restoration will be analyzed.

1.5 Microgap in screwed joints

Microcap, unlike fatigue or self-loosening phenomena, has less theoretical background. Nevertheless, the Oil and Gas industry has endeavored to study and prevent microgaps on pressure vessels and pipelines (used for gas or fluid storage and transportation) in order to avoid leakages.[128–132] In the case of pipelines, bolted joints are used to join several parts, forming the entire pipeline. In this case, in order to avoid leakages, several standards provide various recommendations to perform the assembly process as efficiently as possible.[128,133,134] A sound surface finish must be guaranteed to avoid mismatches, contact surfaces must be cleaned to ensure there is no dust that prevents proper sealing, contact surfaces must be aligned in parallel to ensure uniform load distribution, and so on. Besides this, a gasket is usually used in these bolted joints to ensure sealing.

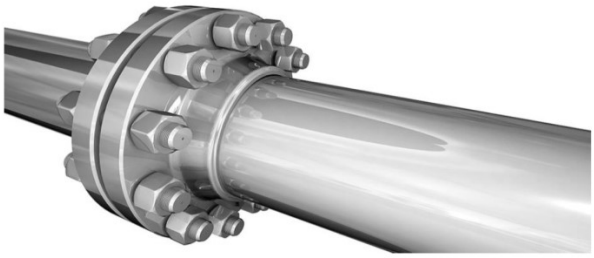

Figure 67. Bolted joint in a pipeline.[135]

Furthermore, the preload must be enough to ensure no service leakage but, at the same time, it cannot be excessive so that other phenomena such as fatigue is not compromised or even bolt damage is caused. The American Society of Mechanical Engineers (ASME) provides two different procedures to calculate target load of the joint.[128] On the one hand, there is a simple method that defines the minimum load on the bolts to avoid leakage. On the other hand, there is another method that calculates the bolt load to ensure structural integrity of the joined elements.

Finally, when tightening several bolts on a joint, the tightening sequence plays an important role. Usually, star pattern or alternating bolts patterns are used, sometimes followed by a final circular pattern.[135]

Unfortunately, this phenomenon is highly dependent on the surface finish and geometrical tolerances. Hence, it is not easy to reproduce microgap formation by means of FEA. Accordingly, this phenomenon is usually studied experimentally using various techniques such as the negative pressure wave

method,[136] the acoustic method,[137,138] the magnetic flux method,[139] the fiber optic sensor method,[140] etc.

Evidently, dental restorations do not suffer leakage as pipelines do in the Oil and Gas industry. However, as briefly mentioned in section 1.2.5, the IAC of dental restorations are subjected to microgaps due to insufficient torque, excessive external loading or inadequate manufacturing tolerances, and therefore cavities are generated that can harbor bacteria and cause clinical problems. The causes of microgap formation at IAC and the factors of dental restorations that have an effect on microgap size will be analyzed in depth in Chapter 6.

1.6 Mechanical of dental implants: a literature review

Since a screw-retained dental restoration is essentially a screwed joint, the same mechanical problems may arise, namely microgap formation, self-loosening or fatigue failure, as explained in section 1.2.5. In this section, first, a literature review of fatigue failure on screw-retained dental restorations is presented as well as an explanation of the ISO 14801 standard[141] that establishes the requirements for dental restoration fatigue testing. This is followed by a literature review of screw-loosening problems on dental restorations. Finally, a state of the art of microgap in IAC is presented, analyzing not only the microgap problem but also the methodologies used to detect it.

1.6.1 Fatigue behavior on dental restorations

Clinical studies report that most failures on dental restorations are caused by fatigue.[36] Depending on the load case and implant position in the mouth, these failures can occur either on the implant, the prosthetic screw, or very seldomly, the abutment. Nevertheless, screw failures are more common,[142,143] especially when mounted on regular or wide implants, usually occurring at the root of the first engaged thread.[144] Implant failures can also occur, especially if the implant is narrow and/or the screw has a high metric value.

Prosthetic screws are generally made of pure or alloyed Titanium, as these are less expensive than gold alloy screws while having excellent biocompatibility, corrosion resistance, machinability, and desirable mechanical and physical properties.[145,146] Machining processes and coatings have a significant effect on the performance of the prosthetic screw and the whole dental restoration.

Darshith et al. stated that rolled threads provide higher fatigue resistance than cut threads.[147] Gil et al. studied the effects of shot blasting on fatigue behavior of Commercially Pure (CP) Titanium, concluding that this treatment leaves a layer of compressive residual stress that improves fatigue life.[148] Park et al. studied the effect of the Tungsten Carbide Carbon (WCC) coating of prosthetic screws on implant preload experimentally obtaining higher preloads than for non-coated screws.[149] Higher preloads have been proven to have a positive effect on the fatigue behavior of dental implants as stated in various studies.[150–152] Evidently, screw metric has a significant effect on fatigue behavior since the higher the screw metric the larger resistant section the screw will have, and, therefore, a longer fatigue life.

Regarding dental implants, these are also commonly made of Titanium or Titanium alloys. In this sense, several publications experimentally characterize the endurance limit,[153] the effect of the mean stress[154,155] and the effect of notches.[94,156–159] Other materials used in dental implants such as zirconia, cobalt alloys or stainless steel were also studied.[160–162] Besides material characterization, some publications study dental implant fatigue from a probabilistic approach,[144,163,164] considering the randomness of some variables such as defects in dental implants and different load conditions that vary depending on the patient.

The fatigue behavior of dental restorations has been studied experimentally as well. Various studies analyzed implant geometrical parameters. The most studied ones have been implant body diameter, implant length, platform diameter and IAC type.

Implant body diameter has been reported to be one of the most important factors with regards to the biomechanical performance of dental restorations. A wider implant is beneficial[12] since it increases the contact surface with the surrounding bone, thus improving stress distribution[165–168] and providing enhanced initial stability.[169,170] In addition to this, with large implant diameters, stresses in the implant are reduced, especially around the implant neck,[171] improving the static and fatigue response of dental restorations.[172,173] However, it should be mentioned that these in vitro studies focused on implant failure while no studies analyzed the effect of implant body diameter on the mechanical performance of the prosthetic screw. This is of extreme importance when the screw is the failing component (when the implant body diameter is medium or large).

Implant length has been a controversial topic, with some authors reporting lower success rates for short and extra short implants,[16–20] whereas others have reported higher survival rates.[174–177] These discrepancies may be explained by the fact that short and extra short implants are mainly used in clinical situations with reduced bone height, where the experience and skills of the clinician are critical. Nevertheless, the effect of implant length has been reported to be much lower than that of other parameters such as implant body diameter.[169,171,178] In fact, in the implant-bone interface, where excessive strain may lead to bone loss, stress is mainly distributed along the first 6 threads of the implant,[179] the peak stress being at the bone crest level.[14,180,181] Consequently, unnecessarily increasing the length of the implant may result in limited improvements, even though a longer implant may improve primary stability in situations where cancellous bone is predominant.[14,15]

The diameter of the implant-abutment platform is also a key geometrical parameter, both clinically and mechanically. From a clinical point of view, the reduction of the contact diameter of the IAC is widely used in the platform switching concept,[182] where an abutment narrower than the implant is used. Platform switching can lead to reduced peri-implant bone loss.[183] Nevertheless, mechanical performance is negatively affected by the reduction of the contact diameter of the IAC because the platform plays a primary role in joint strength, joint stability, and rotational and locational stability.[13] As reported by Minatel et al.,[183] a reduction in the IAC diameter (by using the platform switching concept) can result in higher stress in the retaining screw. In addition to this, Nicolas-Silvente et al.[184] performed experimental fatigue tests where the retaining screws were the failing components and concluded that a higher fatigue limit was obtained with wider platforms, even though this conclusion might be limited by the fact that the specimens tested had different connection types.

External and internal butt-joint connections have also been compared in various studies.[185–190] From a clinical point of view, internal butt-joint connections improve both sealing against microbial ingress[185] and esthetics while providing more platform switching options.[186] From a mechanical point of view, IAC type may determine not only the maximum load of the restoration but also its failure mode.[187] Thus, FEA and experimental studies have determined that internal butt-joint connections have better fatigue performance than external connections.[188–190] However, these studies are focused on implant failure rather than on prosthetic screw failure.

Most of studies cited in this section performed experimental fatigue tests on various dental restorations in order to obtain the mentioned conclusions. The ISO 14801[141] standard establishes the testing conditions for dental restoration fatigue testing. It should be mentioned that the standard does not intend to simulate realistic in-vivo conditions, where the load and boundary conditions may significantly vary for each patient. Hence, the obtained fatigue behavior is not useful for predicting the in-vivo performance of a dental restoration, but rather for comparing dental restorations of different designs, size, assembly conditions, and so on. In short, the implant of the restoration must be fixed in a specimen holder in such a way that it protrudes 3mm±0.5mm. The implant can be fixed by using an embedding material as long as it has a modulus of elasticity higher than 3GPa. The specimen holder must provide a 30º ±2º inclination to the restoration with respect to the load application direction. A hemispherical device shall be mounted on top of the restoration, ensuring that the center of its circumference is placed at 8 mm from the implant connection (11mm from the specimen holder upper surface). In contact with the hemispherical device, the loading device must apply the testing load in such way that no lateral restrictions occur. Figure 68 shows a schematic of the experimental set-up. The load must vary sinusoidally between the maximum load (not exceeding ±5%) and 10% of that value at a maximum frequency of 15Hz. In case of dental restoration including materials where corrosion fatigue has been reported, the fatigue tests shall be performed in a saline medium. The fluid must be kept at 37ºC ±2ºC and the maximum testing frequency must be 2Hz. At least two and preferably three specimens shall be tested at each load level, and at least four load levels must be tested. The lowest load will be considered as the fatigue limit if at least three specimens survive a specified number of cycles. This number of cycles (also known as run-out) must be 5 million cycles if the test is performed at up to 15Hz or 2 million cycles if the test is performed at up to 2Hz. Staircase method (see section 1.3.1.1) is also allowed for fatigue limit determination.

As a result, a complete F-N curve is obtained that relates the fatigue life of a dental restoration with the number of cycles and this can be used to compare different dental restorations under exactly the same conditions.

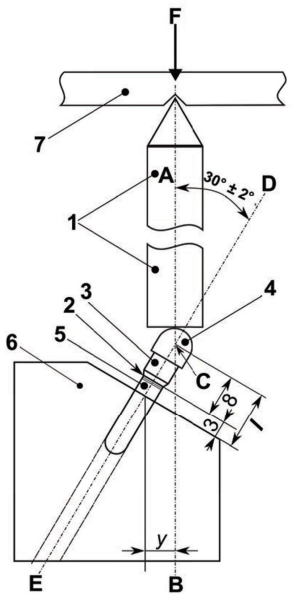

Legend:
1-Loading device
2-Nominal bone level
3-Abutment
4-Hemispherical device
5-Implant body
6-Specimen holder
7-Force application

Figure 68. Schematic of the test set-up for non-angulated dental restorations according to ISO 14801 standard.[141]

1.6.2 Self-loosening of the prosthetic screw

As mentioned, during their life span, dental restorations are subjected to variable loads due to mastication, bruxism, and so on. Axial loads are generally predominant but are always accompanied by lateral forces.[191] As seen in section 1.4, these loads can cause the screw to untighten or preload loss. This is known as the screw self-loosening phenomenon and is mainly produced by the lateral external forces that generate a rotational movement of the screw. As a result, gradual preload loss may occur, leading to micro-movements and eventual structural failure of the dental restoration.[3,4,37–40]

Screw loosening is one of the major mechanical cause of dental implant replacement[192] (along with fatigue failures), affecting between 4.3% and 12.7% of dental restorations according to specialized literature.[193–195] It is well established that screw loosening depends on a large number of parameters, such as tightening torque, preload, occlusal forces, thread embedment and geometrical misfits.[39,196,197] In this sense, screw loosening is generally the result of an inadequate tightening torque, incorrect implant design, manufacturing defects or unexpected load conditions, amongst other factors.[198–200]

Many investigations have studied the effect of different parameters on screw self-loosening. Wu et al. concluded that lubrication reduces friction and consequently increases clamping force, but loosening torque is also reduced.[201] Elias et al. studied the effect of screw coatings that decreases the coefficient of

friction, agreeing with Wu et al. in terms of preload and untightening torque.[202] Park et al. recommend the clinical use of gold-plated screws to prevent screw loosening. Teflon coating is also recommended by these authors as well as avoiding repeated tightening.[203] In several studies, a significant reduction of removal torque after cyclic loading was noticed, demonstrating that screw preload decreases in line with the number of cycles due to screw self-loosening.[38,204] Siamos et al. studied the effect of screw tightening torque and consequently screw preload level and recommended a tightening torque higher than 30 Ncm to minimize screw self-loosening.[205] In this sense, Lang et al. stated that the preload should be 75% of the yield strength of the screw.[5] Aboyoussef et al. concluded that anti-rotation strategies may be used to reduce screw self-loosening problems.[196] In the same vein, Arshad et al. proposed adding an adhesive to the screw joint interface.[199]

1.6.3 Microgap formation at implant-abutment connection

As mentioned in section 1.1, dental implants are subjected to microgap formation in the IAC. These microgaps may be caused by irregularities on the contact surfaces of the IAC[21,22] and/or by the application of occlusal loads.[49,50]

Microgaps can seriously compromise the success of dental restoration. An excessive microgap creates a cavity that favors the colonization of bacteria or even allows them to pass inside the implant and proliferate there.[7–11] These bacteria can move into the peri-implant tissues, leading to inflammation[22–24] and crestal bone resorption.[8,25–29] This can lead to peri-implantitis,[30] the main cause of implant loss.[31–33]

In this literature review, a classification will be made according to the way the microgap at the IAC is detected or studied. On the one hand, those methods that study whether a fluid or gas is capable of leaking through the connection or not will be called Leakage Detection Methods. On the other hand, Microgap Measurement Methods will refer to methods that can directly quantify the size of the microgap in the IAC.

Among Leakage Detection Methods, the Gas Flow Method consists of drilling a hole in the implant and introducing pressurized gas inside the implant.[206,207] In this way, a seal loss would be detected when the gas passes through the connection, which would correspond to a gap large enough for the outside and inside of the implant to be connected. In addition to this, this same group includes the Bacterial Colonization Methods. This technique is one of the most

used among the bibliography. In short, a fluid with bacterial contamination is deposited inside the implant and the abutment and screw are assembled.[9,31,208–222] Once the required tests have been carried out (application of cycles, static load, no load, etc.), the assembly is placed in a sterile medium and checked for bacterial filtration to the outside of the implant. The same technique can be used in the opposite manner, i.e. assemble the dental restoration in a sterile environment, immerse the assembly in an environment with bacterial contamination and, finally, apply the appropriate tests. Bacterial leakage is checked by disassembling the dental restoration and observing the inside of the implant.[10,210,223–232] Finally, the Ink Leakage Method[29,233–235] consists of depositing ink inside the implant and assembling the abutment and screw at the recommended tightening torque. Afterwards, the assembly is generally immersed in a transparent fluid such as water, the dental restoration is subjected to the appropriate test conditions, and leakage is confirmed if the ink escapes to the outside.

Additionally, the Microgap Measurement Methods include the Optical/SEM Measurement Method, in which the microgap at the IAC is measured by viewing it under an optical microscope[236–239] or a Scanning Electron Microscope (SEM).[21,22,210,227,240–249] These microgap measurements are performed after the corresponding loads (if any) have been applied. Finally, X-Ray Measurement Methods, like the previous technique, are used to measure the gap, rather than to detect the leakage event. In this method, the implant is subjected to X-ray exposure.[250–257] The sample will act as a filter between the X-ray source and the receptor so that the thickest areas will allow less radiation to pass through and will appear clearer on the X-ray. If a microgap appears, there will be a minimal thickness wedge that should be detected on the X-ray. For the measurements to be accurate, the energy source must be powerful enough as is the case with hard X-Ray and synchrotron.[250–258]

Most of the studies found investigated microgap formation either in the absence of loads[9,10,21,22,29,31,206–215,217–222,224,225,228,229,231–233,235,237,238,240,242,243,245,248,258–260] or after applying a cyclic load[223,226,227,230,234,236,239,241,244,246,247,249,251,256,257,261,262] on the restoration. However, few studies have been found that investigate the microgap under in-situ loading[250,252–255,257,263,264] due to the difficulty of the method which requires measuring the microgap at the same time as the load is applied. However, this type of microgap can also host bacteria inside it. In addition to this, the intermittent nature of chewing forces can cause a suction

and pumping process that can send these bacteria to the area surrounding the implant.

Regarding the variables under review and the conclusions of various studies, many of the latter analyze the effects of the IAC type (e.g., butt joint versus tapered) on the microgap formation. Gil et al. concluded that internal butt-joint connections present smaller microgaps than external ones.[248] Despite high expectations, even tapered connections cannot prevent the risk of bacterial leakage.[222,232,265] In addition to this, their microgap is hard to measure since the IAC is located inside the implant.[252] The effect of the tightening torque applied to the screw on the structural integrity of the restoration and the formation of the microgap has also been studied.[3] Gehrke et al. found that greater torque reduces the IAC microgap.[266] Tonin et al. reached the same conclusion. Their study applies larger screw preloads (by means of a stronger screw tightening torque).[267] Smith et al. also agreed with this conclusion.[210] Yet, a high tightening torque does not completely close the IAC microgap and thus cannot prevent bacterial leakage.[209,227]

2 Tools used for simulations and experimental tests

Beyond analytical developments, in this PhD Thesis, two analysis methods are used to study the mechanical behavior of dental restorations. On the one hand, the Finite Element Method (FEM) and, on the other hand, experimental methods. Therefore, this chapter aims to serve as a guide to understand and reproduce both the FEA and the experimental tests that have been carried out during the PhD Thesis for two purposes. Firstly, to simulate and understand the performance of dental restorations under the phenomena of fatigue and screw loosening. Secondly, to develop, based on these, methodologies by which such behavior can be predicted efficiently, whereby they serve as a design tool to obtain dental restorations with improved mechanical performance.

Before describing the FE models and the experimental test setups, the chapter begins with a description of the types of dental restorations to be analyzed and tested, identifying their components and detailing the characteristics of the materials they are made of.

Furthermore, the experimental tests carried out to obtain the friction coefficients between the contact surfaces of the elements that compose the dental restorations are also described. The measured values will be used to feed the FE model.

Next, the FE model will be described in depth in terms of geometry, materials, meshing, loading and boundary conditions, etc. Although there are many FEAs throughout the PhD Thesis, most of them are structured in a similar way with little variation from one to another, except the FE models used in Chapter 5 that have some specific features that are explained in a different subsection. Moreover, specimen FEAs were also performed in Chapter 5, that are also described in this chapter.

Regarding the experimental tests carried out, this chapter also details the test benches used, as well as the set-up and preparation of the tests and specimens.

Finally, at the end of the chapter, a prototype of an innovative fatigue test bench developed in this PhD Thesis is presented, which is capable of testing 8 dental restorations at the same time for a very low cost. This test bench therefore represents an important advance in the technology available for fatigue testing of dental restorations.

2.1 Geometries, materials, and coefficients of friction of dental restorations

2.1.1 Geometries and materials

In this PhD Thesis various implant geometries and prosthetic components will be analyzed, which can be grouped into two main groups as we have already seen in the section 1.1: implant-supported restorations and transepithelial-supported restorations. The first ones are the simplest and consist of an implant and an abutment, both joined by a prosthetic screw. The second ones, which are more complex, are composed of the implant, a transepithelial element composed of a sleeve that is attached to the implant by means of a first screw and an abutment that is attached to the rest of the assembly by means of a second screw. In this way, the second screw threads onto the first screw, which has a female thread on its head. Figure 69 shows the main elements of an implant-supported restoration and a transepithelial-supported restoration.

All the dental restorations analyzed in this PhD Thesis were manufactured and provided by Biotechnology Institute (BTI),[268] whose facilities are located in Vitoria (Spain). As mentioned in section 1.6.1, most of implants and prosthetic components are made of Titanium or Titanium alloys. In the case of BTI restorations, all implants, transepithelial sleeves and abutments are made of Commercially Pure Grade 4 (CP4) Titanium, which is more biocompatible than alloyed Titanium. In contrast, the prosthetic screws of BTI are made of Ti6Al4V Extra Low Interstitial (ELI), also known as Grade 5 (GR5) Titanium, which provides better mechanical performance and does not require such a high degree of biocompatibility, since it is not in contact with any human tissue. The chemical composition of both materials is described in Table 4, meeting the requirements of ISO5832-2[269] and ASTM F67[270] for CP4 Titanium and ISO5832-3[271] and ASTM F136[272] for GR5 Titanium.

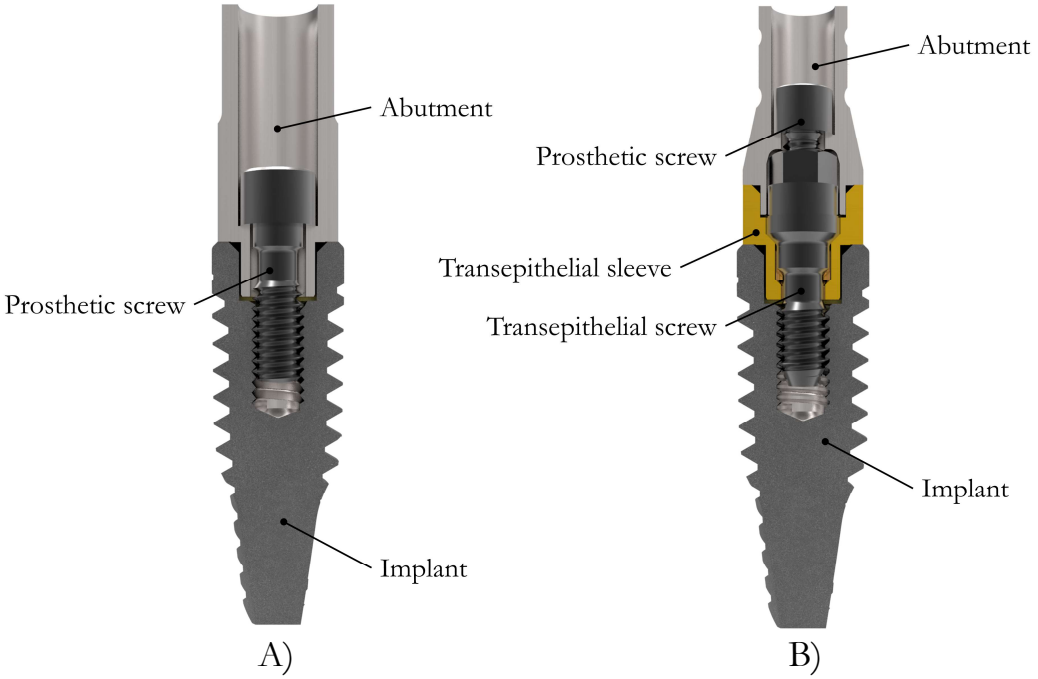

Figure 69. Main elements of a screw-retained dental restoration. A, Implant-supported restoration. B, Transepithelial-supported restoration.

Table 4. Chemical composition of materials used in implant and prosthetic component manufacturing process.

Ti 6Al 4V ELI (GR5 Titanium)		CP4 Titanium	
Composition	**Wt. %**	**Composition**	**Wt. %**
Al	5.5–6.5	N(max)	0.05
V	3.5–4.5	C(max)	0.08
Fe(max)	0.25	Fe(max)	0.5
O(max)	0.13	O(max)	0.4
C(max)	0.08	H(max)	0.0125
N(max)	0.05	-	-
H(max)	0.012	-	-

2.1.2 Coefficients of friction

Measurements of coefficients of friction of contact surfaces between the implant and the prosthetic components were performed in order to properly characterize the contact behavior in the FE models that will be explained in section 2.2.2. Moreover, torque-preload equation[3,46] must be also fed by the values of these coefficients of friction so that the screw preload is properly determined as described in section 2.2.5. Both contact behavior and screw preload were used in the FEA explained further below.

Two types of contacts were analyzed. On the one hand, the contact between the screw surfaces, that are made of Ti6Al4V ELI with a WCC coating, with the inner part of the implant and abutment, that are made of CP4 Titanium. On

the other hand, the contact between the implant, made of anodized CP4 Titanium, and the abutment, made of non-anodized CP4 Titanium.

The tests were performed in the MicroTest SMT-A/0200 pin-on-disk tribometer shown in Figure 70A. The disks were made of CP4 Titanium (representing both the inner part of the implant and the abutment) while the pins were made of WCC coated Ti-6Al4V ELI (representing the prosthetic screw) and anodized CP4 Titanium (representing the implant connection). As shown in Figure 70B, the end of the pin used is rounded (3mm diameter). 1N load was applied on the pin in order to obtain a pressure value similar to the one that the prosthetic components are subjected to according to the FEA results obtained in this study.[273]

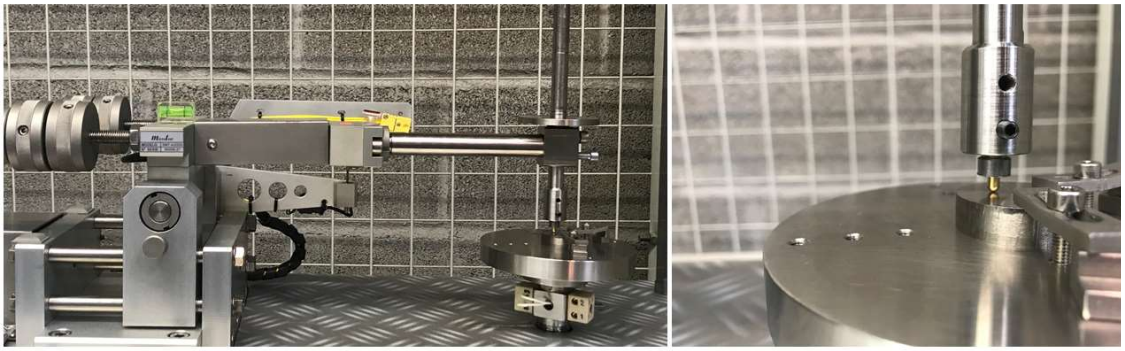

A) B)

Figure 70. Pin-on-disk test. A, pin-on-disk tribometer MicroTest SMT-A/0200. B, Detail view of the test.

Table 5 shows the coefficient of friction values obtained in each test, with 0.17 being the mean value for the screw-implant and screw-abutment contacts, and 0.21 the mean value in the case of the implant-abutment contact surface. These values are the ones used to define the contacts as well as for preload determination in section 2.2.

Table 5. Coefficients of friction values measured in the pin-on-disk test.

Implant-abutment contact		Screw-implant and screw-abutment contacts	
Test Number	**Coefficient of friction**	**Test Number**	**Coefficient of friction**
1	0.220	1	0.162
2	0.208	2	0.237
3	0.237	3	0.151
4	0.189	4	0.134
5	0.196	5	0.175
6	0.197	6	0.162
7	0.201	7	0.237
8	0.224	-	-
9	0.181	-	-
Mean value:	0.21	Mean value:	0.17
Std Dev:	0.02	Std Dev:	0.04

2.2 Finite Element models of dental restorations

As mentioned at the beginning of the chapter, various FEAs were carried out throughout this PhD Thesis, studying different phenomena, with different FE models of dental restorations used for this purpose. However, all of them are similar, with small variations between one model and another. These variations can be the geometry of the dental restoration, the preload of the screw, the external load applied, and similar aspects.

Regarding the output obtained from the FEA, in Chapter 3 and 7 only the contact moment and force reactions are recorded from the FEA performed, while in Chapter 5 a more finely meshed FE model is used to obtain, in a very precise way, the effective stress at the notch where the failure begins.

As a whole, this section serves as a guide to explain the FEA performed on dental restorations by using Ansys Workbench 19 R1 software that will be used throughout the document.

2.2.1 Geometry and materials

In the FE models used in this PhD Thesis, it was decided to model only half geometry (see Figure 71) taking advantage of the symmetry of the load and geometry, which saves computational cost. Indeed, the threads are helical, and therefore the geometry is not fully symmetrical. However, it was decided to model the threads of the prosthetic screw and the internal threads of the implant as cylindrical (axisymmetric) rather than helical, since preliminary

analyses showed that this simplification resulted in an error of less than 5% in terms of force and moment reactions in the prosthetic screw.

The materials mentioned in section 2.1.1 were assigned to the implants and prosthetic components modelled. The materials were modelled as linear elastic materials, with E=103 GPa, ν=0.35 for CP4 Titanium and ν=0.31 for Ti6Al4V ELI.

Regarding dental restoration geometry, the implant must be embedded in a specimen holder made of steel according to ISO 14801[141] (see section 1.6.1). This specimen holder must have a hole with the same diameter as the implant body diameter plus 0.05mm. The specimen holder is 10mm high so that the implant protrudes 3mm as required by the standard (since all the implants tested will be 13mm long).

The external threads of the implant are the only ones that are not modified with respect to the original geometry, i.e. they remain helical.

Regarding the abutment, the only simplification that is carried out is to cut it at a height of 8mm from the IAC (or 11mm from the specimen holder) in order to apply the load directly at that height specified in the above mentioned ISO 14801[141] (see section 1.6.1), avoiding the use of a hemispherical device, which is used in the experimental tests that will be explained later on. Finally, the prosthetic screw receives two horizontal cuts in the shank. This will serve to apply the preload as will be explained in section 2.2.5. Figure 71A shows the modeled geometry for an implant-supported restoration.

Finally, if a transepithelial component is added to the restoration, the transepithelial sleeve will not undergo any simplification while the transepithelial screw undergoes the same simplifications mentioned for the screw used in implant-supported restorations, these being, cylindrical threads and two horizontal cuts in the shank for preload introduction. In the same way, the second prosthetic screw used in transepithelial-supported restorations will undergo the same two simplifications as well. Figure 71B shows the modeled geometry for a transepithelial-supported restoration.

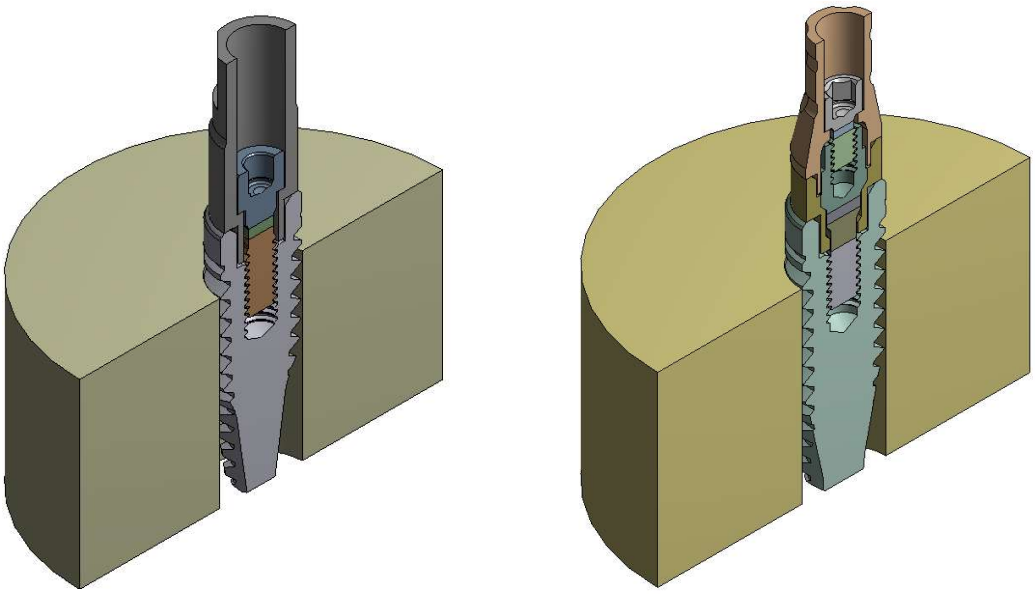

A) B)

Figure 71. FE models of dental restorations. A, Implant-supported restoration. B, transepithelial-supported restoration.

2.2.2 Contacts

Contacts are modelled as frictional, using the coefficients of friction obtained in section 2.1.2. Hence, a coefficient of friction of 0.17 is set for contacts between the prosthetic screw and the inner part of the implant and abutment and a coefficient of friction of 0.21 is set for the IAC contact surface. In the experimental setup, the specimen holder is filled with an embedding material (Loctite 401) as suggested in ISO 14801.[141] This boundary condition is modelled as a frictional contact (with a coefficient of friction of 0.5 and adjust to touch restriction) so that vertical movement is allowed, allowing material deformation when preloaded and compressed, but not allowing lateral movement.

2.2.3 Mesh

The mesh presented in this section (see Figure 72) has been determined using sensitivity analysis, so that it provides very similar results, in terms of moment and force reactions on the screw, to finer meshes, but with an optimal computational cost.

The specimen holder is meshed with 1mm second order tetrahedra with a refinement of up to 0.15mm element size on the implant contact face. The rest of the parts are meshed with second order hexahedra. The implant is meshed with 0.1mm elements, with a refinement of 0.05mm on the surface of the internal threads. The abutment is meshed with 0.15mm elements, taking

advantage of the simplicity of the geometry. The screws, except for the threads, are meshed with 0.13mm elements. Finally, the screw threads are meshed with 0.1mm elements and with a refinement of 0.05mm on the contact surfaces. In the case of transepithelial-supported restorations, the body of transepithelial components should be meshed with 0.13mm elements (see Figure 73). Figure 74 shows closer views of both meshes presented in this section.

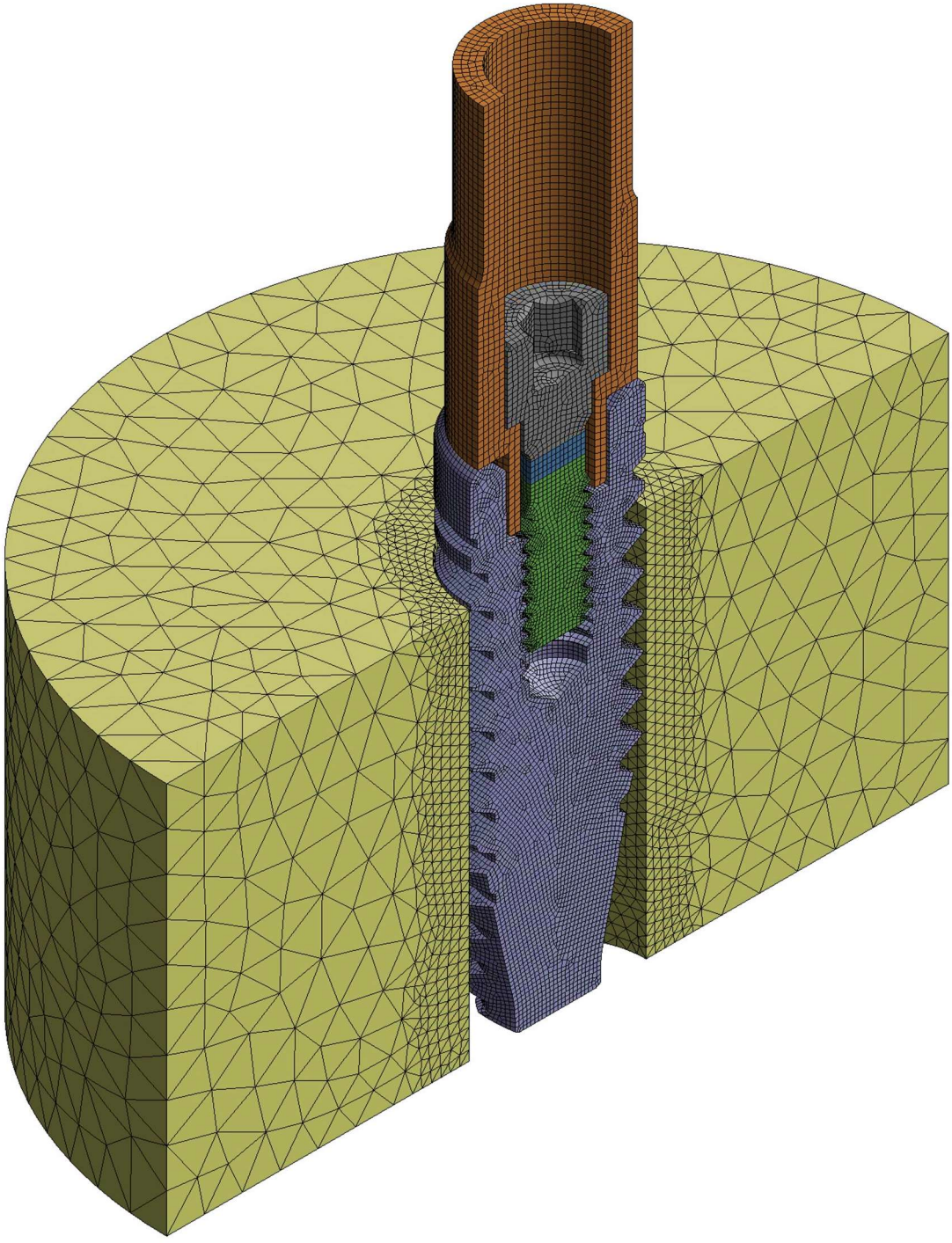

Figure 72. Mesh of a FE model of an implant-supported restoration.

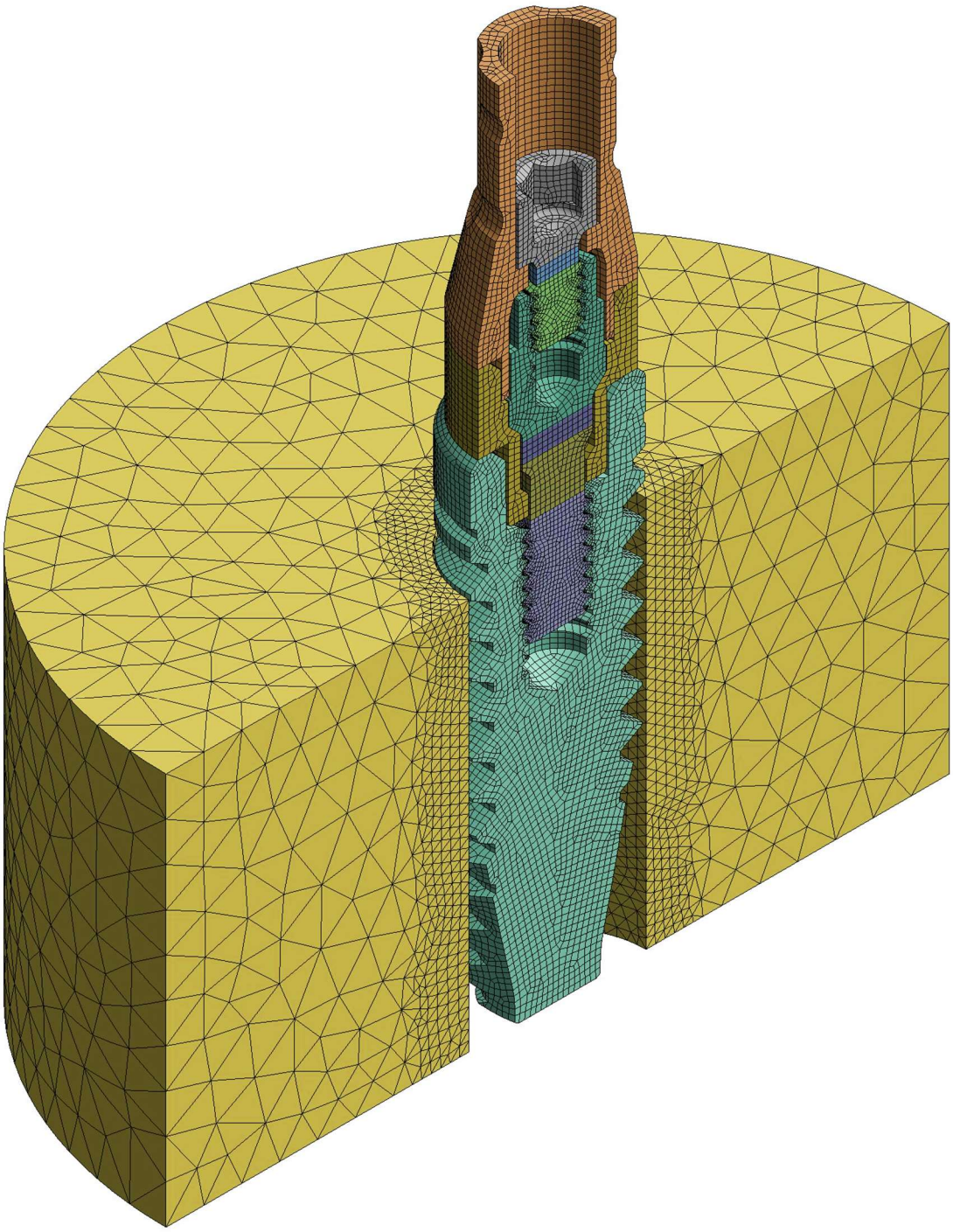

Figure 73. Mesh of a FE model of a transepithelial-supported restoration.

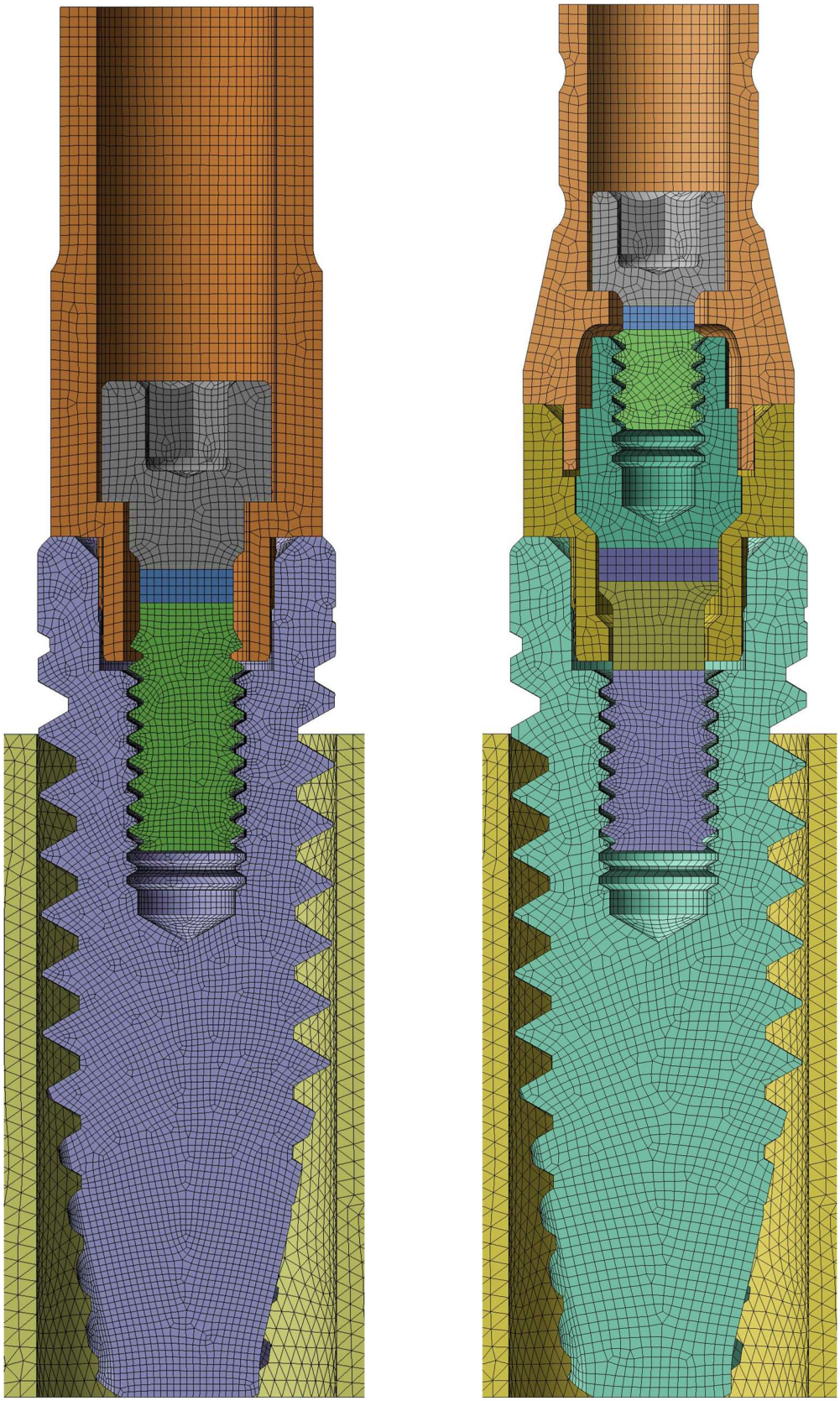

A) B)

Figure 74. Close views of meshes of the FE models. A, Implant-supported restoration. B, Transepithelial-supported restoration.

2.2.4 Boundary conditions

Fixed support is applied to the model at the base and side of the specimen holder as well as at the base of the implant (see Figure 75). In addition to this, since only half geometry is modeled, the symmetry condition is applied by imposing a zero-displacement condition on the axis perpendicular to the symmetry plane (red axis in Figure 75) and free on the other two axes.

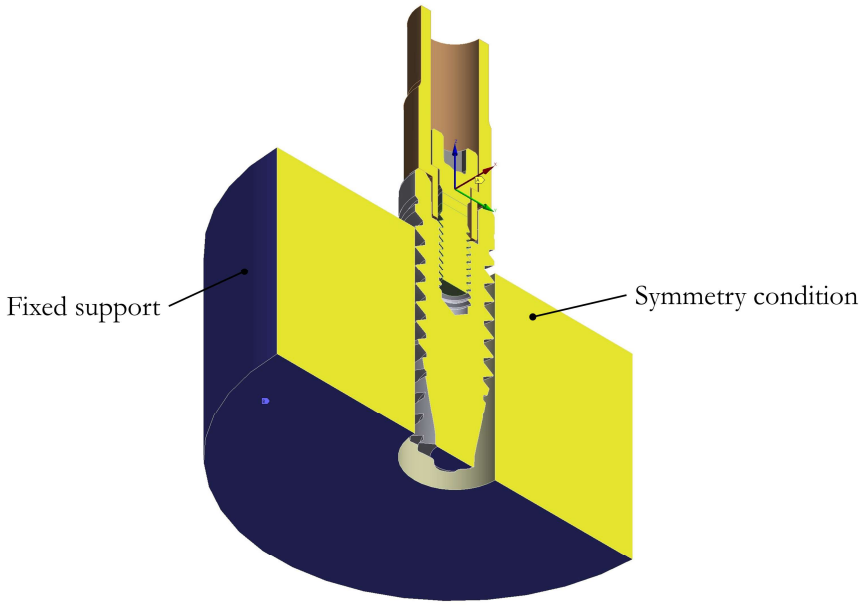

Figure 75. Boundary conditions of the model.

2.2.5 Screw preload and external loads

FEAs consist of two load steps (three steps in the case of transepithelial-supported restorations). In the first step, the screw (the lower screw in the case of transepithelial-supported restorations) is preloaded by using a pretension section, creating an initial axial load that corresponds to its tightening torque. The preload values F_p are calculated from the torque-preload relationship in equation (15), obtaining equation (131). For screws with a countersunk head, equation (132) must be used.

$$F_p = \frac{T_T}{\mu_h \cdot r_h + \mu_t \cdot \frac{r_t}{\cos\alpha} + \tan\beta \cdot r_t} \tag{131}$$

$$F_p = \frac{T_T}{\frac{\mu_h \cdot r_h}{cos\rho} + \mu_t \cdot \frac{r_t}{\cos\alpha} + \tan\beta \cdot r_t} \tag{132}$$

Where, as already explained in section 1.2.4, F_p is the screw preload, T_T is the screw tightening torque, μ_h and μ_t are respectively the coefficients of friction

of the screw head and thread contacts, α is the half-angle of the thread profile, β is the helix angle, ρ is the screw head contact surface angle, and finally, r_h and r_t are respectively the screw head and thread mean contact radii that may be obtained from equations (13) and (14). When a transepithelial-supported restoration is to be analyzed, a second step is used to preload the upper screw. Note that both screws cannot be preloaded in the same load step since this is not a realistic situation. In experimental tests, first the lower screw is tightened and then the upper one will interact, during its tightening, with the lower one, altering its preload. Hence, applying the preloads in different load steps will reproduce the real performance in a more accurate fashion. It must be mentioned that since half geometry was modelled, half the preload shall be applied as well. Finally, in a last load step the external load is applied. This step will vary depending on the phenomenon that is to be analyzed. In short, when aiming to reproduce fatigue tests as will be seen in Chapter 3 and 5, the load will be applied at 30º on the top of the sectioned abutment (at 8mm from the platform, as shown in Figure 76A). An increasing load slope must be applied from zero to the maximum testing load needed, so that intermediate values are also available for further calculations. If screw loosening is to be reproduced as explained in Chapter 7, an increasing transverse load is applied at the bottom of the abutment from zero to the maximum testing load needed. To ensure load application at the desired point, a ring was modelled surrounding the abutment at 1mm from the implant-abutment platform and the load was applied on it (see Figure 76B). Again, a half load must be applied since half geometry is modelled.

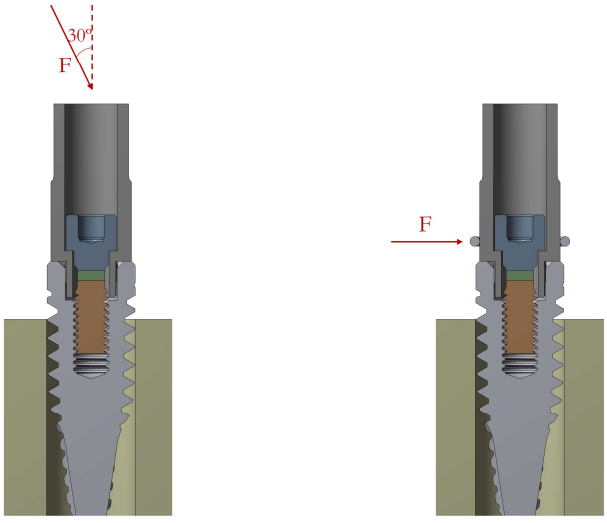

Figure 76. Load application. A, Fatigue load case. B, Screw loosening load case.

2.2.6 Specific Features of the Finite Element models used in Chapter 5

As mentioned in the introduction of section 2.2, most FE models in this PhD Thesis are used to obtain the moment and force reactions on the prosthetic screw, either to analyze the fatigue of the screw itself (Chapter 3) or to analyze the self-loosening phenomenon (Chapter 7). In these cases, since the FEA output is the same, the FE models differ minimally. However, in Chapter 5, the fatigue behavior of the dental implant is analyzed and, for this purpose, the effective stress at the notch where implant failure occurs is obtained. Therefore, there are some elements that differ from the FE model explained so far, which are discussed below.

First, the whole geometry of the dental restoration must be modeled, since the external thread of the implant is not simplified (is not assumed to be cylindrical), with the notch of the thread being the critical point at which the stresses are studied.

Secondly, the mesh also undergoes some modifications. The abutment and the screw-pretension section are the only bodies in which second order hexahedra are used. On the rest of the bodies, second order tetrahedra are used to favor transitions between different element sizes. The specimen holder is meshed with 1mm element size with a refinement up to 0.15mm element size on the implant contact surface. The abutment is meshed with 0.1mm elements. The screw is entirely meshed with 0.1mm elements with a refinement of 0.025mm on the thread contact faces. The implant is meshed with 0.1mm elements, with a refinement of 0.025mm on the surface of the internal threads. Moreover, the implant has a progressive spherical refinement in 4 phases with the center of the spheres located at the root of the notch where the crack starts. The refinement starts with a first sphere with a radius of 0.3mm and an element size of 0.03mm, followed by a second sphere with a radius of 0.2mm and an element size of 0.008mm, continuing with a third sphere with a radius of 0.08mm and an element size of 0.004mm, and concluding with a final sphere with a radius of 0.02mm and an element size of 0.001mm. Figure 77 shows the meshed model presented in this section.

Regarding boundary conditions, evidently, since the whole geometry is modeled, no symmetry conditions are necessary and only a fixed support is applied to the model at the base and side of the specimen holder as well as at the base of the implant. In the same way, both the entire external load and entire

screw preload shall be applied, rather than the half load. The external load is applied as shown in Figure 76A, following the ISO 14801 standard.[141]

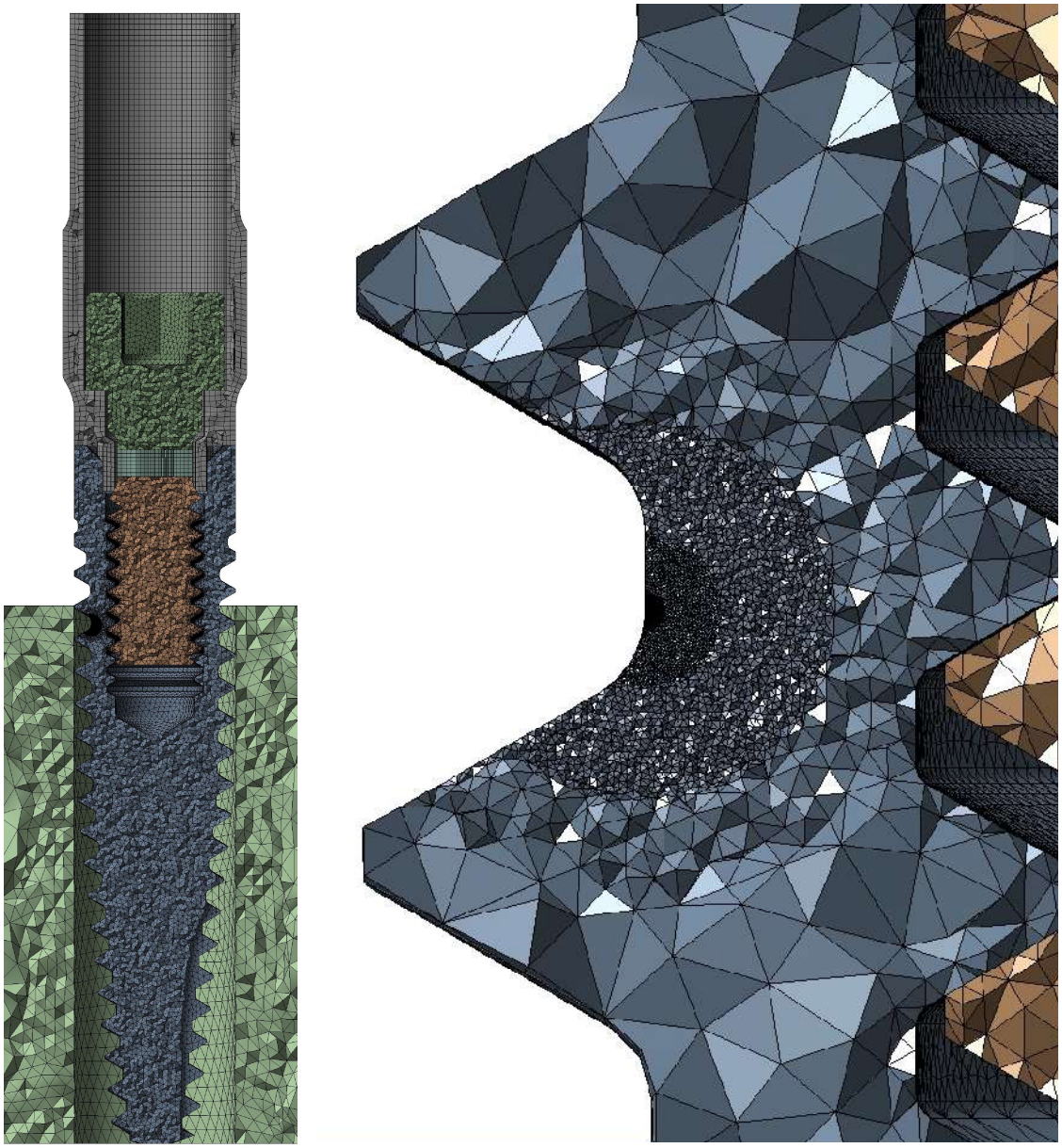

A) B)

Figure 77. Model of an implant-supported restoration with a sphere refinement. A, section view. B, Detail of the progressive spherical refinement.

2.3 Finite Element model of standardized specimens

In Chapter 5, FEA are performed on CP4 Titanium standardized specimens. These FEAs simulate the conditions of experimental uniaxial fatigue tests on hourglass specimens. It is, therefore, a relatively simple FEA with the only complication being a progressive spherical refinement that is applied to obtain

accurate stresses at the notch at which the crack occurs, as was performed on the implants in the previous section.

This section serves as a guide to explain the FEAs performed on standardized specimens by using Ansys Workbench 19 R1 software that will be used in Chapter 5.

2.3.1 Geometry and materials

Regarding the geometry, only a quarter of the specimen is modeled, taking advantage of the axisymmetry of the geometry and the axial load. The axisymmetric 2-dimensional model was not used since it would be incompatible with the Volume Method (sphere) applied to obtain the effective stress for fatigue calculations, explained in detail in Chapter 5. Figure 78 shows the modeled geometry of a specimen. Regarding the material, as the goal is to characterize the material from which the implants are made, the specimens have been manufactured from the same CP4 Titanium bars used to manufacture the implants as well, whose properties are presented in Table 4 and are modeled by using a linear elastic material of E=103 GPa and ν=0.35.

Figure 78. FE model of quarter of the specimen geometry.

2.3.2 Mesh

Model mesh is performed by means of second order tetrahedra. Specimen shoulders are meshed by using an element side of 0.3mm while specimen neck is meshed by using an element size of 0.1mm. As was done for implants in section 2.2.6, the specimen has a progressive spherical refinement in 4 phases with the center of the spheres located at the root of the notch where the failure starts. The refinement starts with a first sphere with a radius of 0.3mm and an element size of 0.03mm, followed by a second sphere with a radius of 0.2mm and an element size of 0.008mm, continuing with a third sphere with a radius of 0.08mm and an element size of 0.004mm, and concluding with a final sphere with a radius of 0.02mm and an element size of 0.001mm. Figure 79 shows the meshed model.

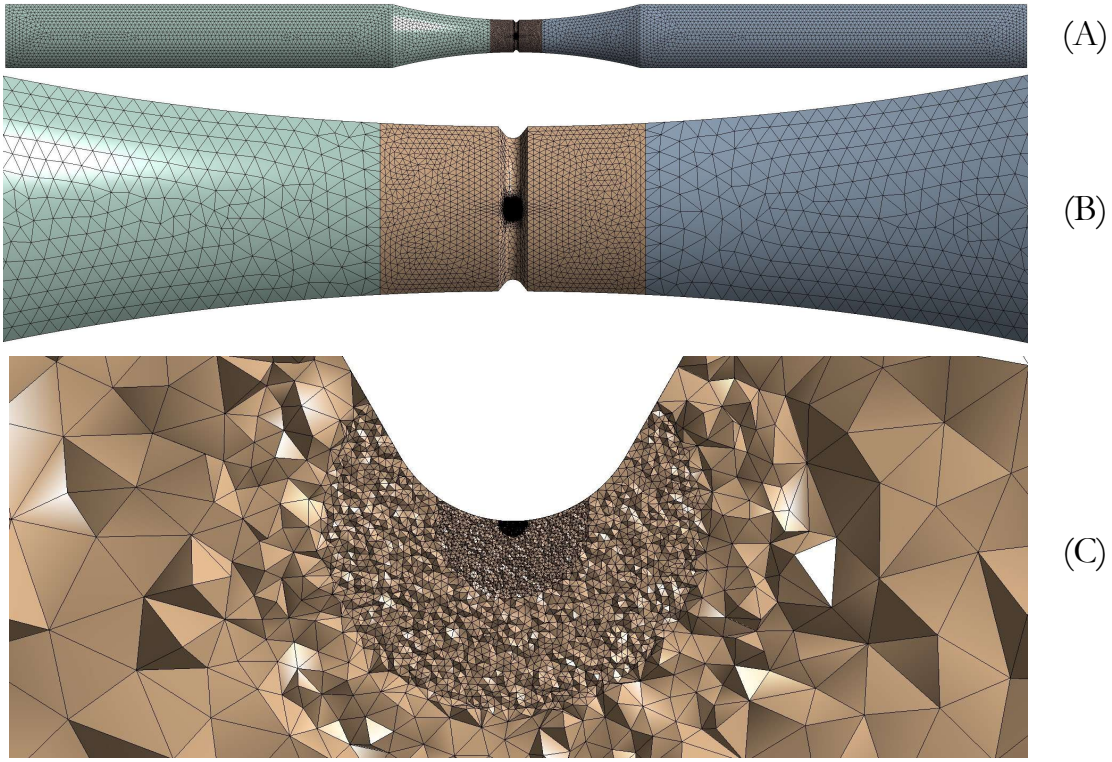

Figure 79. Mesh of a notched specimen FE model. A, Complete model. B, Closer view of the notch. C, Detail of the progressive sphere refinement.

2.3.3 Boundary conditions and external load

Fixed support is applied to the specimen model at the base of one of the shoulders while the fourth part of the desired external axial load is applied at the base of the opposite shoulder. Moreover, since a quarter of the geometry is modelled, two symmetry conditions are applied by imposing a zero-displacement condition on the axes perpendicular to the longitudinal sections and free on the other two axes (see Figure 80).

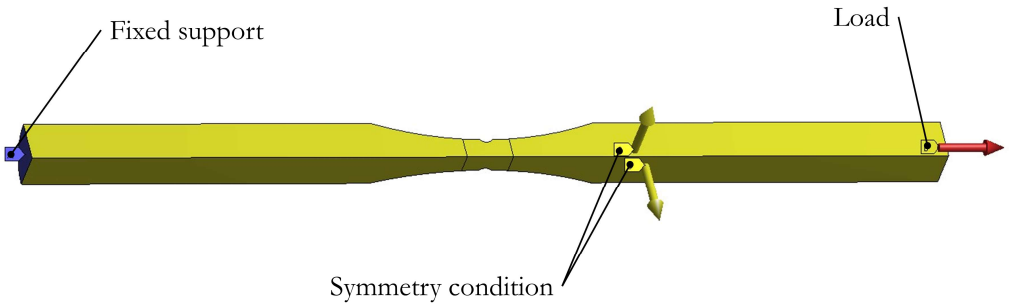

Figure 80. Boundary conditions of the model and external load application.

2.4 Test Benches

In addition to the tribometer used to measure the coefficients of friction among dental restoration contact surfaces (see section 2.1.2), several test benches have been used for the different experimental tests carried out throughout this PhD Thesis. On the one hand, all the fatigue and static fracture tests on implants were performed on an INSTRON E3000 Electropuls test bench. On the other hand, screw loosening tests on dental restorations and fatigue tests on cylindrical specimens were performed on an INSTRON 8801 test bench.

2.4.1 INSTRON E3000 Electropuls for fatigue tests

All fatigue tests of all dental restorations tested throughout this PhD Thesis (which will figure in Chapters 3, 4 and 5) have been performed on the INSTRON E3000 Electropuls fatigue test bench (see Figure 81A) located at BTI facilities. All fatigue tests have been performed according to ISO 14801 standard,[141] the requirements of which are explained in section 1.6.1. The bench is equipped with a specimen holder capable of imposing different angles to the implant (see Figure 81B). In order to fulfill the requirements of the ISO 14801 standard,[141] the tooling was always set at 30º. The dental restoration will mount a hemispherical device on the top that will transmit the load coming from the actuator block (see Figure 81B). The block is able to transmit the vertical load avoiding lateral restrictions thanks to a slide composed of rollers. This load is generated by a linear motor capable of producing a force of up to 3kN measured at any time by means of a DYNACELLTM 2527-153 load cell with a load range of ±5kN.

To perform the test, the implant is positioned in the hole of the specimen holder and glued with an embedding material (Loctite 401). Then, the abutment is mounted and, finally, the prosthetic screw is tightened to the corresponding tightening torque. Finally, the hemispherical device is positioned and the corresponding fatigue load is applied.

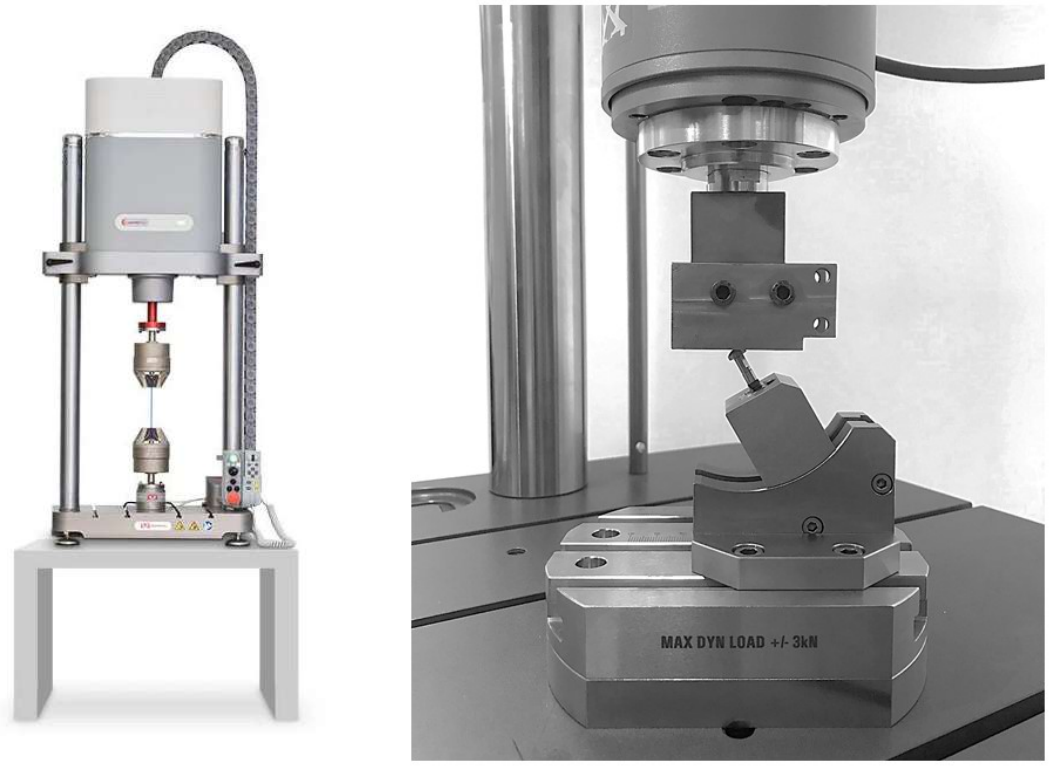

A) B)

Figure 81. INSTRON E3000 Electropuls. A, General view with a generic set-up. Image courtesy of Instron B, Set-up for dental implant testing according to ISO 14801.[141]

2.4.2 INSTRON 8801 for screw loosening and standardized specimens fatigue tests

The INSTRON 8801 hydraulic test bench (see Figure 25A), with a higher capacity (loads up to 100kN) and higher versatility than the previous one, is located in the laboratory of the Mechanical Engineering Department of the University of the Basque Country UPV/EHU in Bilbao (Spain) and has been used to perform two types of tests. On the one hand, loosening tests have been performed on dental restorations, which will be discussed in Chapter 7. On the other hand, fatigue tests have been performed on standardized specimens for the analysis of implant fatigue, which will be discussed in Chapter 5.

2.4.2.1 Dental restoration screw loosening tests

As will be demonstrated in Chapter 7, the experimental screw loosening tests performed on dental restorations aim to apply a transverse displacement between the elements joined by the prosthetic screw (implant and abutment). For this purpose, a special fixture tooling was designed so that the specimen

holder (along with the dental restoration) is positioned horizontally (see Figure 82).

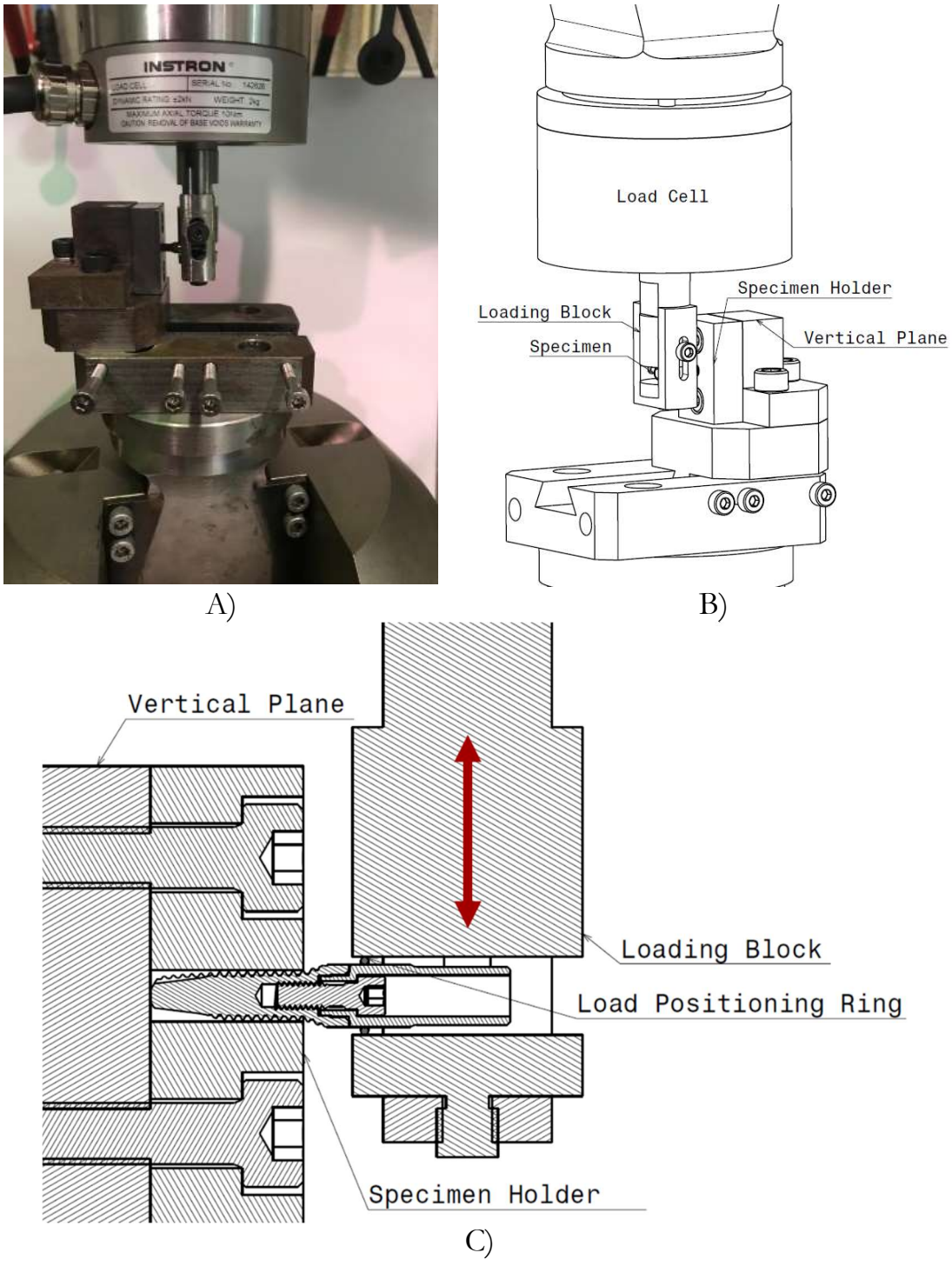

Figure 82. A, Assembly of the fixture tooling designed for self-loosening tests. B, Drawing of the fixture tooling. C, Section view.

As explained in section 2.4.1, the implant is inserted into the specimen holder and fixed by using an embedding material (Loctite 401). Then, the abutment is positioned and clamped into the implant by means of a properly tightened

prosthetic screw. A steel ring was installed around the abutment outside surface at 1mm from the IAC and was held by the loading block without clearance so that the imposed alternating external load is transmitted properly to the bottom of the implant. Finally, the specimen holder is mounted on the fixture tooling.

As previously mentioned, the INSTRON 8801 test bench is able to perform a load of up to 100kN. Nevertheless, the loads needed for dental restorations tests are much lower. Hence a special load cell, DYNACELL 2527-129, with a load range of ±2kN was mounted to measure the applied load more precisely.

2.4.2.2 Standardized specimen fatigue tests

As will be seen later in Chapter 5, several experimental tests have been carried out on CP4 Titanium standardized specimens to characterize the fatigue behavior of the material of dental implants and to study the influence of stress concentration caused by different notches. These results have been used in the multiaxial fatigue study carried out to analyze the fatigue of dental restorations where the critical component is the implant. Figure 83 shows the hourglass geometry chosen for the specimens obtained from the same bars of material from which dental implants are made, which have been axially tested according to the ASTM E-739 standard.[64] The specimens are clamped by means of grips (see Figure 84) which distribute the forces along the shoulders of the specimen. Since the specimens are very thin (6.9mm diameter since they are manufactured from 7mm diameter bars), they are more likely to incur non-negligible damage due to small misalignments.

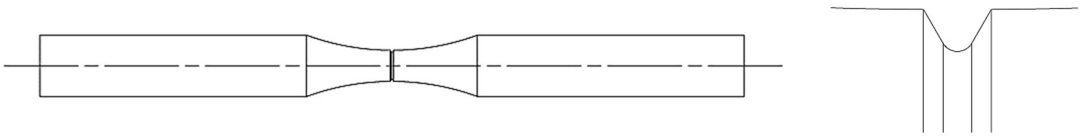

A) B)

Figure 83. Hourglass shaped specimens made of CP4 Titanium. A, Whole specimen. B, View of the notch.

A) B)

Figure 84. Test bench set-up for specimen fatigue tests. A, General view. B, View of the specimen and grips.

In a preliminary experimental test campaign performed along with the DUMAS research team at the ENSAM University, whose facilities are located in Bordeaux-Talence (France), it was found that a small misalignment between specimen and axial force can cause unpredictable fatigue life values, making the correct characterization of the material difficult. Figure 85A, shows the failure of a specimen in a Zwick/Roell Amsler 150 HFP 5100 where, after failure, the stresses are released and each half of the specimen is aligned to a different side. This indicates that initially the specimen (whole) was supporting a bending moment along with a transverse load. To correct this, it was decided to use the INSTRON 8801 from the UPV/EHU facilities, taking special care to choose a frame and actuator position so that the specimen is positioned as closely as possible to the load application. Preliminary tests showed that in this case the alignment of the two halves of the specimen does not change when the stresses due to the rupture are released (see Figure 85B). To ensure that this alignment does not change throughout the test campaign, a tooling was installed to limit the degree of rotational freedom that the lower head (actuator) had since it was assumed that a possible twist could result in an eccentricity in the assembly. Figure 86 shows the assembly of the tooling that limits the rotation of the lower head by means of a guide and bearings.

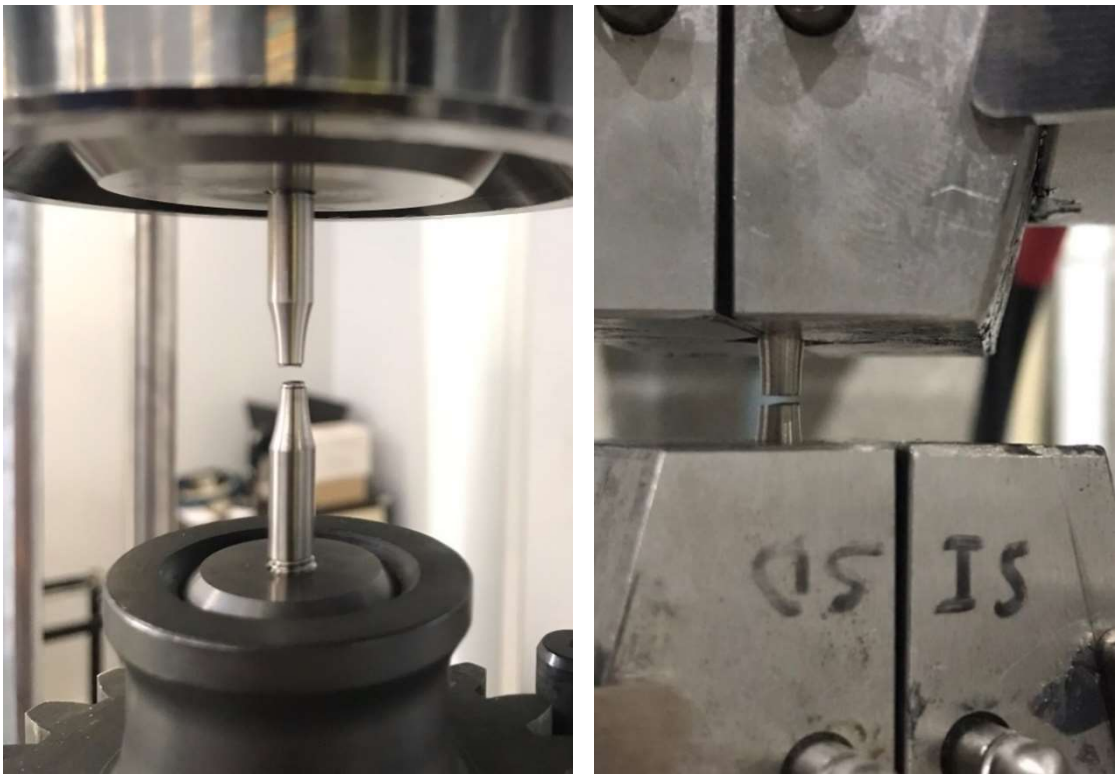

A) B)

Figure 85. Specimen failures. A, Specimen with a non-negligible misalingment. B, Aligned specimen.

A) B)

Figure 86. Designed tooling to limit the rotation of the lower head (actuator). A, General view. B, Close up view.

2.5 Development of an innovative fatigue test bench prototype

Throughout this PhD Thesis, numerous experimental fatigue tests have been performed on dental restorations using commercial test benches such as those described in section 2.3. These machines are powerful and very versatile test benches, as they can be adapted to a multitude of different tests: automotive mechanical components, material specimens, dental implants, or even the damping of sport shoes or computer keyboards, among many other varied applications. Usually, these machines are equipped with hydraulic actuators or linear motors capable of generating very high loads and different waveforms adapting to the specific requirements of each particular test. This is why generic commercial test benches of this type are technologically complex and expensive to purchase and maintain. On the other hand, these machines are normally capable of testing only one implant at a time. Taking into account that ISO 14801[141] does not allow testing at a frequency of more than 15Hz, a fatigue test on a single implant can take up to almost 4 days (setting a 5 million cycles run-out as specified in the standard). Therefore, if the frequency of testing cannot be increased, different implants need to be tested at the same time if the timescales are to be shortened.

Therefore, within the framework of this PhD Thesis, a simple and, therefore, affordable to acquire and maintain test bench design was developed that allows for various implants to be tested at the same time in compliance with the requirements of the ISO 14801 standard.[141] The bench presented in this section, instead of using hydraulic actuators or linear motors, uses a mechanism based on the cam-follower concept (see Figure 87A), inspired by the radial engines used in aviation (see Figure 87B).

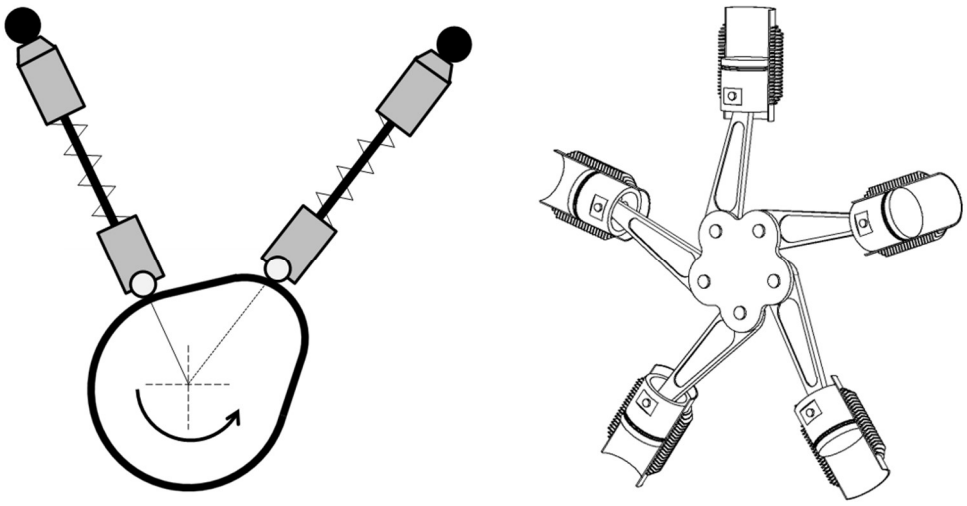

A) B)

Figure 87. A, Schematic of a cam-follower mechanism. B, Schematic of a radial engine used in aviation.

2.5.1 Mechanism description

The bench is governed by a cam that rotates by means of a 1100W electric motor. This cam has three lobes and a sinusoidal profile with a distance between peak and valley of 20mm. A follower (see Figure 88) will be responsible for transforming the rotary motion of the cam into alternating linear displacement. This follower, together with the loading block, which will be presented later, is assembled on a linear guide so that the displacement is limited to a single direction. Since the cam has 3 lobes, the follower will impose three cycles of linear displacement with a total amplitude of 20mm for each rotation of the cam.

A calibrated compression spring is attached to the follower (see Figure 88). This spring will exert a force proportional to the displacement imposed by the follower. Note that the stiffness of the spring remains constant over the range of displacement. Therefore, if the displacement imposed by the cam is sinusoidal, the function of the force generated by the spring will also be sinusoidal. On the other side of the compression spring, there is a DDEAI-450N-002-000 load cell from Applied Measurements with a ±450N force range. This is followed by the loading block, whose sole function is to transmit the load to the implant in an appropriate manner. According to ISO 14801,[141] the restoration must be able to deform in the direction perpendicular to the load application without force restrictions. To achieve this, the block has a movable

plate that moves freely in the vertical direction and rollers that reduce the friction to a negligible value (see Figure 89).

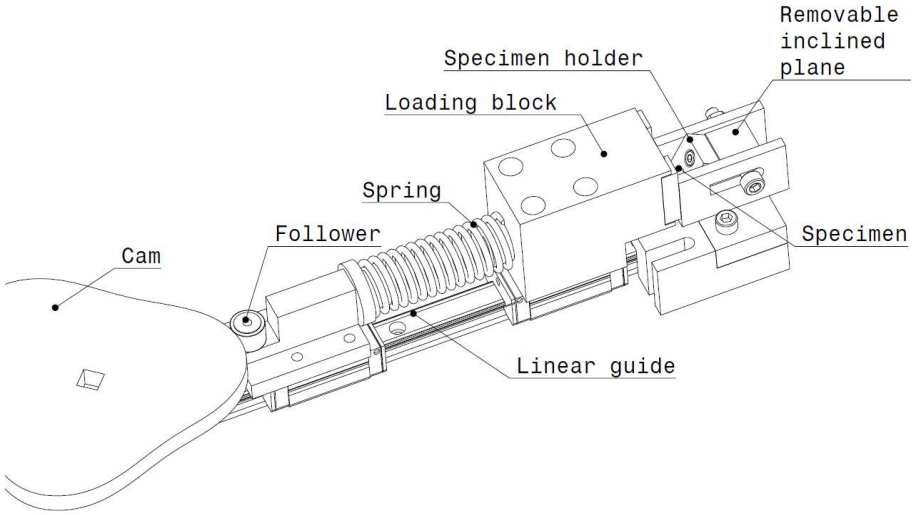

Figure 88. Detail of the mechanism of one arm of the test bench.

The tested restoration may be found in contact with the loading block, which is housed in a specimen holder (see Figure 89) embedded 10mm and fulfilling the distances set out in ISO 14801 standard[141](see section 1.6.1).

Lastly, the removable inclined plane (see Figure 88 and Figure 89) imposes the 30º inclination at which the dental restoration must be with respect to the load, in addition to allowing disassembly of its base to make it easier to remove the specimen once it has been tested and to fit a new one. This base is screwed to the table so that the total distance of the assembly can be varied to adapt to the length of the dental restoration.

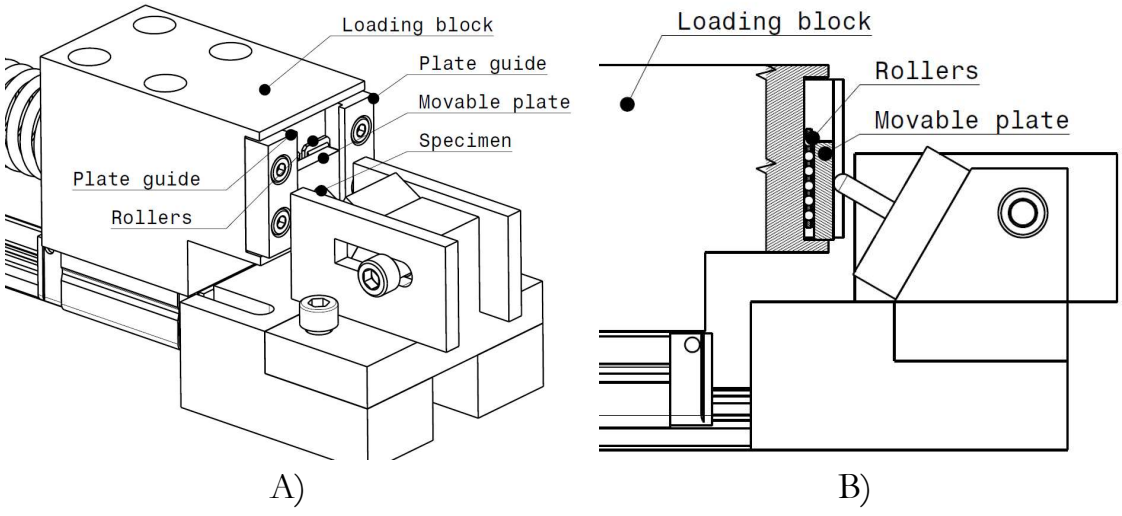

Figure 89. A, Loading block with the removable plate in contact with the specimen. B, Detailed view of the removable plate and the rollers.

2.5.2 Mechanical considerations

In the design stage of the fatigue test bench, various mechanical analyses were performed to ensure that the bench works properly. One critical aspect is the choice of the spring. As seen before, the spring, and specifically its stiffness, is responsible for applying the final force of the test. For this reason, it must be ensured that it works properly. On the one hand, springs were designed to have infinite fatigue life. On the other hand, bearing in mind that the working frequency is 15Hz, it was checked that their first natural frequency is 15 to 20 times higher in order to ensure quasi-static working conditions. These calculations have been performed according to reference literature.[43]

As required by the ISO 14801 standard,[141] the load must vary between the maximum load and 10% of that value. Therefore, the compression spring when the follower passes through the cam valley (0mm displacement) must apply a force of 10%; i.e., the springs must start the test pre-compressed. Hence, an initial compression of approximately 2.22mm is applied (it is compressed until the load cell marks 10% of the test load) and during the test the aforementioned 20mm are applied, giving a total of 22.2mm of total compression of the spring. As mentioned above, the base on which the inclined plane is bolted to the bench, so it can be untightened and moved by pushing the restoration until adequate precompression is achieved, and then, tightened again.

The bench has been designed to characterize the fatigue behavior of restorations over narrow and medium implants, such as those used to replace incisors and canines. Therefore, springs capable of applying test loads between 100 and 350N have been chosen. Table 6 shows the springs designed for this test bench and their stiffness and maximum working loads. If dental restorations requiring a higher load range are to be tested, it will probably be necessary to vary the dimensions of the bench to accommodate larger springs or to vary the dimensions of the cam.

Table 6. Stiffness and maximum working loads of the springs used on the test bench.

Load [N]	100	150	200	250	300	350
Spring stiffness [N/mm]	4.5	6.8	9.0	11.3	13.5	15.8

In addition to the spring calculations, the rigid body dynamics of the mechanism have been studied. Figure 90 shows that the resultant force (red) of the sum of the follower inertial force (blue) and the spring reaction force (green) is always directed towards the cam. For this reason, there is no gap at any time during the test between cam and follower. Moreover, the contact between the

specimen and the loading block is also ensured since the displacement of the block is negligible (less than 1mm) as are the inertial forces.[274]

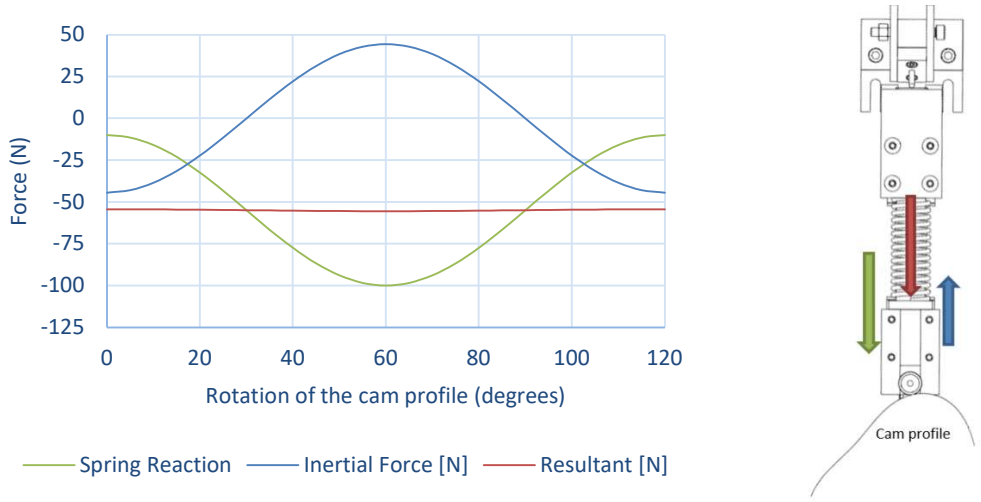

Figure 90. Rigid body dynamics of the mechanism of one arm of the test bench. A, Diagram. B, Schematic with force directions.

Finally, the effect of friction of the linear guides on the test force has been analyzed. This friction occurs on the two components attached to the guide: the follower and the loading block. On the one hand, the frictional force between the guide and the follower is absorbed by the rotating motor, since this displacement is applied by the cam, so this friction does not affect the test load. On the other hand, the friction between the guide and the loading block affects the load reaching the restoration. Therefore, the friction force of the block has been measured by means of a load cell, obtaining a maximum value of 5N. For the lowest test load designed for this bench, i.e. 100N, this friction force value is lower than 5%, complying with ISO 14801[141] specifications.

2.5.3 Overall description of the test bench

Now that the elements that compose each arm of the bench and the mechanical considerations are understood, the complete bench is presented (see Figure 91). As can be seen, the bench is made up of 8 arms controlled by the same cam (and, therefore, by the same rotary motor).

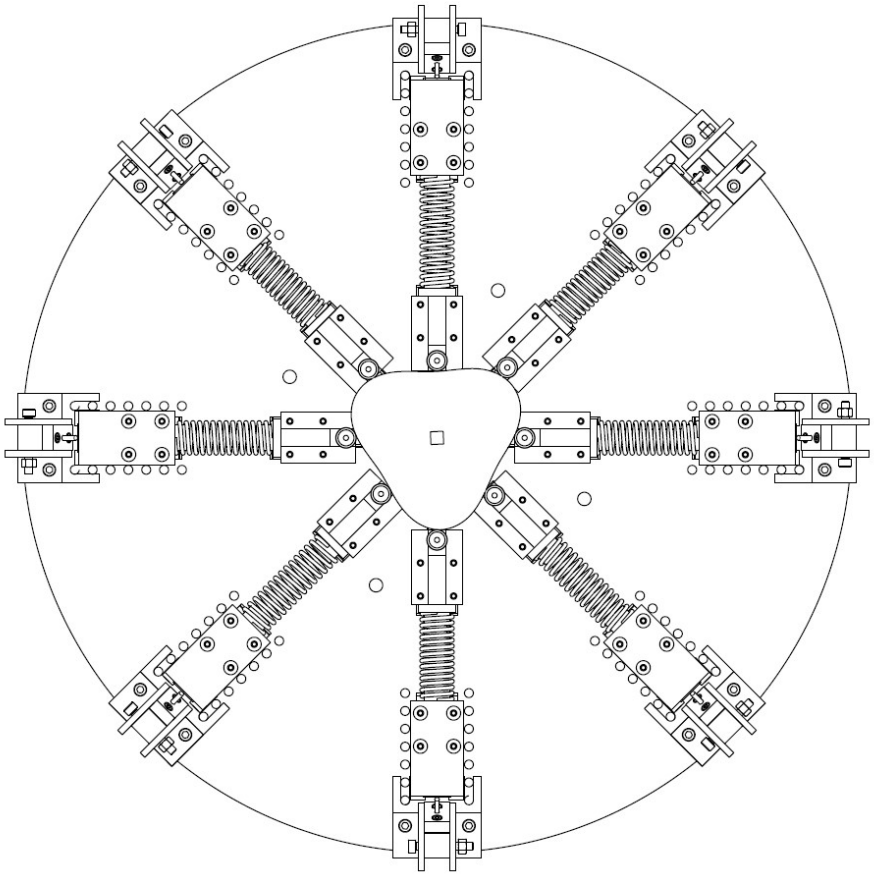

Figure 91. Top view of the test bench.

As previously mentioned, the cam was designed with 3 lobes, in accordance with a study carried out to minimize the resistant torque received by the rotating motor. In this study it was seen that, for the 8-arm design, with the 3-lobe cam the reaction forces generated in the cam were more balanced. As a result, the engine will be subjected to less resistant torque. It is worth mentioning that if different test loads are used on each arm, as discussed below, these forces will be less balanced. Whatever the case, the power of the motor (1100W) is more than enough to not have to worry about this problem.

Regarding signal processing, the bench is equipped with a Beckhoff C6920-0060 industrial PC that receives the signal from the load cells, the signal from the rotary motor encoder and the signal from the limit switches. The software displays the current number of cycles of the test, the test frequency, and the revolutions per minute of the cam. In addition to this, it shows whether each dental restoration has failed or is still functional. In the event of a failure, it records the number of cycles until failure (see Figure 92).

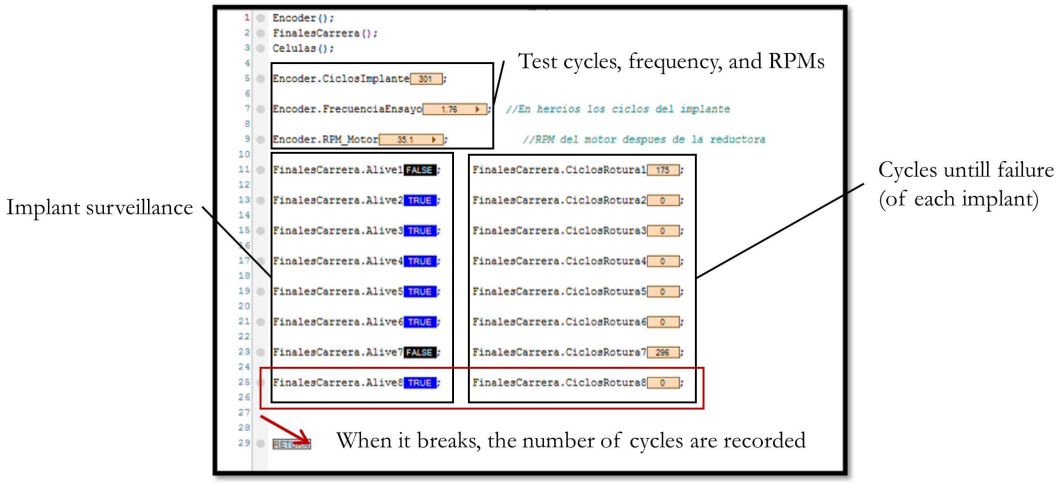

Figure 92. Software interface of the test bench.

The ISO 14801[141] standard recommends testing at least 2 and preferably 3 specimens at each of at least 4 load levels. Besides this, to obtain reliable data, the ASTM[62] standard recommends the use of 12 to 24 specimens and at least 4 specimens and 4 load levels (75% replication) to determine the finite life of a material or component (as explained in section 1.3.1.1). Therefore, with the test strategy presented in Figure 93, a finite life curve of 16 points could be obtained with the duration of only two tests. We would therefore be reducing the time by 8 times compared to a conventional fatigue bench.

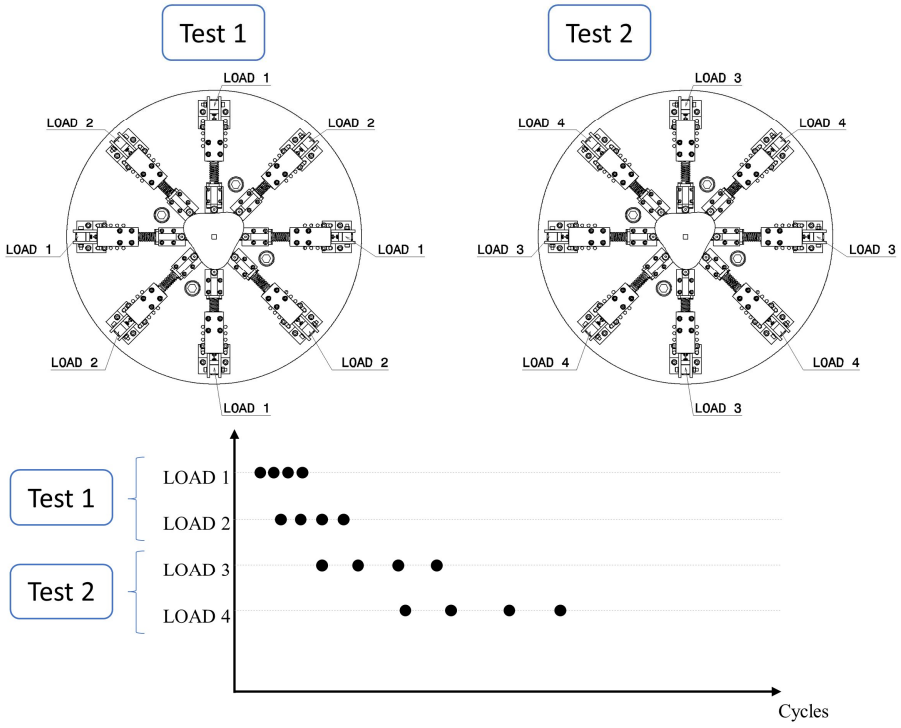

Figure 93. Example of testing to obtain 16 experimental results.

2.5.4 Validation of the new test bench

To verify that the bench presented works correctly, experimental tests have been carried out on the notched pins of Figure 94, which emulate a dental restoration, but for a cheaper price. In addition to its lower cost, using a single piece which concentrates its failure in the notch offers clearly less dispersion in fatigue life than dental restorations with all their components and the dispersion introduced by the preloading of the screw(s).

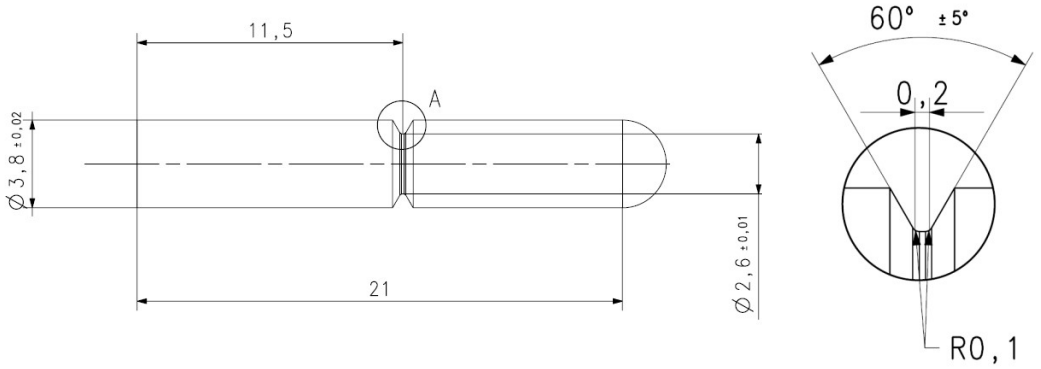

Figure 94. Notched pins for test bench validation. A, General view. B, Notch view.

The pins serve to obtain the F-N (load versus cycles) curve of the pins on different machines, two MTS-858 Mini Bionix II (from BTI facilities), the INSTRON 8801 (see section 2.4.2), and the fatigue bench presented. Figure 95 shows the fatigue results (points) of each fatigue test bench along with the linear F-N models obtained according to the ISO 14801 standard.[141] Moreover, 95% confidence bands of the F-N model of the new test bench are provided. It can be seen how all the linear models fall within the confidence bands of the new test bench and, therefore, they can be assumed to be equal. As a result, it can be confirmed that the performance of the new test bench presented is comparable to other test benches on the market.

This bench is a prototype that was made at the beginning of the PhD Thesis, since fatigue testing was expected to bottleneck in this research. However, the complete availability of test benches by the Mechanical Engineering Department of UPV/EHU with the INSTRON 8801 and by BTI with the INSTRON E3000 and the MTS-858 finally made use of the prototype unnecessary.

The patented prototype (Patent number: P201830801)[275] is currently pending certification by a certified organization and is also awaiting a company interested in its commercial exploitation.

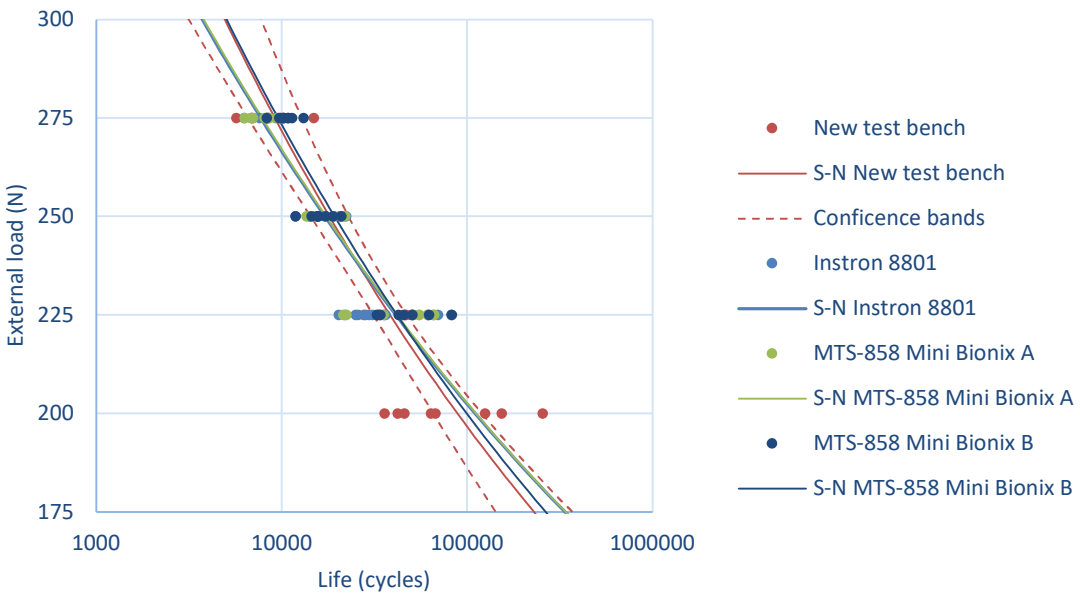

Figure 95. Fatigue data points and linear regression models of all tests benches compared.

3 Fatigue behavior of the prosthetic screw: life prediction methodology

As explained in section 1.6, there are numerous studies in specialized literature that evaluate the fatigue behavior of dental restorations from different approaches. On the one hand, there are studies that evaluate the performance of the restorations in patients' mouths (in-vivo) by means of retrospective studies. These studies do not provide much information beyond whether or not the restoration has satisfactorily withstood the particular conditions that the patient has imposed on it over a more or less prolonged period of use. Secondly, many studies perform experimental in vitro fatigue tests according to ISO14801.[141] As a result of these tests, the F-N curve of the dental restoration is obtained, which provides the number of cycles N supported by the implant as a function of the cyclic load F applied according to the test conditions of the standard (see section 1.6.1). Thus, in these studies, F-N curves are obtained for different types or models of dental restorations (or more usually the N duration for a single F value), and the comparison establishes which restoration performs better under fatigue. Based on this, these publications attempt to infer which material, type of IAC, preload level, platform diameter, etc. provides the best fatigue performance in dental restorations. This type of work, based exclusively on simply comparing fatigue durations, is of interest to clinicians when deciding on a particular dental restoration model, and is therefore very well received in journals whose target audience are these professionals. Finally, there are studies that, in an attempt to go a step further than purely experimental studies, perform FE structural analyses (sometimes exclusively or, in the best of cases, supplementing it with experimental fatigue tests). These FEAs make it possible to see the stress status of the dental restoration and therefore detect the critical component and its potential failure section based on where the peak stress occurs under the maximum load state. However, these studies are not very

rigorous, since in fatigue the load is cyclic and therefore fatigue behavior is not determined by the maximum stress at a point, but by the stress variation. In addition to this, aspects such as notch sensitivity should also be considered if there is a concentration of stresses in the critical section, as is the case in dental restorations.

In short, the literature is full of retrospective in-vivo and experimental in-vitro studies comparing the fatigue behavior of different dental restorations to determine which has a longer fatigue life. Although, as mentioned above, these studies may be interesting (and perhaps sufficient) for clinicians, they far from explain why the failure occurs on one component or another, and which parameters relating to design (geometry, material, etc.), assembly (screw preload) or operation (nature of the loads) have the greatest effect on fatigue behavior. A study of this type would make it possible to understand fatigue failure in dental restorations, and on this basis generate knowledge and even develop analysis and design tools that would make it possible to optimize existing designs to achieve dental restorations with enhanced fatigue behavior. Consequently, the aim of this chapter is specifically to study the fatigue phenomenon in dental restorations from a mechanical perspective that provides an answer to these questions. As a main contribution, a methodology capable of predicting the fatigue life of dental restorations in which the critical element is the prosthetic screw is described, which happens on many occasions as we have seen in section 1.6.1. As a secondary contribution of this chapter, some conclusions on the effect of the most important geometrical parameters on the fatigue behavior of dental restorations in which the critical component is the prosthetic screw have been derived from the experimental tests carried out throughout this PhD Thesis. These same conclusions, and other additional ones, can be drawn from the prediction methodology developed without having to resort to experimental tests, thus making the methodology an efficient and versatile tool for designing dental implants under fatigue.

Accordingly, section 3.1 presents the aforementioned methodology for estimating the fatigue life of dental restorations where the critical component is the prosthetic screw. This is the case, within the BTI catalog that we will use, of dental restorations with a regular and wide implant body diameter. In dental restorations with narrow implants, by contrast, the implant itself will be the critical component, calling for another approach for fatigue calculation, which is presented in Chapter 5. Once the methodology has been developed, its accuracy in estimating the fatigue life of different dental restoration designs is

verified in section 3.2. In section 3.3, conclusions regarding the presented methodology are discussed. Finally, in section 3.4, the experimental tests performed for the validation of the fatigue life prediction methodology have been used to determine the effect of different variables on fatigue behavior: tightening torque applied on the prosthetic screw, implant body diameter, implant platform diameter, connection type (internal versus external) and the addition of a transepithelial element to the restoration (the use of transepithelial-supported restoration versus implant-supported restoration). It should be mentioned that these same conclusions, and many others, could have been reached using only the fatigue prediction methodology. However, as these experimental tests have been necessary to validate the methodology, these tests have also been used to obtain conclusions regarding the effect of the different variables.

3.1 Development of a fatigue life prediction methodology

As mentioned in the introduction of this chapter, to develop the fatigue prediction methodology, on the one hand, a set of experimental fatigue tests of a particular dental restoration were carried out, applying different torque values on the prosthetic screw. On the other hand, FEAs were carried out to reproduce the conditions of these experimental tests from which the reaction forces and moments in the contact of the screw head have been obtained. Using simple calculations of the Theory of Elasticity, the nominal stresses in the screw failure section were obtained. Finally, both the durations obtained experimentally and the nominal stresses calculated from the reactions obtained by FEAs (mean and alternating components) were taken into account and it was found that Walker criterion could represent the behavior correctly. Therefore, a curve fitting procedure was performed to obtain Walker parameters for an optimal performance of the methodology. As a result, at the end of this section the methodology is presented in a more comprehensive manner.

3.1.1 Experimental Fatigue Tests

Several fatigue tests were performed on a BTI INTERNA IIPSCA4513 dental implant joined with an INPPTU44 prosthetic abutment by means of an INTTUH prosthetic screw (see Figure 96), from the BTI product catalogue. The assembly (from now on called IN-I4.5-P4.1) has an implant body diameter

of 4.5mm, a platform diameter of 4.1mm, and an internal butt-joint connection, everything joined by means of an M1.8 prosthetic screw. As explained in section 2.4.1, the implant was placed in a specimen holder and fixed by means of an embedding material (Loctite 401). Then, the abutment was placed on the implant and the prosthetic screw was positioned and tightened. To ensure a wide range of mean stress characterization, three different tightening torque magnitudes were tested: 15, 25, and 35Ncm, with the last one being the value that BTI recommends. Finally, a hemispherical device was placed on the top of the abutment. The tests were carried out on an INSTRON E 3000 Electropuls fatigue test bench, following the ISO 14801 standard[141] requirements, as explained in section 2.4.1.

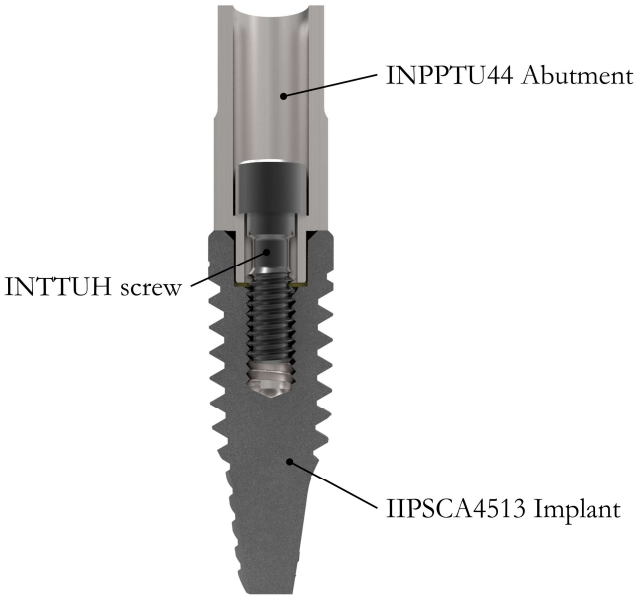

Figure 96. IN-I4.5-P4.1 dental restoration used for experimental tests.

46 dental restorations were tested experimentally, with 13 failures occurring on the screw head (see Figure 97A), 30 in the first thread in contact (see Figure 97B), and 3 survivals (runout of 5 million cycles). Figure 98 shows the fatigue results on an F-N curve (applied load versus fatigue cycles). Each marker color represents a different tightening torque while each marker shape corresponds to a different failure mode/survival. Screw head failures were found to be easily avoidable by changing the manufacturing process of the screw head socket as will be explained in detail in section 4.1. Thus, this work was only focused on the failures on the screw thread. Additionally, the runouts indicate that the tested load levels are not far from the fatigue limit, so it may be considered that the experimental tests are representative of the whole finite life of the screw and, consequently, of the whole dental restoration under study. Thus, Figure 99

shows again the experimental fatigue results of Figure 98 excluding both the survivals and the screw head failures, along with their corresponding linear regressions according to the ASTM E-739 standard.[64]

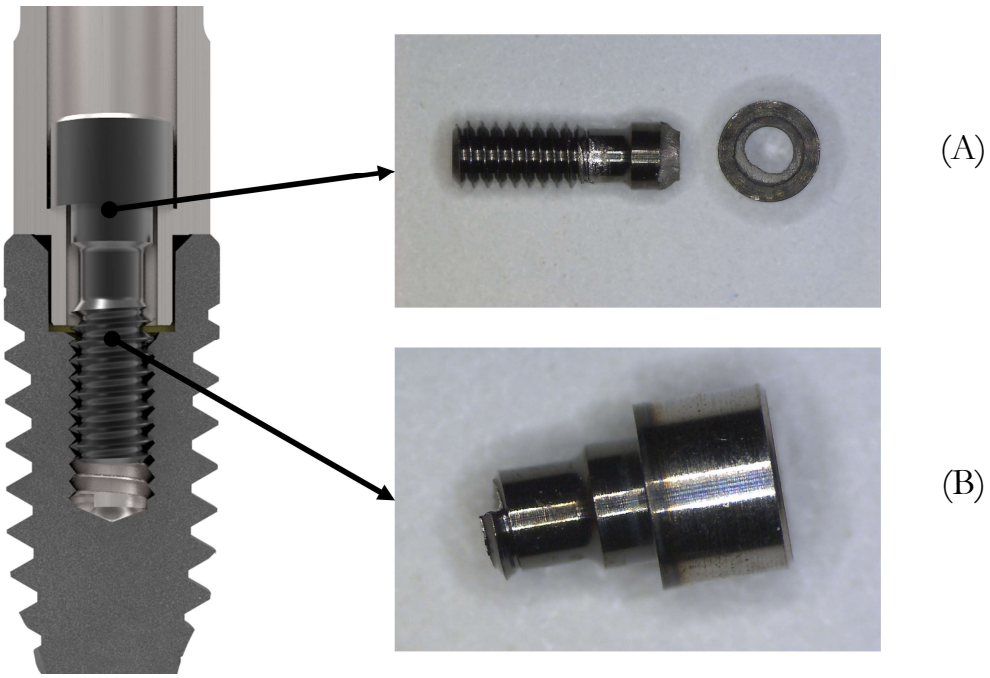

Figure 97. Fatigue failure sections on the prosthetic screws of IN-I4.5-P4.1. A, Screw head. B, First thread in contact.

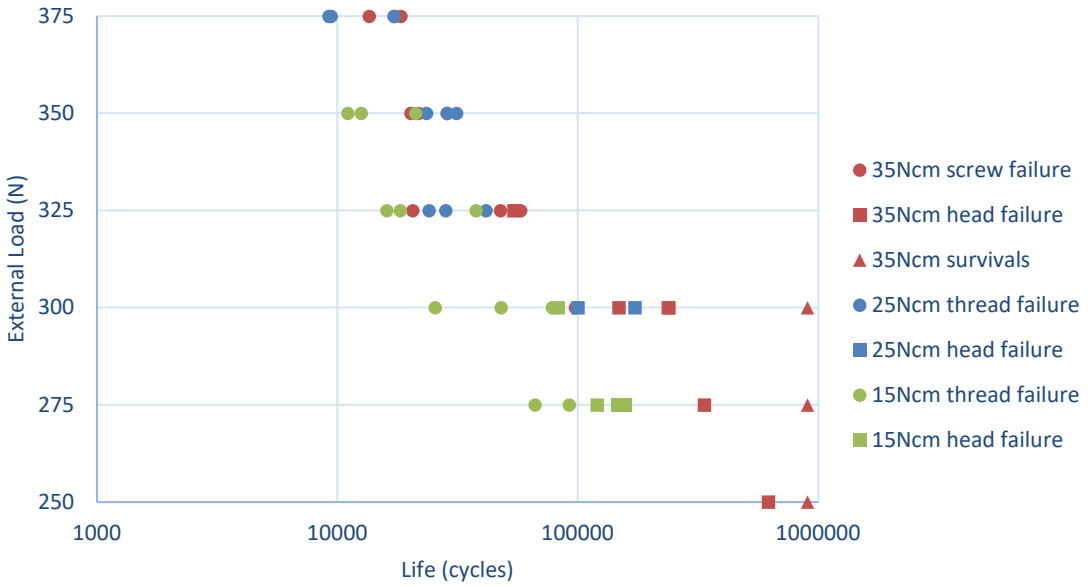

Figure 98. Fatigue results of all fatigue tests performed on the IN-I4.5-P4.1 dental restoration.

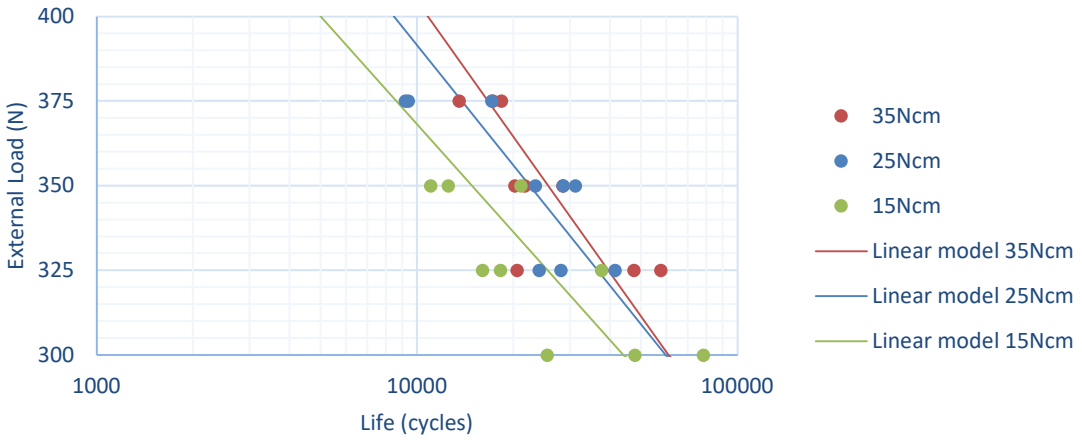

Figure 99. F-N linear models of the IN-I4.5-P4.1 dental restoration at each of the three tightening torques (lines) along with the experimental fatigue results (markers).

3.1.2 Finite Element Analysis

Once the fatigue F-N curve of the IN-I4.5-P4.1 dental restoration has been obtained experimentally according to ISO14801,[141] the next step is to obtain the stresses associated with each tested load F from an FEA (see Figure 100A). As expected, it has been proven in preliminary analyses that under the test conditions of ISO 14801,[141] the screw is subjected to a uniaxial nominal stress status, which is easy to calculate with the Theory of Elasticity formulations. This makes it possible to work with these nominal stresses instead of using the peak linear elastic stresses from the FEA.

The nominal stresses have been calculated by considering the contact reactions at the screw head, i.e., the axial force F_a, the transverse force F_t, and the bending moment M on section A of Figure 100B.

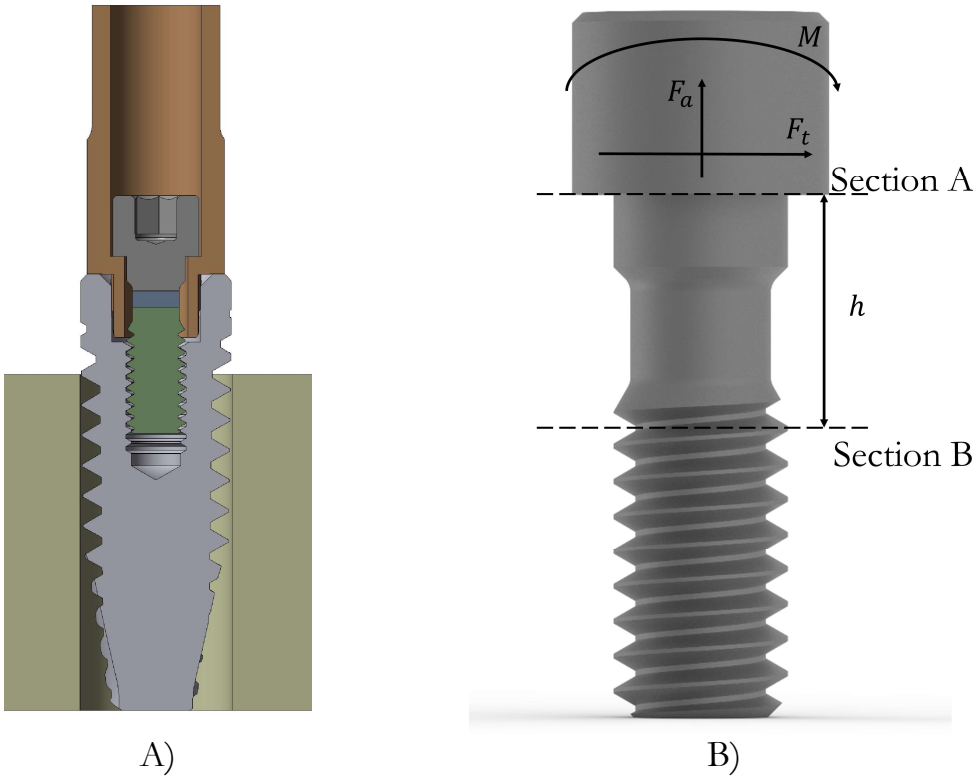

Figure 100. A, FE model of IN-I4.5-P4.1 dental restoration. B, Contact reactions on the screw head contact surface (section A) and fatigue failure section (section B).

In order to obtain these contact reactions, a FEM of the IN-I4.5-P4.1 dental restoration was performed by following the procedure explained in section 2.2, that is, assuming half geometry, cylindrical screw threads, sectioning the abutment so that the 30º load shall be applied at 8mm from the implant platform, embedding the implant in a specimen holder, etc. Three different FEAs were performed varying the tightening torque: 15, 25 and 35Ncm as in the experimental tests. The screw preloads obtained for the INTTUH prosthetic screw (flat screw head) according to equation (131) were 349N for 15Ncm, 581N for 25Ncm, and 814N for 35Ncm. As explained in section 2.2, since half geometry was modelled, half values of preloads were also applied; these are 174.5N, 290.5N, and 407N for 15Ncm, 25Ncm, and 35Ncm, respectively. In a second load step, the external load F was increased from 0 to 400N. Again, half load must be applied for half geometry. Finally, the force reactions on the contact surface under the screw head were recorded (section A in Figure 100B). Figure 101 shows these moment and force reactions under the screw head for the three tightening torques under study.

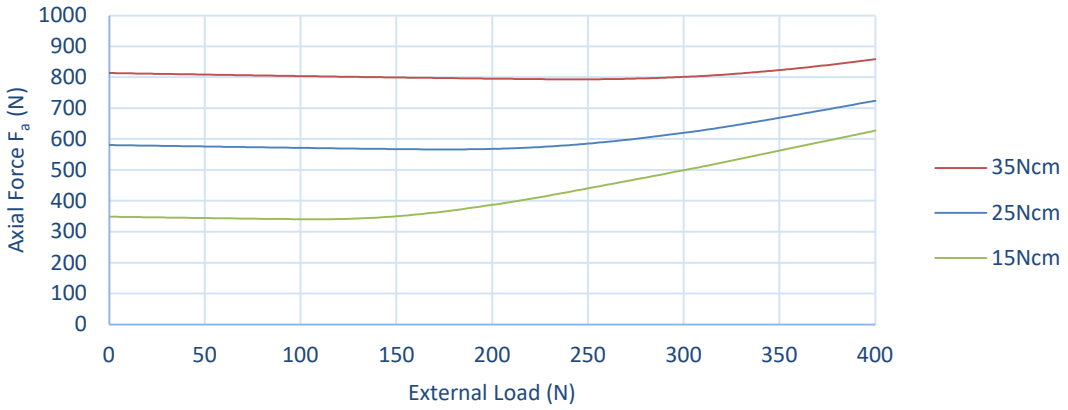

A)

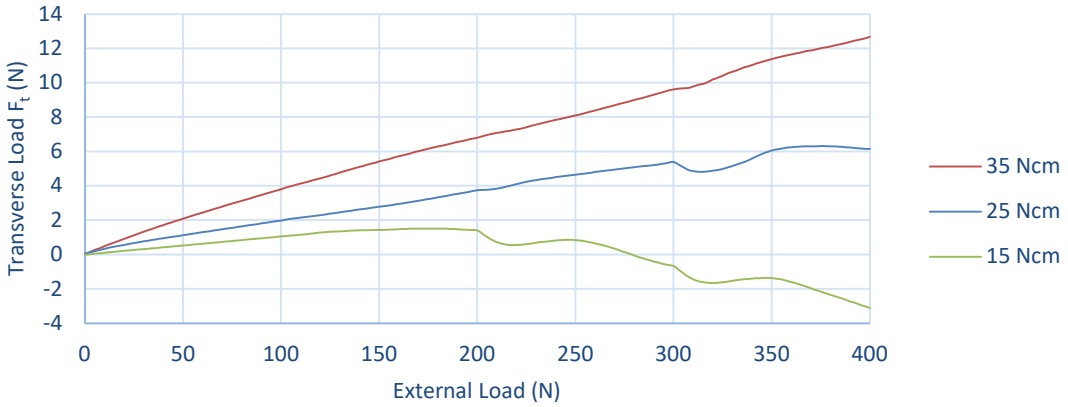

B)

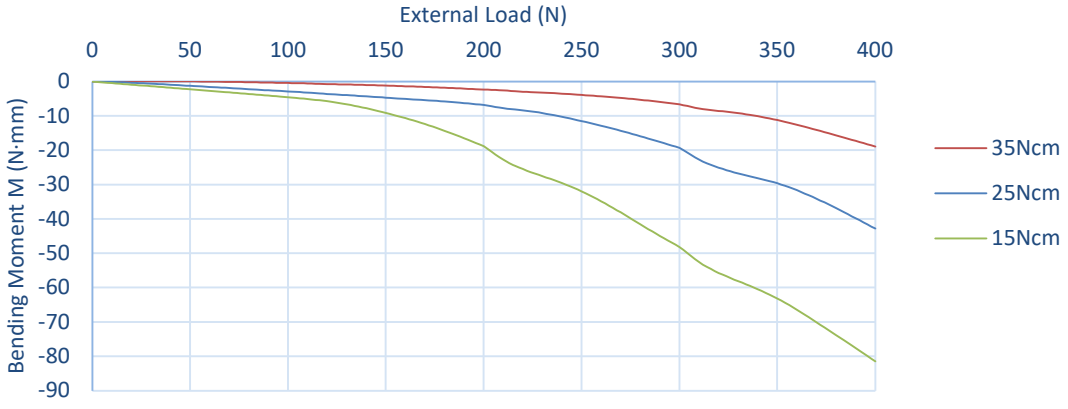

C)

Figure 101. Force reactions under the screw head (section A in Figure 100B). A, Axial force F_a. B, Transverse force F_t. C, Bending moment M.

As mentioned in section 3.1.1, the failure section of the screw is the first engaged thread (section B of Figure 100B). Therefore, the next step is to transfer the forces from section A to section B. In this section, the axial F_a and

transverse F_t forces remain the same, unlike the bending moment that increases up to $M + F_t \cdot h$. Figure 102 shows these forces transferred to the failure section (section B in Figure 100B) for the three tightening torques analyzed. The shear stresses generated by the transverse force F_t were not considered in section B since their values are negligible compared to the values of the normal stresses (necessary condition to assume uniaxial behavior).

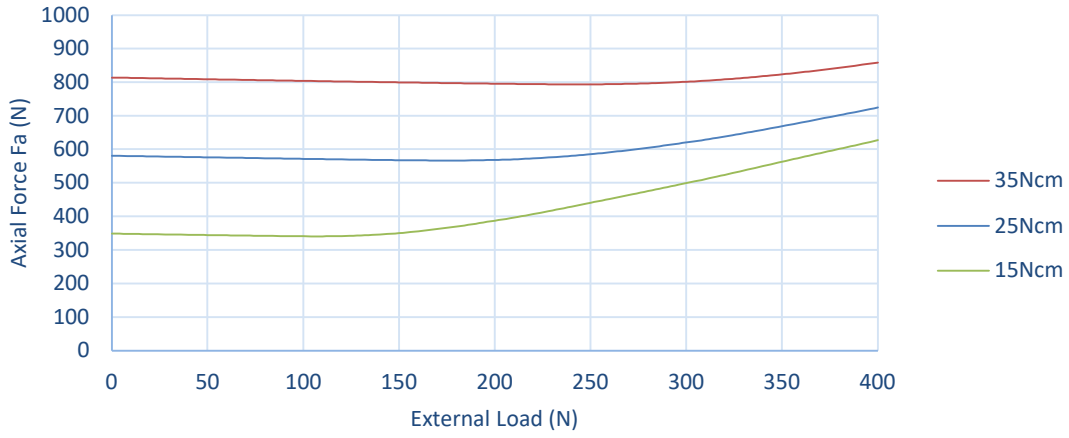

A)

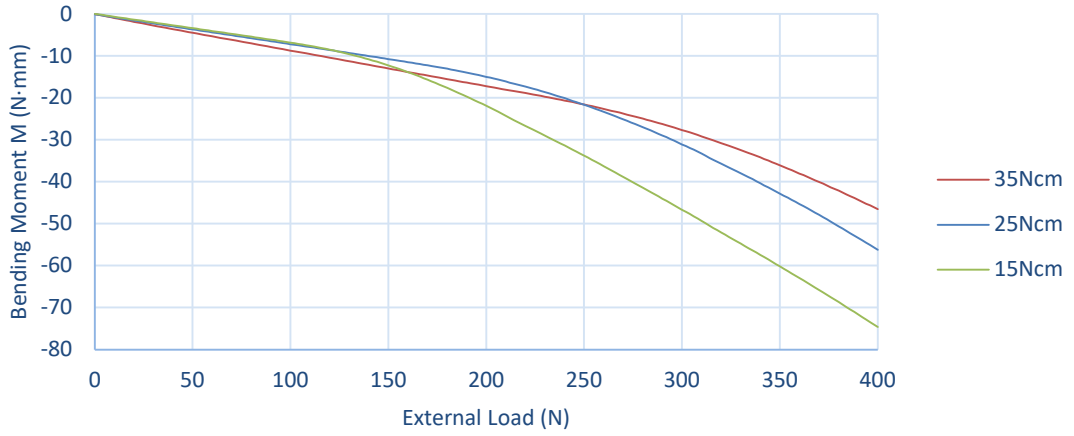

B)

Figure 102. Forces in the failure section (section B in Figure 100B). A, Axial force F_a. B, Bending moment M.

Hence, the nominal uniaxial stress for each applied load F in this critical section B is calculated by using equation (133).

$$\sigma_{nom}(F) = \frac{F_a}{A} + \frac{(F_t \cdot h + M) \cdot r}{I} \tag{133}$$

Where A and I are the area and inertial moment of the critical section, respectively. The calculation of resistant area A and inertial moment I of a threaded part is slightly more complex than on a part with a constant section. For these cases, Bickford[111] recommends an equation that assumes the nominal measurements of a metric. As is usual in metric standards, there are nominal dimensions of the threads but also maximum and minimum values, setting a range within metric dimensions may vary. These variations may be negligible for a large metric screw but in the case of a prosthetic screw (M1.8), any minimal variation in thread geometry may affect the value of the effective area, leading to an error in the calculation of the nominal stress. To avoid this, instead of using the equation proposed by Bickford,[111] two simple FEAs were performed applying an axial load and a bending moment (vertical load that generates a bending moment) on an M1.8 threaded cylinder (with has exactly the same metric dimensions as the screw thread) as shown in Figure 103. Then, the values for the resistant area A and inertial moment I were obtained from the following classical expressions:

$$\sigma = \frac{F}{A} = E \cdot \frac{\delta}{L} \rightarrow A = \frac{F \cdot L}{E \cdot \delta} \tag{134}$$

$$\delta = \frac{F \cdot L^3}{3 \cdot E \cdot I} \tag{135}$$

Where E is the Young modulus, L is the initial length, δ is the deformation and σ is the nominal stress.

A) B)

Figure 103. FEA performed to asses the parameters in equations (134) and (135). A, Axial case to calculate the effective area *A*. B) Bending case to calculate the inertia *I*.

Then, the nominal stresses were worked out by means of equation (133). Figure 104 shows the resulting nominal stress σ_{nom} versus the applied load F calculated. Moreover, the stresses caused by the axial force and bending moment are also shown (the sum of both is the nominal stress).

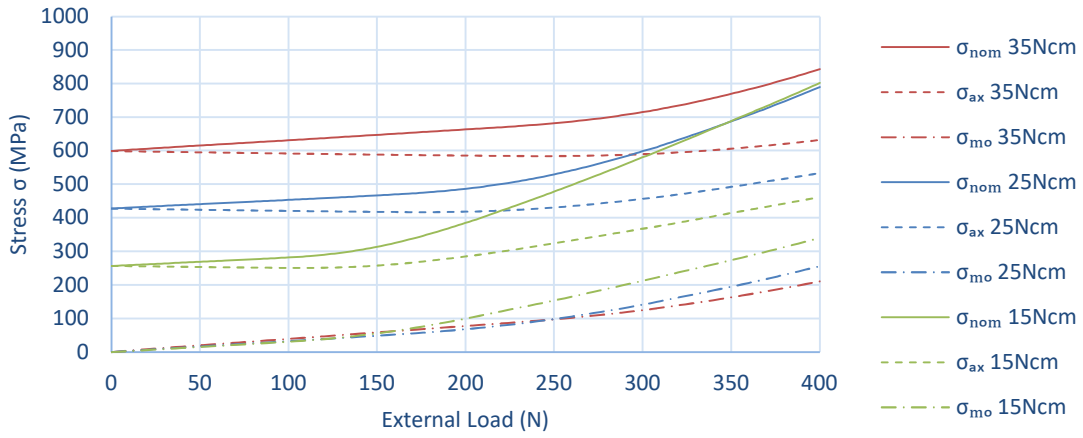

Figure 104. Nominal normal stress (with axial and bending components) in the screw thread according to equation (133).

As has been seen, the nominal stress of the prosthetic screw depends on the force F applied on the top of the dental restoration. As explained in section 1.6.1, after tightening the prosthetic screw, in the fatigue test according to ISO14801[141] a cyclic load F varying between a maximum value and 10% of that value is applied. As the goal of these FEAs is to reproduce these experimental tests, from the values of Figure 104, the mean and alternating nominal stresses are obtained as a function of external load F, by calculating the half-sum and half-subtraction of the nominal stresses (equation (30)) of the fatigue cycle that varies between the maximum value of F and 10% of that value of F (minimum value), the results of which are shown in Figure 105.

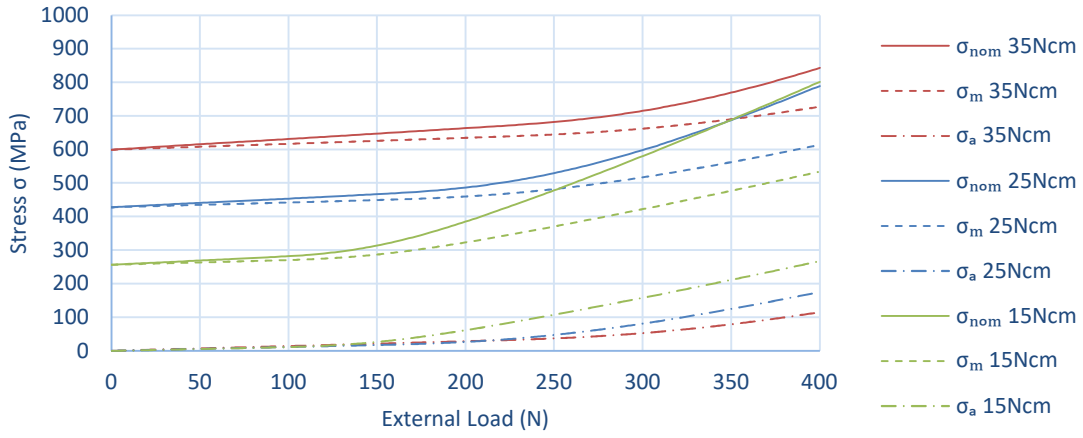

Figure 105. Mean and alternating components of the nominal stress in the screw thread versus the external load F.

3.1.3 Model fitting

Finally, the mean and alternating nominal stress components in the previous section were correlated with the F-N linear models obtained from the experimental fatigue tests in section 3.1.1. Thus, the Haigh diagram[80] in Figure 106 was plotted, which relates mean and alternating stresses with the experimental fatigue life. As can be seen, the Walker[82] criterion fits well the results with the parameters indicated in equation (136), obtained by following the procedure described by Dowling,[276] giving the following expression:

$$N^b = \frac{\sigma_{alternating}^{\gamma}}{\sigma_0} \cdot \left(\sigma_{mean} + \sigma_{alternating}\right)^{1-\gamma}; where \begin{cases} \gamma = 0.21 \\ b = -0.18 \\ \sigma_0 = 3039\ MPa \end{cases} \quad (136)$$

Please note that the characterization was focused on the $0 < R < 1$ zone of Figure 106, which provides a proper representation of the actual operating area of the screw since it always operates with high mean stress due to preloading.

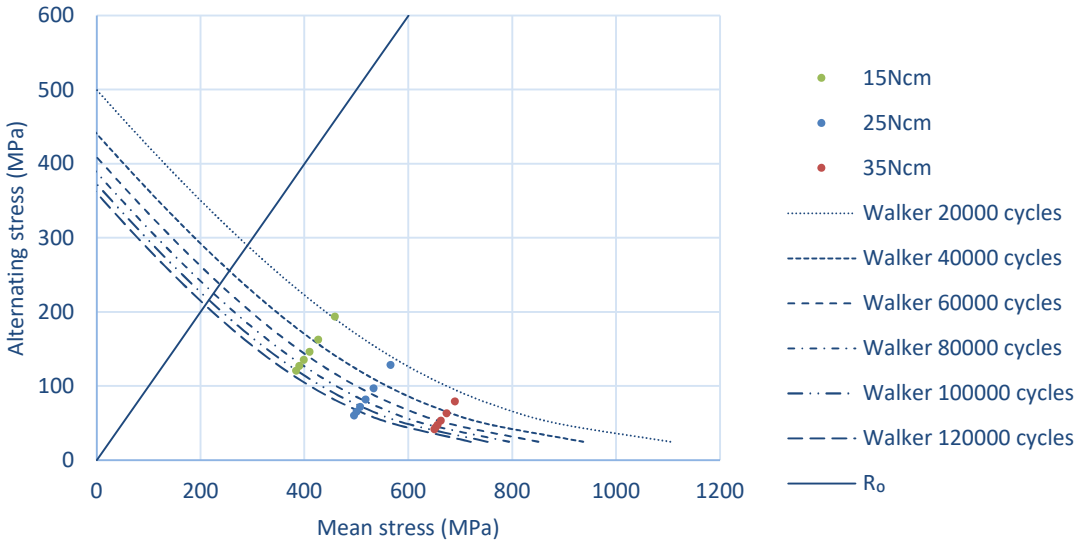

Figure 106. Haigh diagram and Walker fitting curves.

3.1.4 Use of the methodology

The equation (136) obtained in the previous section, with the calculated specific values of adjustment of Walker parameters, should be considered as an equation that serves to predict the fatigue life of the specific prosthetic screw studied here. In other words, it is valid for any dental restoration that applies that specific screw geometry, with that specific material, manufacturing process, size, surface finish, thread profile, etc. If one wants to predict the fatigue life of a dental restoration that uses another prosthetic screw, the process from section

3.1.1 should be repeated so that new values of the fitting parameters of equation (136) are obtained.

Nevertheless, the daily use of this methodology once it has been fitted is much simpler and straightforward. As can be seen in Figure 107, it is sufficient to perform an FEM of the dental restoration to be studied, obtain the force reactions at the contact under the screw head, calculate the mean and alternating nominal stresses in the critical section and enter them in equation (136) to estimate the fatigue life. To obtain the F-N curve of the dental restoration, the process must be repeated obtaining the nominal stresses for various values of external load F and calculating their corresponding number of cycles.

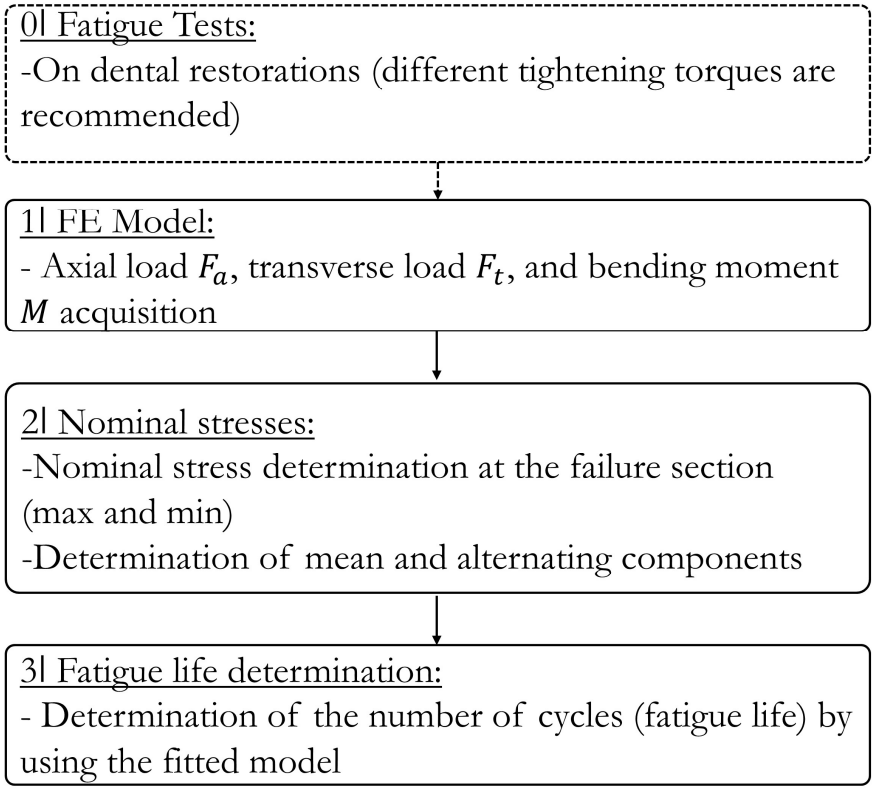

Figure 107. Steps of the methodology proposed to predict the fatigue life of dental restorations in which the critical component is the prosthetic screw.

3.2 Validation of the methodology on different dental restorations

In the previous section, a fatigue life prediction methodology was presented for dental restorations in which the failure component is the prosthetic screw. In addition to this, it has been pointed out that the equation for the methodology

is applicable for the case of a specific model of prosthetic screw, with the methodology being valid for any dental restoration that mounts that screw. In the case of BTI, all implant-supported restorations mount the same prosthetic screw, with the exception of some restorations that mount a slightly larger metric screw (M2 instead of M1.8). Therefore, this section intends to verify the effectiveness of the methodology on other implant-supported restorations that mount the same prosthetic screw, on the aforementioned restorations that mount a slightly larger screw, and on transepithelial-supported restorations. To this end, on the one hand, experimental fatigue tests were performed on the dental restorations to be studied and, on the other hand, the procedure explained in the previous section was followed to predict the fatigue life using the methodology presented. Finally, the results have been compared to see if the methodology was able to perform the predictions accurately.

3.2.1 Implant-supported restorations

Apart from the dental restoration tested in the previous section (IN-I4.5-P4.1), three other implant-supported restorations of the same BTI catalogue were tested experimentally (see Figure 108) so that the results could be compared with the ones obtained from the methodology. Again, as the methodology is focused on the failure of the prosthetic screw, regular and wide implants were chosen, not using narrow restorations where the implant is expected to be the failing component. The aim of these fatigue tests was to cover a wide implant parameter range. IN-I5.5-P4.1 has a 1mm larger implant body diameter than IN-I4.5-P4.1, but the same platform. IN-I5.5-P5.5 has a 1.4mm larger implant platform than IN-I5.5-P4.1 and the same implant body diameter. Finally, EX-I4.5-P4.1 has the same implant body and platform diameters as IN-I4.5-P4.1, but the connection is external rather than internal butt-joint and the mounting prosthetic screw has a slightly larger metric (M2 instead of M1.8). The most important information about each dental restoration is summarized in Table 7. As in IN-I4.5-P4.1, all implants and abutments were made of CP4 Titanium and all prosthetic screws were made of Ti6Al4V ELI with the chemical composition provided in Table 4. Fatigue tests were carried out on the E 3000 Electropuls fatigue testing machine explained in section 2.4.1, following the ISO 14801 standard[141] requirements, explained in section 1.6.1. For each new dental restoration, 3 to 4 specimens were tested at each of the 3 to 5 load levels covering a wide life range. Some further tests were also performed for the IN-I4.5-P4.1 so that a wider cycle range was characterized.

IN-I4.5-P4.1 EX-I4.5-P4.1 IN-I5.5-P4.1 IN-I5.5-P5.5

Figure 108. Dental restorations under study.

Table 7. All the implant-supported restorations under study, including the previously studied IN-I4.5-P4.1.

Restoration	IN-I4.5-P4.1	IN-I5.5-P4.1	IN-I5.5-P5.5	EX-I4.5-P4.1
Implant	IIPSCA4513	IIPSCA5513	IIPACA5513	IRPS4513
Abutment	INPPTU44	INPPTU44	INPPTA54	PPTU44
Screw	INTTUH	INTTUH	INTTUH	TTUH
Body Ø (mm)	4.5	5.5	5.5	4.5
Platform Ø (mm)	4.1	4.1	5.5	4.1
IAC	Internal	Internal	Internal	External
Screw Metric	M1.8	M1.8	M1.8	M2
Torque (Ncm)	35	35	35	35

Figure 109 shows the F-N curves from the experimental fatigue tests of all the dental restorations in Figure 108. In the case of IN-I4.5-P4.1, the tests performed in section 3.1.1 (only the ones tightened at 35Ncm) are marked with rhombus while the additional tests performed for this validation process are marked with points.

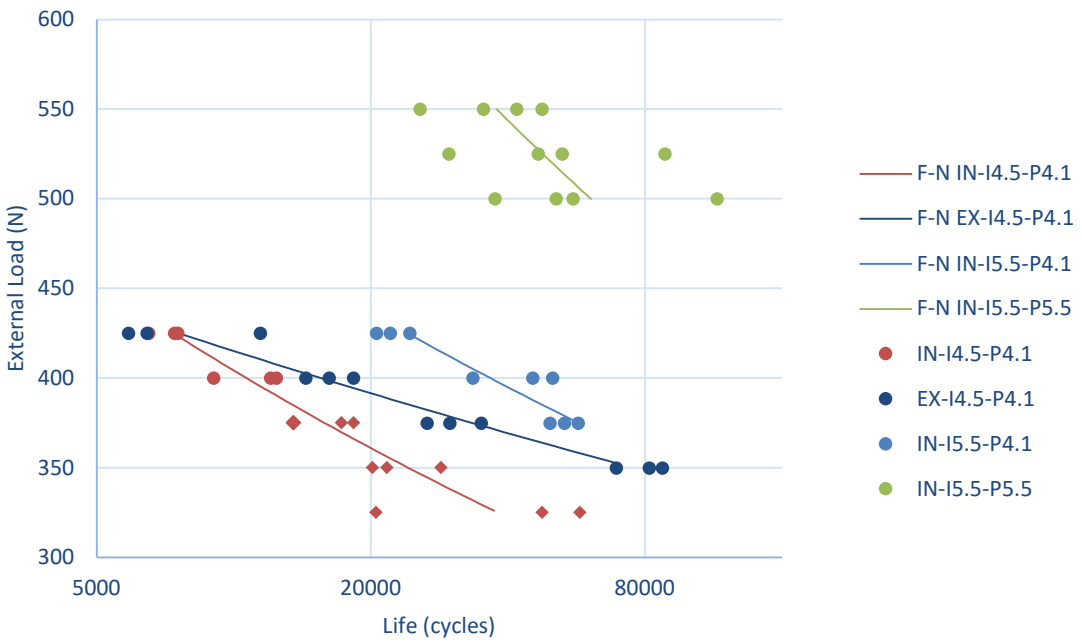

Figure 109. F-N curves of the dental restorations under study: experimental tests (markers) and linear model (lines). Data points with rhombus markers were obtained in the previous test campain (section 3.1.1).

Once the experimental results were obtained, the next step was to use the methodology to predict the fatigue life of IN-I5.5-P4.1, IN-I5.5-P5.5, and EX-I4.5-P4.1 at the same load range used in the experimental fatigue test campaign. FEAs for IN-I4.5-P4.1 were already performed in section 3.1.2. In short, FEAs were performed following the recommendations in section 2.2, applying the load at 30º on the top of the abutment (sectioned at 8mm from the implant platform) and recording the force and moment reactions on the contact surface under the screw head as explained in section 3.1.2. The preload for IN-I5.5-P4.1 and IN-I5.5-P5.5 was 814N for a 35Ncm tightening torque (407N for a half model) while for EX-I4.5-P4.1 the preload was 761N for a 35Ncm tightening torque (380.5N for a half model), according to equation (131). Then, mean and alternating stresses were calculated in the critical section of the prosthetic screw for each load level and each restoration model. Figure 110 shows the geometry of each restoration model. Finally, the nominal stresses were included in equation (136) obtaining the fatigue life prediction for a specific load level. F-N curves for each dental restoration were obtained by following this procedure for the desired load range. Thus, Figure 111, Figure 112, Figure 113, and Figure 114 show the fatigue data obtained experimentally (points), the linear model of these points (solid blue line), 95% confidence bands (dotted lines), 95% prediction intervals (dashed lines) and, finally, the fatigue life prediction obtained using the methodology (solid red line).

As can be seen in Figure 111, the prediction (solid red line) coincides with the linear model of the experimental results (solid blue line). This is to be expected in this case, since the IN-I4.5-P4.1 restoration is the one used for curve fitting for this methodology (in section 3.1). Obviously, it does not fit perfectly because 3 different preloads (15, 25, and 35Ncm) were used to obtain Walker parameters (via curve fitting). Figure 111 shows how the new tests (points) follow the trend of the old ones (rhombus), so the methodology fit is still perfectly valid.

Figure 112 corresponds to the implant with a diameter 1mm larger than the previous one (IN-I4.5-P4.1); i.e. IN-I5.5-P4.1. It can be seen how the model almost overlaps the experimental one, remaining within the limits marked by the 95% confidence curves. Therefore, in this case there is also no doubt that the fit of the methodology is correct.

Figure 113 shows the behavior of the IN-I5.5-P5.5, which has a 1mm larger implant diameter and a 1.4mm larger platform diameter than the implant used for the methodology fitting (IN-I4.5-P4.1). In this case, it can be seen that the experimental models differ slightly. However, it is worth mentioning the extensive scatter of the experimental tests, which may result in the linear regression not being as accurate as desired. This is reflected in the 95% confidence interval, which is considerably wider than in the other cases. Whatever the case, since the prediction falls within the confidence interval, it can be assumed that the prediction is perfectly valid in terms of statistics.

Figure 114 shows the fatigue behavior of the implant with external connection (EX-I4.5-P4.1) which has the same implant diameter and platform as IN-I4.5-P4.1. As can be seen, there was a great deal of dispersion in these tests due to the fact that components from different batches had to be used. To compensate for this dispersion, the decision was made to perform more tests. Whatever the case, it can be seen that the prediction of the methodology falls within the 95% confidence bands of the experimental model, so the prediction is valid.

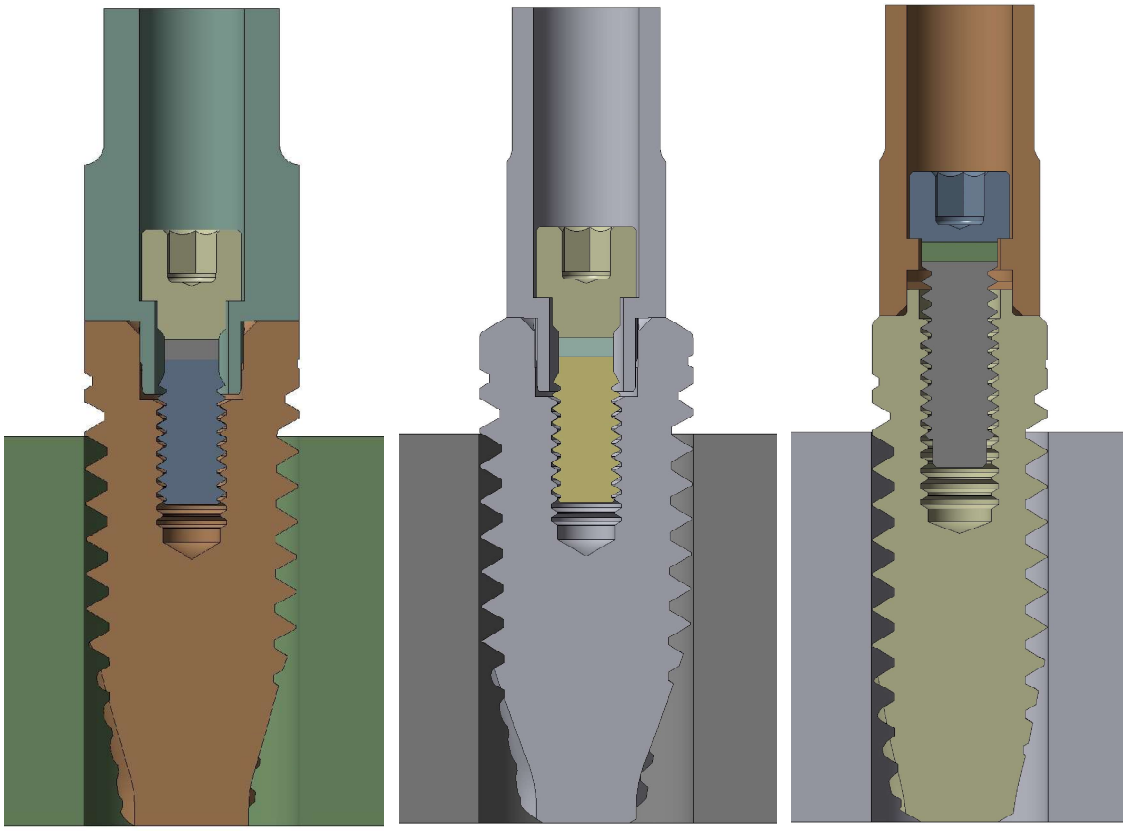

Figure 110. FE models. A, IN-I5.5-P5.5 (2,365,587 DoF). B, IN-I5.5-P4.1 (2,202,267 DoF). C, EX-I4.5-P4.1 (1,671,387 DoF).

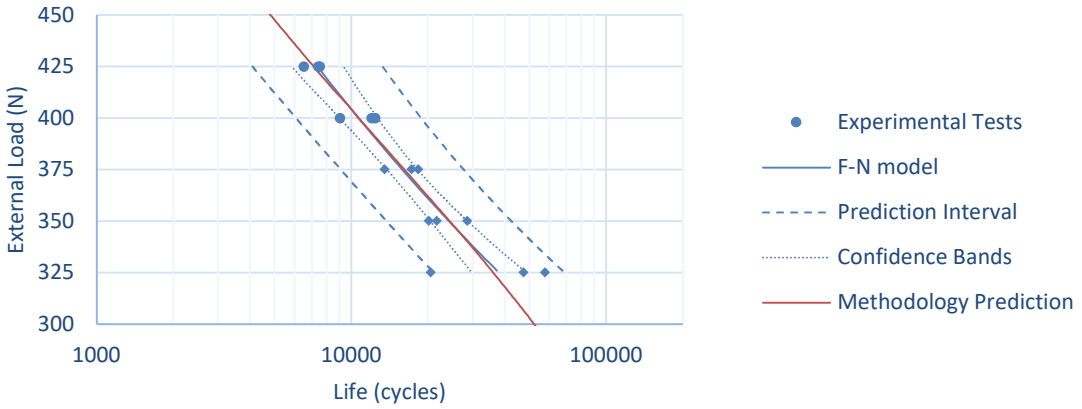

Figure 111. Experimental fatigue data points (markers), F-N linear regression (solid blue line), confidence bands (dotted lines), prediction intervals (dashed lines) and the F-N obtained using the prediction methodology (solid red line) for IN-I4.5-P4.1. Data points with rhombus markers were obtained in a previous test campaign (section 3.1.1).

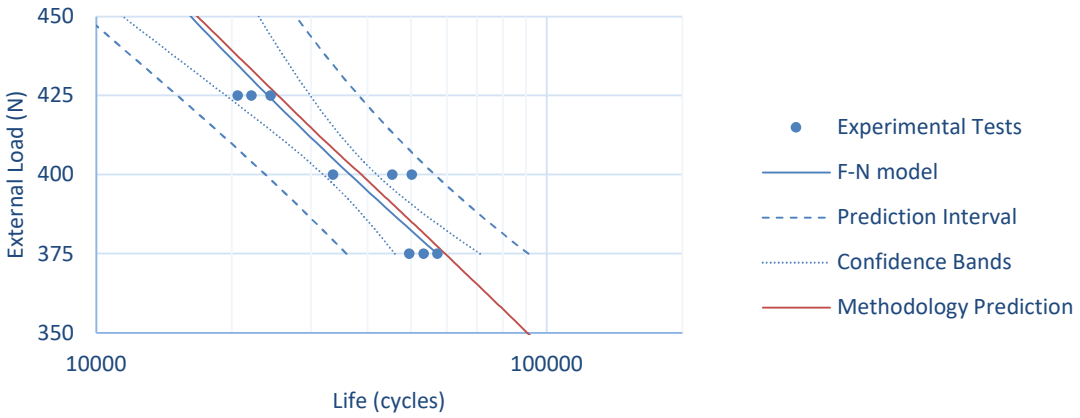

Figure 112. Experimental fatigue data points (markers), F-N linear regression (solid blue line), confidence bands (dotted lines), prediction intervals (dashed lines) and the F-N obtained using the prediction methodology (solid red line) for IN-I5.5-P4.1.

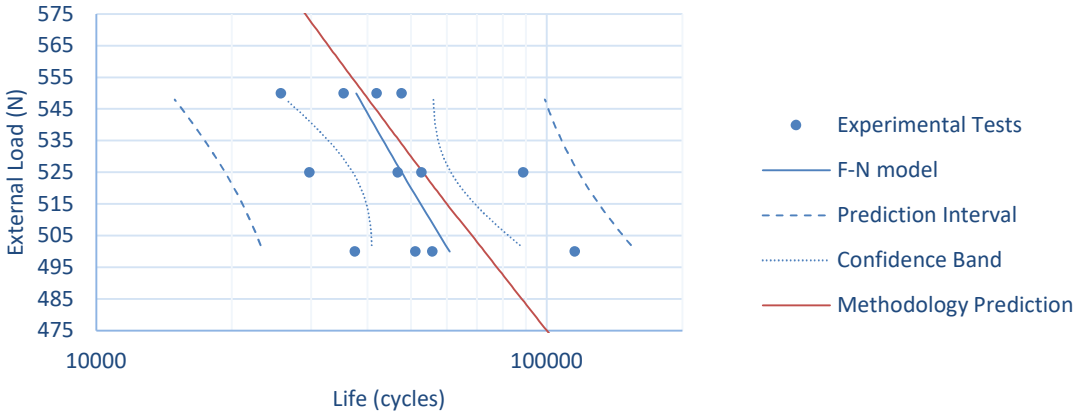

Figure 113. Experimental fatigue data points (markers), F-N linear regression (solid blue line), confidence bands (dotted lines), prediction intervals (dashed lines) and the F-N obtained using the prediction methodology (solid red line) for IN-I5.5-P5.5.

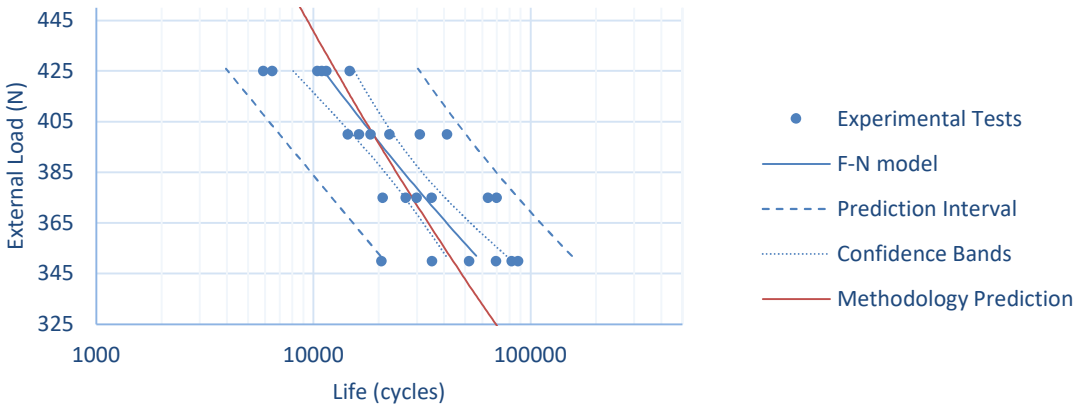

Figure 114. Experimental fatigue data points (markers), F-N linear regression (solid blue line), confidence bands (dotted lines), prediction intervals (dashed lines) and the F-N obtained using the prediction methodology (solid red line) for EX-I4.5-P4.1.

For a more visual comparison, Figure 115 shows all the experimental test results (vertical axis) versus the corresponding fatigue life estimated by the methodology (horizontal axis). The 45-degree blue line represents a perfect methodology-experimental match (experimental life equal to the life predicted by the methodology). Even though a perfect correlation is virtually impossible because of the inherent dispersion of the fatigue phenomenon,[55] as well as the scatter of the torque-preload ratio in screwed joints[3,45] it can be seen how the trend of the points is perfectly aligned with the 45-degree line.

Figure 116 may be more useful than Figure 115 for obtaining conclusions concerning the reliability of the methodology. It shows the mean value of the experimental life at each load level for each dental restoration versus the methodology prediction. Now, it can be seen that despite the considerable scatter seen in Figure 115, the average values in Figure 116 fall within the ±20% bands, expect for the case of EX-I4.5-P41, that fall close to them.

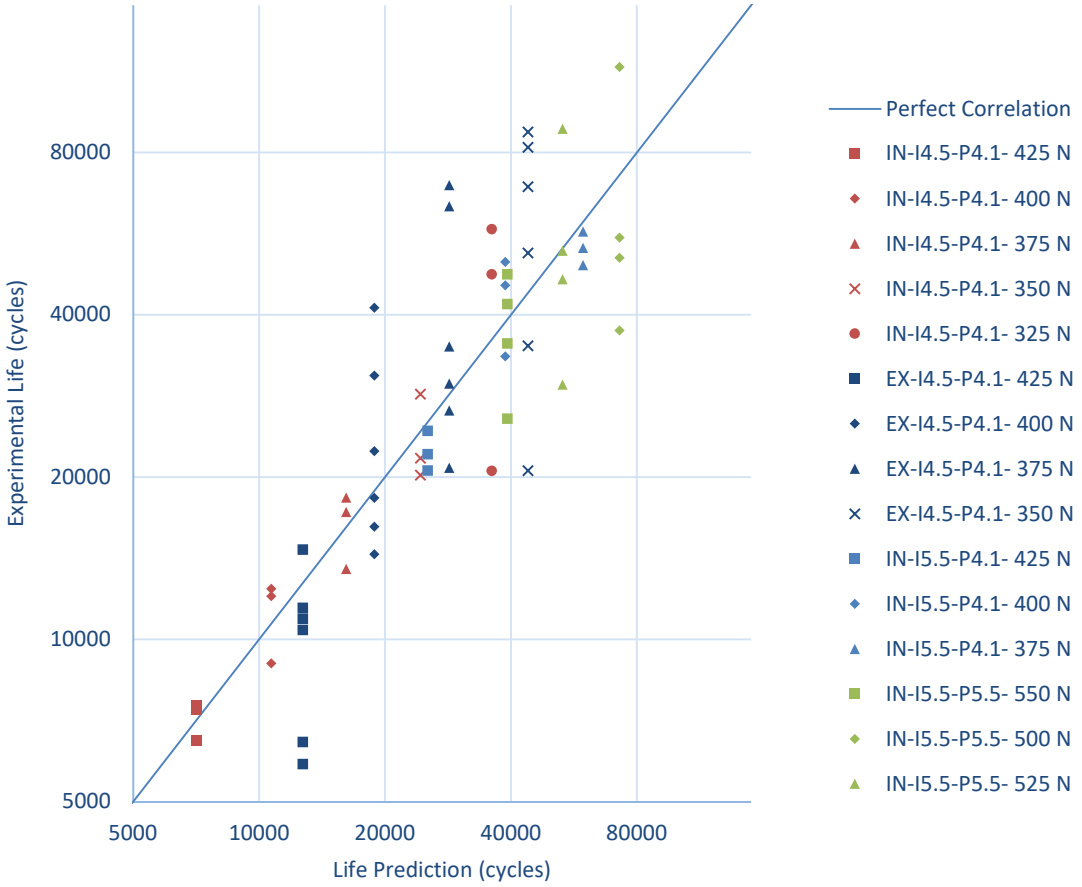

Figure 115. Experimental results versus methodology life prediction (all tests).

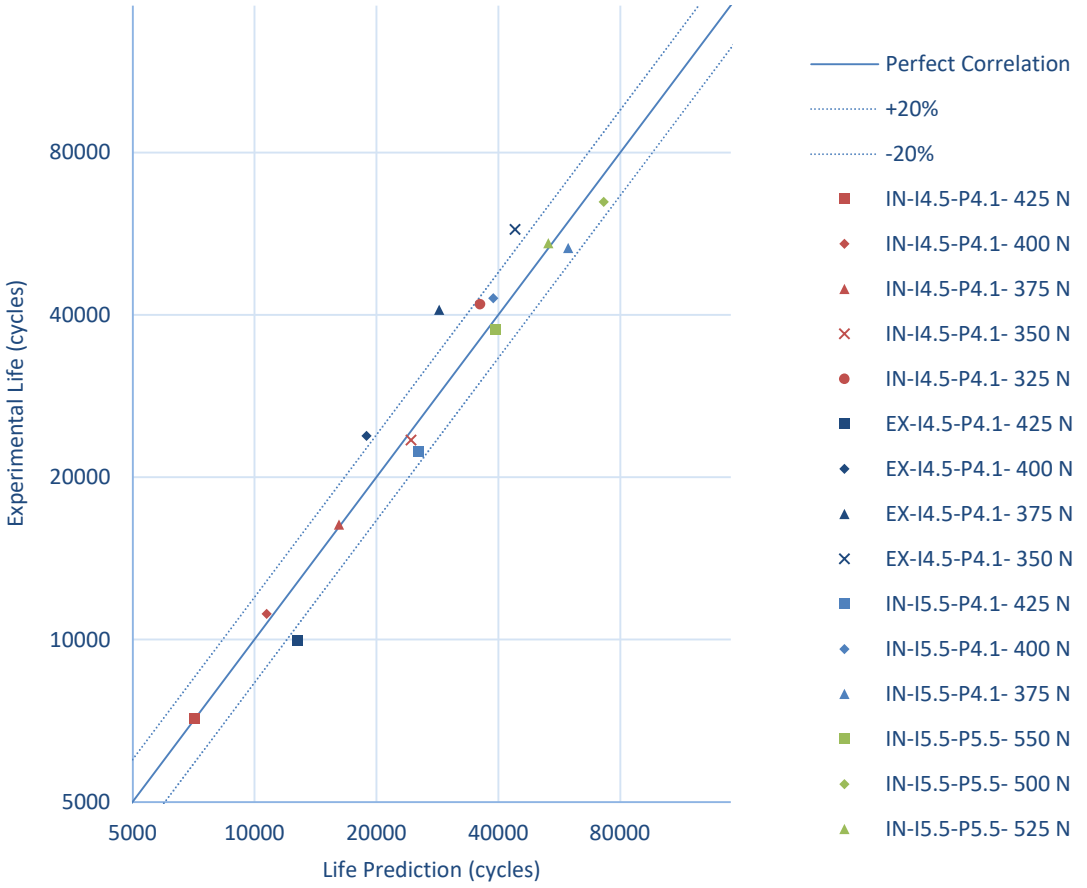

Figure 116. Experimental results versus methodology life prediction (using average life values).

Of course, one can take advantage of all the tests performed in this validation process to readjust the parameters in equation (136), which were obtained exclusively from the tests performed on IN-I4.5-P4.1 dental restorations. Thus, equation (137) shows the new values for the parameters once fitted for all the cases studied up to now. Figure 117 (IN-I4.5-P4.1), Figure 118 (IN-I5.5-P4.1), Figure 119 (IN-I5.5-P5.5) and Figure 120 (EX-I4.5-P4.1) show the experimental F-N curves along with the new fatigue life estimation by means of the readjusted methodology. Moreover, Figure 121 updates Figure 116, showing a slightly better match as it is clear that the accuracy of the methodology increases as more experimental tests are used to fit the life prediction equation.

$$N^b = \frac{\sigma_{alternating}^{\gamma}}{\sigma_0} \cdot \left(\sigma_{mean} + \sigma_{alternating}\right)^{1-\gamma}; where \begin{cases} \gamma = 0.18 \\ b = -0.16 \\ \sigma_0 = 2512\ MPa \end{cases} \quad (137)$$

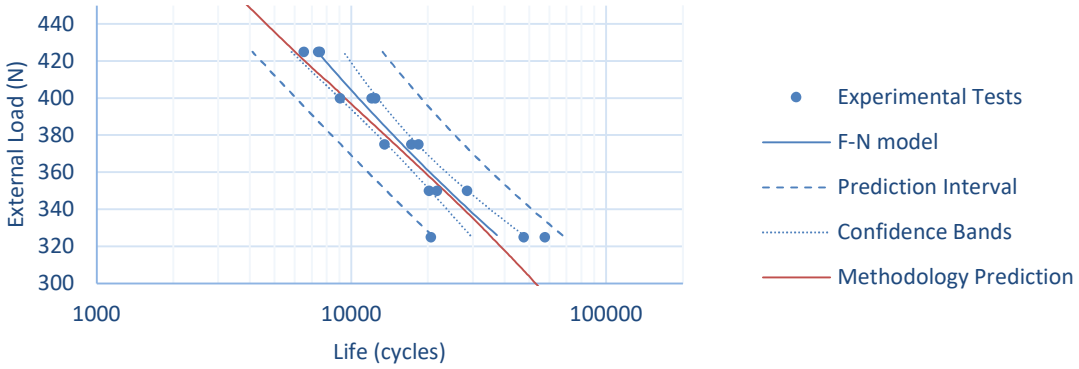

Figure 117. Experimental fatigue data points (markers), F-N linear regression (solid blue line), confidence bands (dotted lines), prediction intervals (dashed lines) and the F-N obtained using the theoretical prediction methodology with the new fitting parameters (solid red line) for IN-I4.5-P4.1.

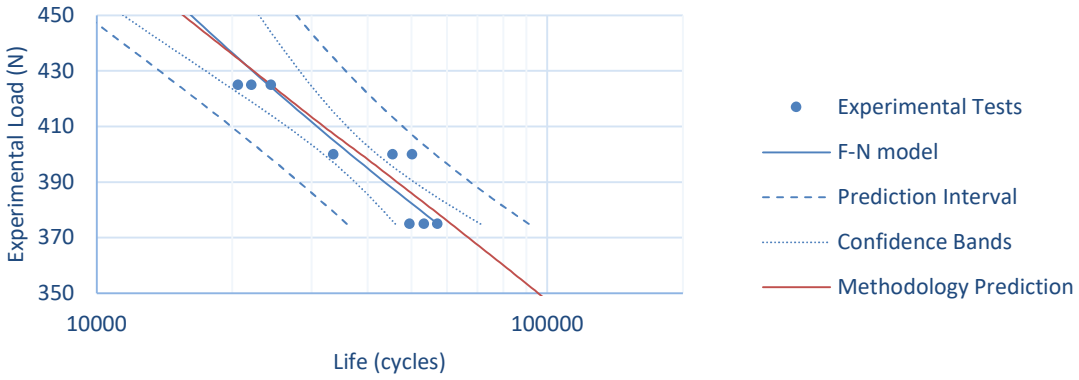

Figure 118. Experimental fatigue data points (markers), F-N linear regression (solid blue line), confidence bands (dotted lines), prediction intervals (dashed lines) and the F-N obtained using the theoretical prediction methodology with the new fitting parametres (solid red line) for IN-I5.5-P4.1.

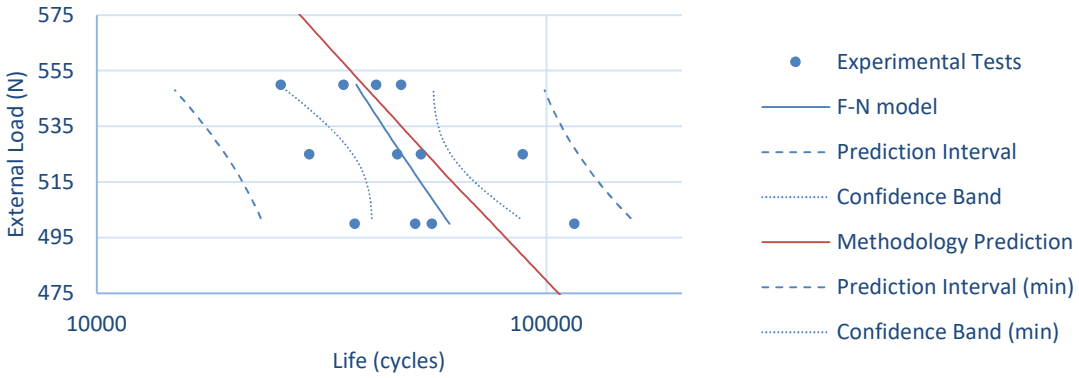

Figure 119. Experimental fatigue data points (markers), F-N linear regression (solid blue line), confidence bands (dotted lines), prediction intervals (dashed lines) and the F-N obtained using the theoretical prediction methodology with the new fitting parametres (solid red line) for IN-I5.5-P5.5.

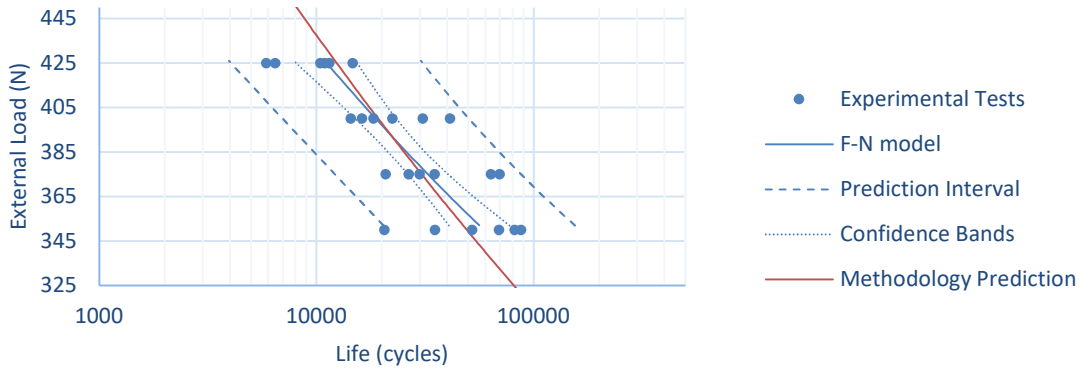

Figure 120. Experimental fatigue data points (markers), F-N linear regression (solid blue line), confidence bands (dotted lines), prediction intervals (dashed lines) and the F-N obtained using the theoretical prediction methodology with the new fitting parametres (solid red line) for EX-I4.5-P4.1.

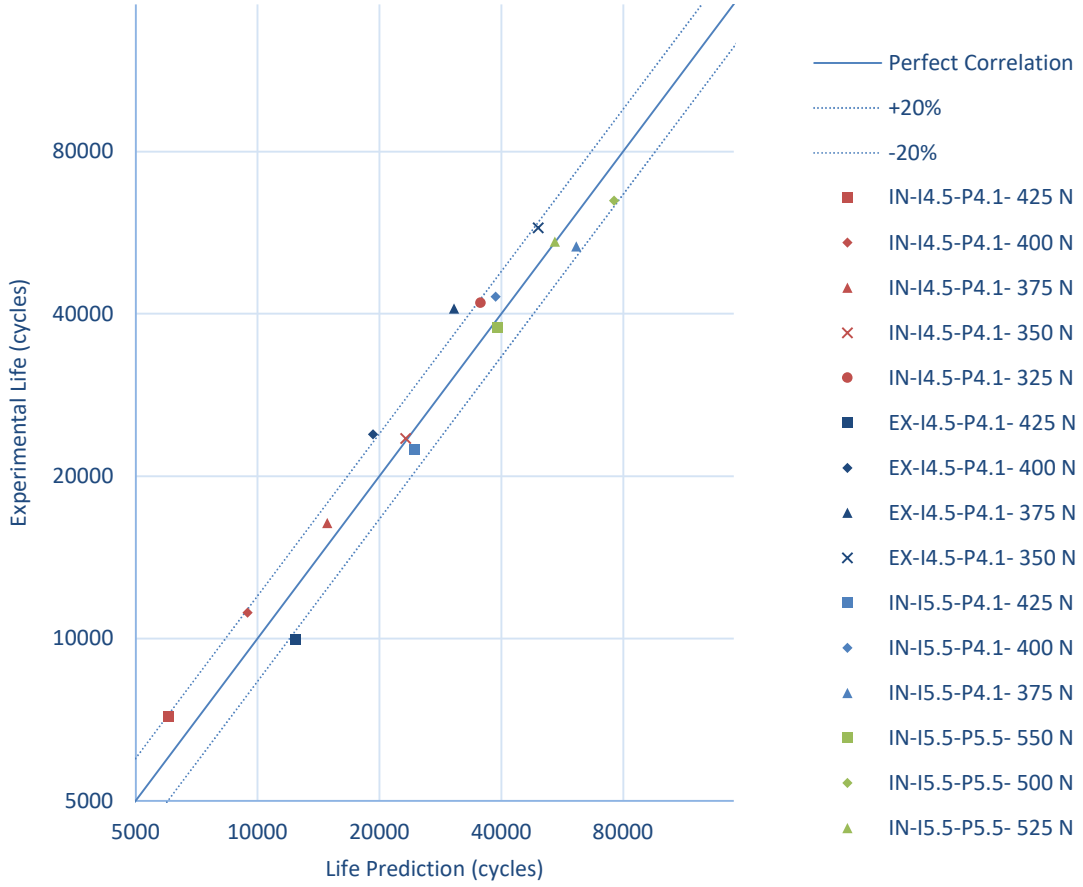

Figure 121. Experimental results versus life prediction with the new fitting parameters (average values).

3.2.2 Transepithelial-supported restorations

Finally, the fatigue prediction methodology is to be tested on transepithelial-supported restorations. As discussed in section 2.1.1, the transepithelial component is mounted between implant and abutment, and consists of two parts: a sleeve and a screw that attaches the sleeve to the implant. Although the screw is different, its metric is still M1.8, so it is assumed that the behavior can also be predicted using the methodology. The abutment is then mounted and attached to the assembly by means of a second, generally smaller, screw which is threaded over the first screw, which has a female thread at the head.

Three different transepithelial-supported restorations have been tested (Figure 122), all of them mounted on the IIPSCA4513 implant, previously used in the IN-I4.5-P4.1 restoration (section 3.1.1). In short, UNIT-H2 restoration mounts a 2mm high transepithelial component designed for single restorations; i.e., it has a tetralobular connection that does not allow rotation of the transepithelial component with respect to the implant. UNIT-H4 restoration is virtually equal to the previous one with the only difference being the height that is 4mm instead of 2mm. Finally, MULTI-IM-H2 restoration also applies a 2mm high transepithelial component as well as UNIT-H2, but, in this case, it has no tetralobular connection so that the rotation with respect to the implant is permitted. Finally, their corresponding abutments are added by means of a second screw. All components are included in Table 8.

Table 8. All the transepithelial-supported restorations under study, all of them mounting a different transepithelial component on the IIPSCA4513 dental implant.

Restoration	UNIT-H2	UNIT-H4	MULTI-IM-H2
Implant	IIPSCA4513	IIPSCA4513	IIPSCA4513
Transepithelial component	INTMIUPU20	INTMIUPU40	INTMIPU20
Transepithelial height(mm)	2	4	2
Screw Metric (trans)	M1.8	M1.8	M1.8
Torque (trans) (Ncm)	35	35	35
Abutment	CPMIUPU	CPMIUPU	CPMIPEU
Prosthetic screw	TTMIR	TTMIR	TTMIR
Screw Metric	M1.4	M1.4	M1.4
Torque (Ncm)	20	20	20

Figure 122. Transepithelial-supported restorations under study: UNIT-H2, UNIT-H4, and MULTI-IM-H2.

Figure 123 shows all the experimental fatigue tests performed on the restorations in Figure 122. Then, the methodology was used to predict the fatigue life at the same load range used in the experimental fatigue tests. The procedure explained in section 3.1.2 was followed with the only specificity being that two preloads had to be added instead of one. Hence, as explained in section 2.2, three load steps were used for the FEA of transepithelial-supported restorations. First, the preload of the lower prosthetic screw was applied (688N corresponding to 35Ncm in a 45-degree countersunk screw head, 344N for half model) according to equation (132). Then, the preload of the upper prosthetic screw was applied in a second load step (572N corresponding to 20Ncm for a flat head screw, 286N for a half model), according to equation (131). Finally, in a third load step, an increasing 30º load was applied from 0 to the maximum load tested experimentally. Figure 124 shows the FE models of the transepithelial-supported restorations analyzed. Further details of the FEA may be found in section 2.2.

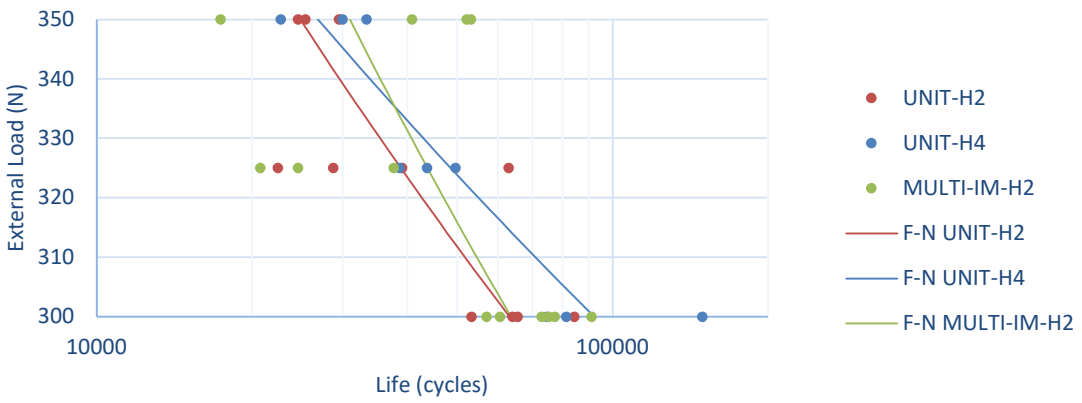

Figure 123. Experimental tests performed on the restorations in Figure 122.

Figure 125 shows the homolog of the chart in Figure 115 (experimental versus fatigue life estimation according to equation (136)) for transepithelial-supported restorations in Table 8. It can be seen that equation (136) (with its parameters) does not provide a good estimate compared to the case of implant-supported restorations in section 3.2.1. It is seen that the points fall above the 45º line, with the slope maintained but displaced upwards. In other words, equation (136) underestimates the fatigue life of all transepithelial-supported restorations studied in this PhD Thesis, thus resulting in a very conservative life prediction.

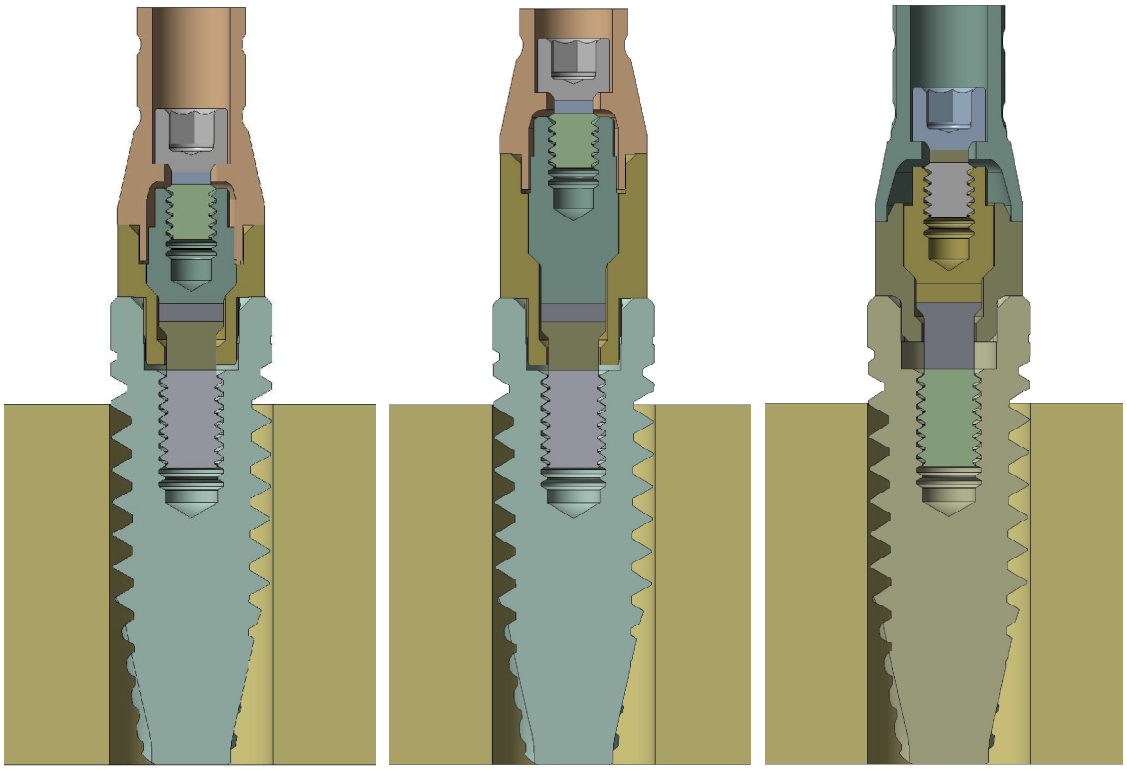

Figure 124. FE models of the transepithelial-supported restorations under study. A, UNIT-H2. B, UNIT-H4. C, MULTI-IM-H2.

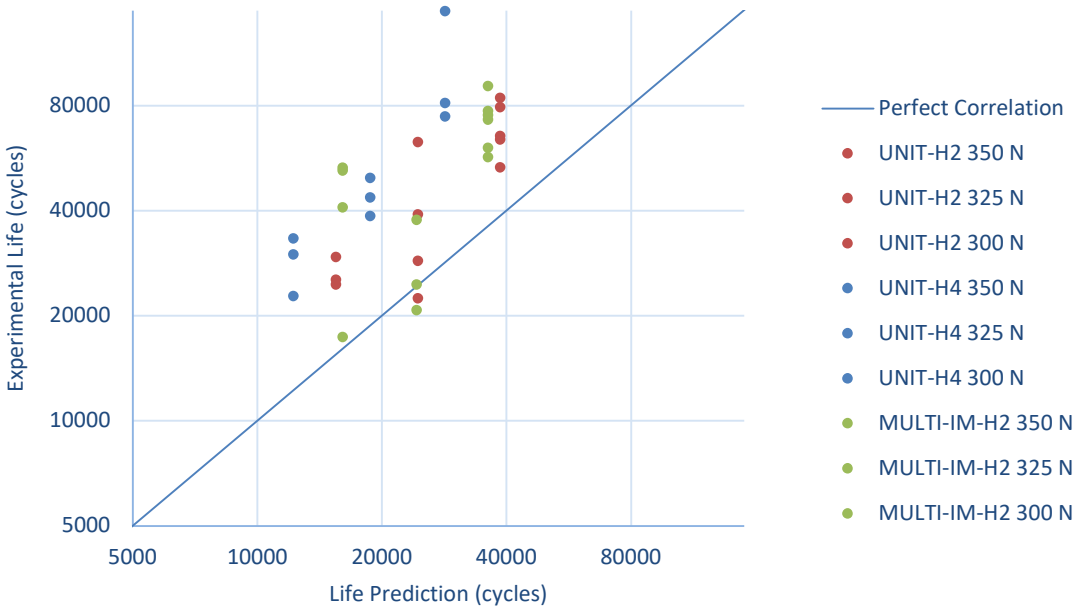

Figure 125. Experimental results versus life prediction for transepithelial-supported restorations (all tests).

Obviously, the first task performed after seeing that the prediction was not as accurate as in the case of implant-supported restoration was to look at the possible reasons for this. After discarding possible errors when simulating the FEA, the next step was to find out more about the manufacturing process. It was found that the screws used for transepithelial-supported restorations are manufactured in a different place than those used for implant-supported restorations whereby the machine used is different. Using different tools, machines, and machining conditions may affect the end product finish and dimensions. Regarding dimensions, the threads of both types of screws pass the same dimensional controls, complying with the tolerance restrictions imposed by the manufacturer, so this could not be related to this reason. However, surface roughness could be an uncontrolled variable. Hence, surface roughness has been measured at the valley of the first thread in contact on the screw, where the breakage of both bolts occurs.

Figure 126 shows the surface aspect of both screws (transepitelial-supported restoration in Figure 126A and implant-supported restoration in Figure 126B) obtained by SEM using a Thermo Scientific Phenom ProX located at BTI facilities. SEM shows that the finish of the screws used for transepithelial-supported restorations is smoother than the screws used for implant-supported restorations. The results were provided after Gaussian filtering (microroughness filter λ_s=20nm and waviness filter λ_c=20µm). Table 9

provides the results of surface roughness average R_a and mean roughness depth R_z for the different paths shown in Figure 126.

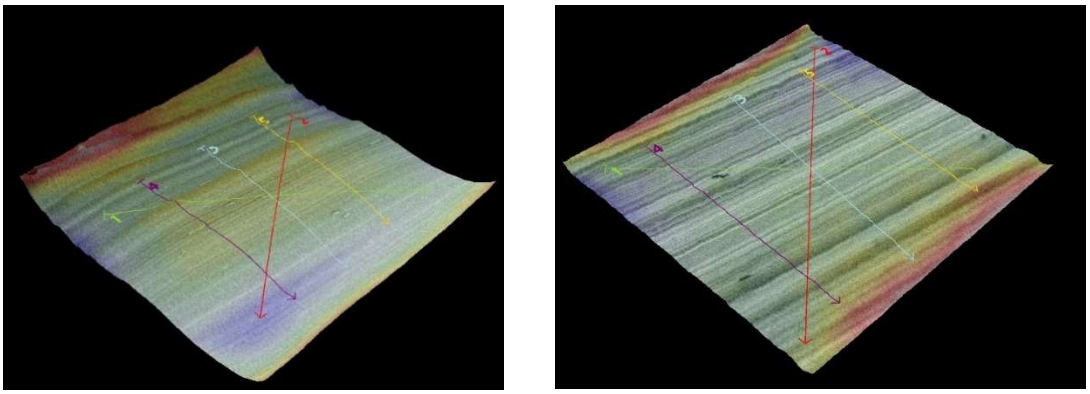

A) B)

Figure 126. Surfaces at the valley of the first engaged thread of the screw. A, Screw used in one of the transepithelial-supported restorations studied. B, Screw used in one of the implant-supported restorations studied.

Table 9. Surface roughness average R_a and mean roughness depth R_z in the different paths shown in Figure 126 of two screws used in: transepithelial-supported restoration and implant-supported restoration.

Screw type:	Transepithelial-supported		Implant-supported	
Path	Rz (nm)	Ra (nm)	Rz (nm)	Ra (nm)
1	571	137	1050	176
2	566	125	977	169
3	625	145	861	158
4	554	144	1020	195
5	651	142	807	161

It can be concluded that the screws used in transepithelial-supported restorations are smoother than the screws used in implant-supported restorations. As was explained in section 1.3.1.1, a smoother surface finish has a positive effect on fatigue behavior. Hence, a different fitting than the one used for equation (136) is necessary, to properly suit this enhanced fatigue behavior. Repeating the curve fitting procedure shown in 3.1.3, in this case using only the transepithelial-supported restorations studied in this section, equation (138) was obtained, providing a more accurate life estimate for all cases as can be seen in Figure 127, that shows the experimental life of each test versus its methodology prediction. Moreover, Figure 128 only shows the mean values and adds the ±20% bands.

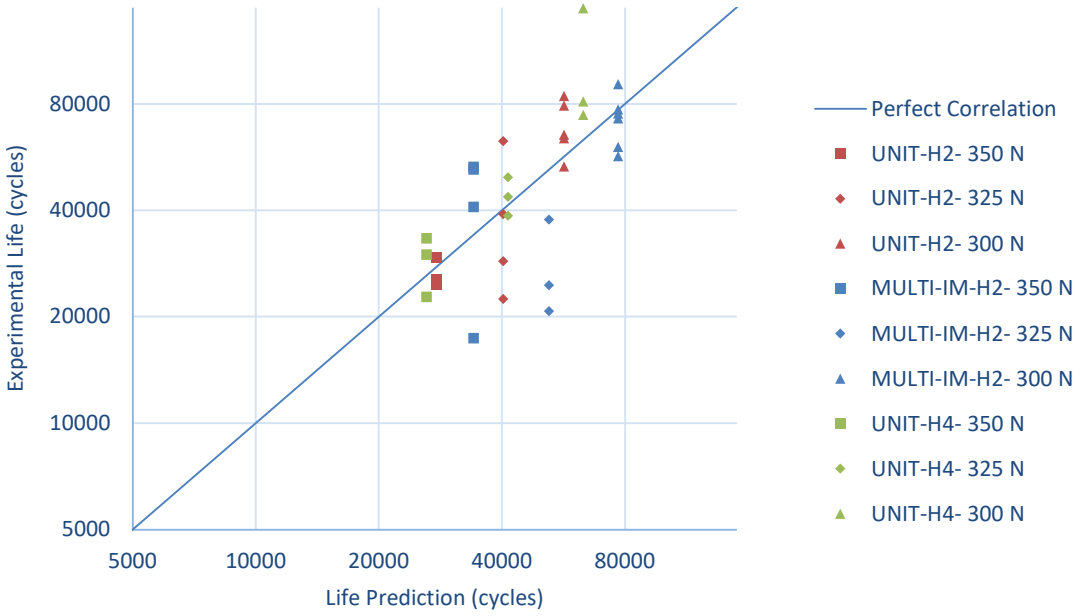

Figure 127. Experimental results versus theoretical life prediction for transepithelial-supported restorations with the new fitting parameters (all tests).

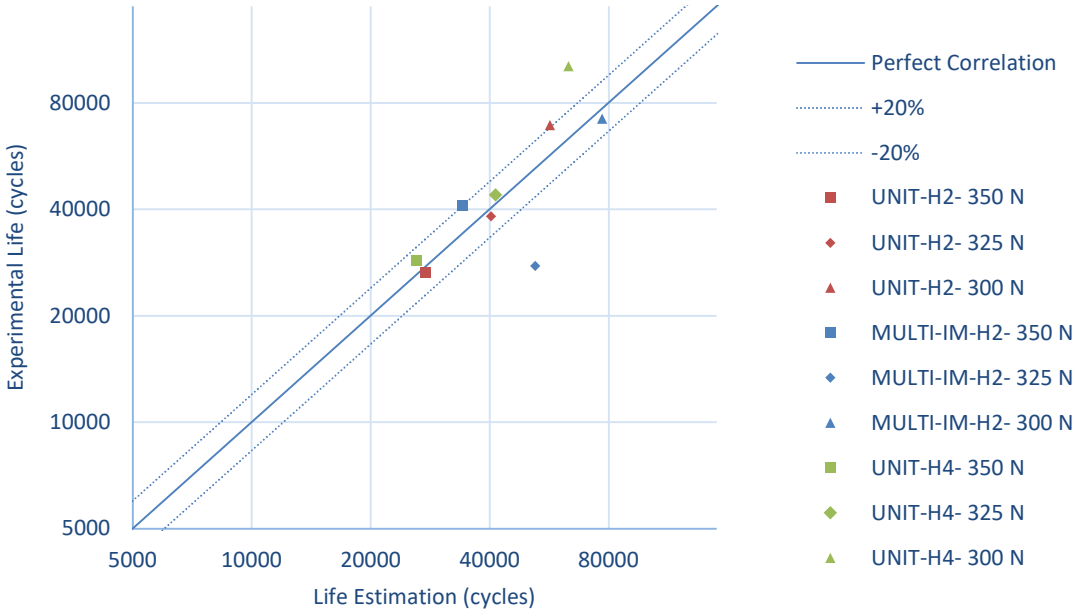

Figure 128. Experimental results versus theoretical life prediction for transepithelial-supported restorations with the new fitting parameters (using average life values).

Figure 129, Figure 130, and Figure 131 show the experimental fatigue data points (markers), F-N linear regression models (solid blue line), 95% confidence bands (dotted lines), 95% prediction intervals (dashed lines), and the F-N predictions using the methodology with the new fitting parameters shown in

equation (138) (solid red line) for UNIT-H2, UNIT-H4, and MULTI-IM-H2, respectively.

It must be mentioned that all the fatigue life predictions fall within the 95% prediction interval range and, therefore, the prediction can be assumed to be accurate. Nevertheless, greater dispersion was noticed among transepithelial-supported restorations as shown in Figure 127, so more restorations should be tested for more accurate results. This dispersion may be caused by the aforementioned use of two prosthetic screws, instead of one as is the case with implant-supported restorations. As mentioned in section 1.2.4, there is a dispersion in the preload obtained for all screwed joints. Hence, greater dispersion is expected when using two screwed joints on the assembly. Finally, despite this dispersion, the methodology is more accurate for transepithelial-supported restorations when equation (138) is applied.

$$N^b = \frac{\sigma_{alternating}^{\gamma}}{\sigma_0} \cdot \left(\sigma_{mean} + \sigma_{alternating}\right)^{1-\gamma}; where \begin{cases} \gamma = 0.05 \\ b = -0.13 \\ \sigma_0 = 2705 \\ MPa \end{cases} \quad (138)$$

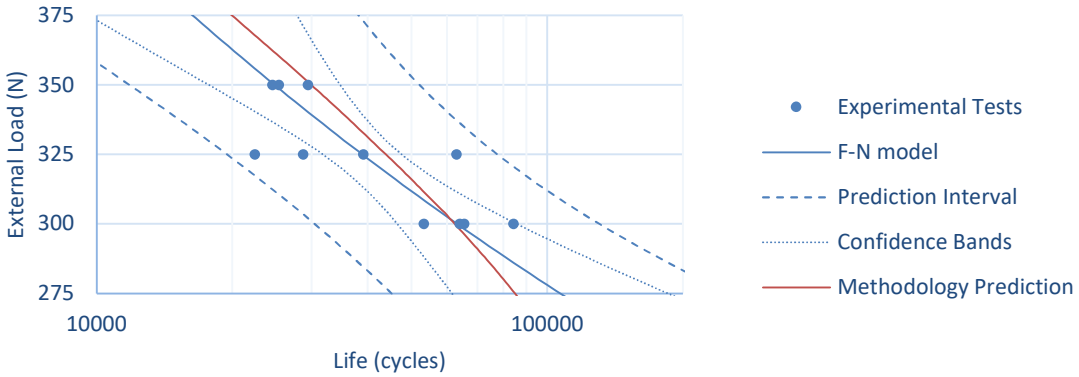

Figure 129. Experimental fatigue data points (markers), F-N linear regression (solid blue line), confidence bands (dotted lines), prediction intervals (dashed lines) and the F-N obtained using the prediction methodology with the new fitting parameters in equation (138) (solid red line) for UNIT-H2.

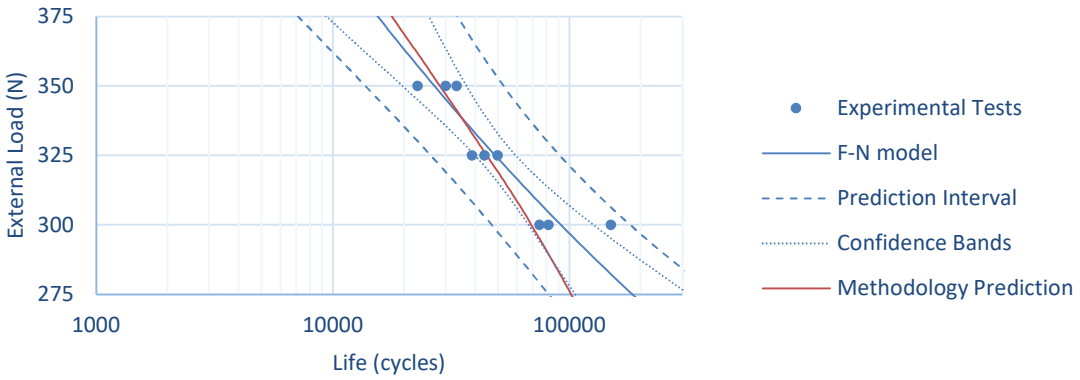

Figure 130. Experimental fatigue data points (markers), F-N linear regression (solid blue line), confidence bands (dotted lines), prediction intervals (dashed lines) and the F-N obtained using the prediction methodology with the new fitting parameters in equation(138) (solid red line) for UNIT H4.

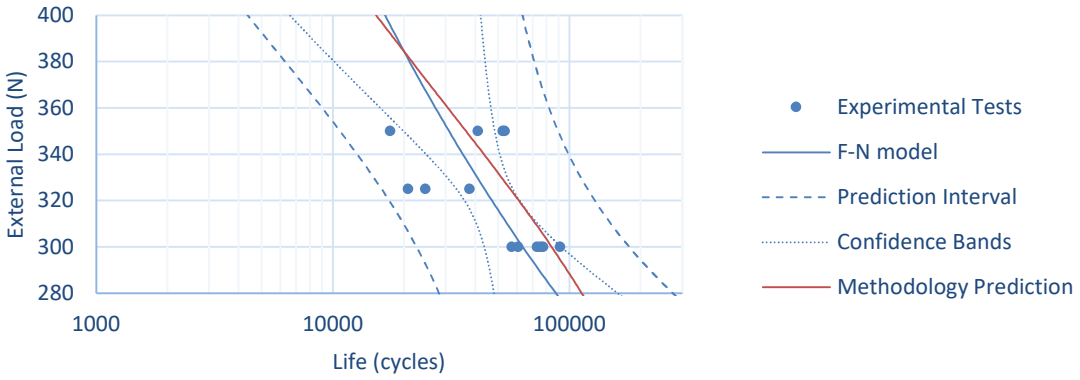

Figure 131. Experimental fatigue data points (markers), F-N linear regression (solid blue line), confidence bands (dotted lines), prediction intervals (dashed lines) and the F-N obtained using the prediction methodology with the new fitting parameters in equation (138) (solid red line) for MULTI-IM H2.

3.3 Conclusions

This chapter has presented a prediction methodology to estimate the fatigue life of dental restorations based on FEAs and classical formulae for fatigue and Theory of Elasticity. First, the process of developing the methodology and adjustment has been explained with experimental tests carried out on a single type of implant-supported restoration (with three different tightening torques). In addition to this, the steps to follow for the regular use of the methodology, which is much simpler than the developing the methodology and adjustment process, have been explained, as well as the uses it has been indicated for.

Once the methodology has been developed and explained, its validity has been tested first on implant-supported restorations, on which it has been shown to predict fatigue life accurately. In addition, it has been proven that the methodology is made more accurate by readjusting Walker expression of the methodology taking into account the new experimental tests of all the implant-supported restorations studied. In other words, it has been proven that the methodology becomes more accurate as it is fed with more experimental tests.

In addition to this, the methodology has been validated in transepithelial-supported restorations. Once it was found that these screws had different surface finishes than the previous ones, it was considered appropriate to use a readjusted methodology. The methodology then provided accurate results for the case of transepithelial-supported restorations.

Therefore, this methodology is capable of accurately estimating the fatigue life of all restorations in the BTI catalog in which the failing component is the prosthetic screw. As demonstrated throughout this chapter, the fatigue life of all implant-supported restorations may be accurately estimated by the methodology using a single expression (equation (136)). In the same way, fatigue life of all transepithelial-supported restorations may also be accurately estimated with another expression (equation (138)). In this way, the methodology covers practically the entire BTI catalog. If a different screw is to be analyzed (different material, size, manufacturing process, surface finish, thread profile...), the parameters will have to be readjusted by repeating the application procedure with new experimental tests.

As a result, using this methodology, the manufacturer can compare the fatigue behavior of all restorations quickly and cost-effectively, without the need for time-consuming fatigue testing campaigns. This allows the manufacturer to obtain an estimate of fatigue life not only for existing restoration designs, but also for new restoration designs even before a prototype is manufactured. Thus, this methodology is a powerful design tool that can be used to compare different dimensions, loading rates, torques, coefficients of friction, etc., in terms of fatigue behavior.

Finally, it must be pointed out that this methodology is only valid when the failing component is the prosthetic screw. A different approach is presented in Chapter 5 when the implant is the critical component.

3.4 Clinical implications derived from experimental fatigue tests

In this section the results obtained from all the experimental fatigue tests performed for both the application and the validation of the methodology presented were analyzed in order to obtain interesting conclusions for clinicians. First, the effect of prosthetic screw tightening torque on the fatigue behavior of an implant-supported restoration is evaluated. Secondly, the effect of various geometrical parameters of the implant on the fatigue behavior of the dental restoration is evaluated: implant body diameter, platform diameter and type of connection (internal versus external). Finally, the effect on fatigue behavior of using a transepithelial-supported restoration instead of the classical implant-supported restoration has been evaluated.

3.4.1 Effect of the tightening torque of the prosthetic screw

Taking advantage of the experimental tests on IN-I4.5-P4.1 at three different tightening torques (15, 25 and 35Ncm) performed to apply with the fatigue prediction methodology in section 3.1.1, the influence on fatigue behavior of the tightening torque applied to the prosthetic screw has been analyzed based on experimental results.

From the graph in Figure 99, it can be deduced that the optimum tightening torque is 35Ncm, which coincides with the tightening torque recommended by the manufacturer. The negative effect of an insufficient tightening torque on fatigue behavior can also be seen, as has already been demonstrated in other studies.[150–152] In the event of an insufficient torque, the mean stress component generated by the preload will be lower, but since structural integrity is not achieved, the alternating stress component (and also mean, although these have less of a fatigue effect) generated by the external load will be very large, causing premature failure. This is explained in detail in section 1.2.2.

3.4.2 Effect of different implant geometry parameters on fatigue behavior

As was performed in the previous section with the screw preload, the experimental fatigue tests performed in section 3.2.1 have been used to evaluate the effect of different geometrical implant parameters on the fatigue behavior of dental restorations. There are numerous studies that evaluate these parameters and their influence on the mechanical behavior on the implant itself.

However, as we have seen in section 1.6.1, most of these studies do not take account of the performance of restorations in which the critical component is the prosthetic screw. This is why it was considered necessary to make this comparison in order to complement the results of the aforementioned works.

The restorations will be compared in pairs, in order to perform the comparisons indicated in Figure 132. An Analysis of Covariance (ANCOVA) will be used to compare the F-N curves of each comparison in Figure 132. In short, ANCOVA sets an initial null hypothesis that assumes the same slope for both linear regression models and, if accepted, a second null hypothesis that assumes the same fatigue behavior (negligible statistical differences between 2 linear regressions). To this end, 95% linear regression confidence bands and 95% prediction intervals were added to the experimental points and linear models according to the ASTM E-739 standard.[64] Thus, Figure 133 compares IN-I4.5-P4.1 and IN-I5.5-P4.1 to study the effect of increasing the implant body diameter by 1mm, Figure 134 compares IN-I5.5-P4.1 and IN-I5.5-P5.5 to obtain the effect of increasing the implant platform diameter by 1.4mm, and, finally, in Figure 135, EX-I4.5-P4.1 and IN-I4.5-P4.1 F-N curves were plotted to evaluate the effect of the IAC type (external versus internal butt-joint). In all the cases, fatigue failure occurred in the first engaged thread of the prosthetic screw, as expected (see Figure 97B).[55,144,277]

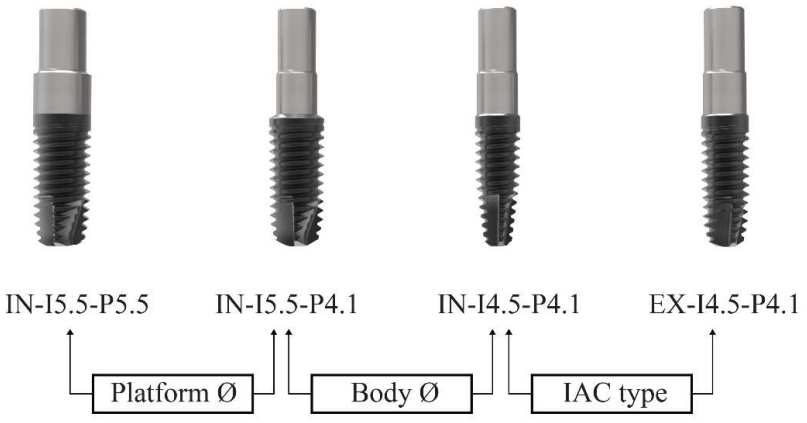

Figure 132. All implant-supported restorations coupled isolating one variable in each case.

Regarding Figure 133, ANCOVA was used to compare both linear models, accepting the first null hypothesis that the slopes were equal (P=.615) and rejecting the second null hypothesis (P<.001); that is, the mean fatigue life was statistically different. Furthermore, once the slopes of both models were determined to be equal, the fatigue life was calculated to be enhanced by 3.5

times when the implant diameter was increased from 4.5 to 5.5mm. This beneficial effect is consistent with Shemtov-Yona et al.[172] and Fan et al.,[173] who also reported improved fatigue response with larger implant diameters. This, together with the reduction of the surrounding bone stresses[165–168] and the enhancement of the initial stability,[169,170] determined that increasing the body diameter will improve the overall performance of the dental restoration. However, even though a large implant body diameter is recommended from a mechanical point of view, horizontal crestal bone atrophy and restricted edentulous area often limit the use of large diameters.[278] By contrast, narrower implants decrease the need for bone augmentations, reducing surgical invasiveness.[279]

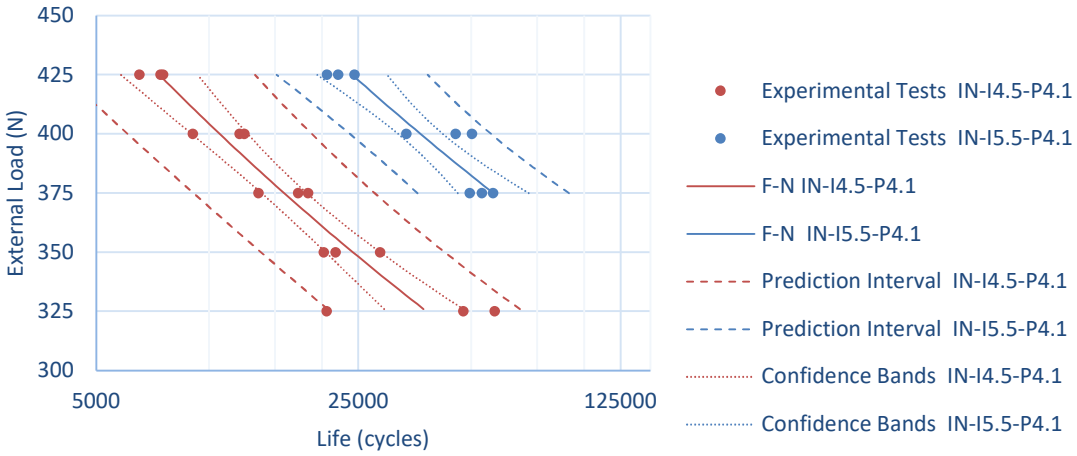

Figure 133. IN-I4.5-P4.1 versus IN-I5.5-P4.1: effect of increasing implant body diameter by 1mm.

IN-I5.5-P4.1 and IN-I5.5-P5.5 could not be tested in the same load range (Figure 134). Thus, the linear model of IN-I5.5-P4.1 was extrapolated to allow a comparison of both models. ANCOVA was used to compare the linear models, accepting the first null hypothesis that the slopes were equal (P=.541) and rejecting the second null hypothesis (P<.001). Moreover, the fatigue life was calculated to be 7 times larger when the platform diameter was increased from 4.1 to 5.5mm. This value resulted from a linear extrapolation and this factor may be even larger because of possible non-linear behavior of the material approaching the LCF domain. Hence, a major improvement in fatigue life was achieved when the platform diameter was increased. These results are consistent with Nicolas-Silvente et al.,[184] who reported lower stresses on the prosthetic screw with larger platform diameters.

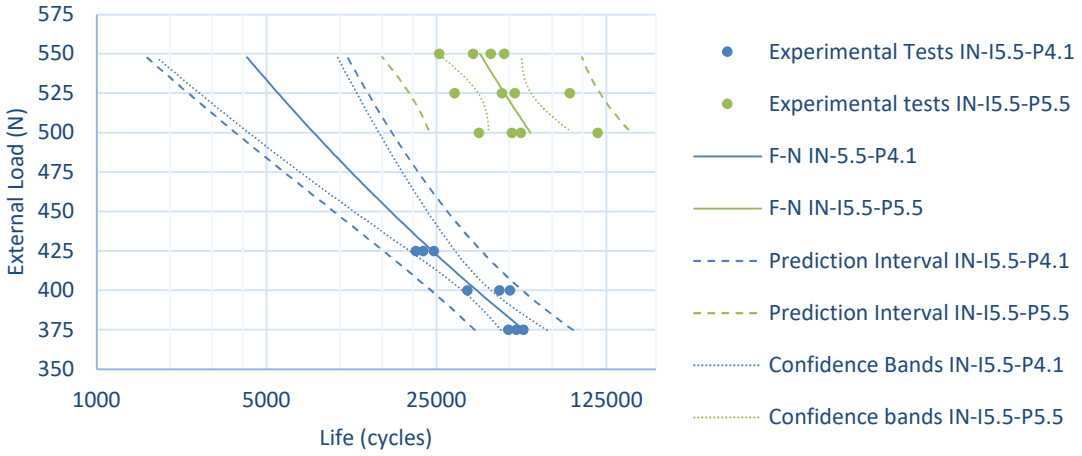

Figure 134. IN-I5.5-P4.1 versus IN-I5.5-P5.5: effect of increasing implant platform diameter by 1.4mm.

Finally, ANCOVA accepted the hypothesis that the slopes are equal (P=.120) for the models compared in Figure 135, and rejected the second null hypothesis (P<.001); where the mean fatigue life was statistically different. Moreover, the fatigue life was calculated to be 2 times larger when using an external butt-joint connection. Nevertheless, before assuming that external connections behave better than internal ones, it should be clarified that, unlike the other two comparisons made in this section (implant body diameter and implant platform diameter) that had only one different parameter, the implants used for internal versus external comparison had two different parameters. Besides the IAC type, EX-I4.5-P4.1 has a larger prosthetic screw (M2) than IN-I4.5-P4.1 (M1.8). It seems reasonable to think that, for the same screw metric the performance of both restorations may be similar or even better in the case of internal butt-joint connections, as suggested by other studies.[188–190] Nevertheless, the effect of the IAC type on the fatigue life of the prosthetic screw was significantly smaller than the other 2 parameters studied, and internal butt-joint connections have other advantages including improved esthetics, sealing capacity on the IAC, and platform switching options.[185,186]

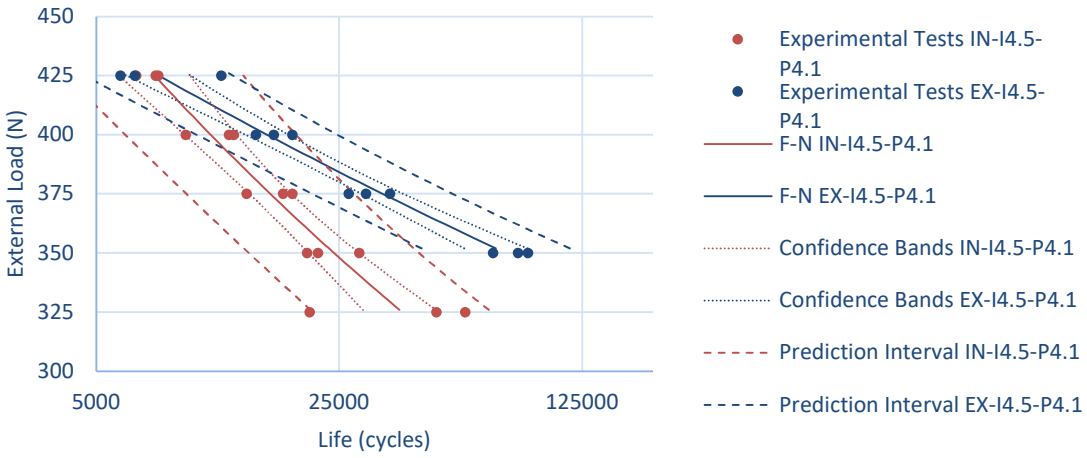

Figure 135. IN-I4.5-P4.1 versus EX-I4.5-P4.1: effect of using an external instead of an internal butt-joint connection.

3.4.3 Influence of the transepithelial component

In this case, the experimental tests carried out in section 3.2.2 have been used to evaluate the effect of using a transepithelial component on the fatigue behavior of dental restorations. The three transepitelial-supported restorations were compared to implant-supported restoration IN-I4.5-P4.1, and among them, since they all use the same implant. UNIT-H2 restoration mounts a 2mm high transepithelial component designed for single restorations; i.e. it has a tetralobular connection that does not allow any rotation of the transepithelial component with respect to the implant. UNIT-H4 restoration is virtually identical to the previous one with the only difference being the height, that is 4mm instead of 2mm. Finally, MULTI-IM-H2 restoration also mounts a 2mm high transepithelial component as well as UNIT-H2, but, in this case, it has no tetralobular connection so that rotation with respect to the implant is permitted. IN-I4.5-P4.1 components are detailed in Table 7, while the components of transepithelial-supported restorations are detailed in Table 8.

The restorations will be compared in pairs; an ANCOVA was performed to compare the pairs shown in Figure 136. Therefore, Figure 137 shows the effect of adding a transepithelial component between the implant and the abutment by comparing the F-N curves of IN-I4.5-P4.1 and UNIT-H2. Figure 138 shows the effect of using a rotational transepithelial instead of a non-rotational one by comparing the fatigue behavior of UNIT-H2 versus MULTI-IM-H2. Finally, Figure 139 shows the effect of transepithelial heigh on the fatigue behavior of the dental restoration by comparing the curves of UNIT-H2 and UNIT-H4.

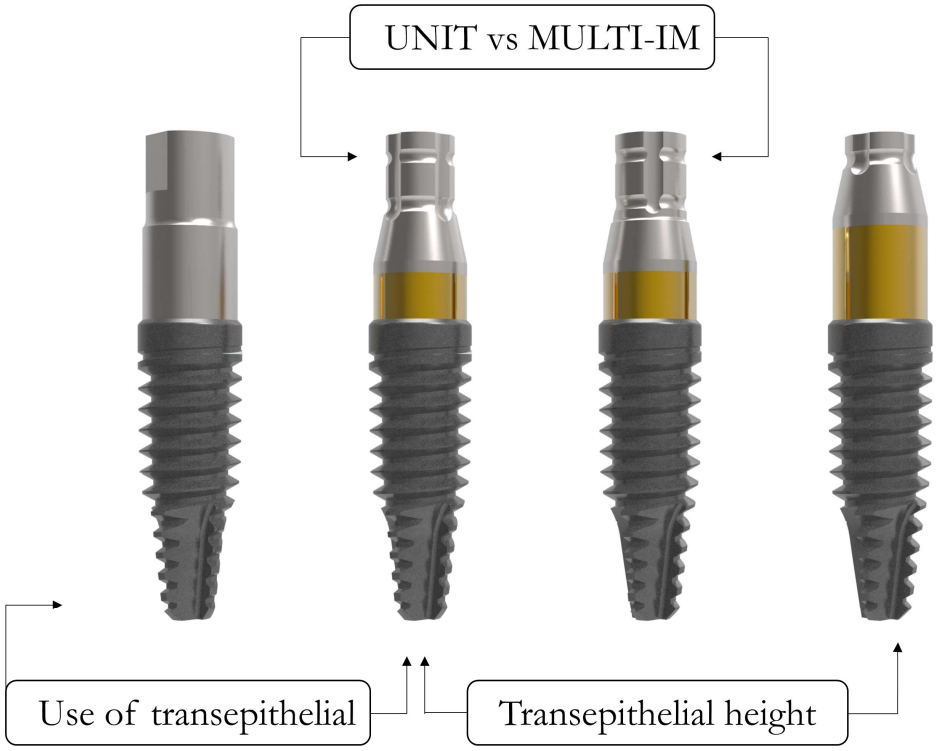

Figure 136. Transepithelial-supported restorations under study: UNIT-H2, UNIT-H4, and MULTI-IM-H2.

Figure 137 shows the F-N curves of IN-I4.5-P4.1 and UNIT-H2. It can be easily seen how the fatigue behavior of both restorations is almost identical since the regression models overlap. Whatever the case, an ANCOVA was used to compare the linear models, accepting both the first (P=.865) and second (P=.964) null hypotheses. That is, the regression models can be assumed to be statistically identical. It is worth mentioning that the 95% confidence bands are slightly wider, indicating that there is more dispersion in the UNIT-H2 tests. As discussed above, introducing a second screw causes a larger scatter in terms of fatigue behavior.

Although the UNIT-H2 and MULTI-IM-H2 regression models in Figure 138 do not overlap as in the previous case, their confidence bands and 95% prediction intervals do. An ANCOVA was used to compare the linear models, accepting both the first (P=.507) and second (P=.566) null hypotheses and proving that there are no statistical differences between both regression models.

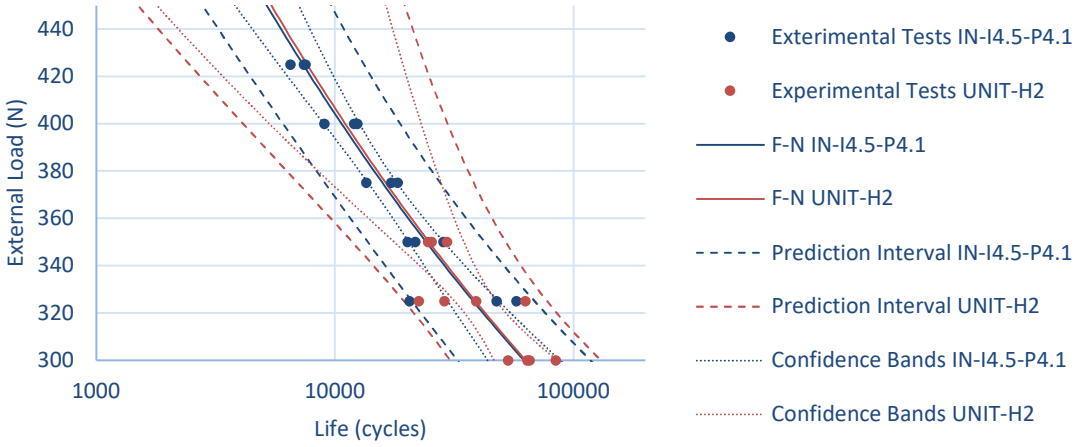

Figure 137. IN-I4.5-P4.1 versus UNIT-H2: effect of using a transepithelial-supported restoration instead of an implant-supported restoration.

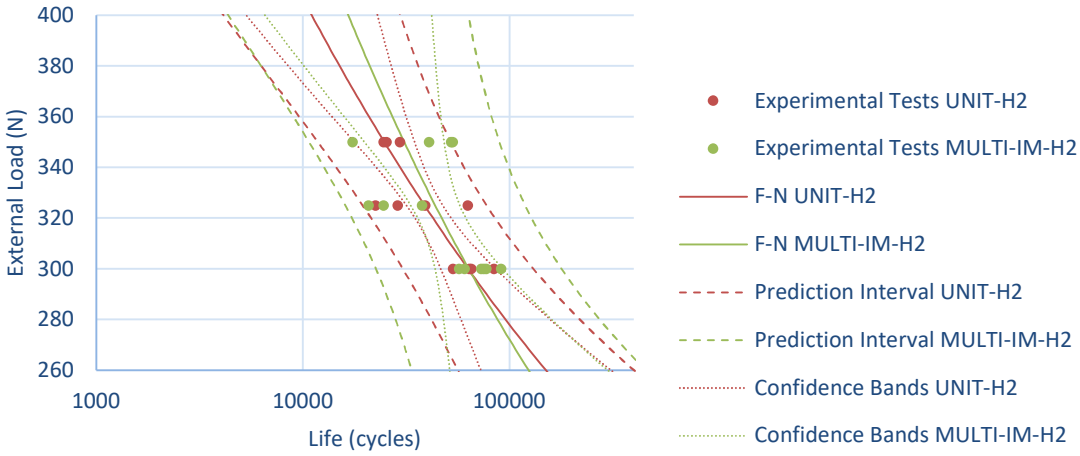

Figure 138. UNIT-H2 versus MULTI-IM-H2: effect of using a non-rotational or rotational connection on fatigue behavior of transepithelial-supported dental restorations.

The same occurs in Figure 139 with UNIT-H2 and UNIT-H4 dental restorations. That is, even though the linear regression models do not overlap, their confidence bands and prediction intervals do. Nevertheless, in this case the ANCOVA does not show that the curves can be assumed to be parallel as clearly as in the two previous cases as it is difficult to accept the first null hypothesis (P=.077). Hence, the comparison here cannot be performed by means of an ANCOVA. In any case, it can be deduced that the behavior is very similar based on the overlapping of the confidence bands and the 95% prediction interval.

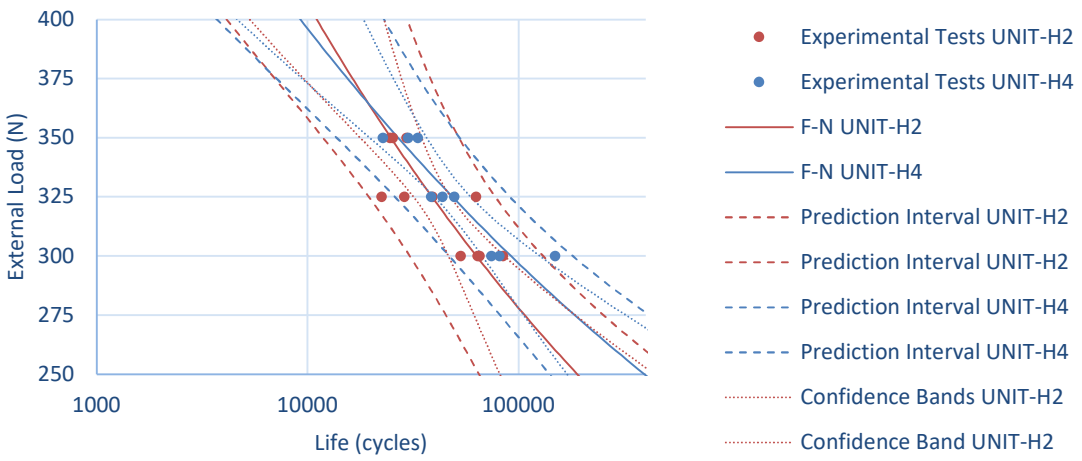

Figure 139. UNIT-H2 versus UNIT-H4: effect of transepithelial heigh on fatigue behavior of dental restorations.

For all these reasons, it can be concluded that an implant such as the IIPSCA4513 has similar fatigue behavior whether mounting an abutment directly onto the implant (IN-I4.5-P4.1) or mounting a transepithelial component between the implant and abutment (UNIT-H2). Likewise, it can be concluded that there is no significant difference in terms of fatigue behavior between using a non-rotating transepithelial (UNIT-H2) and a rotating one (MULTI-IM-H2). Finally, it was found that the transepithelial height does not significantly affect the fatigue behavior of the restoration (UNIT-H2 versus UNIT-H4). An increase in dispersion was also noticed in the tests performed on all transepithelial-supported restorations. It can be assumed that the addition of the second screw could be the reason. Nevertheless, further research may be performed to confirm this assumption.

These conclusions are the first basis for the study of transepithelial-supported restorations since published information is very scarce. Further studies are needed to confirm that these findings are applicable to more dental restoration designs.

4 Fatigue behavior of the prosthetic screw: improvement of the manufacturing process

In Chapter 3 the fatigue behavior of the prosthetic screw was studied by presenting a fatigue life prediction methodology for dental restorations in which the critical component is the prosthetic screw. In addition to this, analysis has been performed on how factors such as screw preload, different geometric parameters, or the inclusion of a transepithelial between implant and abutment affect the fatigue life of the dental restoration. As a way of complementing the design study on the prosthetic screw in this chapter, certain improvements in its manufacturing process are studied in order to further improve its fatigue behavior. On the one hand, in section 4.1, the screw head socket, where the torque tip is inserted to tighten the screw, is proposed to be manufactured by milling instead of broaching. On the other hand, in section 4.2, the screw threads are proposed to be manufactured by rolling instead of cutting. Finally, the conclusions of this manufacturing upgrades are discussed in section 4.3.

4.1 Screw head socket

As already mentioned in section 3.1.1, although the INTTUH screw used in IN-I4.5-P4.1, IN-I5.5-P4.1, and IN-I5.5-P5.5 restorations generally failed under fatigue in the first engaged thread (and, therefore, the fatigue life prediction methodology developed in Chapter 3 focuses on that section), failure sometimes occurred in the head section (see Figure 97A). Observing the stress status of the screw in FEA, it was found that in the failure section of the screw head the stress status was much less critical than in the first engaged thread, and, therefore, the failure in the head was not justified. Consequently, this

failure was assumed to be due to the effect of the broaching used in the manufacturing process of the screw head socket where the tip of the torque wrench is inserted, since this is an aggressive process for the part. Although measurements could not be performed due to the difficulty of accessing that point of the screw (at the bottom of the head socket), a simple inspection using an optical microscope confirmed that the surface finish left by the broaching is very improvable, and residual stresses are also likely to be high. This would justify worse fatigue behavior of this section compared to the section of the first engaged thread despite having lower stresses. To avoid this fatigue failure of the screw head, and thereby improve the performance of the dental restoration, the proposal was made to machine the prosthetic screw head socket by milling it instead of broaching. First of all, it was considered that, by milling, the hexagonal geometry of the socket should be different since milling requires larger fillet radii. Figure 140 shows the original shape (A) and the proposed one (B), compatible with the milling process.

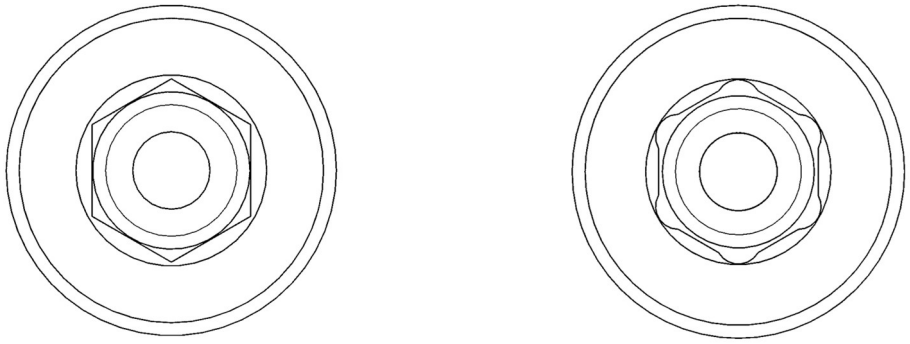

Figure 140. Screw head socket. A, Shape obtained by broaching. B, Shape obtained by milling.

To test the validity of the design, cylinders as shown in Figure 141 were machined with both socket designs and maximum torque tests were performed. Table 10 shows that both designs are equally valid since in both cases the critical component is the torque tip, which fails at the same maximum torque.

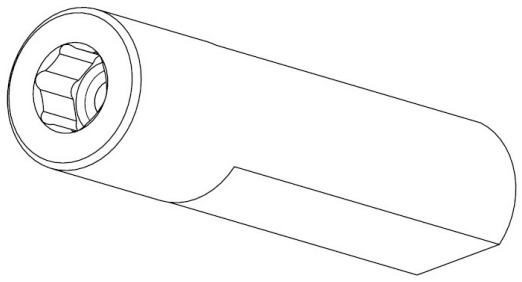

Figure 141. Cylinders with the socket compatible with milling process used in maximum torque tests.

Table 10. Maximum torque test results for both socket designs: original design (can only be produced by broaching) and new design (compatible with milling).

	Test 1	Test 2	Test 3	Average	Failure
Original design	62	62	64	62.7	Screwdriver tip
New design	62	64	62	62.7	Screwdriver tip

The next step was to transfer this design to the screws. Hence, the same screw was now designed and manufactured with the proposed socket design (see Figure 142), and, after applying the same treatments and coatings as the stock prosthetic screw (end product), some fatigue tests were performed on the already extensively-studied IN-I4.5-P4.1 dental restoration.

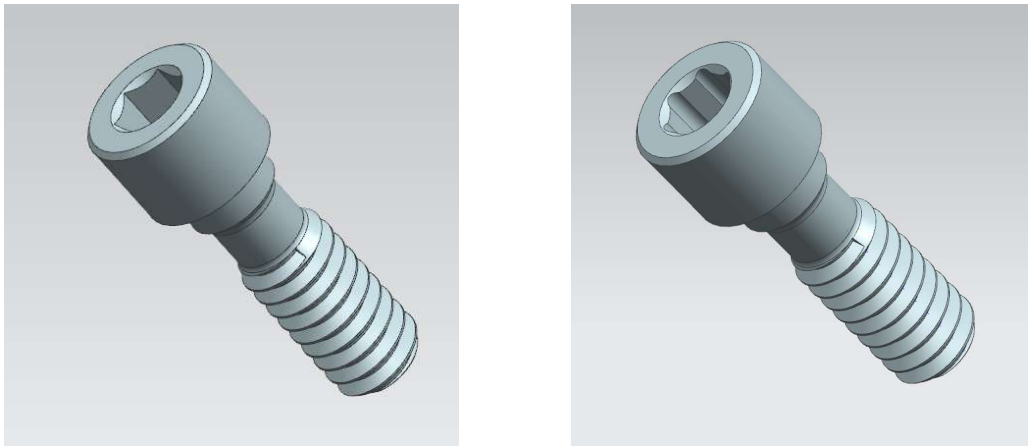

A) B)

Figure 142. A, Original prosthetic screw (INTTUH). B, Proposed screw design with a milling compatible head socket.

A few fatigue tests were necessary to prove that the breakage always occurred on the first thread in contact in the new design (see Figure 143), rather than the screw head as shown in Figure 97A. In this way, it was possible to optimize the design of the prosthetic screw by eliminating the possibility of the screw head being a potential fatigue failure section. Consequently, fatigue failure of the prosthetic screw will always occur on the first engaged thread when tested according to ISO 14801,[141] as seen in Chapter 3.

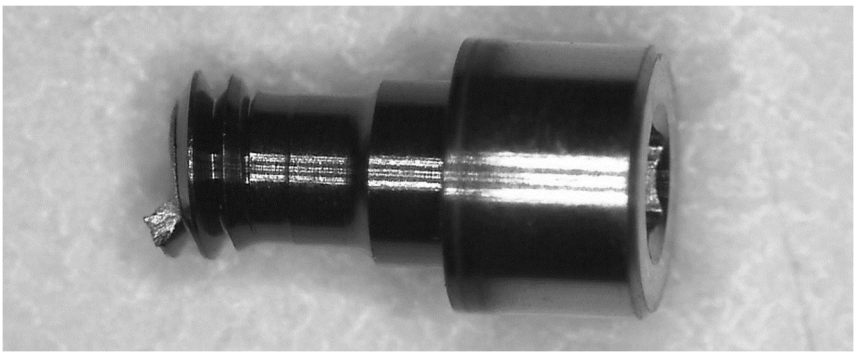

Figure 143. Fatigue failure of the new design of the screw at the first engaged thread.

4.2 Screw thread: rolling versus cutting

Having solved the problem of head failure of the prosthetic screw by modifying the manufacturing process of the screw head socket, thus ensuring that, under the load conditions studied, the failure will always occur on the first thread section, focus was put on the screw thread manufacturing process.

Two processes are widely used for screw thread manufacturing in industry: cutting and cold rolling. In the thread cutting process, material is removed from a cylindrical blank by machining, whereas, in thread rolling, a matching set of dies displaces the material to produce external threads on the cylindrical blank in a cold forming operation with no material losses.[280]

Thread rolling offers many benefits in terms of manufacturing and mechanical performance. The rolling process is less time consuming because the thread may be obtained in a single pass[281,282] with no need for secondary operations,[283] which significantly increases productivity[284] and reduces unit product cost.[281] Regarding mechanical performance, the thread rolling process introduces compressive residual stresses[285] on the thread surface, increasing hardness from strain hardening.[286] Furthermore, since no material is removed, good grain flow is obtained,[147,281] improving surface quality.[282,287] Consequently, rolled threads have been shown to provide better fatigue results than cut threads.[288–290]

Returning to the field of dental implantology, there are studies analyzing different surface treatments or coatings on the threads of prosthetic screws (see section 1.6.1) but, surprisingly, no information has been found regarding the thread rolling process. Even with the wide acceptance of thread rolling in the industry,[281,284,288] as far as the author has been able to find out, most manufacturers produce the prosthetic screw by means of thread cutting.

The purpose of this section is to transfer the proven better fatigue behavior of thread rolling versus cutting in the industry for dental implantology. Then, both fabrication techniques are compared in the extensively-studied INTTUH prosthetic screw in terms of thread profile, residual stresses, surface finish, and finally regarding the fatigue and static behavior.

4.2.1 Sample preparation

In order to analyze the difference between thread rolling and cutting in relation with the performance of the prosthetic screw when assembled on a dental restoration, two batches of the well-known INTTUH prosthetic screw were

manufactured: one with cut threads and the other with rolled threads. Most machining operations were the same for both batches, except for the diameter of blank material before threading, the turning speed, the feed rate, and the number of passes during the thread manufacturing process. For the cut threads, a Ø1.8-mm blank was used, and 20 passes were made at 5000rpm with a 1750 mm/min feed rate. For the rolled threads, a Ø1.5-mm blank was used, and the final profile was obtained by means of 1 pass at 200rpm with a 70mm/min feed rate. In both operations, the same commercially available lubricant was used (Blasomill 10; Blaser Swisslube).

4.2.2 Thread profile, surface roughness, and residual compressive stresses

Cutting and rolling operations may cause slight dimensional differences in the thread profile. Therefore, a multi-sensor measuring machine (Zeiss O-Inspect 322) was used to examine both thread profiles and to measure the thread parameters for one specimen of each batch. Figure 144 shows the profiles of the cut and rolled thread and Table 11 shows the dimensions obtained from both manufacturing processes: the external diameter $\emptyset_{ext}$, the internal diameter $\emptyset_{int}$, the thread pitch p, and the angle of the thread profile α. Unlike cut threads, where thread crests were parallel to the longitudinal axis of the screw, rolled thread crests showed a different shape. Thus, 2 values of the external diameter were measured in this case: maximum and minimum. The equivalent stress area A, which is the effective resistance area for threaded sections, was calculated as explained in section 3.1.2. Cut threads showed an equivalent tensile stress area of 1.37mm^2, while rolled threads showed 1.50mm^2.

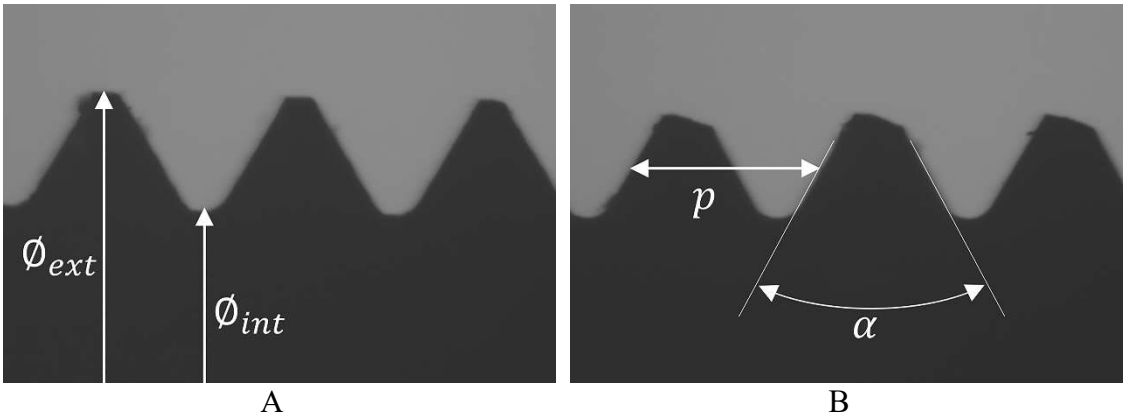

Figure 144. Thread profile. A, Cut thread. B, Rolled thread.

Table 11. Dimensions of thread profile.

	$\emptyset_{ext}$ (mm)	$\emptyset_{int}$ (mm)	Pitch (mm)	α (degrees)
Cut thread	1.74	1.24	0.35	60.5
Rolled thread	1.69/1.60	1.30	0.35	58.8

Moreover, differences between the surface finishes left by each manufacturing process were expected. As shown in section 1.3.1.1, a slightly different surface roughness may alter the fatigue behavior of the screw. To control this, the surface roughness of one specimen of each batch was measured by using SEM (Thermo Scientific Phenom ProX). Surface analyses were performed for a field of view of 53.7µm, and the results were provided after Gaussian filtering (micro-roughness filter λ_s=20nm and waviness filter λ_c=20µm). Figure 145 shows the surface roughness obtained from both manufacturing processes. The cutting process removed material, leaving transverse lines from the irregular shape of the turning insert caused by wear and the several passes used in this manufacturing process. In contrast, material flow was seen with the rolling process, indicating that material was formed rather than removed. Table 12 gives the results of the surface roughness measurements: area roughness average S_a was obtained for the whole field of view, while roughness average R_a and mean roughness depth R_z of a path perpendicular to the cutting or rolling direction were calculated.

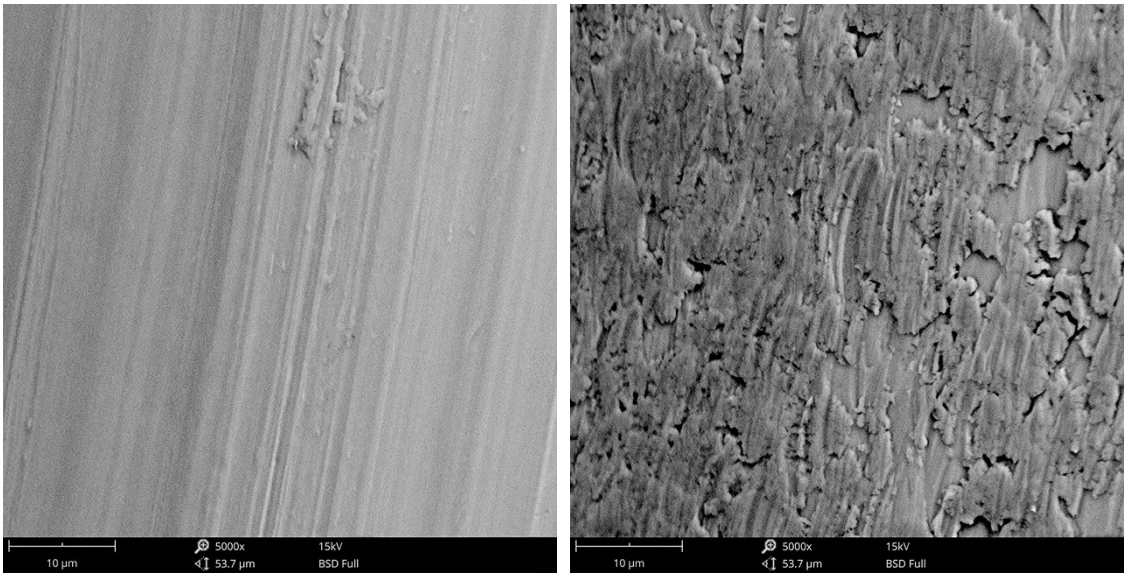

A B

Figure 145. Surface roughness measurements. A, Cut thread. B, Rolled thread.

Table 12. Surface roughness parameters.

	S_a (nm)	R_a (nm)	R_z (µm)
Cut thread	430	446	1.95
Rolled thread	333	434	1.83

Thread rolling is assumed to apply higher residual stresses on thread surface. Hence, the residual compressive stresses on the screw thread surface were measured on 3 specimens for each manufacturing technique (thread rolling and cutting) by using a diffractometer (Bruker D8 Discover; Bruker) equipped with a Chromium Point or Line Focus X-ray tube, V filter (λ=2.2911 Å), PolyCapTM (1-µm single crystal cylinders) system for parallel beam generation (divergence of 0.25 degrees), and a 1-D detector (LynxEye; Bruker) with active length on 2θ 2.7 degrees. The twist X-ray tubes allowed for the quick selection change between point and line focus.[291–293] The prosthetic screws were mounted on a Eulerian Cradle with an automatically controlled X-Y-Z stage. Data was collected from 59 to 64.2 degrees 2θ (step size=0.05 and time per step=7.5 seconds). Strain values in the side inclination mode were recorded for different specimen tilt angles (0, 18.4, 26.6, 33.2, 39.2, 45.0, 50.8, and 56.8 degrees) at constant azimuth angles phi. Strain - Sin2 ψ was plotted to estimate the stress values. In order to obtain a complete evaluation, at least 6 measurements were needed on Strain- Sin2 ψ plot by using 3 different values of phi, and 0, 45, and 90 degrees were chosen in negative and positive values. Stress was evaluated from strain values by using the Young modulus E (111 982 MPa) and Poisson ratio ν (0.330) and by taking into consideration the elastic constants s1 (-2.947×10-6) and ½ s2 (1.188×10-5) of the material. A single peak (101), available at 61.4 value of 2θ, was used for the analysis. The obtained results were adjusted by using software (Leptos 7.03; Bruker AXS GmbH). The data was corrected for absorption, background (5 points at edges), polarization, smoothness, and K alpha2 subtraction, and the peak evaluation was applied with the Pearson VII function. The determined values were obtained by using a biaxial mode with the Psi splitting function because of the shear stress components. Figure 146 shows the experimental set up of the diffractometer.

Table 13 shows the compressive residual stresses in the longitudinal direction of the screw. The specimen geometry (screw thread) and the material absorption generated high standard errors in the measurements, as a consequence of a high dispersion of the measured data. Nevertheless, the measurements confirmed, at least qualitatively, that thread rolling resulted in considerably higher compressive residual stresses than thread cutting.

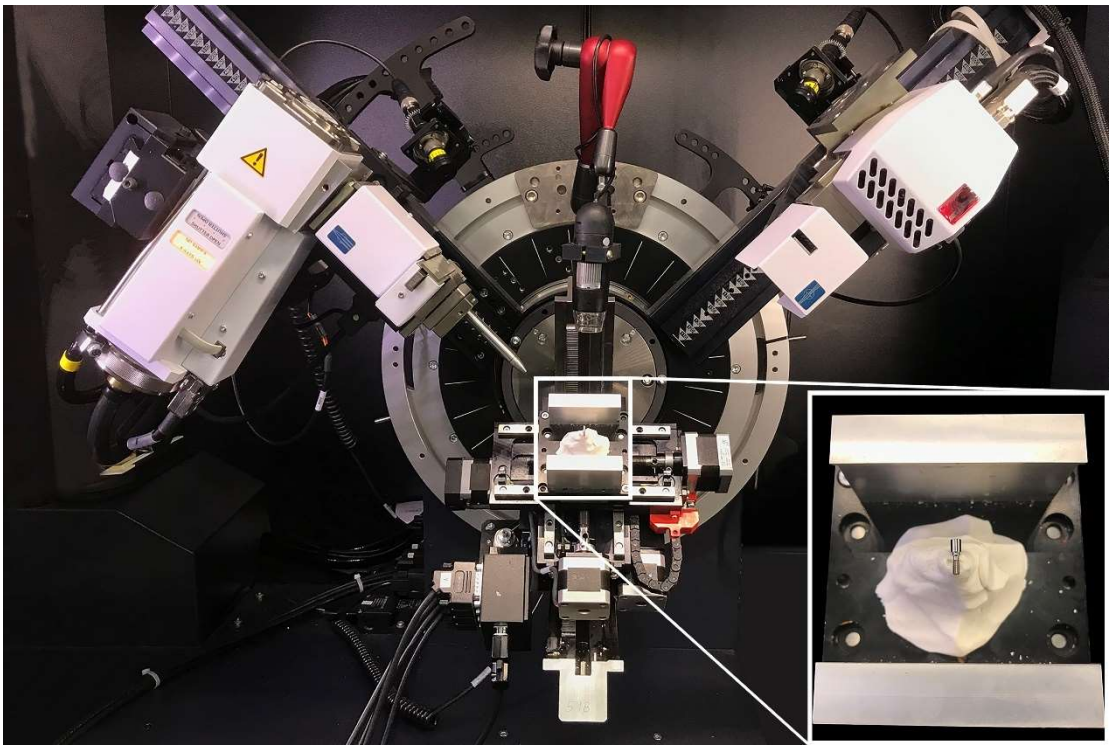

Figure 146. Diffractometer: general view and detail of the specimen.

Table 13. Mean values and standard errors of compressive residual stresses in threaded area.

Residual stresses (MPa)		
N=48 (per test)	**Cut Thread**	**Rolled Thread**
Test 1	281.5 ±136.1	569.5 ±87.7
Test 2	264.9 ±119.3	480.0 ±103.6
Test 3	297.0 ±124.8	496.0 ±87.2

Note that for the measurements of the thread profile, surface roughness, and compressive residual stress, the coating normally applied in the INTTUH prosthetic screw was not added. Concerning the thread profile measurement, because the objective is to measure the dimensions of the resistant part, without including the possible scatter of the coating treatment, although it is presumed to be small. Regarding the surface roughness measurement, because it is obvious that the coating would alter the results of the surface roughness of the part. Finally, with regard to the compressive residual stress measurements, the coating would completely distort the values obtained by the diffractometer.

To sum up, rolled threads showed a moderately higher equivalent stress area, slightly lower surface roughness values, and considerably higher compressive residual stresses than cut threads.

4.2.3 Mechanical behavior

Finally, the effects, in terms of mechanical behavior, of mounting a roll threaded prosthetic screw instead of a cut threaded one on an implant-supported restoration was also characterized. The INTTUH prosthetic screw was coated with WCC (as in the end product), mounted on the IN-I4.5-P4.1 restoration (IIPSCA4513 with INPPTU44), and tightened at 35 Ncm. As mentioned in section 2.1, the prosthetic screw was made of Ti 6Al 4V ELI (GR5 Titanium), while the implant and the abutment were made of CP4 Titanium. The chemical composition is provided in Table 4. The dental implant assembly (Figure 96) was tested under static and cyclic loading conditions to evaluate its mechanical strength by means of the previously-described direct stress fatigue test bench E 3000 Electropuls (see section 2.4.1), following the requirements of the ISO 14801 standard[141] (see section 1.6.1).

The experimental fatigue tests performed on the IN-I4.5-P4.1 in section 3.1.1 were used to determine the fatigue behavior of the cut threaded INTTUH prosthetic screw (3 specimens per load level at 3 load levels, making a total of 9 tests). In this section, 15 tests at the same 3 load levels (5 specimens per load level) were performed on the same IN-I4.5-P4.1 but mounting the roll threaded prosthetic screw. Moreover, the fatigue tests performed on IN-I4.5-P4.1 with cut threaded screws performed in section 3.2.1, were also added to the comparison, even though these tests were performed in a posterior test campaign, making a total of 15 tests at 5 different load levels for cut threaded screws. Figure 147 shows the experimental results along with the linear models log(F)-log(cycles) and 95% confidence bands according to the ASTM E-739 standard.[64]

Figure 148A shows the failure section of the screws manufactured by means of thread cutting. The rolled screws, after eliminating the failures mentioned in section 4.1, should also break at the first thread in contact. Nevertheless, as can be seen in Figure 148B, the failure occurs under the screw head, initiating at the fillet and propagating perpendicular to the screw axis. It is therefore deduced that the improvement brought about by the rolling process on the threads is such that the critical section moves from the first thread in contact to the next weaker zone. This new failure section is not to be confused with the one shown in Figure 97A where the failure section is not perpendicular to the axis, because that was affected by the manufacturing process of the head shank mentioned in section 4.1. The failure section in Figure 148B is perpendicular to the screw axis, as may be expected once the head shank is not critical anymore.

ANCOVA was used to compare both linear models, accepting the first null hypothesis that the slopes were equal (P=1) and rejecting the second null hypothesis (P<.001); i.e. the mean fatigue life was statistically different. Furthermore, once the slopes of both models were determined to be the same, the fatigue life was calculated to be 9 times larger for roll threaded screws.

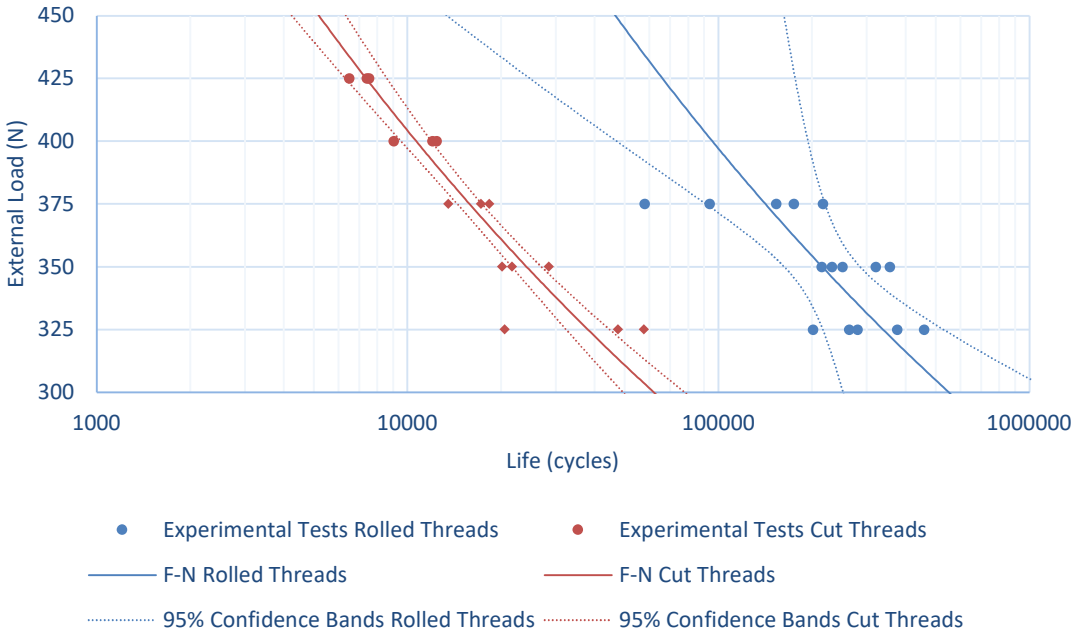

Figure 147. Fatigue data, linear models (F-N curves), and 95% confidence bands for IN-I-4.5P-4.1 dental implants assemblies mounting cut- and roll-threaded screws. In the case of cut-threaded screws, data with rhombus markers were obtained in section 3.1.1 while those marked with points were obtained in section 3.2.1.

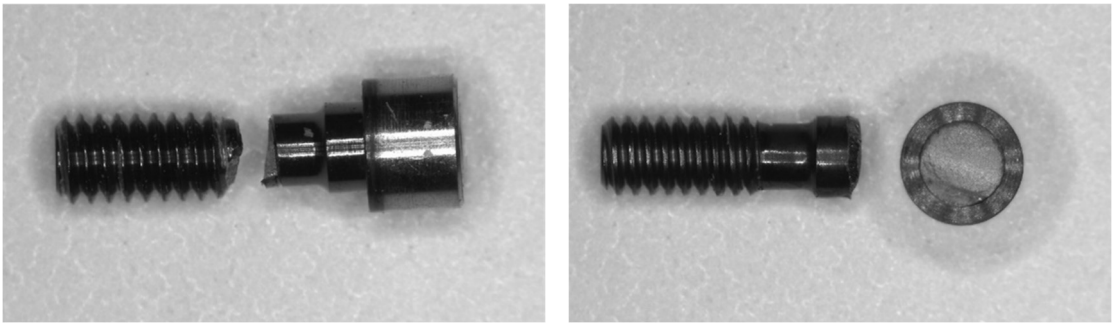

A) B)

Figure 148. Fatigue failure of the prosthetic screw. A, First engaged thread in cut-threaded screw. B, Head-shank transition in roll-threaded screw.

Regarding the static tests, the same set up was used as for fatigue tests. The load was quasi-statically increased until collapsing occurred, and the maximum load was reported as a result. Five specimens were tested for both cut and rolled threads, with the results provided in Table 14. In this case, the failure on both cut and rolled threads occurred in the first engaged thread (Figure 148B). T test

was carried out for the static loads recorded in Table 14. The null hypothesis was accepted (P=.54); i.e. the static load was assumed to be statistically the same for both manufacturing processes.

Table 14. Maximum loads measured in static tests.

Maximum static loads (N)		
	Cut Thread	**Rolled Thread**
Test 1	676	602
Test 2	622	656
Test 3	568	705
Test 4	600	593
Test 5	689	704
Mean value:	631	652
Std Dev:	51	54

4.3 Conclusions

In this chapter, the study carried out in Chapter 3 has been complemented by studying the manufacturing processes of the INTTUH prosthetic screw.

On the one hand, broaching has been shown to result in damages to the screw head socket that causes some screws to fail in an unexpected region during fatigue tests performed on implant-supported restorations. Hence, the proposition has been made to replace broaching with a milling process, which is less aggressive on the part. Experimental tests have confirmed that the aforementioned failure no longer occurs when the broaching is eliminated, with the first engaged thread being the only failure section.

On the other hand, the manufacturing process of the threads of the prosthetic screw has been analyzed. The same screw was manufactured by thread rolling and cutting, and their shape and surface was analyzed, with experimental mechanical tests also carried out. The rolled threads had lower surface roughness parameter values, i.e. better surface finish and quality, consistent with previous studies.[281,287,294,295] The surface finish was mainly affected by the residual compressive stresses on the thread surface caused by the rolling process,[285,290] even though the obtained residual compressive stress values showed a high degree of scatter. Using synchrotron radiation to evaluate surface properties should improve the quality of the data and allow for more accurate stress extrapolation.[296–298] Regarding thread geometries, even though both the thread shapes obtained by rolling and cutting were similar and functional, the crests of the rolled thread poorly reproduced the desired geometry. This shape was obtained because of grain flow caused by the rolling process.[299,300] Some

manufacturing parameters such as blank diameter or speed should be optimized so that the rolled thread shape is improved. Finally, the prosthetic screws showed significantly better fatigue response with thread rolling, consistent with roll threaded screws used in industry.[288–290] Linear regression models showed a fatigue life 9 times higher for roll threaded screws. In fact, the performance of the rolled thread is so superior to the cut thread that the roll threaded screws did not even fail at the thread but rather at the head-shank transition section. Presumably, the improved fatigue behavior of rolled threads was mainly a result of the larger compressive residual stresses, since differences in the surface roughness and tensile stress area were small. The static load at failure was statistically similar for both manufacturing processes.

Two possible options for future lines of action are proposed to further optimize screw fatigue performance. On the one hand, the study of different rolling parameters such as the optimum value of thread blank diameter so that the thread geometry is as desired while the residual stresses are as high as possible to make the rolled threads even stronger. On the other hand, the improvement of the shank-head section by, for example, increasing the fillet radius of the section, something that is very simple and is expected to improve fatigue response by reducing stress concentration on the section.

5 Fatigue behavior of the dental implant: life prediction methodology

In Chapter 3, a methodology for fatigue life prediction of dental restorations in which the critical component is the prosthetic screw was presented. This is the case for restorations with regular and wide implants. However, the dental implantology industry is focusing its efforts on making narrower implants. Although the ideal scenario would be for the prosthetic screw to always be the critical restoration element, since it is an economical and easy-to-replace element; in the case of dental restorations with narrow implants the implant is precisely the element that suffers the most. Therefore, it is expected to be the critical element.

Prosthetic screw analysis is relatively straightforward, since this undergoes a uniaxial stress status and this allows the engineer to obtain the nominal stress of the critical section by means of the simple Theory of Elasticity formulation. For this purpose, as already explained in section 3.1.2, it is only necessary to obtain the reactions on the prosthetic screw by means of a simple FEA.

Analysis of the implant, however, is more complex. Due to its complex geometry and thin section, in addition to the loads it is subjected to, it undergoes a multiaxial stress status. For this reason, advanced multiaxial fatigue calculation methods must be used, such as critical plane methods, to obtain an equivalent stress value. Moreover, since the stress concentration in the failure section of the implant varies among the different models, the TCD must be used to obtain an effective stress value for fatigue life estimation.

This chapter develops a fatigue life prediction methodology for dental restorations in which the critical element is the dental implant. To develop the methodology, in section 5.1 the fatigue behavior of CP4 titanium - the material

the implants studied in this PhD Thesis are made of - is studied on standardized specimens. The effect of the notches, i.e., the stress concentration zones, on the fatigue behavior of the material is determined. In section 5.2, FEA of the same, tested specimens are performed and the critical distances whose effective stresses result in the theoretical fatigue calculations matching the experimental tests are determined, according to the TCD. Once these studies have been completed, section 5.3 provides the proposed fatigue prediction methodology and explains the steps to be followed for the life estimation of dental restorations whose critical element is the dental implant.

Finally, the methodology is validated on two dental restorations. First, the dental restorations are experimentally tested in section 5.4.1. Then, the methodology is applied and the fatigue life of the restorations is predicted in section 5.4.2. Finally, conclusions about this methodology are provided in section 5.5.

This study was devised by, and some experimental tests were carried out at, the ENSAM University (in Bordeaux-Talence, France) in collaboration with Professor Nicolas Saintier, head of DuMAS.

5.1 Determination of the notch effect on fatigue behavior

Specimens of CP4 titanium were tested under axial load- this material being what the implants of the BTI catalog are made of, which included those studied in this PhD Thesis. Figure 149A shows the geometry of the hourglass specimen tested, with a diameter in the critical section (neck) of 3.5mm. In addition to this specimen, specimens of the same material with different notches were tested in order to analyze the effect of stress concentration on fatigue behavior. On these specimens, a diameter after the notch of 3 mm was left, with only the radius of the notch root changing. Three different radii were tested: 0.137mm (see Figure 149B), 0.164mm (see Figure 149C), and 0.650mm (see Figure 149D).

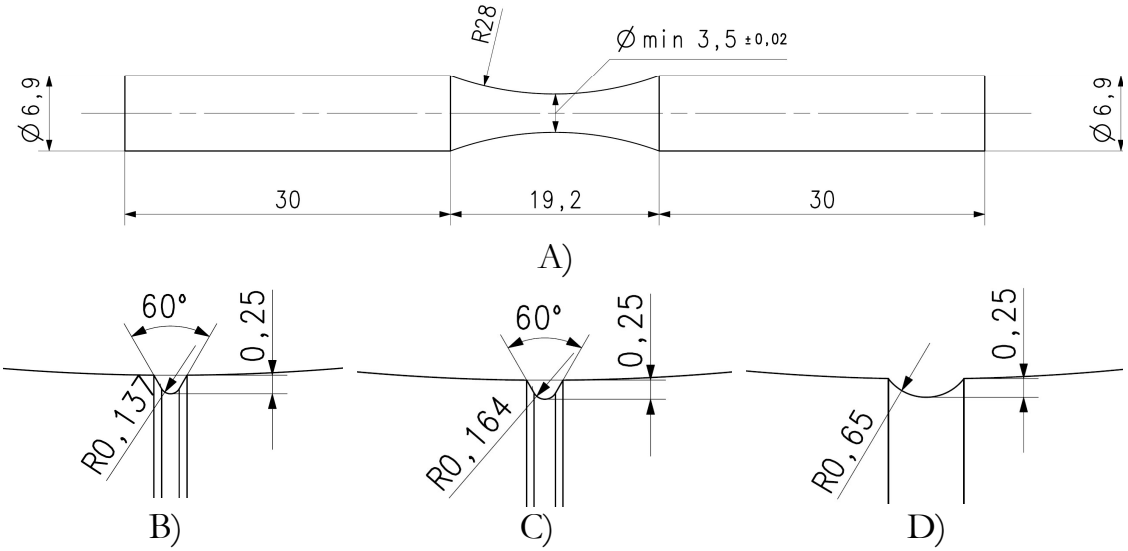

Figure 149. A, Unnotched hourglass specimens used for fatigue characterization of CP4 Titanium. B, Detail of R0.137 notched specimen. C, Detail of R0.164 notched specimen. D, Detail of R0.650 notched specimen.

The fatigue tests were performed at pure alternating axial stress (R_{-1}) on the INSTRON 8801 hydraulic test bench, in section 2.4.2.2. The specimens were clamped by means of grips (see Figure 84) which distribute the forces along the shoulders of the specimen. For each type of specimen tested, the finite life part was obtained by testing 2-3 specimens at each of the 4-5 load levels. Figure 150 shows the experimental fatigue results (markers) together with the linear regression models according to ASTM E739[64] determined by equations (139)-(142).

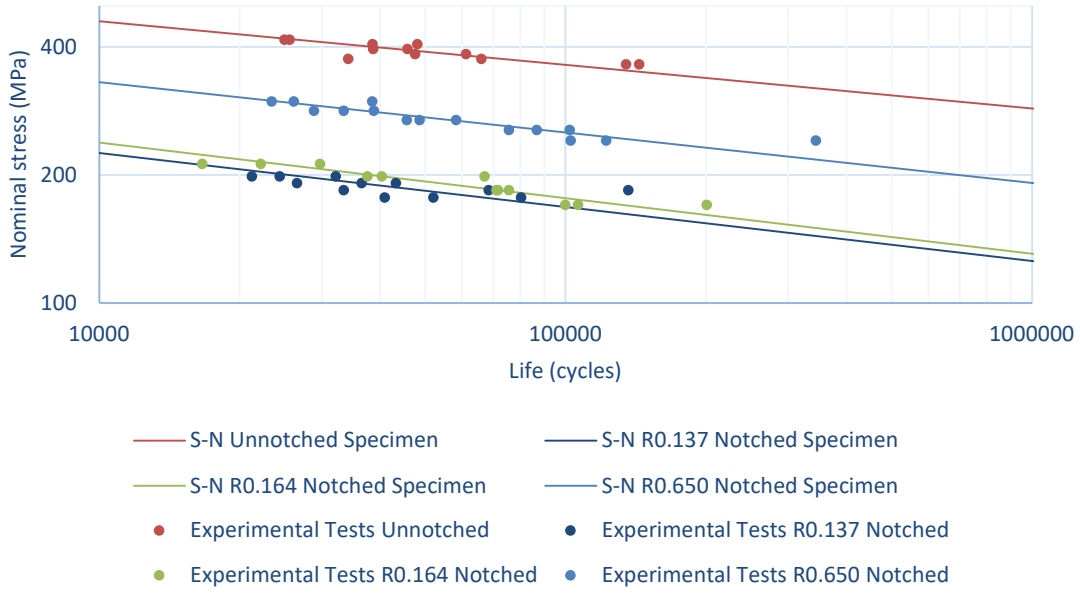

Figure 150. Fatigue data (markers) and linear regression models (lines) of all tested specimens.

Unnotched: $\log(N) = 29.96 - 9.75 \cdot \log(\sigma)$ (139)
R0.134mm: $\log(N) = 22.54 - 7.88 \cdot \log(\sigma)$ (140)
R0.164mm: $\log(N) = 22.20 - 7.66 \cdot \log(\sigma)$ (141)
R0.650mm: $\log(N) = 25.27 - 8.44 \cdot \log(\sigma)$ (142)

As can be seen from the linear models in Figure 150, the slopes of the finite life are virtually parallel. This indicates that, despite expectations, the effect of the stress concentration of each of the notches on fatigue behavior is practically constant throughout the cycles. The ratios of the nominal stresses of the notched specimens with respect to the unnotched specimen have been obtained for 10,000, 50,000, and 100,000 cycles and are given in Table 15.

Table 15. $(\sigma_{nom})_{unnotched}/(\sigma_{nom})_{notched}$ ratio versus the number of cycles.

$\frac{(\sigma_{nom})_{unnotched}}{(\sigma_{nom})_{notched}}$	10,000 cycles	50,000 cycles	100,000 cycles
R0.134 Notch	2.04	2.12	2.16
R0.164 Notch	1.93	2.01	2.06
R0.650 Notch	1.39	1.43	1.44

It is found, again, that the difference between the ratios obtained over the cycles is practically constant. Whatever the case, the ratios for 50,000 cycles are used, since they represent a midpoint in the finite life range.

It should be mentioned that, although the results of Table 15 show that the ratios obtained between the nominal stresses of notched and unnotched specimens virtually do not vary throughout the cycles, this is not always the case. Evidently, stress concentration has a negative effect on fatigue behavior causing the S-N curve to decrease with respect to its equivalent without stress concentration. Authors usually ensure that both curves (notched and unnotched) coincide at 1 or 1000 cycles.[53] However, this is simply a calculation recommendation, with it being more thorough to perform experimental tests and obtain real fatigue behavior, as has been done in this section.

5.2 Determination of critical distances via Finite Element Analyses

Once the effect of stress concentrations of 3 different notches on the fatigue performance of CP4 Titanium has been obtained experimentally, the next step is to select a method by which to obtain the stress value to assign the experimental results in terms of fatigue life.

For this purpose, TCD has been used which, as explained in section 1.3.1.3.3, focuses on obtaining an effective stress level at a specific distance (critical

distance) from the root of the notch (or stress concentration element) equivalent, in theory, to that which would be reached using other methods, such as the method using nominal stresses multiplied by the fatigue notch factor k_f explained in section 1.3.1.3.1. As shown in Figure 45, both effective stresses will be equal regardless of the chosen method.

As explained in section 1.3.1.3.3, there are various methods that use the TCD and are classified according to the geometry of the part they cover to calculate effective stress (see Figure 46). The Point Method uses the stress value at a single point located at a specific distance d_{PM}. This is the case shown in Figure 45. The Line Method, by contrast, calculates effective stress by averaging the elastic strain along the line between the root of the notch and the critical distance d_{LM}. The Area Method also obtains the average of the elastic stresses, but, in this case, along a half circle whose center is located at the notch root and the radius is equal to the critical distance d_{AM}. Finally, the Volume Method does the same as the previous method, but with a sphere of radius d_{VM} rather than a circle.

Again, it must be taken into account that the methodology will be used on dental implants where the direction of the failure section is difficult to predict, i.e., the breakage will not be perpendicular to the longitudinal axis of the implant. Generally, it will follow an irregular path in a poorly defined direction (the weaker route in each case). For this reason, the Volume Method has been chosen because this volume contains, and therefore considers, all possible crack spreading directions, instead of other methods, that consider a single direction or, at most, a single plane.

Even though the TCD was developed for infinite life (fatigue limit), it can also be used for finite life, as explained in section 1.3.1.3.3. Susmel,[94] which proposes a critical distance as a function of cycles following equation (52). However, as seen in the previous section, the S-N curves of the notched specimens tested can be assumed to be parallel with respect to the S-N curve of the unnotched specimen. Hence, it can be guaranteed that the stress concentration is constant along the cycle range studied and, therefore, the critical distance does not vary with respect to finite life cycles.

Therefore, FEA has been performed on the same specimens tested experimentally, following the indications set out in section 2.3. In each FEA an axial load has been applied so that the specimen undergoes the stress corresponding to the 50,000 cycles obtained from its S-N curve shown in the

previous section. Figure 151 shows how the nominal stresses corresponding to the 50,000 cycles are obtained for each of the S-N curves previously shown in Figure 150. In addition to this, Table 16 shows the values of these nominal stresses obtained from Figure 151 (or equations (139)-(142)) as well as the axial loads required to produce these stresses.

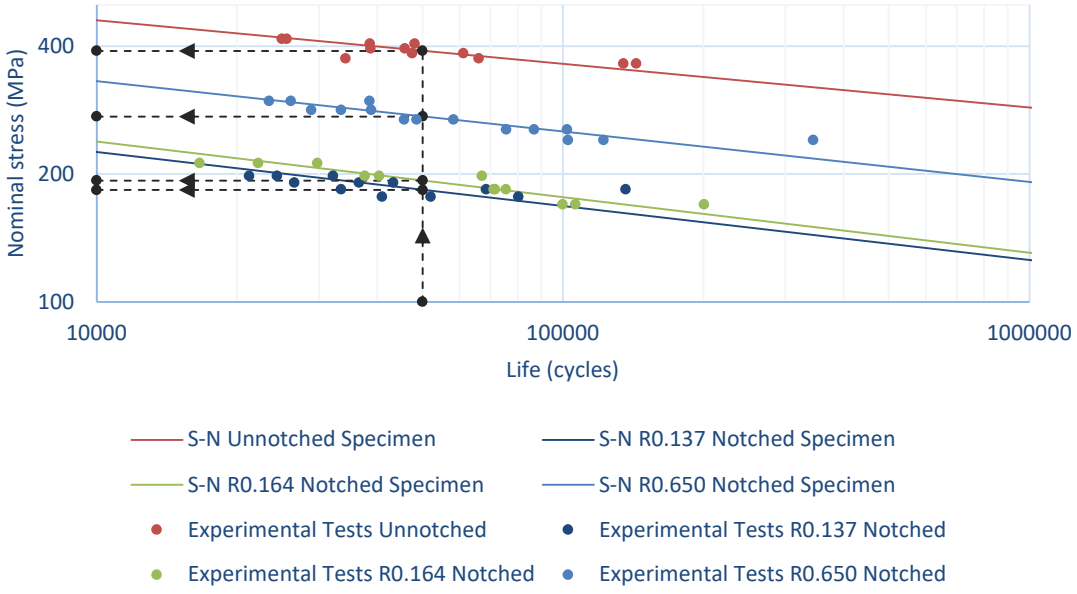

Figure 151. Nominal stresses corresponding to 50,000 cycles for each specimen under study.

Table 16. Nominal stresses (at 50,000 cycles) and their corresponding axial loads.

	Nominal stress (MPa)	Axial load (kN)
Unnotched	389.65	3.749
R0.134 Notch	183.60	1.298
R0.164 Notch	193.08	1.365
R0.650 Notch	273.12	1.931

As mentioned at the beginning of this section, the effective stress for fatigue calculations was obtained by means of the Volume Method. Therefore, the FE models were meshed with a progressive spherical refinement in 4 phases with the center of the spheres located at the root of the notch where the crack starts, as explained in section 2.2.6. Figure 152 shows the case with the R0.137mm-notched specimen.

From the FEA, the elements of a sphere with a radius of 0.2mm whose center is located at the root of the notch are selected. Then, the X, Y, and Z coordinates of the centroid of each element, its associated volume, and their 6 stress components are obtained. The FEA results were post-processed in Matlab R2019b, obtaining the equivalent Findley and Dang Van alternating

stresses of each element (see section 1.3.2.4.3). Then, the averaged value of the stress, i.e., the effective stress, was obtained as a function of the critical distance (radius of sphere) for the Volume Method (see Figure 153). It is seen, as expected, that both methods provide similar results.

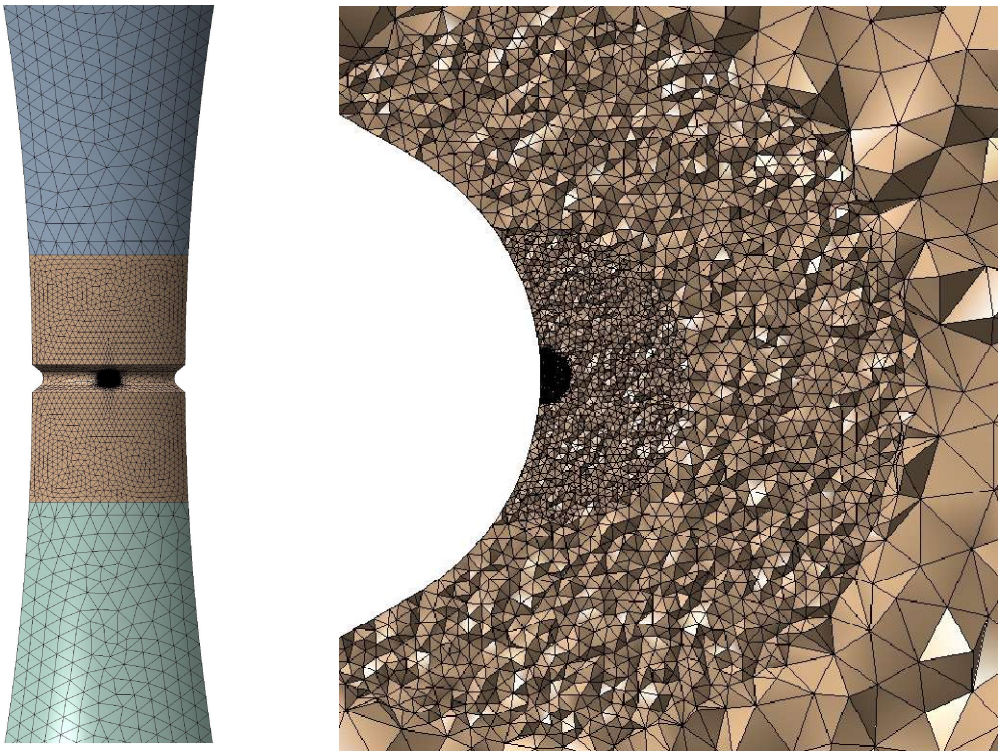

A) B)

Figure 152. EF model of the R0.137mm notched specimen. A, Complete model. B, Closer view of the notch. C, Detail of the progressive sphere refinement.

Once the value of the effective stress has been calculated according to both methods as a function of the sphere radius for the three-notched specimens in Figure 153. The next step is to determine the value of the critical distance to be used for fatigue calculations. As already discussed in section 1.3.1.3.3, the TCD and, in particular the Volume Method, obtains an effective stress value at a certain critical distance (sphere radius) which can be used in the S-N curve of the material (equation (139), that corresponds to the unnotched specimen S-N curve). As seen in Table 16, for 50,000 cycles, the stress in the absence of stress concentration (unnotched specimen) is 389.65MPa. Therefore, the effective stress on the other three notched specimens will also be the same at 50,000 cycles and the critical distance will be the one that gives a stress of 389.65MPa in Figure 153. Table 17 provides the values of Findley and Dang Van critical distances for the three notched specimens under study.

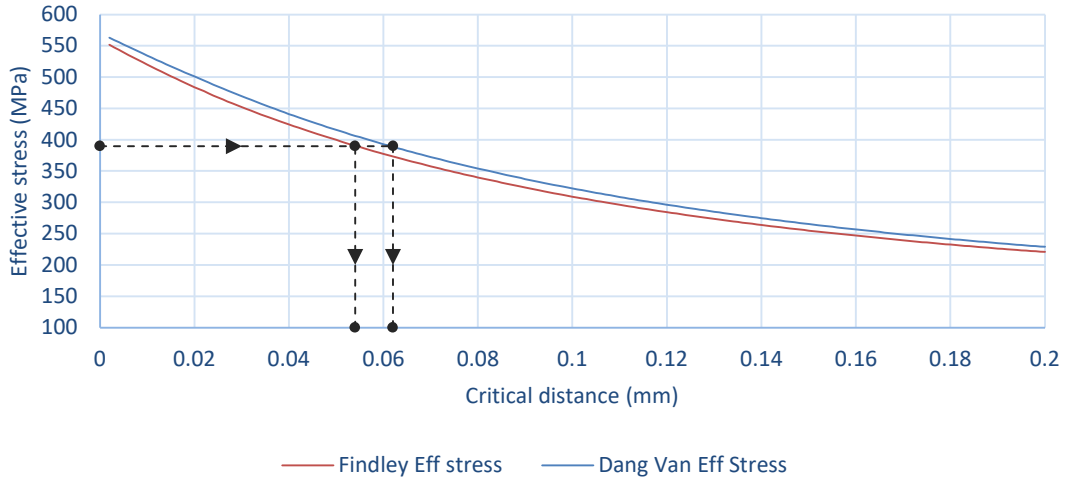

A)

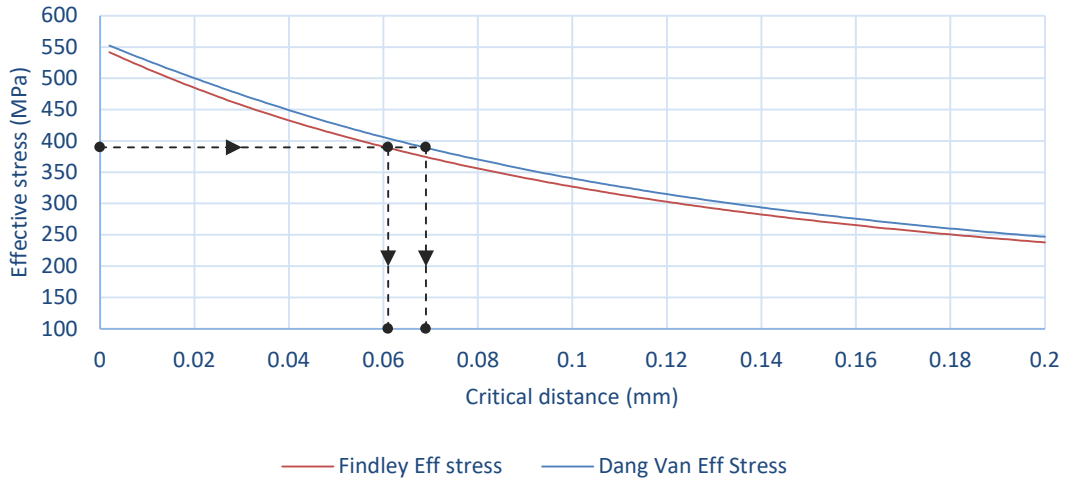

B)

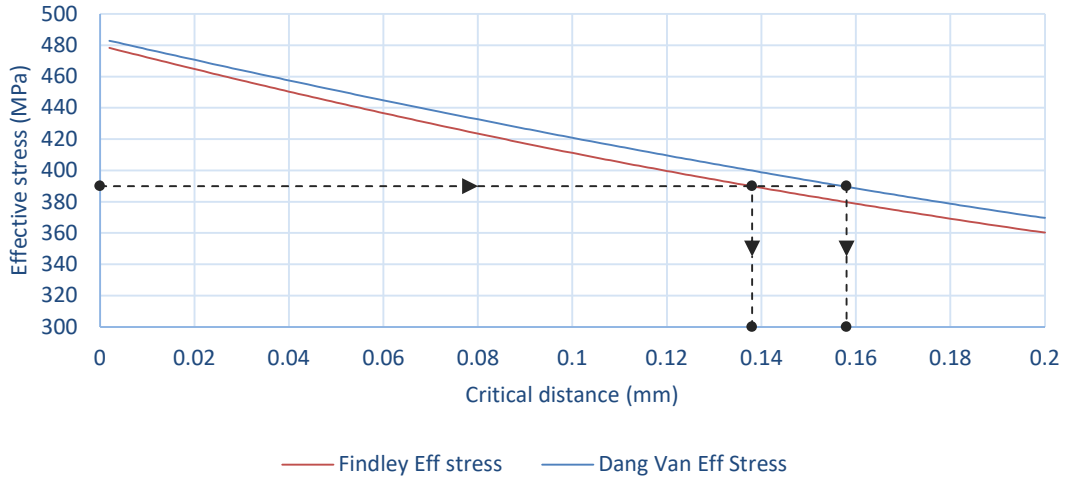

C)

Figure 153. Findley and Dang Van effective stresses versus the sphere radius (critical distance) and the critical distances corresponding to effective stress at 50,000 cycles. A, R0.137mm notched specimen. B, R0.164mm notched specimen. C, R0.650mm notched specimen.

Table 17. Findley and Dang Van critical distances for the three notched specimens under study.

	Findley critical distance (mm)	Dang Van critical distance (mm)
R0.134 Notch	0.054	0.062
R0.164 Notch	0.061	0.069
R0.650 Notch	0.138	0.158

It can be seen that the critical distance is not constant along the different notches in contrast to what was initially assumed. According to the theory explained in section 1.3.1.3.3, the critical distance is, in principle, a property of the material (and of the load ratio R), and should therefore have a single value for the 3 notches tested.[94] However, several studies show that the notch type and size have an effect on critical distance.[159,301] In this sense, the normalized stress gradient appears to be a suitable parameter to characterize the notch geometry's effect on critical distance, rather than the notch radius or the notch factor.[302–305]

Therefore, the decision was made to calculate the normalized stress gradient at the notch root for each of the three notched specimens from the effective stress already obtained in Figure 153. Figure 154 shows how the stress gradient is obtained, whose value is then divided by the maximum stress for normalization purposes. Table 18 shows the normalized stress gradient obtained from Figure 154 for both methods, Findley and Dang Van. As a result, an approximate linear relationship was found between the normalized stress gradient and critical distance. Figure 155 shows the critical distance values obtained as a function of the normalized stress gradient (for both methods) at the notch root for the three specimens and the linear relationship obtained by a least-squares fit. The linear model equations of the normalized stress gradient versus critical distance for Findley and Dang Van are shown in equations (149) and, (148) respectively.

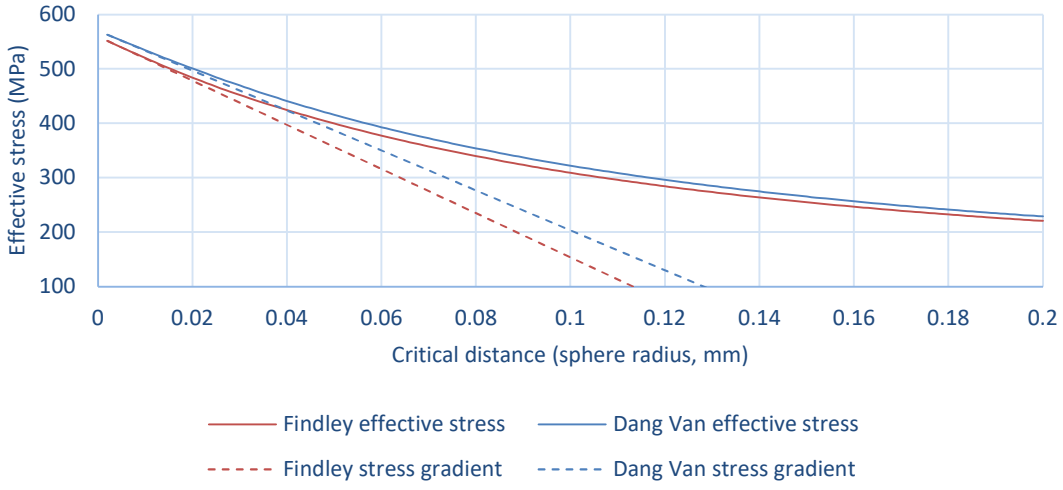

A)

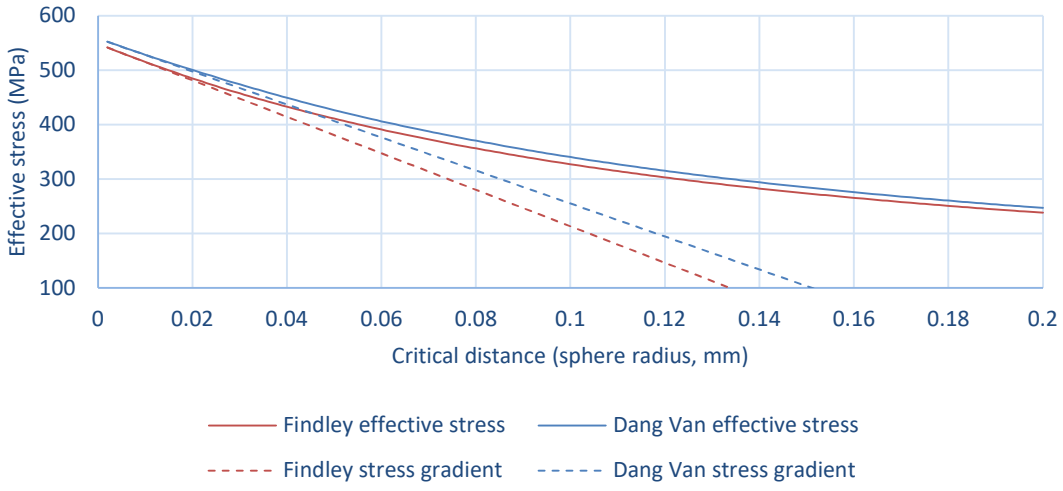

B)

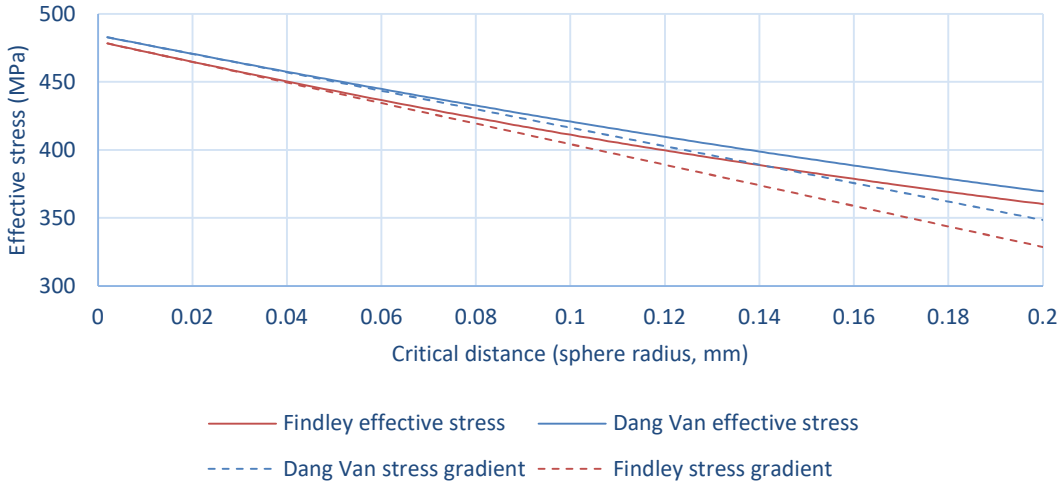

C)

Figure 154. Findley and Dang Van effective stresses versus the sphere radius (critical distance) and their corresponding stress gradients at the root of the notch. A, R0.137mm notched specimen. B, R0.164mm notched specimen. C, R0.650mm notched specimen.

Table 18. Normalized stress gradients for Findley and Dang Van methods for the three notched specimens under study.

	Findley normalized stress gradient (mm^{-1})	Dang Van normalized stress gradient (mm^{-1})
R0.134 Notch	7.360	6.517
R0.164 Notch	6.191	5.494
R0.650 Notch	1.580	1.406

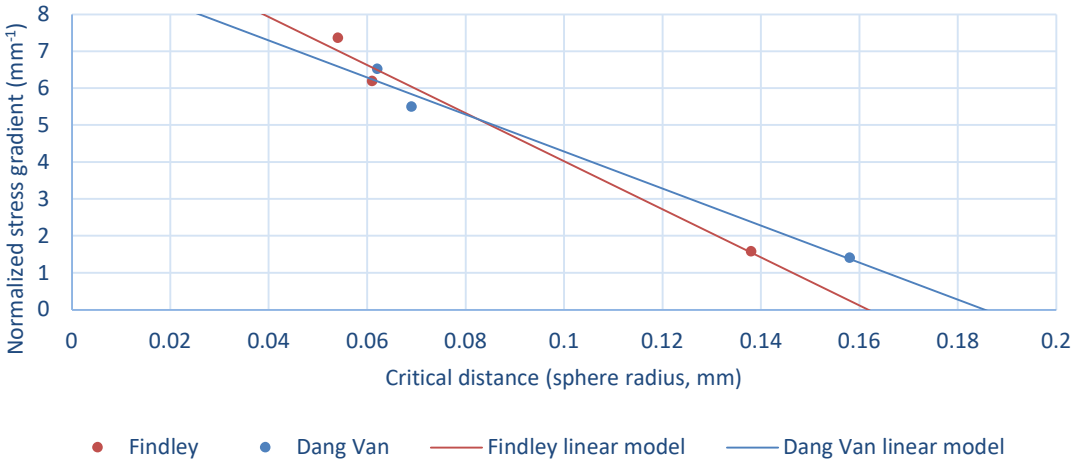

Figure 155. Critical distance (sphere radius) versus normalized stress gradient for the three notched specimens, along with the linear models proposed.

$$\text{Findley: } \nabla\sigma_{Fin} = -65.1 \cdot d_{VM_{Fin}} + 10.5 \quad (143)$$

$$\text{Dang Van: } \nabla\sigma_{DV} = -50.1 \cdot d_{VM_{DV}} + 9.3 \quad (144)$$

In short, the TCD is used to consider the notch effect on fatigue behavior of CP4 Titanium, by using the Volume Method in which, for this specific case, the critical distance is not cycle dependent, but rather stress gradient dependent.

5.3 Fatigue life prediction methodology for dental implants

Based on what has been studied so far, a methodology is proposed to predict the fatigue life of dental restorations in which the critical component is the dental implant, with the steps to follow described below and briefly presented in Figure 156.

First, it is necessary to follow sections 5.1 and 5.2 in order to characterize the material making up the implants under study. Therefore, the S-N curve of the implant material to be analyzed (unnotched specimen, R_{-1}) is obtained as well as the model that relates the normalized stress gradient at the root of the notch versus the value of the critical distance to be used for fatigue calculations.

Once these previous steps have been carried out on standardized specimens, in order to predict the fatigue life of dental implants, the first step is to perform an FEA of the model of the dental restoration to be studied at the desired load.

The FE model needed is similar to those seen in Chapter 3 (following the instructions in section 2.2) but with some specifics indicated in section 2.2.6, i.e., a progressive spherical volume refinement whose center is located at the root of the notch, i.e., at the point where the crack starts. Obviously, it is recommended that a previous experimental test be performed on the dental restoration to verify that the crack starts at the expected point.

From the FEA, the elements of the aforementioned sphere with a radius of 0.2mm are selected. Then, the X, Y, and Z coordinates of the centroid of each element, its associated volume, and their 6 stress components are obtained. Note that this data should be recorded for the maximum and minimum fatigue cycle force value (as specified in ISO 14801).[141] Once the FEA data has been collected, the equivalent Findley or Dang Van alternating stresses should be calculated for each finite element selected. These methods transform, for each element, the multiaxial stresses at a given stress ratio R into a uniaxial equivalent alternating stress R_{-1} as explained in section 1.3.2.4.3.

Then, the Volume Method is used to determine the effective stress for each of these methods (Findley and Dang Van) as a function of the critical distance (radius of sphere), obtaining a graph similar to the one shown in Figure 153 for standardized specimens, but now for the dental implant under study.

Next, the normalized stress gradient at the root of the notch must be determined. With the value of the normalized stress gradient, the critical distance is determined by means of the linear model obtained in section 5.2. In the case of the CP4 Titanium analyzed, the models in Figure 155 are obtained, also expressed in equations (143) and (144).

Then, the effective stress for the calculated critical distance must be obtained. With this stress, fatigue life is calculated according to the S-N curve of the unnotched specimen; in this case expressed in equation (139).

This methodology can be used for any geometry and working conditions (external load, screw preload, among others) as long as the material of the dental implant is maintained. If an implant made of another material needs to be analyzed, the methodology should be readjusted by repeating the steps explained in sections 5.1 and 5.2.

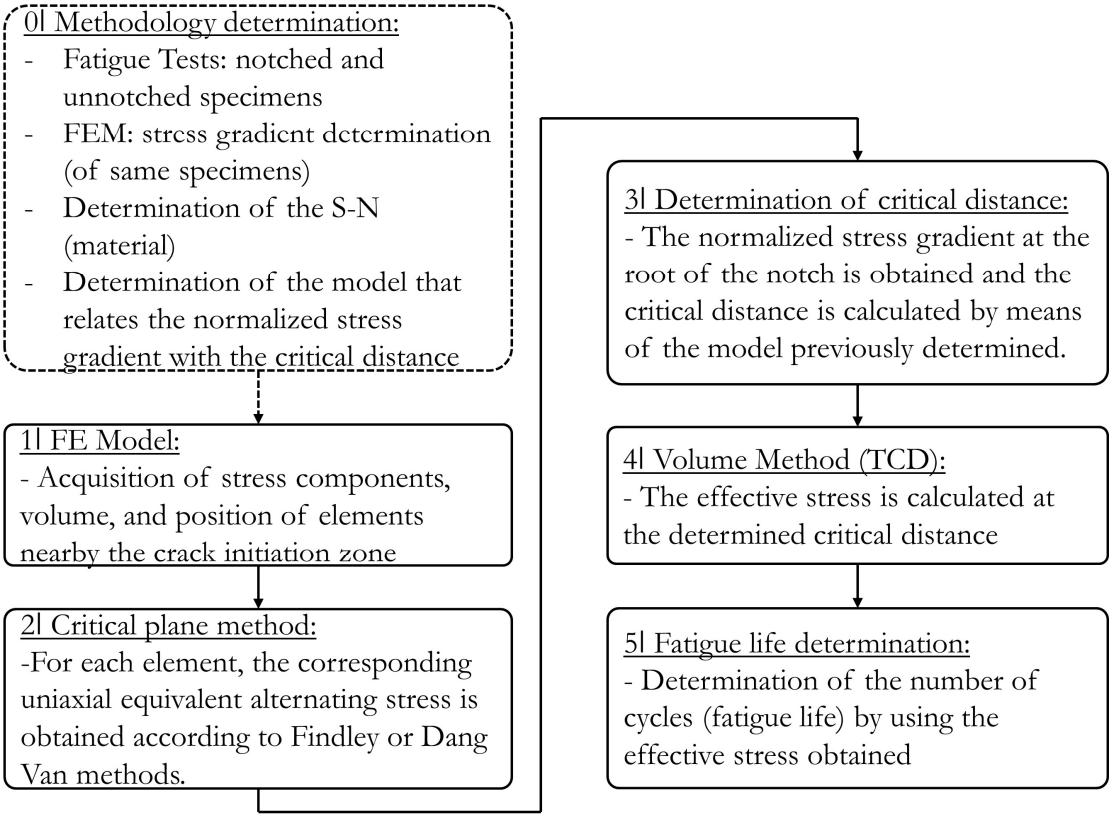

Figure 156. Steps of the methodology proposed to predict fatigue life of dental restorations whose critical component is the dental implant.

5.4 Validation of the methodology

Having developed and presented the methodology for fatigue life prediction of dental restorations in which the implant is the critical component, the prediction accuracy of the methodology is tested in this section.

For this purpose, three dental restoration models were first tested experimentally. Then, the methodology was used to predict their fatigue life and the difference between the experimental and predicted values was analyzed to verify the accuracy of the methodology presented in this chapter.

5.4.1 Experimental validation

Three dental restoration models were tested. All of them were mounted on narrow implants, to ensure that breakage occurred at the implant rather than the prosthetic screw. The first dental restoration, hereinafter IN-I3.3-P4.1, consists of a BTI INTERNA IIPUCA3313 implant with a 3.3mm body diameter and a 4.1mm platform diameter, and the already known INPPTU44 abutment and INTTUH prosthetic screw. The second dental restoration,

hereinafter IN-I3.0-P3.0, consists of a BTI INTERNA IIP3CA3013 implant with a 3mm body diameter and a 3mm platform diameter, a INPPT3B34 abutment, and INTTUH prosthetic screw. The third dental restoration, hereinafter EX-I2.5-P3.5, consists of a BTI EXTERNA IRTCA2513 implant with a 2.5mm body diameter and a 3.5mm platform diameter, a PPATEB44 abutment, and TTTH prosthetic screw. All dental restorations are shown in Figure 157 and most important information about each dental restoration is summarized in Table 19. As is the case with all dental restorations studied so far, both the implant and the abutment are made of CP4 Titanium while the prosthetic screw is made of Ti6Al4V ELI, and the chemical composition of these materials is provided in Table 4.

Table 19. All the narrow implant-supported restorations under study.

Restoration	IN-I3.3-P4.1	IN-I3.0-P3.0	EX-I2.5-P3.5
Implant	IIPUCA3313	IIP3CA3013	IRTCA2513
Abutment	INPPTU44	INPPT3B34	PPATEB44
Screw	INTTUH	INTTUH	TTTH
Body Ø (mm)	3.3	3.0	2.5
Platform Ø (mm)	4.1	3.0	3.5
IAC	Internal	Internal	External
Screw Metric	M1.8	M1.8	M2
Torque (Ncm)	35	35	35

Experimental fatigue tests were carried out on the INSTRON E3000 Electropuls, as explained in section 2.4.1 and following the recommendations of ISO 14801,[141] explained in detail in section 1.6.1. In short, the abutment was placed on the implant and the prosthetic screw was tightened at 35Ncm, as recommended by the manufacturer. The whole assembly was embedded in a specimen holder and placed at 30º to the vertical axis. Then, vertical load cycles were applied up to the fatigue failure of the restoration.

In preliminary tests, it was found that the range of loads that result in finite life failure is relatively narrow for the implants under study. For this reason, a complete fatigue curve for the finite life of each dental implant was not obtained, since this would mean covering both very low and very high cycles, which could distort the results. Note that the case of low cycles corresponds to non-common load values that are not very representative in the habitual use of dental implants, and besides this, in this range a strain-stress approach (LCF) is usually employed, as explained in section 1.3.1.1, and in the case of high cycles, high dispersion in tests is expected. Therefore, a single load level located in the middle range of the finite life was chosen: 220N for IN-I3.3-P4.1, 140N for IN-I3.0-P3.0, and 130N for EX-I2.5-P3.5. Figure 158 shows the fatigue results

of all implant models under the aforementioned loads. The Anderson-Darling test was performed in all cases to verify that there is not enough evidence that the sample data departs significantly from log-normal distribution for a significance level of 0.05, whereby log-normality cannot be rejected ($p=0.5938$ for IN-I3.3-P4.1, $p=0.2243$ for IN-I3.0-P3.0, and $p=0.3219$ for EX-I2.5-P3.5). Figure 159, shows that the implant failure occurs at the thread immediately below the limit of the embedment of the implant with the specimen holder.

Figure 157. Dental restorations under study. A, IN-I3.3-P4.1. B, IN-I3.0-P3.0. C, EX-I2.5-P3.5.

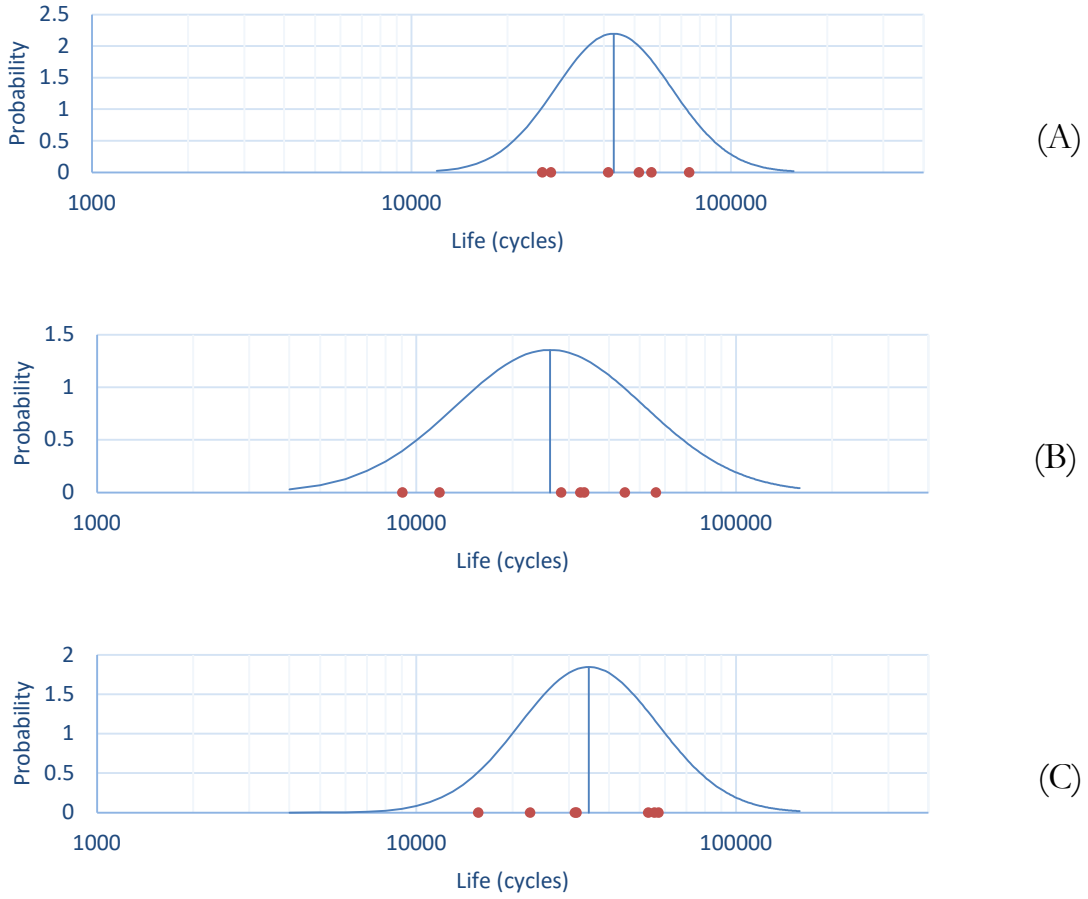

Figure 158. Experimental fatigue results of each dental implant tested along with their normal distribution function, and the mean value. A, IN-I3.3-P4.1 tested at 220N. B, IN-I3.0-P3.0 tested at 140N. C, EX-I2.5-P3.5 tested at 130N.

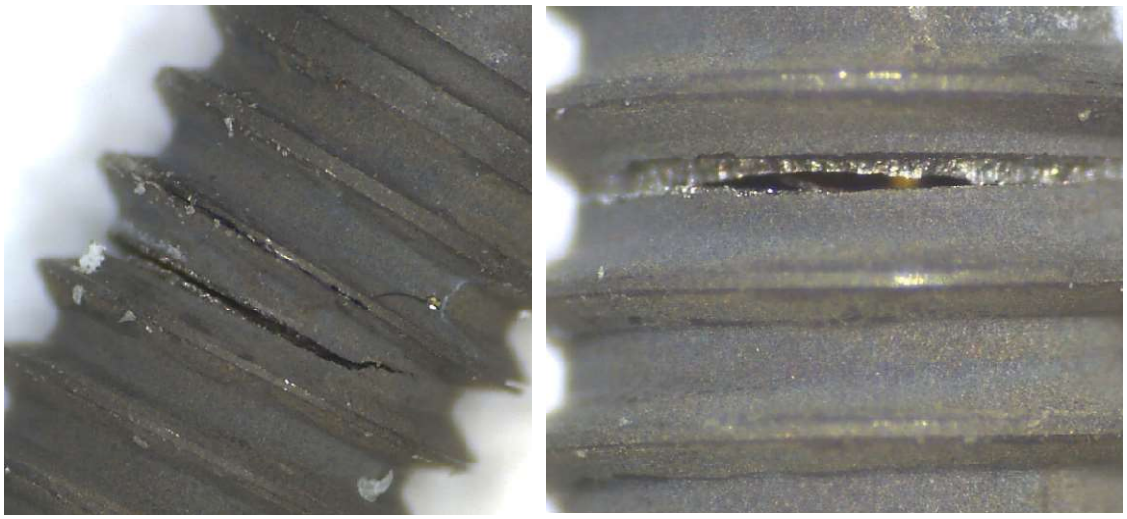

Figure 159. Crack initiation section located at the thread notch immediately below the limit of the embedment of the implant with the specimen holder (IN-I3.0-P3.0).

5.4.2 Methodology prediction

Once known the loads applied in the experimental tests that gave rise to the fatigue failure of each dental restoration, the FEA of these dental restorations were carried out under the same loads. The FE models are similar to those seen in Chapter 3 (following the indications in section 2.2) but with some specifics indicated in section 2.2.6. First, the whole geometry of the dental restoration is modeled, since the external thread of the implant is not simplified (is not assumed to be cylindrical), with the notch of the thread being the critical point at which the stresses are studied. Secondly, the implant has a progressive spherical refinement in 4 phases with the center of the spheres located at the root of the notch where the crack starts. Moreover, the elements of a sphere with a radius of 0.2mm are selected whose centers are located at the root of the notch, i.e., at the crack initiation point. Then, the X, Y, and Z coordinates of the centroid of each element, the associated volume, and their 6 stress components are obtained. Note that this data should be recorded for the maximum (220N in the case of IN-I3.3-P4.1, 140N in the case of IN-I3.0-P3.0, and 130N in the case of EX-2.5-P3.5) and minimum (22N in the case of IN-I3.3-P4.1, 14N in the case of IN-I3.0-P3.0, and 13N in the case of EX-I2.5-P3.5) load values of the fatigue cycle (as specified in ISO 14801).[141] Figure 160 shows the models of the three restorations analyzed and the details of the refinements in the thread root immediately below the embedment limit of the specimen holder.

Then, Findley and Dang Van methods were applied to obtain the equivalent alternating stresses of the selected elements using the aforementioned sphere. With these alternating stress values, the effective stress of the Volume Method is calculated for a sphere with its center at the root of the notch and an increasing radius from 0 to 0.2mm. Figure 161 shows the Findley and Dang Van effective stresses as a function of the critical distance (sphere radius) in the cases of IN-I3.3-P4.1 (at 220N), IN-I3.0-P3.0 (at 140N), and EX-I2.5-P3.5 (at 130N). From the same graph, the stress gradient was also obtained at the root of the notch for all dental restorations under review. Table 20 shows the normalized stress gradient obtained for Findley and Dang Van effective stresses at the root of the notch of all restorations. Once the normalized stress gradient is obtained, the linear model determined in section 5.2 (Figure 155 and equations (143)and (144)) provides the critical distance that must be used for fatigue calculations. Figure 162 shows that the normalized stress gradient

obtained at the root of the implant notches falls within the range of the normalized stress gradients obtained on the standardized specimens.

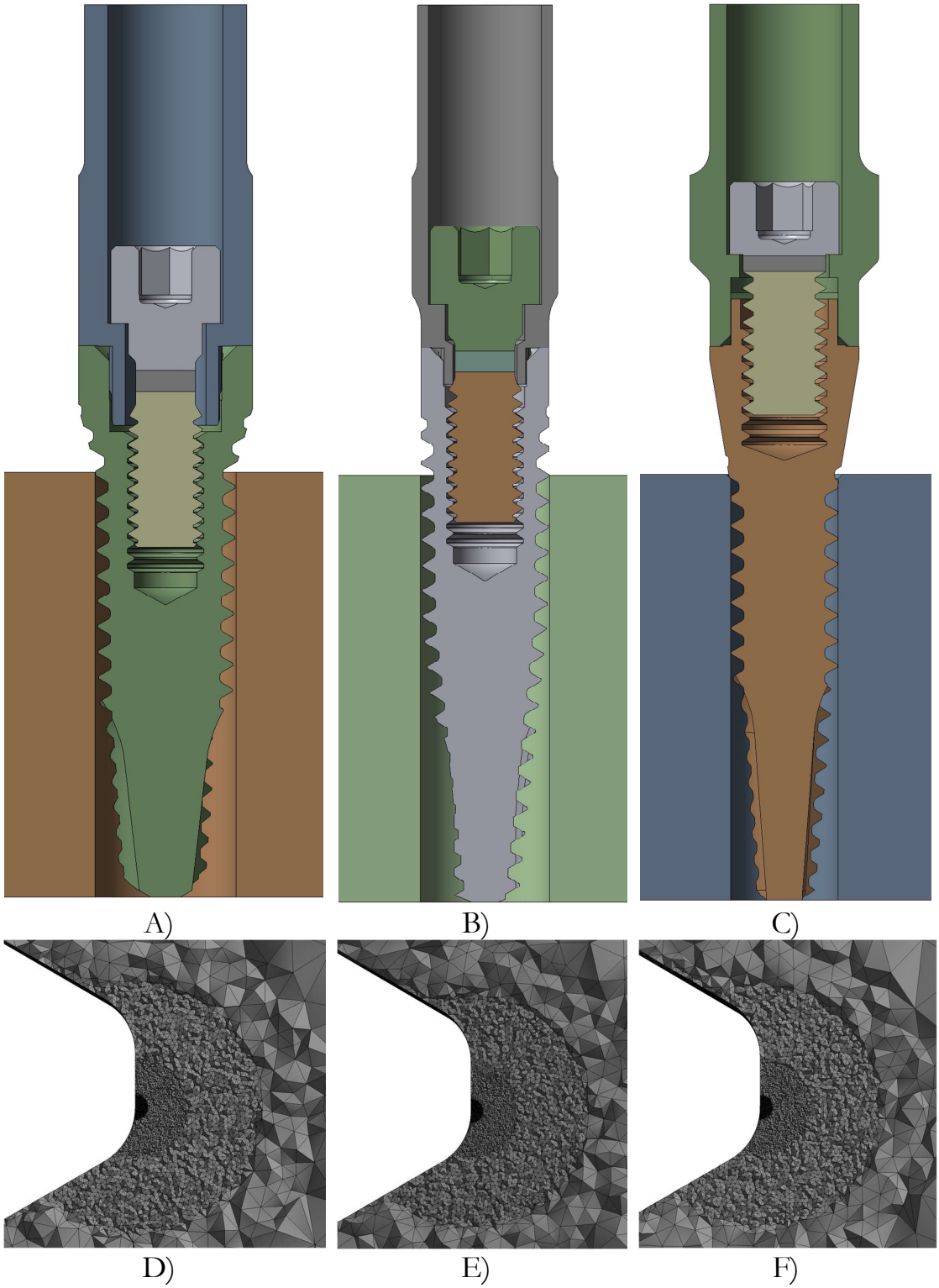

Figure 160. FE models and details of the mesh of the crack initiation point. A, IN-I3.3-P4.1 model section. B, IN-I3.0-P3.0 FE model section. C, EX-I2.5-P3.5 model section. D, Crack initiation point mesh refinement of IN-I3.3-P4.1. E, Crack initiation point mesh refinement of IN-I3.0-P3.0. F, Crack initiation point mesh refinement of EX-I2.5-P3.5.

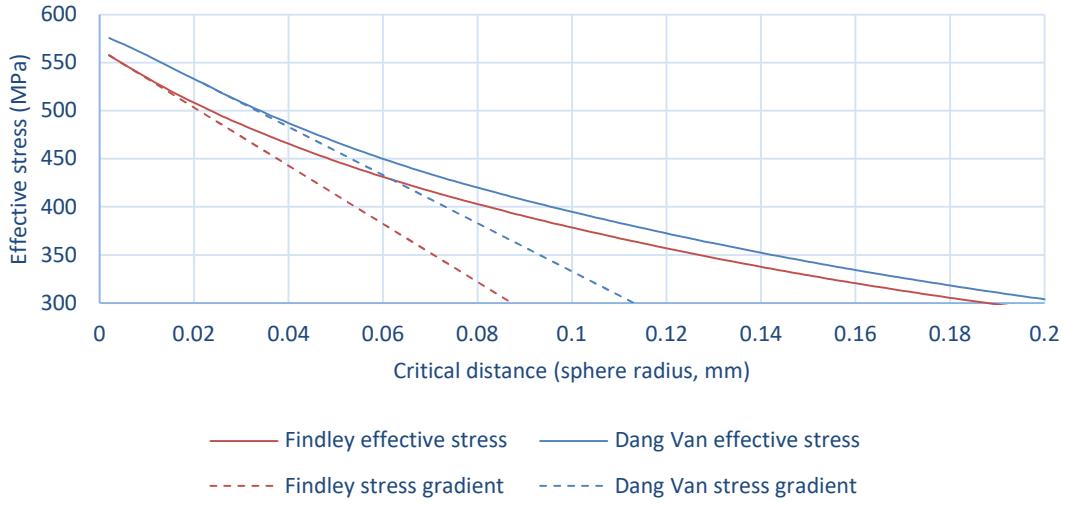

A)

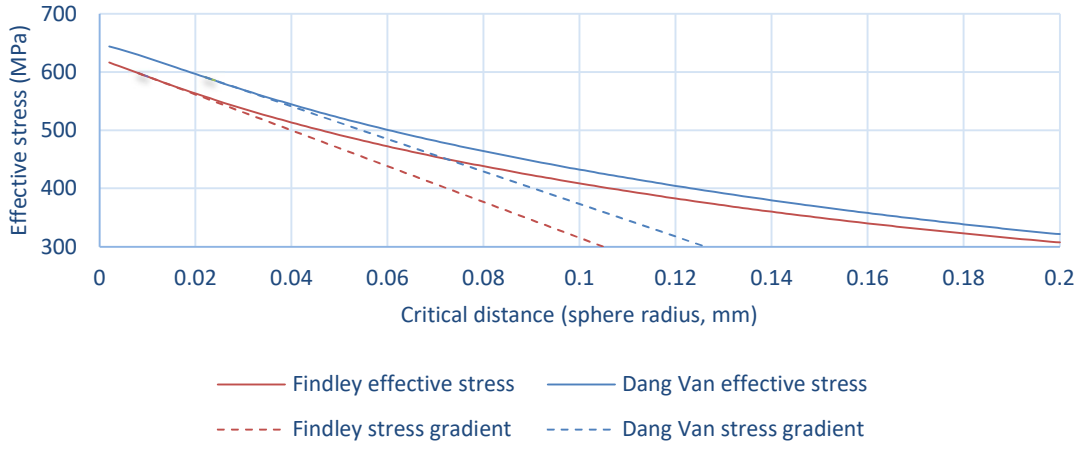

B)

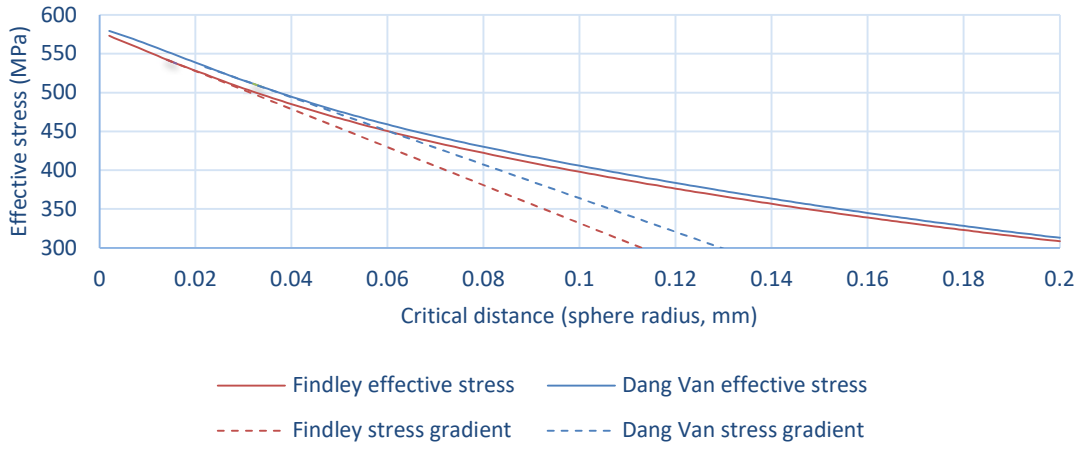

C)

Figure 161. Findley and Dang Van effective stress versus the sphere radius (critical distance) and the stress gradients at the root of the notch. A, IN-I3.3-P4.1. B, IN-I3.0-P3.0. C, EX-I2.5-P3.5.

Table 20. Findley and Dang Van stress gradient values at the root of the notch for all dental restorations under study.

	Findley normalized stress gradient (mm^{-1})	Dang Van normalized stress gradient (mm^{-1})
IN-I3.3-P4.1	5.420	3.636
IN-I3.0-P3.0	4.914	3.607
EX-I2.5-P3.5	4.449	3.486

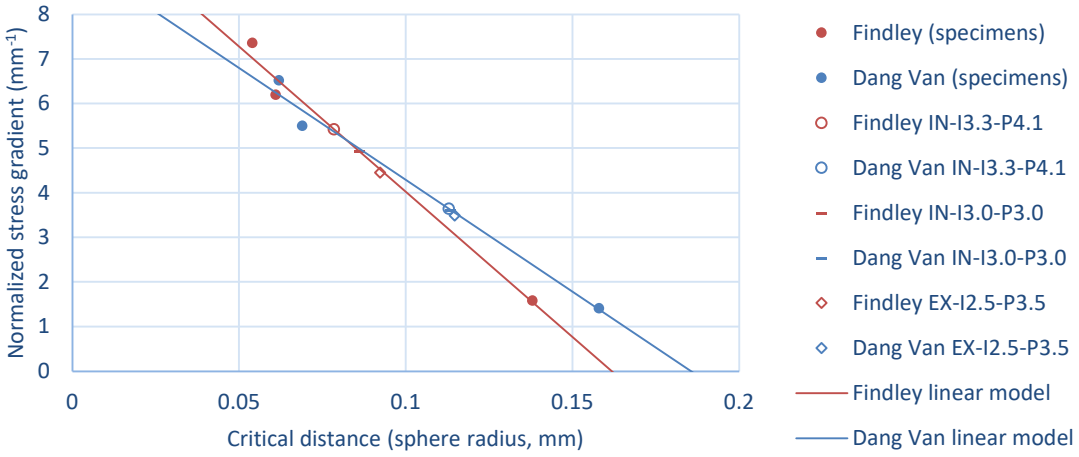

Figure 162. Critical distance (sphere radius) versus normalized stress gradient for the dental restorations under study with the linear models proposed.

Table 21 shows the critical distance values obtained from the linear models of Figure 162. With these values of critical distance, Figure 161 is consulted, which shows the equivalent Findley and Dang Van stresses as a function of the critical distance (radius of the sphere). This figure is updated in Figure 163, showing the effective stress values obtained for all the cases studied. The obtained values of the effective fatigue stress are shown in Table 22.

Table 21. Findley and Dang Van critical distance values for all dental restorations under study.

	Findley critical distance (mm)	Dang Van critical distance (mm)
IN-I3.3-P4.1	0.079	0.113
IN-I3.0-P3.0	0.086	0.114
EX-I2.5-P3.5	0.092	0.115

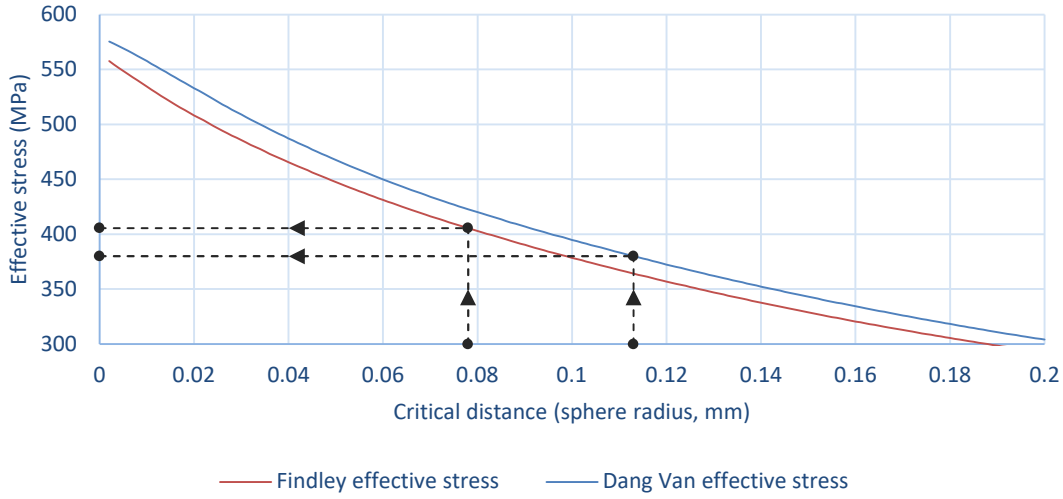

A)

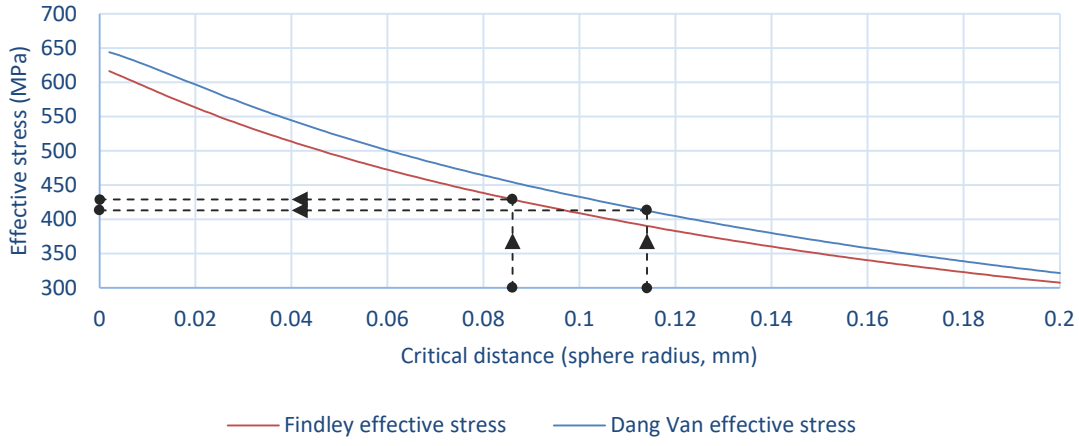

B)

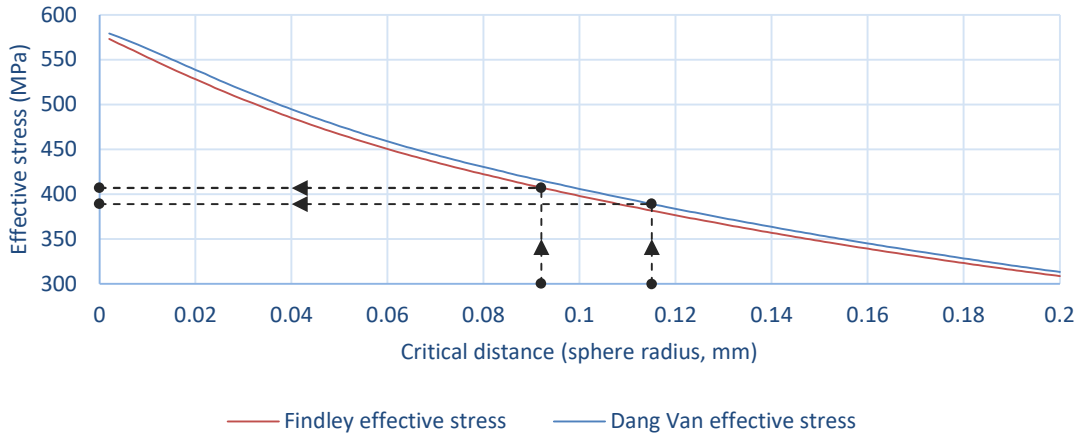

C)

Figure 163. Findley and Dang Van effective stress values obtained for fatigue calculations. A, IN-I3.3-P4.1. B, IN-I3.0-P3.0. C, EX-I2.5-P3.5.

Table 22. Findley and Dang Van effective stress values for all dental restorations under study.

	Findley effective stress (MPa)	Dang Van effective stress (MPa)
IN-I3.3-P4.1	405.6	380.1
IN-I3.0-P3.0	429.0	412.5
EX-I2.5-P3.5	407.4	389.1

Finally, the fatigue life predictions for IN-I3.3-P4.1, IN-I3.0-P3.0, and EX-I2.5-P3.5 are obtained using equation (139) with the values of effective stresses from Table 22. Figure 164 shows the values of the predictions using the Findley method, the S-N of the material (unnotched specimen, R_{-1}) which, obviously, passes through the three prediction points, and the different values of fatigue life obtained experimentally (including the mean value and its log-normal probability function). Similarly, Figure 165 shows the predictions obtained with the Dang Van method. In both cases, it is shown how the predictions of the methodology fit the experimental results very well for all the dental restorations under study, with Findley being more conservative than Dang Van.

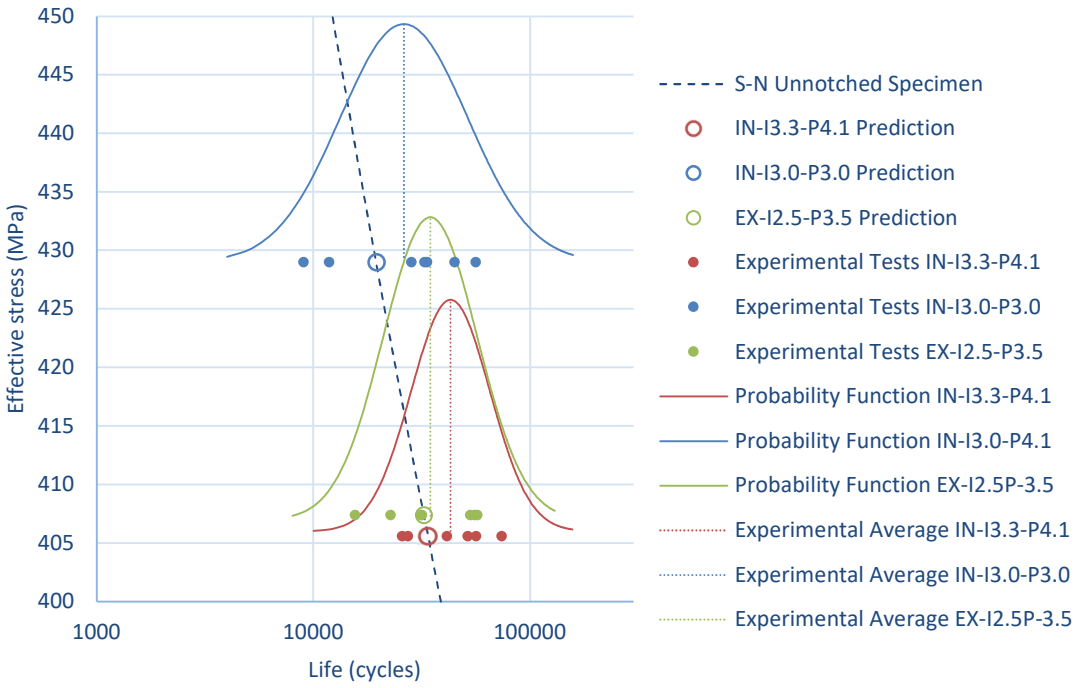

Figure 164. Experimental fatigue results of each dental implant tested and the fatigue life prediction by using the proposed methodology and Findley effective stresses.

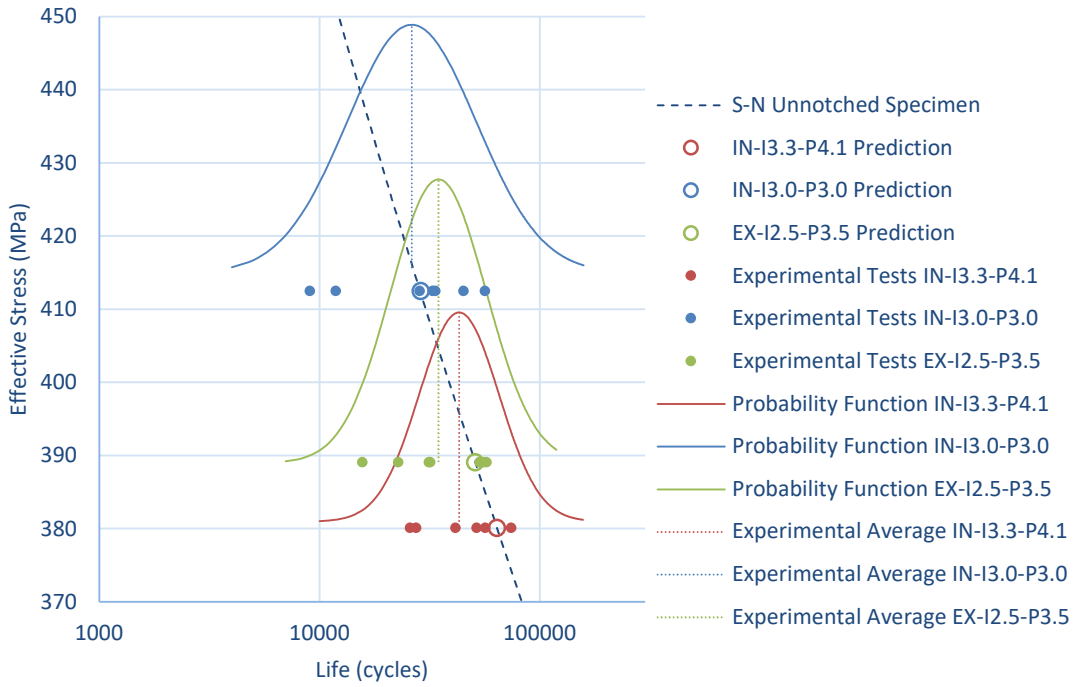

Figure 165. Experimental fatigue results of each dental implant tested and the fatigue life prediction by using the proposed methodology and Dang Van effective stresses.

Finally, Figure 166 shows all the experimental test results (vertical axis) versus the corresponding fatigue life estimated by the methodology (horizontal axis) using Findley method. Figure 167 does the same for Dang Van method. The 45-degree blue line represents a perfect methodology-experimental match (experimental life equal to the life predicted by the methodology). As it was concluded in Chapter 3, a perfect correlation is virtually impossible because of the inherent dispersion of the fatigue phenomenon,[55] as well as the scatter of the torque-preload ratio in screwed joints.[3,45] However, taking into account the aforementioned dispersion sources, the prediction can be considered to be appropriate.

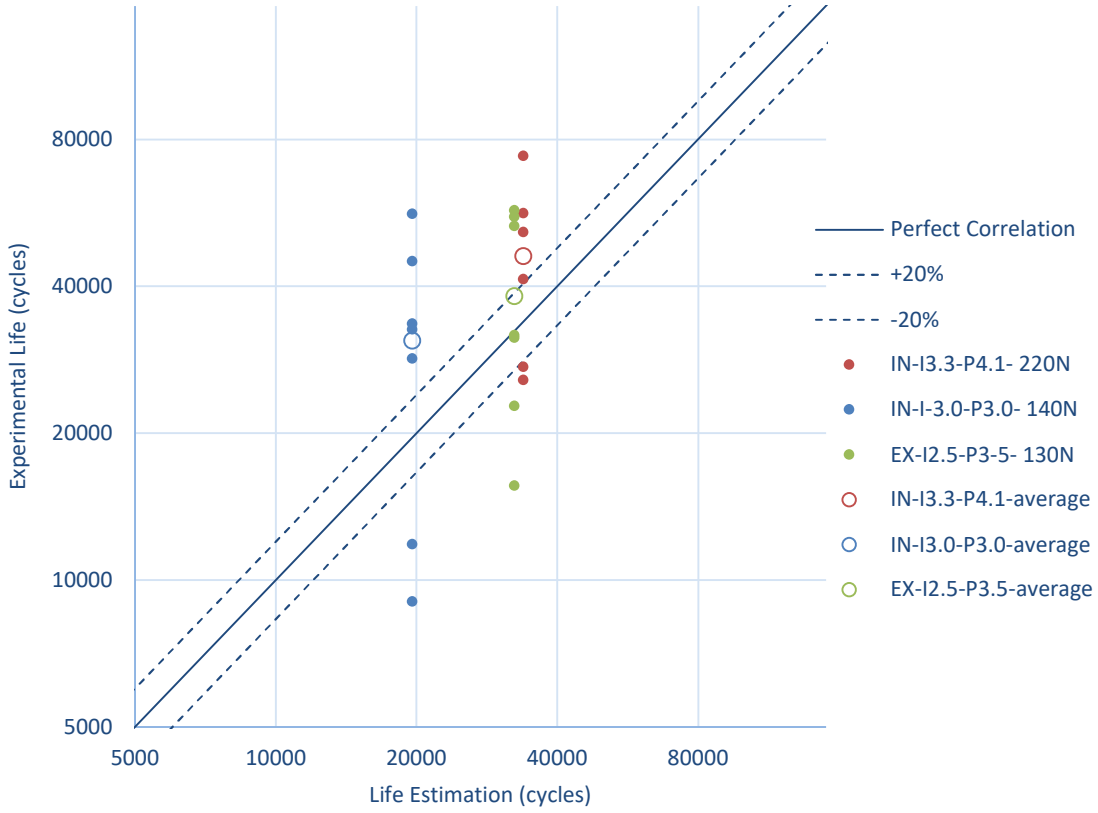

Figure 166. Experimental results versus methodology life prediction (Findley).

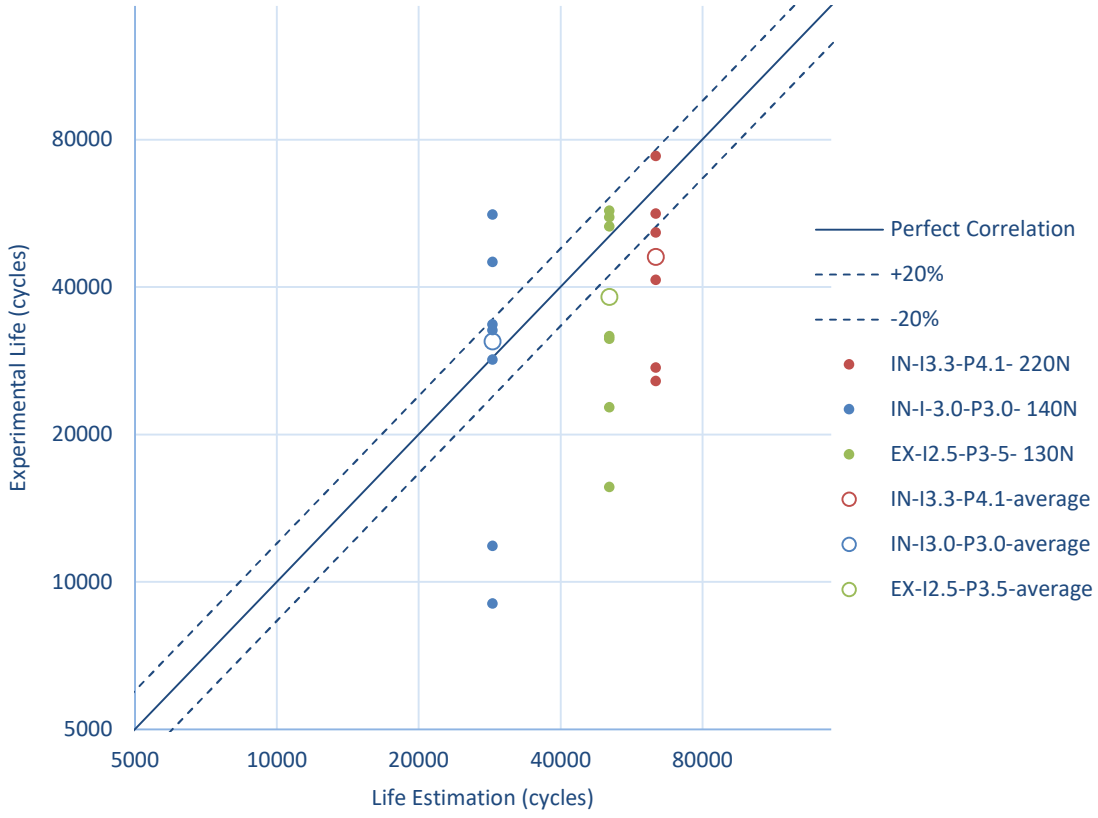

Figure 167. Experimental results versus methodology life prediction (Dang Van).

5.5 Conclusions

In this chapter, a methodology is presented to predict the fatigue life of dental restorations in which the critical component is the dental implant. This methodology is based on two well distinguished steps.

First, the fatigue behavior of the material the implants studied are made from is analyzed. In addition to this, the effect of stress concentrations on fatigue behavior is evaluated. This study has shown that the relationship between the fatigue behavior of a notched and an unnotched specimen remains constant throughout the cycles in the case of the analyzed CP4 Titanium. This does not have to be so; in some books it is assumed that this ratio is equal to one in the first cycle and then increases until reaching the fatigue limit. Other studies suggest that the ratio is equal to one at 1000 cycles and then it increases. However, these are assumptions to use with theoretical S-N curves, with it being more thorough to make - as has been done in this chapter - a campaign of experimental fatigue tests and determining real behavior. In this particular case, the curves were parallel, but the behavior could be very different for any other material.

Second, the 6 stress components in the vicinity of the notch of the same specimens experimentally tested are obtained by FEA. Then, the FEA results were post-processed, obtaining the equivalent stresses from Findley and Dang Van critical plane methods for each of the elements selected in the vicinity of the notch. Then, the TCD is used, applied at the volume of a sphere (Volume Method), and a linear model that relates the critical distance to be used in fatigue calculations with the normalized stress gradient at the root of the notch is proposed, following the same direction as recent investigations.[302–305] Once the normalized stress gradient has been calculated, the proposed model provides the critical distance to be used for fatigue calculations. Then, the effective stresses corresponding to the experimental fatigue life are obtained.

Regarding the TDC, Susmel[94] proposes also using it for finite life by using a linear model that relates the critical distance and the number of cycles (in log-log scale). However, in the case of the material studied in this chapter, the stress concentration effect is virtually constant throughout the number of cycles, as demonstrated in section 5.1 and reiterated at the beginning of this section. However, if the methodology is to be used to predict the fatigue life of dental implants made from another material, there is the possibility that this constant stress concentration effect cannot be assumed and the procedure proposed by

Susmel[94] must be followed, resulting in a more complex process. Regarding multiaxial fatigue methods, as explained in section 1.3.2.4.3, these are normally used for infinite life; i.e., to determine whether a part will survive or not. Socie,[110] however, proposes using any of the critical plane methods in section 1.3.2.4.3 and applying the S-N curve to calculate finite life as well.

Regarding the accuracy of the methodology, a fatigue life prediction very close to the average of the experimental tests was obtained, taking into account the scatter inherent to the fatigue phenomenon, the difference in results from the multiaxial fatigue methods themselves due to the complexity of the phenomenon, and the effect on fatigue behavior of the surface treatments performed only on dental implants but not on standardized specimens, even though the experimental results proved to be very minor if not negligible. Taking all of this into account, it would appear that there is little room for improvement in the results, beyond validating them with other dental implant models. In any case, the consideration of other critical plane methods in this methodology is established as a future line.

6 Microgap at the Implant-Abutment Connection

As already mentioned in section 1.6.3, screw-retained dental restorations are subjected to microgap formation at the IAC. These microgaps are cavities in which bacteria can colonize or even pass into the implant, proliferate, and seriously compromise the success of the dental restoration. Therefore, the goals of dental implant manufacturers are to design a connection that minimizes the value of this microgap to avoid possible complications over the lifetime of dental restorations.

This chapter analyzes the microgap of different dental restorations under different loads applied in-situ. For this purpose, a portable device capable of applying static loads on any dental restoration has been developed. Since it is portable, the device could be placed in a Micro-CT cabin, so radiographs of the microgap at the IAC could be taken on different implants under different applied loads. The purpose of this chapter is to compare microgap values on different dental restorations and to evaluate the effect of parameters such as implant body diameter, platform diameter and the use of a transepithelial element between the implant and the abutment on microgap formation. The study was experimental, rather than numerical, in order to realistically consider the effects of torque-preload scatter and manufacturing tolerances. This study was carried out entirely at the University of Würzburg (Germany) in collaboration with Professor Simon Zabler and his X-ray microscopy team (Lehrstuhl für Röntgenmikroskopie).

6.1 Introduction

As mentioned in section 1.6.3, dental restorations are subject to microgap formation at the IAC, which may be caused by irregularities in the IAC contact surfaces[21,22] and/or by the application of occlusal loads[49,50] along with an inappropriate tightening torque.[3,266,267]

After a preliminary observational study, it has been determined that different types of microgaps can be distinguished among butt-joint connections, depending on the load applied and the size of the gap generated in the connection. Elastic microgaps are caused by low to moderate occlusal loads, which are usually the most frequent. This microgap disappears when the force does too, resulting in a large and intermittent microgap. Plastic microgaps occur as a result of high or very high occlusal loads, which are less frequent. When the load is applied, the deformation will have an elastic and a plastic component, leading to a very high microgap. When the force ceases, the elastic component disappears but the plastic component remains. This microgap is usually small but permanent unless the dental restoration has collapsed, in which case the microgap will be large and would be called a macrogap. Finally, microgaps resulting from a mismatch in the IAC appear when the prosthetic components are mounted on the implant and are caused by inappropriate tolerances, an irregular surface finish or, directly by a poor design. They are therefore very small but permanent microgaps.

As explained in the literature review in section 1.6.3, microgaps can seriously compromise the success of dental restorations by creating a cavity that favors bacterial colonization.[7–11] This can lead to peri-implantitits,[30] the main cause of implant loss.[31–33]

This review has also explained that most of investigations study microgaps in the absence of occlusal loads,[9,10,21,22,29,31,33,206–215,217–222,224,225,228,229,231–233,235,237,238,240,242,243,245,248,258–260] which would be equivalent to measuring (or detecting) microgaps caused by implant and abutment mismatches. This may be caused by surface irregularities or poor tolerances. Other investigations study microgaps after having applied an external cyclic load,[223,226,227,230,234,236,239,241,244,246,247,249,251,256,257,261,262] in which case, what is being measured is the aforementioned residual plastic gap. However, elastic gaps have been investigated much less since the load must be applied at the time the measurement is made (in-situ). This type of elastic microgap can seriously compromise the restoration as intermittent microgaps that open and close occur as masticatory loads are applied, creating a suction and pumping sequence that can project bacteria to the areas surrounding of the dental restoration.

Therefore, this chapter studies this type of microgap at IAC in different dental restorations. The microgap in the IAC was measured by using hard X-ray radiography obtained at the same time as the load was applied (in-situ). From the tests, the effect of the diameter of the implant body, the diameter of the

platform or the use of a transepithelial abutments on microgap formation instead of a directly attached implant-supported restoration is analyzed.

6.2 Experimental tests

As mentioned in the previous section, the effect of implant body diameter, platform diameter, and the use of transepithelial-supported instead of implant-supported restoration on microgap formation at IAC is investigated in this chapter. For that purpose, four dental restorations were studied: IN-I5.5-P5.5, IN-I5.5-P4.1, IN-I4.5-P4.1, and MULTI-IM-H2 (see Figure 168), whose chemical composition is provided in Table 4. Further information about these dental restorations may be found in section 3.2. Microgaps were compared by grouping the restorations in pairs as illustrated in Figure 168, thereby isolating the variables of interest: implant body diameter (IN-I4.5-P4.1 versus IN-I5.5-P4.1), implant platform diameter (IN-I5.5-P4.1 versus IN-I5.5-P5.5), and the use of a transepithelial-supported restoration instead of an implant-supported restoration (IN-I4.5-P4.1 versus MULTI-IM-H2).

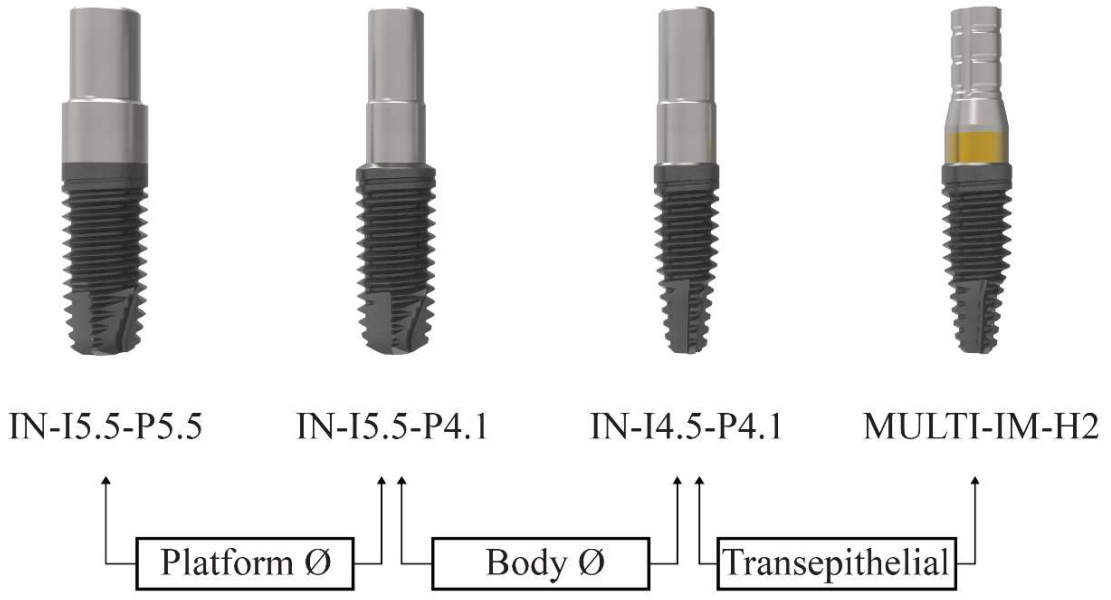

Figure 168. All dental restorations under study coupled isolating one variable in each case: Platform diameter, implant body diameter, and the use of a transepithelial-supported restorion versus an implant-supported restoration.

As mentioned in the previous section, the aim of this study was to evaluate the in-situ microgap; i.e. while the load is being applied. For that reason, a special

portable device (see Figure 169) was designed and manufactured to perform a static load meeting the requirements of ISO 14801,[141] described in section 1.6.1. Due to the small dimensions and weight of the portable device, unlike bigger testing machines, it can be easily placed into the cabin of the MicroCT to obtain the X-ray images. The device consists of two fixed plates (upper and lower) and two cylindrical guides. Static load is applied by tightening a bolt that compresses a spring, which in turn transmits this load to the movable plate (in the middle) and then to the dental restoration. The load applied to the movable plate is measured by load cell Interface INF-USB2-C10-2, capable of measuring loads of up to 900N. On the other side of the movable plate, i.e., between the plate and the implant, there is a linear bearing so that the implant can be deformed without any lateral restrictions on the contact. The movable plate is guided on the vertical axis (and powered by the tightened bolt) by means of two linear bearings and the cylindrical guides. The friction on the guides was proved to be negligible while the weight of the movable plate (that has influence on the load transmitted to the implant but not measured by the load cell) was also considered and added to the load cell recordings. Each dental restoration was placed in the specimen holder and tightened at the torque recommended by the manufacturer (35Ncm for the prosthetic screws attached to the implant and 20Ncm for the screw attached to the transepithelial). Next, a hemispherical device was assembled on the top of the dental restoration so that the load is applied normal to the hemisphere, at 30° to the restoration axis as established in ISO 14801.[141]

Finally, the loading device (see Figure 170) was placed in the Micro-CT cabin of Lehrstuhl für Röntgenmikroskopie (Würzburg University, Germany) to measure the IAC microgap with an applied load (in-situ). The X-ray cone-beam was thereby orthogonal to the restoration and to the load axis, and parallel to the microgap opening forming at the IAC.

The X-ray parameters were 180kV anode voltage with a target power of approximately 4W (transmission target in micro-focal mode). The X-rays were pre-filtered by 2mm of copper and 1mm of steel, the detector was at a focus-detector distance of 550mm, which yielded 18.75 geometric magnification, hence 4μm/pixel sampling at the IAC level (detector pixel-size was 74.8μm/pixel). Transmission images of the loaded IAC were taken with 500ms exposure time and 20-times averaging, hence 10s total exposure time. All images were normalized with respect to pixel dark current and detector brightfield intensity (both 250 times averaged).

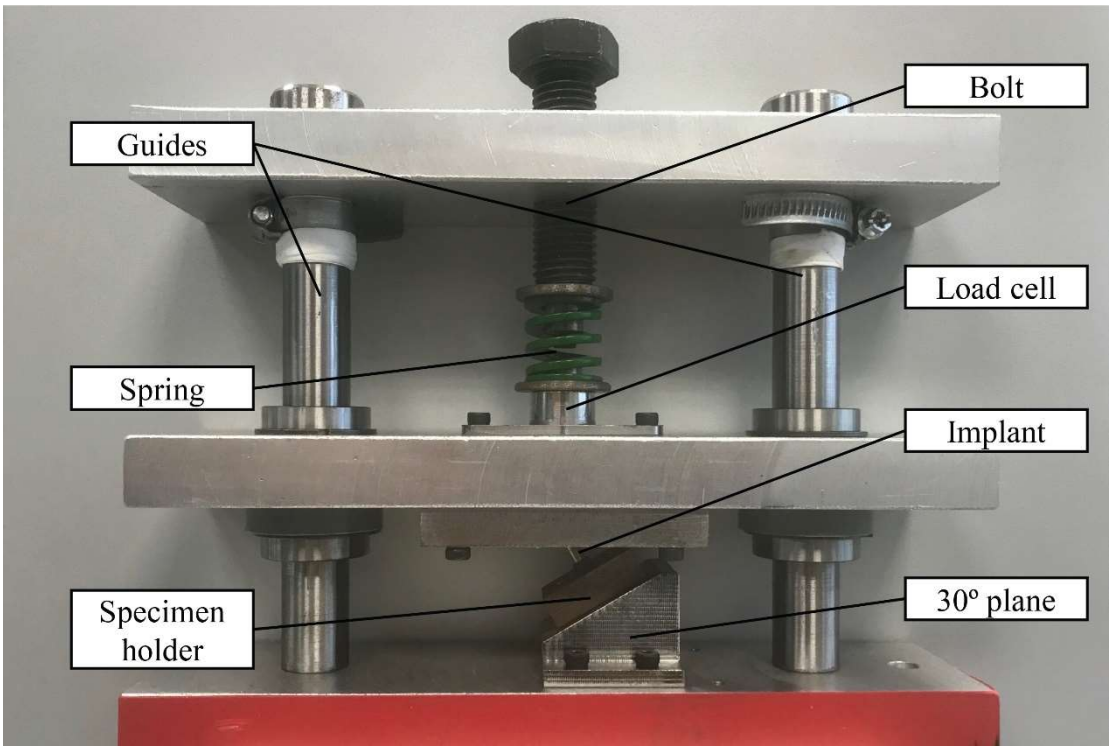

Figure 169. Portable device able to perform a static load meeting the requirements in ISO 14801.[141]

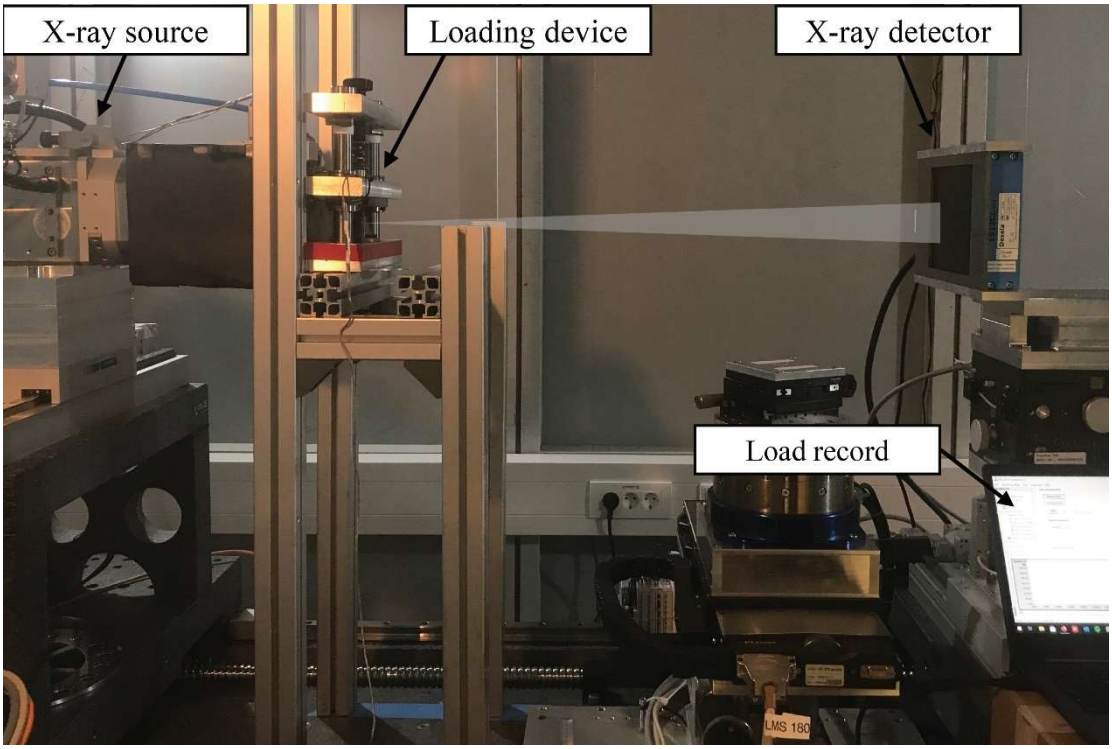

Figure 170. Experimental setup in the Micro-CT cabin.

In this investigation, specimens were loaded up to 400N or 500N, depending on the restoration, with load level increases of 50N. A radiography was obtained for every load step, and the IAC microgap was computed from the normalized

X-ray radiographs by measuring the angle formed between the three points marked in Figure 171, with the following expression:

$$\text{Microgap} = \sin(\alpha) \cdot \emptyset_{platform} \quad (145)$$

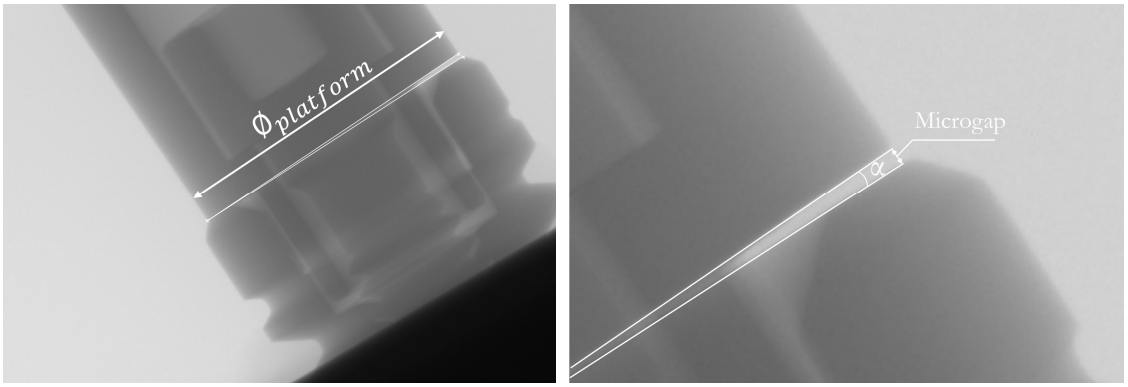

Figure 171. Radiograph of loaded implant at 4µm/pixel sampling. Gap measurement. A, General view. B, Detail of the IAC microgap. Measurements were taken manually using ImageJ2 software.

Figure 172, Figure 173, Figure 174, and Figure 175 show the microgap measurement results for IN-I4.5-P4.1, IN-I5.5-P4.1, IN-I5.5-P5.5, and MULTI-IM-H2, respectively. 4 specimens (plotted with different markers) were tested for each dental restoration under study, with load steps of 50N. Measurements below the indicated range were not considered because the microgap size was lower than the resolution of the images obtained. Besides this, the maximum load level was set to 400N or 500N depending on the dental restoration, as plastic collapses were reported for higher loads. A power regression function was assigned to the results of each dental restoration, shown as solid lines. The scatter among the microgap results of each of the 4 tests for each restoration is understood to be mainly due to the dispersion in the prosthetic screw preload. In effect, although the same tightening torque was applied to all the specimens, scatter in the resulting screw preload is unavoidable, mainly due to the coefficient of friction scatter.[3] The preload is responsible for joining the abutment to the implant, thereby providing structural integrity to the IAC,[306] therefore a smaller preload will result in a larger IAC microgap for the same external load.[23,185] To a lesser extent, manufacturing tolerances on the abutment and implant contact surfaces also lead to scatter in the microgap results. Both sources of scatter are not only unavoidable but also representative of actual dental restoration performance since they will also exist in-vivo. Other small sources of dispersion are attributable to the experimental setup, such as errors in specimen positioning (small deviations with respect to the nominal inclination of 30º, already

considered in ISO 14801[141]) or in the load cell measurements. Finally, for comparison purposes, Figure 176 shows all the power regression models together.

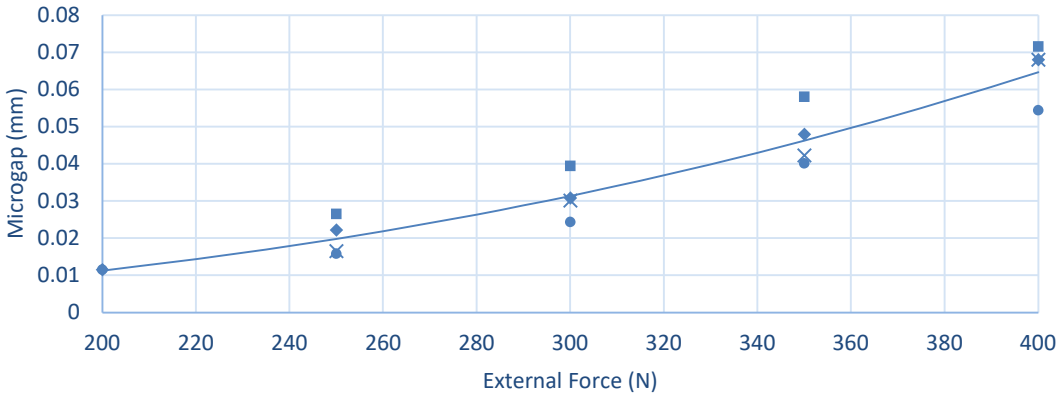

Figure 172. IAC microgap measurements versus applied load and the power regression model for IN-I4.5-P4.1. Each marker corresponds to a different sample.

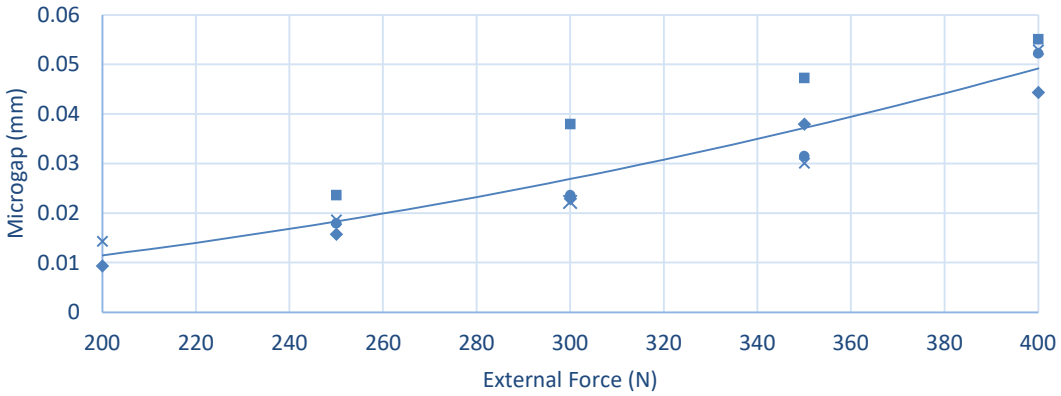

Figure 173. IAC microgap measurements versus applied load and the power regression model for IN-I5.5-P4.1. Each marker corresponds to a different sample.

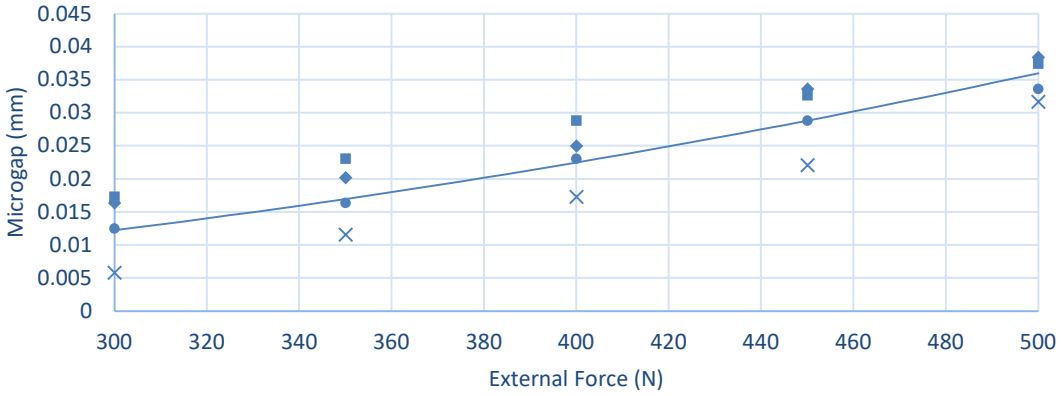

Figure 174. IAC microgap measurements versus applied load and the power regression model for IN-I5.5-P5.5. Each marker corresponds to a different sample.

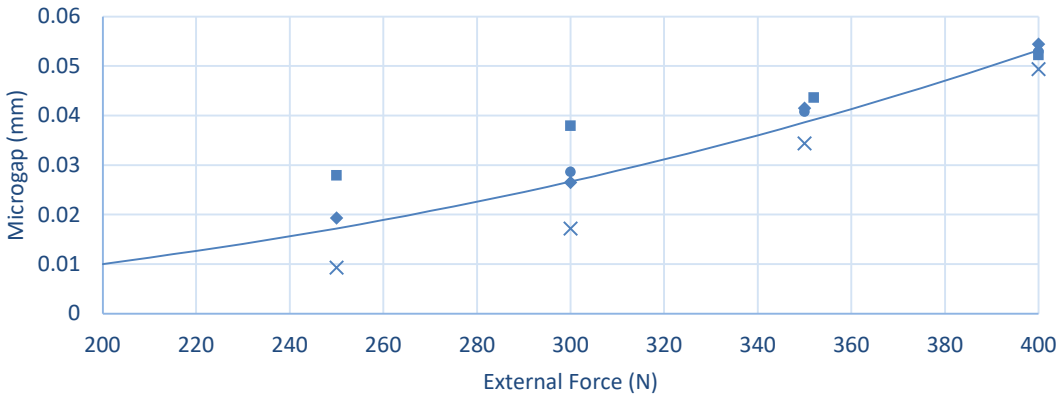

Figure 175. IAC microgap measurements versus applied load and the power regression model for MULTI-IM-H2. Each marker corresponds to a different sample.

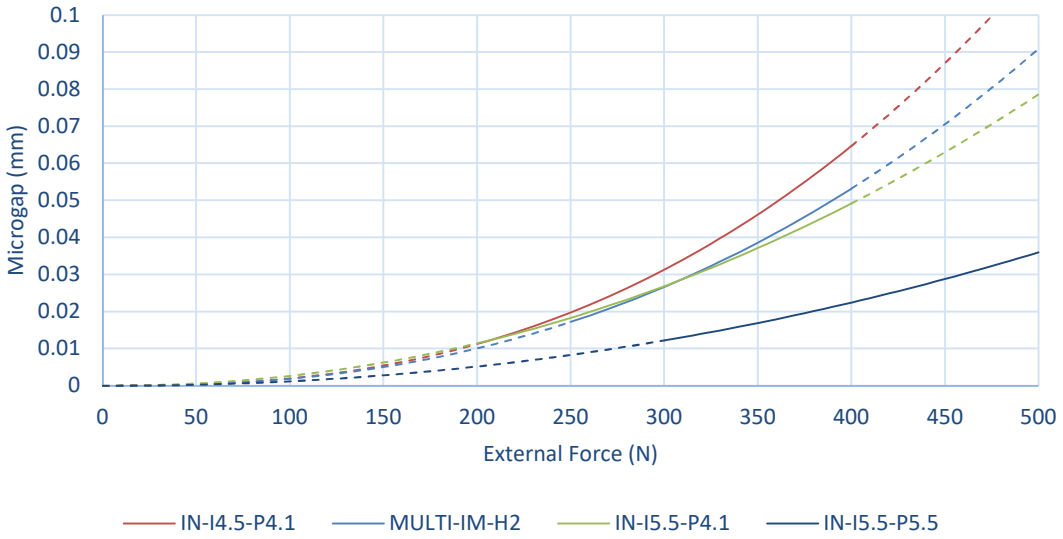

Figure 176. Power regression models of microgap value versus external applied load for each dental restoration under study. Solid lines correspond to the tested load range. Dashed lines correspond to model extrapolation.

In order to analyze the effect of each variable, the experimental results were converted into a logarithmic scale and compared via ANCOVA. In addition to this, the microgap values obtained experimentally were compared by means of t tests (α=.05) and the differences between the means were calculated.

Regarding the effect of using a transepithelial-supported restoration instead of an implant-supported restoration on microgap formation, the performance of IN-I4.5-P4.1 and MULTI-IM-H2 (Figure 172 and Figure 175) were compared. The first null hypothesis of the ANCOVA was accepted (P=.767); i.e., it can be assumed that the slopes were equal, and the second null hypothesis was rejected (P=.038) therefore assuming that the microgaps obtained in these two dental

restorations were statistically different. A microgap reduction of 12% between IN-I4.5-P4.1 and MULTI-IM-H2 was identified at 300N. Nevertheless, the null hypothesis of the t test was rejected (P=.527); i.e., the values of both restorations cannot be guaranteed to be statistically different. In contrast, at 400N microgap reduction increased up to 20% and the t test accepted the null hypothesis (P=.044).

Regarding the 1mm diameter increase of the implant body, the microgaps of IN-I4.5-P4.1 and IN-I5.5-P4.1 (see Figure 172 and Figure 173) were compared. In this case, ANCOVA could not guarantee that the slopes of both models were statistically equal (P=.113) and therefore the difference in terms of microgaps cannot be studied in this way. A 14% reduction between IN-I4.5-P4.1 and IN-I5.5-P4.1 was identified at 300N. Again, the t test rejected the null hypothesis (P=.395). However, at 400N, a 22% microgap reduction was identified and the null hypothesis was accepted (P=.024).

Finally, IN-I5.5-P4.1 and IN-I5.5-P5.5 (see Figure 173 and Figure 174) were compared to quantify the effect of increasing implant platform diameter by 1.4mm. ANCOVA accepted the first null hypothesis that the slopes were equal (P=.973) and rejected the second null hypothesis (P<.001) guaranteeing a difference in terms of microgaps. A 51% reduction between IN-I5.5-P4.1 and IN-I5.5-P5.5 was identified at 300N and 54% at 400. In both cases the null hypothesis was accepted (P=.031 and P<.001, respectively).

6.3 Conclusions

Increasing implant body diameter by 1mm reduced IAC microgaps between 14 and 22% in the load range studied. To the author´s knowledge, no other studies analyzed the effect of the implant body diameter on microgap size. However, various studies demonstrated that increasing the implant body diameter significantly improves the overall mechanical performance of dental restorations. The reason for this is that, from a mechanical point of view, the stresses on the implant decrease,[171] which improves the static and fatigue response of the restoration.[172,173] In parallel, from a clinical point of view, increasing the implant diameter increases the implant-bone contact surface, thus reducing bone stresses[165–168] and enhancing initial stability.[169,170] As a drawback, this recommendation is limited by horizontal crestal bone atrophy and a restricted edentulous area.[278] Furthermore, narrower implants decrease the need for bone augmentations, reducing surgical invasiveness.[279]

Increasing platform diameter led to the most remarkable IAC microgap reduction. A 51-54% reduction was found when the platform diameter was increased by 1.4mm. Again, no studies were found to directly agree with this conclusion, even though some studies proved that IAC platform diameter plays an important role on other mechanical aspects such as joint strength, joint stability and fatigue behavior.[13] Nevertheless, from a clinical point of view, the platform switching concept, where an abutment narrower than the implant is used, can reduce peri-implant bone loss.[182,183]

The use of a transepithelial-supported restoration instead of an implant-supported restoration significantly reduced microgaps, with 12-20% gap reduction in the load range tested. Thus, this may be a simple and effective strategy to reduce microgaps since no invasive actions are required by the clinician. Nevertheless, further research is necessary to ensure that using a transepithelial element does not compromise other mechanical aspects of dental restorations.

Finally, it also has been seen that under lower loads the differences among the dental restorations under study were small, except for the wide platform that showed a big difference, with the scatter being more relevant than the possible differences among the mean microgap values. Moreover, in this study, microgaps below 200N were not measured due to experimental testing limitations. Even though it may be assumed that the conclusions obtained for high loads can be extrapolated to lower loads, if more confident microgap measurements under lower loads are pursued, further experimental tests would be necessary, using more advanced experimental technologies, such as a synchrotron hard X-ray radiography, which provides greater precision.[252] Another limitation of this study is that only one connection type was investigated. Other connection designs such as external butt joints or conical connections could be analyzed in further research.

7 Self- loosening of the prosthetic screw

As discussed in section 1.4, dental restorations are subjected to variable masticatory forces throughout their life span. These forces can cause relative displacement between the abutment, the screw and the implant, overcoming existing frictional forces and allowing the screw to slip, leading to a progressive loss of preload. As seen in sections 1.6.1, 1.6.3, and 3.4.1, a proper preload is crucial for optimum fatigue behavior and to reduce microgap formation. Therefore, it is of vital importance to avoid self-loosening of prosthetic screw in dental restorations as far as is possible.

In section 1.6.2, an explanation was provided as to how there are numerous studies analyzing the phenomenon of self-loosening in the prosthetic screw of a dental restoration. These studies are carried out from different perspectives. On the one hand, there are retrospective studies, which indicate how frequent the prosthetic screw loosening problem occurs in clinical cases (in-vivo). On the other hand, most of the studies found are in-vitro experimental studies that analyze the effect of different parameters of the restorations on the loosening of the prosthetic screw such as the effect of lubricants or saliva contamination, different screw materials and coatings, effect of re-tightening, etc.

Similar to the published studies on fatigue of dental restorations (see Chapter 3), these studies are useful for clinicians to consider the importance of the phenomenon, in this case the loosening phenomenon, and to take account of the keys to choose an appropriate dental restoration. However, in the dental implantology field, no studies have been found that go any further and analyze the screw loosening phenomenon in depth.

Beyond the field of dental implantology, there are numerous studies on screwed joints subjected to transverse loads that provide models by which to predict not only the conditions under which the screw loosening phenomenon occurs but

also the process of progressive preload loss. This PhD Thesis is based on the numerical model of Nassar, explained in detail in section 1.4, which can be used to calculate the loosening (or untightening) torque T_L necessary to loosen a screw subjected to a given transverse force F_t, and can even be used to calculate the critical value at which screw self-loosening occurs in the absence of an external untightening torque (value for F_t for which $T_L = 0$). However, the Nassar model requires numerical integration, which makes its use tedious. Moreover, this model requires the value of the transverse load F_t the screw is subjected to be known, and often, as is the case with dental restoration, obtaining this value from the external load applied on the screwed joint is not straightforward.

For all of the above, this chapter develops a methodology by which to predict the loosening phenomenon on prosthetic screws in dental restorations based on an existing analytical model (explained in section 1.4). To make its application more direct and simpler, simplifying the model by means of a parabola obtained by curve fitting is proposed, thereby avoiding numerical integration. This equation will be fed with the axial F_a and transverse force F_t reactions acting on the screw head contact as a consequence of the external load applied to the dental restoration, which will be obtained by means of a simple FEA. As a result, the methodology will predict whether or not the screw will loosen under the conditions studied. Finally, the methodology is experimentally validated against various tightening torque cases.

Therefore, the purpose of this chapter is to transfer current knowledge regarding the loosening phenomenon in the field of screwed joints to the dental implantology industry, adapting and simplifying an existing and proven model for direct, simple and versatile application.

Accordingly, section 7.1 provides details of the simplification process of the Nassar et al.[125,126] model by means of curve fitting, obtaining the equation for a parabola. Following that, section 7.2 presents the methodology for predicting screw loosening. In section 7.3, the methodology is validated by means of various case studies in which the predictions made using the methodology are compared with experimentally obtained results. Finally, section 7.4, draws conclusions about the methodology and highlights various clinical implications obtained using the methodology itself.

7.1 Simplified model for loosening torque determination under external loading

As mentioned in the introduction of this chapter, the self-loosening prediction methodology which will be detailed in section 7.2 is based on the analytical model of Nassar,[125,126] explained in section 1.4. It should be remembered that an external transverse load may help overcome the friction resistance on the screw head and thread contacts. Consequently, resistance torques under the screw head and on the thread contact surface T_h and T_t become smaller and therefore a lower loosening torque T_L is needed to untighten the screw, as can be deducted from equation (11).

The resistant torque under screw head T_h (calculated in the first term of equation (16) in the absence of external loads) can be calculated by using equation (95) when a transverse load F_{t_h} is acting under the screw head. Similarly, the resistant torque on the screw thread T_t (calculated in the second term of equation (16) in the absence of external loads) can be calculated using equation (120) when a transverse F_{t_t} is acting on the threads. Finally, the value of the pitch torque T_p remains constant and can be calculated as shown in the third term of equation (16), regardless of the transverse load acting on the screw.

Accordingly, the loosening torque T_L can be finally calculated by updating equation (16) by substituting the values of T_h and T_t obtained from equation (95) and equation (120), obtaining equation (130). The relationship can be plotted in the normalized graph shown in Figure 66, with $T_h/F_a - F_t/F_a$ and $T_t/F_a - F_t/F_a$ and the resulting $T_L/F_a - F_t/F_a$. Note that, in the absence of transverse load (F_t=0), the untightening torque values are those in equation (16), which correspond to the point indicated with a white triangle in the graph in Figure 66. In contrast, screw self-loosening occurs when the transverse load F_t reaches a critical value for which the external loosening torque T_L needed to untighten the screw is null, which corresponds to the point indicated with a black triangle in Figure 66, as explained in section 1.4.3.

This numerical model forms the basis of the mechanical foundations of the self-loosening phenomenon and quantifies the effect of different parameters. As a drawback, its application is not straightforward because the equations must be solved by using numerical integration.

To overcome this problem, the expressions $T_h/F_a - F_t/F_a$ and $T_t/F_a - F_t/F_a$ and the resulting $T_L/F_a - F_t/F_a$ (previously shown in Figure 66) were approximated by parabolic curves by means of curve fitting so that the loosening torque T_L can be predicted in a straightforward manner, obtaining equations (146) and (147), shown in Figure 177. The parabolas are defined by setting the vertex at the values of F_t/F_a where T_h and T_t drop to zero (horizontal axis) and forcing them to pass the values of T_h/F_a and T_t/F_a where F_t falls to zero (vertical axis):

$$\left(\frac{T_h/F_a}{\mu_h \cdot r_h}\right)^2 + \frac{F_t/F_a}{\mu_h} = 1 \tag{146}$$

$$\left(\frac{T_t/F_a}{\mu_t \cdot \frac{r_t}{cos\alpha}}\right)^2 + \frac{F_t/F_a}{\frac{\mu_t}{\delta}} = 1 \tag{147}$$

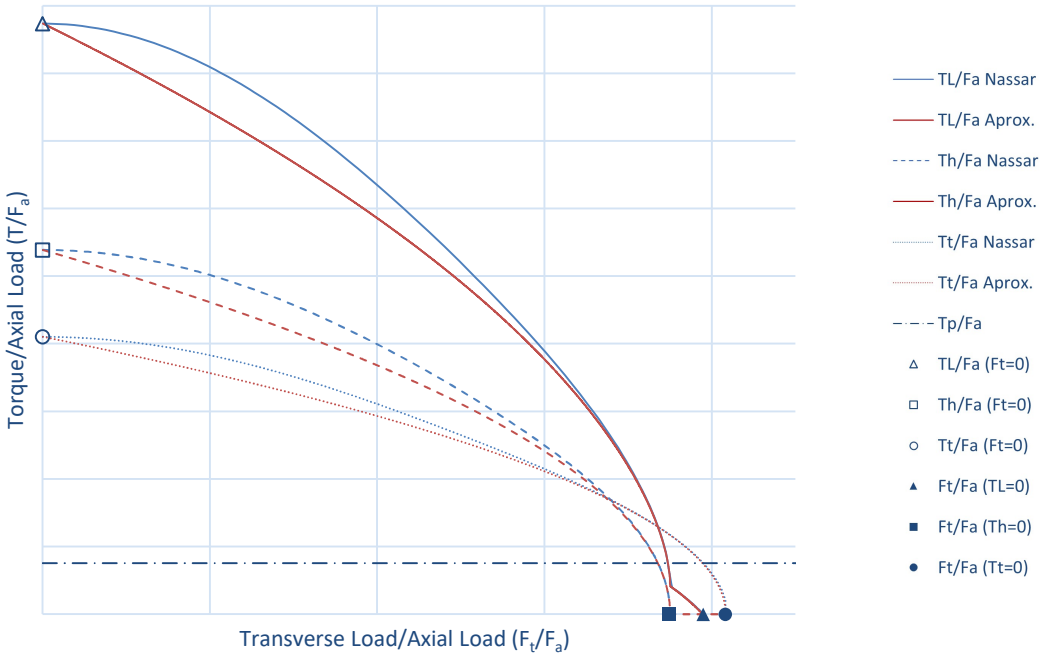

Figure 177. Torque versus transverse load: slip limit curves. Nassar model[125,126] and new equations approximated by parabolic curves.

Even though other geometrical curves, such as a rotated ellipse, provide a better overall approximation, there are two main advantages to using a parabola. First, its formulation is simpler, and leads to simple mathematical expressions for estimating screw self-loosening. Secondly, even though the parabola does not fit well for low values of F_t/F_a, the error for high values of F_t/F_a, where self-loosening occurs, is small since there is a good fit in that zone as shown in Figure 177. A wide parameter range was studied (with μ_h=μ_t=0.02-0.50, α=0-45°, β=2-12°) comparing both models (the numerical equation by Nassar and

the parabolic curve proposed here) with a maximum difference of 1.4% obtained.

Hence, equations (95) and (120) can be rewritten as:

$$T_h = \mu_h \cdot F_a \cdot r_h \cdot \sqrt{\langle 1 - \frac{F_t}{\mu_h \cdot F_a} \rangle} \tag{148}$$

$$T_t = \mu_t \cdot F_a \cdot \frac{r_t}{cos\alpha} \cdot \sqrt{\langle 1 - \delta \cdot \frac{F_t}{\mu_t \cdot F_a} \rangle} \tag{149}$$

It must be mentioned that the values of T_h and T_t cannot be negative and, therefore, once the expression between the Macaulay brackets becomes negative, the term is set to zero. Accordingly, the equation (130) can be simplified as follows:

$$T_L = \mu_h \cdot F_a \cdot r_h \cdot \sqrt{\langle 1 - \frac{F_t}{\mu_h \cdot F_a} \rangle} + \mu_t \cdot F_a \cdot \frac{r_t}{cos\alpha} \cdot \sqrt{\langle 1 - \delta \cdot \frac{F_t}{\mu_t \cdot F_a} \rangle} - (F_a \cdot tan\beta \cdot r_t) \tag{150}$$

It can also be noted that the three terms in equation (150) correspond to the ones in equation (16). Hence, a generalized Motosh equation can be considered to calculate the torque required to loosen a screw. Its main advantage is that, unlike the Motosh equation, this new expression also considers the effect of transverse forces F_t, and can even be used to calculate the value of this transverse force F_t at which loosening phenomenon occurs (F_t at which T_L=0). Unlike the Nassar model, in this case numerical integration is not needed.

7.2 Methodology to predict self-loosening of prosthetic screws on dental restorations

The previous section presented a simplified equation for calculating the loosening torque T_L that considers the transverse forces acting on the screw. Unlike in the case of some simple screwed joints, when it comes to dental restoration, it is difficult to estimate the forces acting on the prosthetic screw due to the complex geometry of the assembly and the load conditions. Hence, the most suitable way to obtain the axial F_a and transverse F_t forces acting on the screw (required to feed equation (150)) is by performing an FEA of the dental restoration. Section 2.2 explains how the FE model must be prepared. In short, dental restoration is modelled assuming half geometry and screw cylindrical threads. Screw preload is applied in a first load step while external

load is applied in a second load step. As explained, since half geometry is modelled, half values of preload and external load must be applied.

Once the FEA has been solved, the axial F_a and transverse F_t forces under the screw head are recorded. It should be noted that, as mentioned above, the axial load F_a may be different to the screw preload F_p, because both the axial and transverse components of the external force F may alter the initial preload of the screw.

Accordingly, F_t and F_a obtained from the FEA are entered in equation (150). If T_L>0, the dental restoration under study, assembled with tightening torque T_T and subjected to masticatory load F will not suffer screw self-loosening. Therefore, this methodology can be used either to compare two different dental restoration designs to find out which design will perform better against self-loosening (the one with a larger value of T_L) or to optimize the design of a dental restoration by analyzing the effect of each parameter on its performance against self-loosening (only focusing on the ones that have the greatest effect on T_L). In other words, this methodology can be used to evaluate improvements in the design of the dental restoration in order to improve performance against prosthetic screw loosening. Figure 178 provides a brief explanation of the steps the proposed methodology consists of.

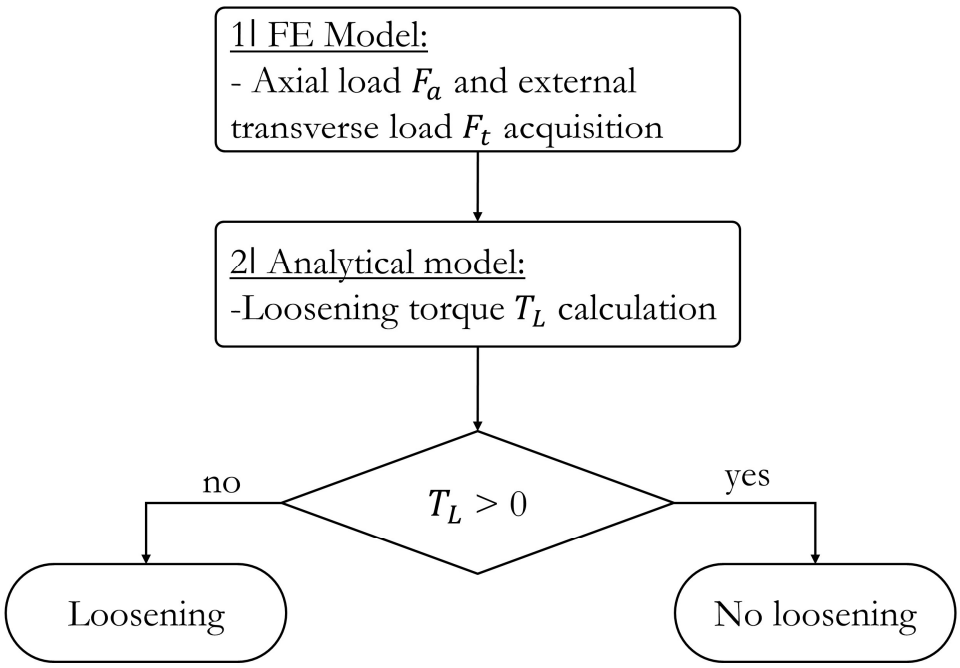

Figure 178. Steps of the methodology proposed.

7.3 Validation of the methodology

Having described the methodology, its accuracy will be tested in this section by analyzing the loosening phenomenon of a prosthetic screw when mounted on a previously known implant-supported restoration IN-I3.3-P4.1. This narrow dental restoration, already fatigue-tested in Chapter 5, comprises a BTI INTERNA IIPUCA3313 implant with a body diameter of 3.3mm and a platform diameter of 4.1mm, INPPTU44 abutment, and INTTUH prosthetic screw (see Figure 157A), whose chemical composition is included in Table 4.

In a preliminary study, it was seen that in IN-I3.3-P4.1 dental restoration under moderate external loads applied at 30° and following ISO 14801 standard,[141] the tightening torque recommended by the manufacturer (35 Ncm) is sufficient to prevent self-loosening. Higher load values might bring about self-loosening, but they are not permitted since they may structurally damage the dental implant, as seen in Chapter 5. As the purpose of this section is to validate the screw loosening methodology, some modifications were applied to promote the self-loosening phenomenon on the dental restoration under study. First, the screw tightening torque was reduced to 10, 15 and 20 Ncm. Then, the thickness of the abutment tetralobular connection was reduced by 0.19mm in diameter to allow bigger lateral movements of the abutment (see Figure 179). Finally, the cyclic external load F was applied in both directions (pure alternating sinusoidal force) on the bottom of the abutment perpendicular to the axis of the dental implant (i.e., with an inclination of 90°) rather than applying it at 30° as indicated in ISO 14801 standard.[141]

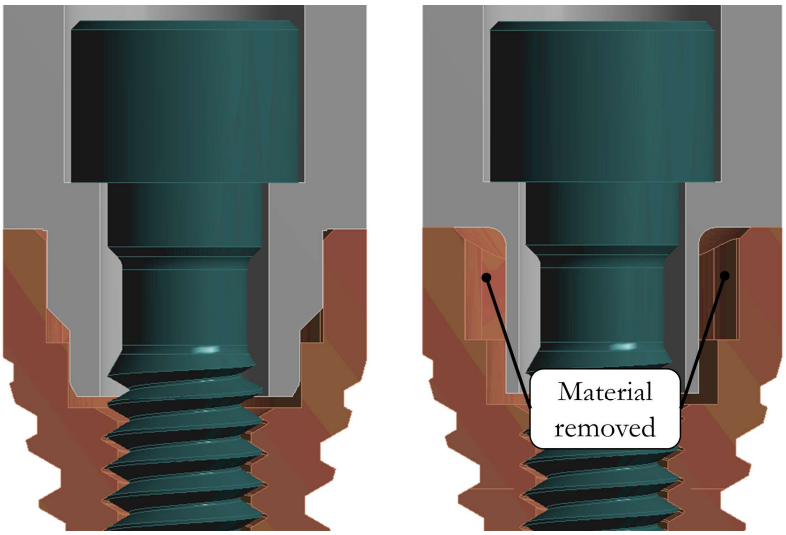

Figure 179. IN-I3.3-P4.1 dental restoration. A, Original tetralobular connection. B, Modification on abutment tetralobular connection to bring about self loosening.

The validation process started by applying the methodology to the three cases under study; i.e. 10, 15, and 20Ncm tightening torques applied to the IN-I3.3-P4.1 dental restoration. First, an FEM of the restoration was created following the recommendations in section 2.2. Then, the preloads corresponding to each of the three tightening torques were calculated according to equation (131), with 232N, 349N, and 465N for 10Ncm, 15Ncm, and 20Ncm, respectively. Since half geometry is modelled, half preload was applied to the FEM. In a second load step, an increasing external load was applied from 0 to a high enough value of F (half load since half geometry is modelled). The load was applied to the abutment through the ring shown in Figure 180 in order to reproduce the experimental conditions described before. Further information regarding materials, contacts, and meshing is explained in section 2.2. Finally, once the three FEA were solved, axial load F_a and transverse load F_t acting under the screw head contact were recorded for the wide range of applied external load F.

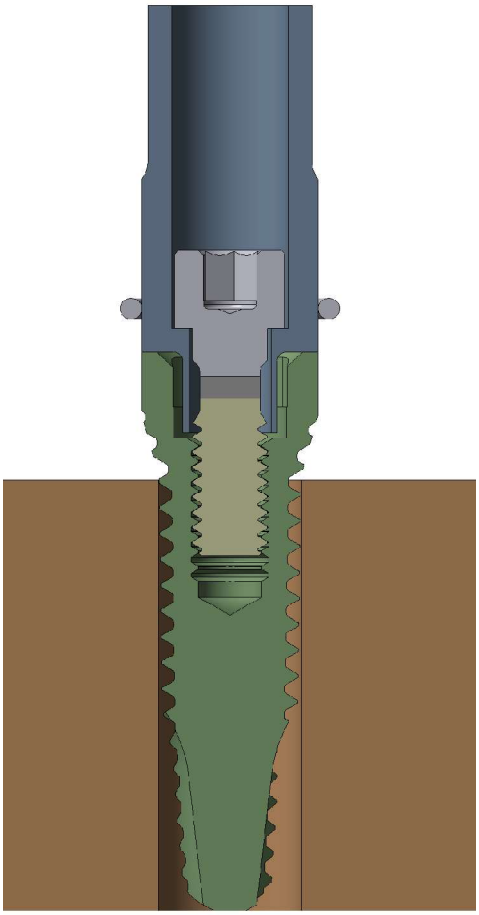

Figure 180. FE model of IN-I3.3-P4.1.

Once the values of the axial load F_a and the transverse load F_t were recorded for each value of the external load F, equation (150) must be fed to obtain the

value of the loosening torque T_L. This process must be repeated by increasing the external load F (more precisely, its corresponding axial load F_a and the transverse load F_t recorded) until T_L falls to zero. Table 23 shows the value of the external force F at which the T_L falls to zero; i.e. when the screw self-loosening process starts. The corresponding axial load F_a and transverse load F_t under the screw head for each of the three tightening torques analyzed is also shown.

Table 23. Predicted external load values that cause self-loosening in the dental implant under study at each tightening torque: 10, 15, and 20 Ncm.

T_T (Ncm)	F_{pred} (N)	F_a (N)	F_t (N)
10	64.5	217.7	36.1
15	96.7	326.1	53.7
20	128.3	433.9	72.6

Then, the next step was to experimentally verify the predicted values of the external forces F_{pred} that cause self-loosening for the three initial tightening torques. First of all, a criterion must be established to determine experimentally whether loosening has occurred on the dental restoration. Experimentally, loosening is usually detected and quantified by measuring the change of axial load on the screw by means of gauges.[307] Unfortunately, screws in dental implants are very small and barely accessible, so the option of installing strain gauges was discarded. As a well-established alternative in dental implant literature, the untightening torque after a number of external load cycles can be measured, since torque is proportional to preload.[38,112,125–127,308] Accordingly, 30 tightening and untightening operations were performed before testing (without applying external load cycles between both operations) in each preload case in order to set the mean value of the loosening torque T_{Li} (hereinafter referred to as initial untightening torque) and its standard deviation σ, inherent to the tightening operation.[3] T_{Li} values of 7.45, 11.6 and 16.0Ncm with standard deviations of 0.4, 0.5 and 0.6Ncm for the 10, 15 and 20Ncm tightening torques were obtained, respectively. Figure 181 shows the scatter of untightening torques measured for each tightening torque.

Subsequently, the self-loosening experimental tests were carried out by applying a cyclic load on the implant using the INSTRON 8801 test bench as explained in section 2.4.2.1. In short, the dental restoration was positioned horizontally using a special fixture tooling designed and manufactured specifically for these tests. This tooling transmits the external load F applied by the test bench vertically to the bottom of the abutment as shown in Figure 82. A steel ring is installed around the abutment outside the surface at 1mm from the IAC to

ensure a point load application on the bottom of the abutment. Under these deliberately unfavorable conditions, screw self-loosening occurs under reasonable external load magnitudes, whereby the methodology can be experimentally validated.

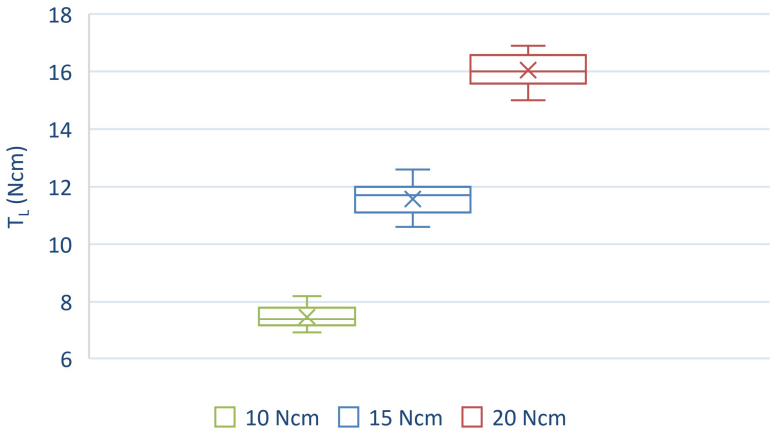

Figure 181. Box and whisker plot of all untightening operations performed before cyclic loading.

The cyclic load was applied to the tested dental restoration. Preliminary results indicated that, for the dental restoration tested in this study, when self-loosening occurs, 1000 cycles were enough to bring about significant loosening. Accordingly, in each experimental test, the final untightening torque T_L was measured after applying 1000 load cycles and compared with T_{Li}. Self-loosening was considered to take place if $T_{Lf} < T_{Li} - 2\sigma$. The 2σ criterion was established assuming normal distribution of the untightening torque values[3] and assuming that the probability of fulfilling such criterion without self-loosening occurring is only 2.1%. This procedure was repeated in the 30 tests for each of the three initial tightening torques. Furthermore, in order to experimentally obtain the critical external load value that causes self-loosening F_{exp} and compare it with the theoretical one F_{pred}, a method similar to the staircase method under fatigue was used.[62] This procedure, as explained in section 1.3.1.1, is widely used in fatigue testing to obtain the fatigue limit value. Accordingly, an initial arbitrary external load F is applied in the first test; if the screw self-loosens, the external load is decreased by 5N; if it does not, the external load is increased by 5N. Figure 182 shows the experimental results: tests where self-loosening occurred are marked with an 'x', while 'o' indicates tests with no loosening. Finally, the external load which causes self-loosening experimentally F_{ex} is calculated as the average of the values indicated with black marks in Figure 182 while the grey marks are not regarded. Table 24 summarizes the values of F_{exp}, their

corresponding standard deviations σ_{exp} and the difference between the experimental F_{exp} and predicted F_{pred} results.

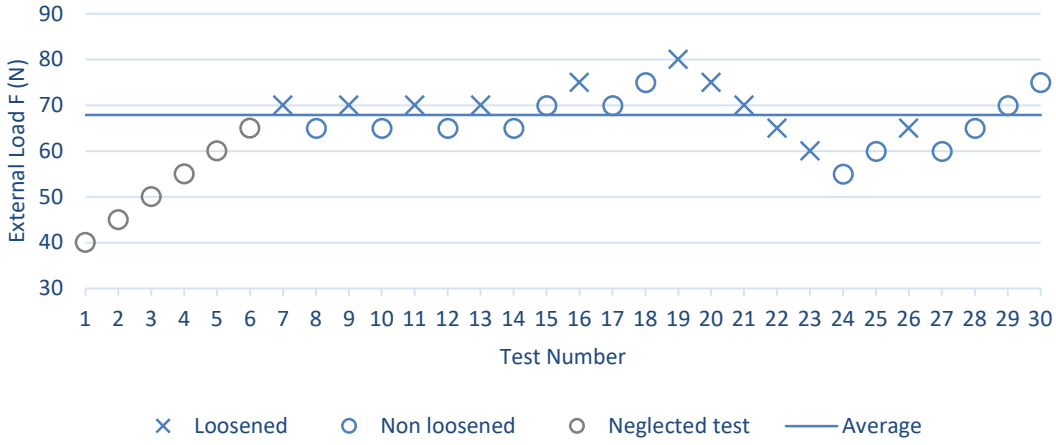

A)

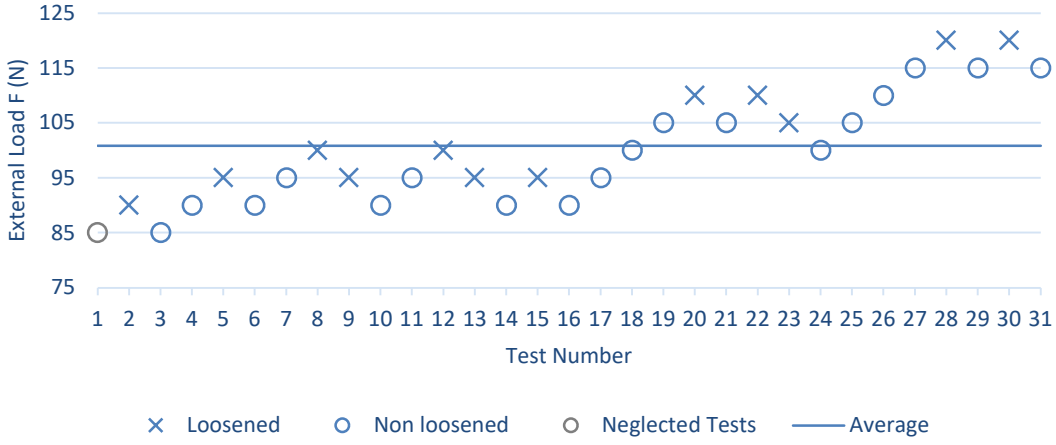

B)

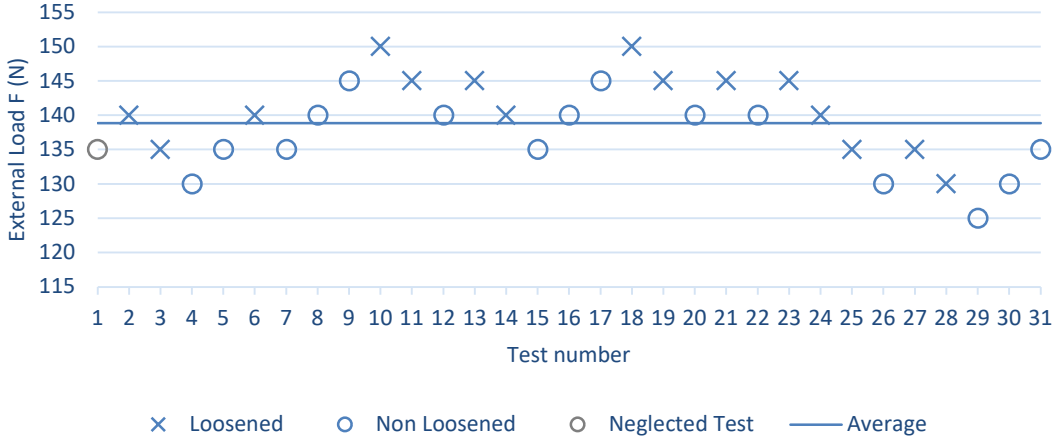

C)

Figure 182. External load values that cause self-loosening obtained by using the staircase method at three tightening torques. A, 10Ncm. B, 15Ncm. C, 20Ncm.

Table 24. External load values that cause self-loosening in the dental implant under study: methodology prediction versus experimental results.

T_T (Ncm)	F_{pred} (N)	F_{exp} (N)	σ_{exp} (N)	Error (%)
10	64.5	67.9	5.9	5
15	96.7	100.8	9.9	4.1
20	128.3	138.9	6.2	7.6

The sound correlation between the theoretical F_{pred} and experimental F_{exp} results validate the proposed methodology. Moreover, the theoretical results obtained by using the simplified approach F_{pred} were compared with the results of the numerical model of Nassar et al.[125,126] with a difference of less than 1% obtained in all the cases studied in this investigation.

7.4 Conclusions and clinical implications

The experimentally validated methodology developed in this PhD Thesis can be used to predict self-loosening of dental restorations. In this sense, it is an extremely useful, efficient and versatile design tool for dental implant manufacturers and designers to select the appropriate geometry, thread configuration, coefficient of friction, or screw tightening torque in order to minimize screw self-loosening problems and consequently guarantee the long-term stability and clinical success of dental implant fixation.

The proposed methodology is able not only to predict self-loosening under certain working conditions, but it can also be used to understand how each variable affects the screwed joint performance against self-loosening. From equation (150) it can be deducted that a high preload is recommended to avoid screw loosening. This conclusion agrees with Siamos et al.[205] and Guda et al.[309] Coefficients of friction of the screw head and thread contacts μ_h and μ_t are also found to have a significant effect on performance against self-loosening. Therefore, for a given preload, a high coefficient of friction is recommended to avoid screw loosening according to the presented analytical tool and in accordance with Wu et al. and Elias et al.[201,202] There are some other studies in which the coefficient of friction is reduced in the screwed joint contact by a coating or lubrication, obtaining better performance against self-loosening.[310,311] This seems to disagree with the last statement. Nevertheless, in those studies different coefficients of friction are studied for the same tightening torque, rather than the same preload. Hence, the results are not comparable since the coefficient of friction also affects the obtained preload.[5,312] Evidently, a higher

tightening torque will lead to a higher preload and, therefore, to a better response against self-loosening.

The amount of transverse load withstood by the screw head also plays an important role in self-loosening.[38,191,196,204] From equation (150) it can be concluded that a robust design where the screw head suffers the least transverse load possible is desired since transverse slippage causes rotation, preload loss and, therefore, screw loosening. Interesting future research would be to find an optimal IAC design to ensure the best performance against self-loosening.

Finally, thread parameters also affect the performance of screwed joints against self-loosening. On the one hand, for the same preload value, a small thread pitch helps to prevent self-loosening. According to Nassar et al., screws with coarse threads would require less loosening torque than those with fine threads.[126] This statement also agrees with Fort et al.[127] and Yang et al.[313] On the other hand, and also for the same preload value, it is recommended that the half angle of the thread profile be as high as possible according to Nassar et al.[126] From equation (150), it can be concluded that a high angle of thread profile will lead to a higher frictional force on the threads, improving the screw-loosening response.

It must be noted that modifying some of the parameters mentioned in this conclusion, i.e. coefficients of friction, thread pitch, thread profile angle or the screw head and thread mean contact radii will alter the obtained preload. In view of this, their value should be carefully modified and checked with the presented methodology to ensure optimum dental restoration performance against self-loosening.

8 Conclusions

8.1 Conclusions and further research

This PhD Thesis brings together a significant part of the knowledge the screwed joints industry has amassed over the years and transfers it to the field of dental implantology, creating predictive methodologies and in-depth studies that help to better understand the phenomena that cause the most common mechanical problems in dental restorations: fatigue failure, microgap formation, and loosening of the prosthetic screw. The knowledge and methodologies presented in this PhD Thesis are intended to allow engineers and R&D departments to predict these phenomena and prevent them in future dental restoration designs.

Regarding prosthetic screw fatigue behavior, a prediction methodology to estimate the fatigue life of dental restorations in which the critical component is the prosthetic screw has been developed. This methodology is based on FEA, classical formulation of uniaxial fatigue, and the Theory of Elasticity. The methodology was experimentally validated obtaining accurate results for both implant-supported restorations and transepithelial-supported restorations. In this way, the methodology can predict the most common types of fatigue failure, that usually correspond to regular and wide implants. The best-fit methodology was established by performing experimental fatigue tests on dental restorations since the prosthetic screw, or at least its failure section, generally does not vary considerably across the whole product catalog. Accordingly, the methodology can be fitted in a straightforward manner by characterizing the behavior of a single dental restoration model (whose critical component is the prosthetic screw). Nevertheless, if the product catalog consists of various, and very different, prosthetic screws, characterization of fatigue behavior by performing experimental tests on standardized specimens is recommended; as performed for the methodology used for the fatigue life of dental restorations whose critical component is the implant.

Beyond the fatigue life prediction methodology, some modifications of the prosthetic screw manufacturing processes were proposed in order to improve

fatigue performance. On the one hand, manufacturing the screw head socket using a milling procedure was proven to be less harmful than broaching, preventing unexpected fatigue failures on the screw head. On the other hand, it was shown that manufacturing the screw threads using a rolling procedure rather than cutting results in less surface roughness, a better surface finish, and higher residual compressive stresses on the thread surface, enhancing the fatigue life of the prosthetic screw by one order of magnitude. The improvement is so impressive that the critical section is moved from the first engaged thread to the screw head, which can be easily improved by increasing the radius of agreement.

Regarding dental implant fatigue performance, there is a wide variety of dimensions in dental implant manufacturers' catalogs. This renders it unfeasible for the methodology to be based on experimental tests performed on dental restorations, as was performed for the previous methodology focused on the screw. Instead of this, the methodology is based on tests performed on standardized specimens with notches that result in different stress gradients, accordingly characterizing the effect of the stress concentration of the material. Thereafter, combining multi-axial fatigue critical plane methods and the TCD (Volume Method), a specific methodology has been developed to predict the fatigue life of dental restorations in which the critical component is the implant. Even though the methodology predictions were proven to be accurate by means of experimental validation, with a view towards the future, the methodology is yet to be validated on more dental restorations and use of the Point Method must be investigated with a view towards saving computational cost. In the same way, the authors consider that the mechanical performance of dental implants could be improved by varying, in some way, the manufacturing processes of the external surface, looking for ways of applying compressive residual stresses using methods such as shot peening or sandblasting and by means of thread rolling.

As a result, using both methodologies, manufacturers can compare the fatigue behavior of all dental restorations quickly and cost-effectively, without the need for time-consuming fatigue testing campaigns.

Moreover, an experimental study was performed on different dental restorations by using highly magnified X-ray projections while applying different static loads on various dental restorations. In this way, the effect of different implant parameters on microgap size at the implant-abutment connection was analyzed. With a view towards the future, the precision of the method should be improved under low masticatory loads (very small microgaps) by using synchrotron as the energy source. In this way, more

complex connections, such as conical connections, could also be studied in a precise manner.

Finally, a semi-analytical methodology by which to predict self-loosening of prosthetic screws when mounted on a dental restoration under masticatory loads is proposed. This methodology is based on a mathematical expression similar to the widely known formulation of Motosh, which generalizes it to include the effect of transverse forces acting on the screw. Although the experimental results of the model have proven its validity, further research will aim to generalize this model for dynamic loading conditions.

8.2 Research work dissemination

The research work performed in this PhD Thesis has given rise to various publications and congress presentations.

Publications:

- Armentia M, Abasolo M, Coria I, Bouzid AH. On the use of a simplified slip limit equation to predict screw self-loosening of dental implants subjected to external cycling loading. Applied Sciences. 2020;10:6748. https://doi.org/10.3390/app10196748
- Armentia M, Abasolo M, Coria I, Albizuri J. Fatigue design of dental implant assemblies: a nominal stress approach. Metals (Basel). 2020;10:744. https://doi.org/10.3390/met10060744
- Armentia M, Abasolo M, Coria I, Sainitier N. Effect of the geometry of butt-joint implant-supported restorations on the fatigue life of prosthetic screws. Journal of Prosthetic Dentistry. 2022;127(3):477.e1-477.e9. https://doi.org/10.1016/j.prosdent.2021.12.010
- Armentia M, Abasolo M, Coria I, Albizuri J, Aguirrebeitia J. Fatigue performance of prosthetic screws used in dental implant restorations: Rolled versus cut threads. Journal of Prosthetic Dentistry. 2021;126(3):406.e1-406.e8. https://doi.org/10.1016/j.prosdent.2021.06.035
- Armentia M, Abasolo M, Coria I, Zabler S. Evaluation of implant body diameter, platform diameter and the use of a transepithelial component on IAC microgap: an in-vitro study with in-situ hard X-ray radiography. The International Journal of Oral & Maxillofacial Implants. 2022 (Accepted: 7/10/22. Publication pending).

Congress presentations:

- Armentia M, Abasolo M, Coria I, Heras I, Vallejo J, Aguirrebeitia J. Design of an innovative fatigue test bench for dental implants. In: Mechanisms and Machine Science. Springer Science and Business Media B.V.; 2019. p. 103–11.
- Armentia M, Abasolo M, Coria I, Cosgaya R. Fatigue Life Estimation of Dental Implants Using Classical Fatigue Methods. In: Abstracts from the 44th Annual Conference of the European Prosthodontic Association (EPA) 30th September - 2 October 2021 Athens, Greece. European Journal of Prosthodontics and Restorative Dentistry. 2021; 29(3):14.
- Armentia M, Abasolo M, Coria I, Cosgaya R. Fatigue Life Estimation of Dental Implants Using Classical Fatigue Methods (Part II): Influence of Different Geometry Parameters and the Importance of the Screw Tightening Torque on Fatigue Life. In: Abstracts from the 44th Annual Conference of the European Prosthodontic Association (EPA) 30th September - 2 October 2021 Athens, Greece. European Journal of Prosthodontics and Restorative Dentistry. 2021; 29(3):14.

References

1. Warreth A, Fesharaki H, McConville R, McReynolds D. An introduction to single implant abutments. Dent Update. 2013;40(1):7–17.

2. Anitua E. BTI Implant System Surgical Techniques. Step by step. Team Work Media Spain; 2017.

3. Bickford JH. Introduction to the design and behavior of bolted joints. 4th ed. New York: CRC Press; 2008. 1–14 p.

4. Stüker RA, Teixeira ER, Beck JCP, da Costa NP. Preload and torque removal evaluation of three different abutment screws for single standing implant restorations. Journal of Applied Oral Science. 2008;16:55–8.

5. Lang LA, Kang B, Wang RF, Lang BR. Finite element analysis to determine implant preload. Journal of Prosthetic Dentistry. 2003;90:539–46.

6. Barbosa GS, da Silva-Neto JP, Simamoto-Júnior PC, das Neves FD, da Gloria Chiarello de Mattos M, Ribeiro RF. Evaluation of screw loosening on new abutment screws and after successive tightening. Braz Dent J. 2011;22:51–5.

7. Lindhe J, Berglundh T, Ericsson I, Liljenberg B, Marinello C. Experimental breakdown of peri-implant and periodontal tissues. A study in the beagle dog. Clin Oral Implants Res. 1992;3:9–16.

8. Broggini N, McManus LM, Hermann JS, Medina RU, Oates TW, Schenk RK, et al. Persistent acute inflammation at the implant-abutment interface. J Dent Res. 2003;82:232–7.

9. Rismanchian M, Hatami M, Badrian H, Khalighinejad N, Goroohi H. Evaluation of microgap size and microbial leakage in the connection area of 4 abutments with straumann (ITI) implant. Journal of Oral Implantology. 2012;38:677–85.

10. do Nascimento C, Pedrazzi V, Miani PK, Moreira LD, de Albuquerque RF. Influence of repeated screw tightening on bacterial leakage along the implant-abutment interface. Clin Oral Implants Res. 2009;20:1394–7.

11. Steinebrunner L, Wolfart S, Bössmann K, Kern M. In vitro evaluation of bacterial leakage along the implant-abutment interface of different implant systems. Int J Oral Maxillofac Implants. 2005;20:875–81.

12. Kang N, Wu YY, Gong P, Yue L, Ou GM. A study of force distribution of loading stresses on implant-bone interface on short implant length using 3-dimensional finite element analysis. Oral Surg Oral Med Oral Pathol Oral Radiol. 2014;118(5):519–23.

13. Shadid R, Sadaqah N, Al-Omari W, Abu-Naba'a L. Comparison between the butt-joint and morse taper implant-abutment connection: a literature review. Journal of implant and advanced clinical dentistry. 2013;5:33–40.

14. Baggi L, Cappelloni I, di Girolamo M, Maceri F, Vairo G. The influence of implant diameter and length on stress distribution of osseointegrated implants related to crestal bone geometry: A three-dimensional finite element analysis. Journal of Prosthetic Dentistry. 2008;100:422–31.

15. Hingsammer L, Pommer B, Hunger S, Stehrer R, Watzek G, Insua A. Influence of Implant Length and Associated Parameters Upon Biomechanical Forces in Finite Element Analyses: A Systematic Review. Implant Dent. 2019;28:296–305.

16. Horiuchi K, Uchida H, Yamamoto K, Sugimura M. Immediate Loading of Branemark System Implants Following Placement in Edentulous Patients: A Clinical Report. Int J Oral Maxillofac Implants. 2000;15:824–30.

17. Chiapasco M, Abati S, Romeo E, Vogel G. Implant-retained Mandibular Overdentures with Branemark System MKII Implants: A Prospective Comparative Study between Delayed and Immediate Loading. Int J Oral Maxillofac Implants. 2001;16:537–46.

18. Bakaeen LG, Winkler S, Neff PA. The effect of implant diameter, restoration design, and occlusal table variations on screw loosening of posterior single-tooth implant restorations. J Oral Implantol. 2001;17:63–72.

19. Winkler S, Morris HF, Ochi S. Implant survival to 36 months as related to length and diameter. Annals of Periodontology / The American Academy of Periodontology. 2000;5:22–31.

20. Wyatt C, Zarb G. Treatment outcomes of patients with implant-supported fixed partial prostheses. International Journal of Oral and Maxillofacial Implants. 1998;13:204–11.

21. Khongkhunthian P, Khongkhunthian S, Weerawatprachya W, Pongpat K, Aunmeungtong W. Comparative study of torque resistance and microgaps between a combined Octatorx-cone connection and an internal hexagon implant-abutment connection. Journal of Prosthetic Dentistry. 2015;113:420–4.

22. Fernández M, Delgado L, Molmeneu M, García D, Rodríguez D. Analysis of the misfit of dental implant-supported prostheses made with three manufacturing processes. Journal of Prosthetic Dentistry. 2014;111:116–23.

23. Aguirrebeitia J, Abasolo M, Vallejo J, Ansola R. Dental Implants with Conical Implant-Abutment Interface: Influence of the Conical Angle Difference on the Mechanical Behavior of the Implant. Int J Oral Maxillofac Implants. 2013;28:e72–82.

24. Broggini N, McManus LM, Hermann JS, Medina R, Schenk RK, Buser D, et al. Peri-implant inflammation defined by the implant-abutment interface. J Dent Res. 2006;85:473–8.

25. Boynueğri AD, Yalim M, Nemli SK, Ergüder BI, Gökalp P. Effect of different localizations of microgap on clinical parameters and inflammatory cytokines in peri-implant crevicular fluid: A prospective comparative study. Clin Oral Investig. 2012;16:353–61.

26. Carinci F, Girardi A, Palmieri A, Martinelli M, Scapoli L, Avntaggiato A, et al. Peri-Implantitis and bacteriological analysis. Eur J Inflamm. 2012;10:91–3.

27. Hermann JS, Buser D, Schenk RK, Cochran DL. Crestal Bone Changes Around Titanium Implants. A Histometric Evaluation of Unloaded Non-Submerged and Submerged Implants in the Canine Mandible. J Periodontol. 2000;71:1412–24.

28. Hermann JS, Cochran DL, Nummikoski P v., Buser D. Crestal Bone Changes Around Titanium Implants. A Radiographic Evaluation of Unloaded Nonsubmerged and Submerged Implants in the Canine Mandible. J Periodontol. 1997;68:1117–30.

29. Gross M, Abramovich I, Weiss E. Microleakage at the abutment-implant interface of osseointegrated implants: a comparative study. Int J Oral Maxillofac Implants. 1999;14:94–100.

30. Galindo-Moreno P, León-Cano A, Ortega-Oller I, Monje A, O'valle F, Catena A. Marginal bone loss as success criterion in implant dentistry: Beyond 2 mm. Clin Oral Implants Res. 2015;26:e28–34.

31. Carinci F, Lauritano D, Cura F, Lopez MA, Bassi MA, Confalone L, et al. Prevention of bacterial leakage at implant-Abutment connection level: An in vitro study of the efficacy of three different implant systems. J Biol Regul Homeost Agents. 2016;30:69–73.

32. Oh TJ, Yoon J, Misch CE, Wang HL. The Causes of Early Implant Bone Loss: Myth or Science? J Periodontol. 2002;73:322–33.

33. Weng D, Nagata MJH, Bell M, Bosco AF, de Melo LGN, Richter EJ. Influence of microgap location and configuration on the periimplant bone morphology in submerged implants. An experimental study in dogs. Clin Oral Implants Res. 2008;19:1141–7.

34. Ayllón JM, Navarro C, Vázquez J, Domínguez J. Fatigue life estimation in dental implants. Eng Fract Mech. 2014; 123:34–43.

35. Abasolo M, Aguirrebeitia J, Vallejo J, Albizuri J, Coria I. Influence of vertical misfit in screw fatigue behavior in dental implants: A three-dimensional finite element approach. Proc Inst Mech Eng H. 2018;232:1117–28.

36. Shemtov-Yona K, Rittel D. Fatigue of dental implants: facts and fallacies. Dent J (Basel). 2016;4:1–16.

37. Zeno HA, Buitrago RL, Sternberger SS, Patt ME, Tovar N, Coelho P, et al. The Effect of Tissue Entrapment on Screw Loosening at the Implant/Abutment Interface of External- and Internal-Connection Implants: An In Vitro Study. Journal of Prosthodontics. 2016;25:216–23.

38. Paepoemsin T, Reichart PA, Chaijareenont P, Strietzel FP, Khongkhunthian P. Removal torque evaluation of three different abutment screws for single implant restorations after mechanical cyclic loading. Oral Implantol (Rome). 2016;9:213–21.

39. Schwarz MS. Mechanical complications of dental implants. Clin Oral Implants Res. 2000;11:156–8.

40. Jeng MD, Lin YS, Lin CL. Biomechanical Evaluation of the Effects of Implant Neck Wall Thickness and Abutment Screw Size: A 3D Nonlinear Finite Element Analysis. Applied Sciences. 2020;10:3471.

41. Juvinall RC, Marshek KM. Fundamentals of Machine Component Design. 6th ed. Journal of Mechanisms, Transmissions, and Automation in Design. Wiley; 2018.

42. Norton RL. Machine Design: An Integrated Approach. 3rd ed. Pearson; 2005.

43. Budynas R, Nisbett JK. Shigley's Mechanical Engineering Design. 8th ed. New York: McGraw-Hill; 2006.

44. Abasolo M. Metamodelo para la simulación y optimización de secuencias de atornillado en uniones de torres de aerogenerador. PhD Thesis. University of the Basque Country; 2012.

45. Armentia M, Abasolo M, Coria I, Bouzid AH. On the use of a simplified slip limit equation to predict screw self-loosening of dental implants subjected to external cycling loading. Applied Sciences. 2020;10:6748.

46. Motosh N. Development of design charts for bolts preloaded up to the plastic range. Journal of Manufacturing Science and Engineering, Transactions of the ASME. 1976;98:849–951.

47. Eshghy S. LRM Fastening System. In: Technical Paper - Society of Manufacturing Engineers AD. 1977.

48. Kulak GL, Fisher JW, Struik JHA. Guide to Design Criteria for Bolted and Riveted Joints. 2nd ed. American Institute of Steel Construction Inc; 2001.

49. Baixe S, Tenenbaum H, Etienne O. Microbial contamination of the implant-abutment connections: Review of the literature. Rev Stomatol Chir Maxillofac Chir Orale. 2016;117:20–5.

50. Misch CE, Dietsh-Misch F, Hoar J, Beck G, Hazen R, Misch CM. A bone quality-based implant system: first year of prosthetic loading. J Oral Implantol. 1999;25:185–97.

51. ASTM. E-1823: Standard Terminology Relating to Fatigue and Fracture Testing. 2021.

52. Stephens RI, Fatemi A. Metal Fatigue in Engineering. 2nd ed. Wiley; 2000.

53. Avilés Gonzalez R. Métodos de cálculo de fatiga para ingeniería. Metales. 1st ed. Paraninfo; 2015.

54. Griza S, da Silva MEG, dos Santos SV, Pizzio E, Strohaecker TR. The effect of bolt length in the fatigue strength of M24×3 bolt studs. Eng Fail Anal. 2013;34:397–406.

55. Schijve J. Fatigue and scatter. In: Fatigue of Structures and Materials. Dordrecht: Springer Netherlands; 2009. p. 373–94.

56. DIN 50113: Testing of metallic materials - Rotating bar bending fatigue test.

57. ISO 1143 - Metallic materials — Rotating bar bending fatigue testing. 2010.

58. ASTM E-2948-16a: Standard Test Method for Conducting Rotating Bending Fatigue Tests of Solid Round Fine Wire. 2022.

59. ASTM E-466: Standard Practice for Conducting Force Controlled Constant Amplitude Axial Fatigue Tests of Metallic Materials. 2015.

60. ISO 1099: Metallic materials — Fatigue testing — Axial force-controlled method. 2017.

61. DIN 50100: Execution and evaluation of cyclic tests at constant load amplitudes. 2016.

62. Little R. Manual on Statistical Planning and Analysis. 17th ed. Philadelphia: ASTM International; 1975. 46–61 p.

63. Milella PP. Fatigue and corrosion in metals. Springer-Verlag Wien; 2013.

64. ASTM E-739: Standard practice for statistical analysis of linear or linearized stress-life (S–N) and strain-life (e–N) fatigue data. 2004.

65. Dixon WJ, Mood AM. A Method for Obtaining and Analyzing Sensitivity Data. J Am Stat Assoc. 1948;43(241):109–26.

66. ISO 4287: Geometrical Product Specifications (GPS) — Surface texture: Profile method — Terms, definitions and surface texture parameters. 1997.

67. ASME B46.1: Surface Texture (Surface Roughness, Waviness, and Lay). 2010.

68. Faupel JH. Engineering design. 2nd ed. Wiley; 1981.

69. FKM-guideline : Analytical strength assessment of components in mechanical engineering. 5th ed. Forschungskuratorium Maschinenbau; 2003.

70. Mylonas GI, Labeas G. Numerical modelling of shot peening process and corresponding products: Residual stress, surface roughness and cold work prediction. Surf Coat Technol. 2011;205(19):4480–94.

71. Chaise T, Li J, Nélias D, Kubler R, Taheri S, Douchet G, et al. Modelling of multiple impacts for the prediction of distortions and residual stresses induced by ultrasonic shot peening (USP). J Mater Process Technol. 2012;212(10):2080–90.

72. Guo Y, Sealy MP, Guo C. Significant improvement of corrosion resistance of biodegradable metallic implants processed by laser shock peening. CIRP Ann Manuf Technol. 2012;61(1):583–6.

73. Avilés R, Albizuri J, Rodríguez A, López De Lacalle LN. Influence of low-plasticity ball burnishing on the high-cycle fatigue strength of medium carbon AISI 1045 steel. Int J Fatigue. 2013;55:230–44.

74. Prevéy PS, Cammett JT. The influence of surface enhancement by low plasticity burnishing on the corrosion fatigue performance of AA7075-T6. Int J Fatigue. 2004;26(9):975–82.

75. Rodríguez A, López de Lacalle LN, Celaya A, Lamikiz A, Albizuri J. Surface improvement of shafts by the deep ball-burnishing technique. Surf Coat Technol. 2012;206(11–12):2817–24.

76. Paul P, Jack T, Timothy G, Pete K. FOD resistance and fatigue crack arrest in low plasticity burnished IN718. In: 5th National Turbine Engine High Cycle Fatigue Conference. 2000.

77. Meyer D. Cryogenic deep rolling - An energy based approach for enhanced cold surface hardening. CIRP Ann Manuf Technol. 2012;61(1):543–6.

78. Tian Y, Shin YC. Laser-assisted burnishing of metals. Int J Mach Tools Manuf. 2007;47(1):14–22.

79. Maximov JT, Kuzmanov T v., Duncheva G v., Ganev N. Spherical motion burnishing implemented on lathes. Int J Mach Tools Manuf. 2009;49(11):824–31.

80. Haigh BP. Report on alternating stress tests of a sample of mild dteel received from the British Association Stress Committee. Report British Association n85. 1915;163–70.

81. Niesłony A, Böhm M. Mean stress effect correction using constant stress ratio S-N curves. Int J Fatigue. 2013;52:49–56.

82. Walker K. The Effect of Stress Ratio During Crack Propagation and Fatigue for 2024-T3 and 7075-T6 Aluminum. In: Effects of Environment and Complex Load History on Fatigue Life. 2009.

83. Dowling NE, Calhoun CA, Arcari A. Mean stress effects in stress-life fatigue and Walker equation. Fatigue Fract Eng Mater Struct. 2009;32:163–79.

84. Smith KN, Watson P, Topper TH. A stress–strain function for the fatigue of metals. J Mater. 1970;5(4):767–78.

85. Ashcroft IA, Mubashar A. Fatigue. In: Adhesive Bonding: Science, Technology and Applications. Elsevier; 2021. p. 317–66.

86. Pallarés-Santasmartas L, Albizuri J, Avilés A, Avilés R. Mean Stress Effect on the Axial Fatigue Strength of DIN 34CrNiMo6 Quenched and Tempered Steel. 2018; 8(4). Article ID: 213.

87. Rankine WJM. On the causes of the unexpected breakage of the journals of railway axles; and on the mean of preventing such accidents by observing the law of continuity in their construction. J Franklin Inst. 1843;36(3):178–80.

88. Pilkey WD, Pilkey DF, Bi Z. Peterson's Stress Concentration Factors, 4th Edition | Wiley. 4th ed. Wiley; 2020.

89. Orgood CC. Fatigue Design. 2nd ed. Pergamon; 1982.

90. Sines G. Metal Fatigue. McGraw-Hill; 1959.

91. Neuber H. Kerbspannungslehre. Kerbspannungslehre. Springer Berlin Heidelberg; 2001.

92. Kuhn P, Hardrath H. An engineering method for estimating notch-size effect in fatigue tests on steel. Material Science. 1952.

93. Taylor D. The Theory of Critical Distances. The Theory of Critical Distances. Elsevier Ltd; 2007.

94. Susmel L. The theory of critical distances: a review of its applications in fatigue. Eng Fract Mech. 2008;75(7):1706–24.

95. BISS: Static & Dynamic Mechanical Testing OEM [Internet]. [cited 2022 Nov 19]. Available from: https://www.biss.in/bi-axial.php

96. Montalvão D, Wren A. Redesigning axial-axial (biaxial) cruciform specimens for very high cycle fatigue ultrasonic testing machines. Heliyon. 2017;3:466.

97. Pejkowski Ł, Karuskevich M, Maslak T. Extrusion/intrusion structure as a fatigue indicator for uniaxial and multiaxial loading. Fatigue Fract Eng Mater Struct. 2019;42(10):2315–24.

98. Fatemi A, Molaei R. Novel specimen geometries for fatigue testing of additive manufactured metals under axial, torsion, and combined axial-torsion loadings. Int J Fatigue. 2020;130:105287.

99. Sága M, Blatnický M, Vaško M, Dižo J, Kopas P, Gerlici J. Experimental determination of the manson−coffin curves for an original unconventional vehicle frame. Materials. 2020;13(20):1–20.

100. Smith JO. The effect of range of stress on the fatigue strenght of metals. Bulletin series n. 337. Illinois: University of Illinois Engineering Experiment Station; 1942.

101. Sines G. Failure of Materials Under Combined Repeated Stresses with Superimposed Static Stresses. NACA Technical Note 3495. 1955.

102. Crossland B. Effect of large hydrostatic pressure on the torsional fatigue strenght of an alloy steel. Proceedings of international conference on fatigue of metals (Institution of Mechanical Engineers). 1956.

103. Gough H, Pollard H v., Clenshaw WJ. Some experiments on the resistance of metals to fatigue under combined stresses part I and part II. Reports and Memoranda No 2522. 1952.

104. W.N.Findley. Combined-stress fatigue strength of 76S-T61 aluminum alloy with superimposed mean stresses and corrections for yielding. Technical Paper. National Aeronautics and Space Administration. 1953.

105. Matsuichi M, Endo T. Fatigue of metals subjected to varying stress. 1968.

106. Miner MA. Cumulative Damage in Fatigue. J Appl Mech. 1945;12(3):A159–64.

107. Papuga J. A survey on evaluating the fatigue limit under multiaxial loading. Int J Fatigue. 2011;33(2):153–65.

108. Taylor GI. Plastic strain in metals. Twenty-eighth May Lecture to the Institute of Metals. 1938.

109. Lin TH. Analysis of elastic and plastic strains of a face-centred cubic crystal. J Mech Phys Solids. 1957;5(2).

110. Socie D. Multiaxial Fatigue. Warrendale, PA: SAE International; 1999.

111. Bickford J. Handbook of Bolts and Bolted Joints. Handbook of Bolts and Bolted Joints. 1998.

112. Junker GH. New criteria for self-loosening of fasteners under vibration. SAE Technical Papers. 1969.

113. Shoji Y, Sawa T, Yamanaka H. Self-loosening mechanism of nuts due to lateral motion of fastened plate. In: American Society of Mechanical

Engineers, Pressure Vessels and Piping Division (Publication) PVP. 2008. p. 223–30.

114. Pai NG, Hess DP. Experimental study of loosening of threaded fasteners due to dynamic shear loads. J Sound Vib. 2002;253(3):585–602.

115. Jiang Y, Zhang M, Park TW, Lee CH. An experimental study of self-loosening of bolted joints. Journal of Mechanical Design, Transactions of the ASME. 2004;126(5):925–31.

116. Baek KH, Jeong NT, Hong HR, Choi S bin, Lee ES, Kim HM, et al. Loosening mechanism of threaded fastener for complex structures. Journal of Mechanical Science and Technology. 2019;33(4):1689–702.

117. Nichols JM, Trickey ST, Seaver M, Motley SR, Eisner ED. Using ambient vibrations to detect loosening of a composite-to-metal bolted joint in the presence of strong temperature fluctuations. Journal of Vibration and Acoustics, Transactions of the ASME. 2007;129(6):710–7.

118. SAKAI T. Investigations of Bolt Loosening Mechanisms : 1st Report, On the Bolts of Transversely Loaded Joints. Bulletin of JSME. 1978;21(159):1385–90.

119. Haviland GS. Designing with threaded fasteners. Mechanical Engineering. 1983;105(10).

120. Yamamoto A, Kasei S. Solutions for self-loosening mechanism of threaded fasteners under transverse vibration. Bulletin of the Japan Society of Precision Engineering. 1984.

121. Tanaka M, Hongo K, Asaba E. Finite Element analysis of the threaded connections subjected to external loads. Bulletin of the JSME. 1982;25(200).

122. Vinogradov O, Huang X. On a high frequency mechanism of self-loosening of fasteners. In: American Society of Mechanical Engineers, Design Engineering Division (Publication) DE. 1989.

123. Zadoks RI, Yu X. An investigation of the self-loosening behavior of bolts under transverse vibration. J Sound Vib. 1997;208(2).

124. Zadoks RI, Yu X. Preliminary study of self-loosening in bolted connections. In: American Society of Mechanical Engineers, Design Engineering Division (Publication) DE. 1993.

125. Nassar SA, Yang X. A mathematical model for vibration-induced loosening of preloaded threaded fasteners. Journal of Vibration and Acoustics, Transactions of the ASME. 2009;131:2–13.

126. Nassar SA, Xianjie Y. Novel formulation of the tightening and breakaway torque components in threaded fasteners. Journal of Pressure Vessel Technology, Transactions of the ASME. 2007;129:653–63.

127. Fort V, Bouzid AH, Gratton M. Analytical Modeling of Self-Loosening of Bolted Joints Subjected to Transverse Loading. Journal of Pressure Vessel Technology, Transactions of the ASME. 2019;141:1–11.

128. PCC-1 Guidelines for Pressure Boundary Bolted Flange Joint Assembly. 2022.

129. ASME B16.5 - Pipe Flanges & Flanged Fitting. 2020.

130. ASME B16.20: Metallic Gaskets for Pipe Flanges. 2017.

131. ASME B31.3: Process Piping. 2022.

132. ASME BPVC-VIII-1: Rules for Construction of Pressure Vessels.

133. API SPEC 17D - Design and Operation of Subsea Production Systems—Subsea Wellhead and Tree Equipment.

134. Lassesen S, Eriksen T, Teller F. NORSOK L-005; Compact Flanged Connections (CFC) - The new flange standard. In: American Society of Mechanical Engineers, Pressure Vessels and Piping Division (Publication) PVP. 2002. p. 189–95.

135. Coria Martínez I. Tetraparametric Assembly Method for the simulation and optimization of bolt tightening sequences in ASME ring type joints. PhD Thesis. University of the Basque Country; 2018.

136. Lu W, Liang W, Zhang L, Liu W. A novel noise reduction method applied in negative pressure wave for pipeline leakage localization. Process Safety and Environmental Protection. 2016;104:142–9.

137. Liu CW, Li YX, Yan YK, Fu JT, Zhang YQ. A new leak location method based on leakage acoustic waves for oil and gas pipelines. J Loss Prev Process Ind. 2015;35:236–46.

138. Eriksen PK. Leakage detection utilizing active acoustic systems. In: Society of Petroleum Engineers - Arctic Technology Conference 2012. Society of Petroleum Engineers; 2012. p. 30–7.

139. Shi Y, Zhang C, Li R, Cai M, Jia G. Theory and application of magnetic flux leakage pipeline detection. Sensors (Switzerland). 2015;15(12):31036–55.

140. Bhuiyan MAS, Hossain MA, Alam JM. A computational model of thermal monitoring at a leakage in pipelines. Int J Heat Mass Transf. 2016;92:330–8.

141. ISO 14801:2007. Dentistry. Implants. Dynamic fatigue test for endosseous dental implants. International Organization for Standardization. 2007.

142. Pjetursson B, Asgeirsson A, Zwahlen M, Sailer I. Improvements in implant dentistry over the last decade: comparison of survival and complication rates in older and newer publications. Int J Oral Maxillofac Implants. 2014;29:308–24.

143. Dhima M, Paulusova V, Lohse C, Salinas TJ, Carr AB. Practice-based evidence from 29-year outcome analysis of management of the edentulous jaw using osseointegrated dental implants. Journal of Prosthodontics. 2014;23:173–81.

144. Pérez MA. Life prediction of different commercial dental implants as influence by uncertainties in their fatigue material properties and loading conditions. Comput Methods Programs Biomed. 2012;108:1277–86.

145. Wang RR, Fenton A. Titanium for prosthodontic applications: a review of the literature. Quintessence Int. 1996;27(6):401–8.

146. Ohkubo C, Watanabe I, Ford JP, Nakajima H, Hosoi T, Okabe T. The machinability of cast titanium and Ti-6Al-4V. Biomaterials. 2000;21(4):421–8.

147. Darshith S, Ramesh Babu K, Manjunath S S. Comprehensive study of cut and roll threads. IOSR Journal of Mechanical and Civil Engineering. 2014;11(2):91–6.

148. Javier Gil F, Planell JA, Padrós A, Aparicio C. The effect of shot blasting and heat treatment on the fatigue behavior of titanium for dental implant applications. Dental Materials. 2007;23:486–91.

149. Park JK, Choi JU, Jeon YC, Choi KS, Jeong CM. Effects of abutment screw coating on implant preload. Journal of Prosthodontics. 2010;19:458–64.

150. Jeng MD, Liu PY, Kuo JH, Lin CL. Load fatigue performance evaluation on two internal tapered abutment-implant connection implants under different screw tightening torques. Journal of Oral Implantology. 2017;43:107–13.

151. Quek H, Tan K, Nicholls J. Load fatigue performance of four implant-abutment interface designs: Effect of torque level and implant system. J Prosthet Dent. 2008;23:253–62.

152. Xia D, Lin H, Yuan S, Bai W, Zheng G. Dynamic fatigue performance of implantabutment assemblies with different tightening torque values. Biomed Mater Eng. 2014;24:2143–9.

153. Janeček M, Nový F, Harcuba P, Stráský J, Trško L, Mhaede M, et al. The very high cycle fatigue behaviour of Ti-6Al-4V alloy. Acta Phys Pol A. 2015;128:497–503.

154. Carrion PE, Shamsaei N. Strain-based fatigue data for Ti-6Al-4V ELI under fully-reversed and mean strain loads. Data Brief. 2016;7:12–5.

155. Carrion PE, Shamsaei N, Daniewicz SR, Moser RD. Fatigue behavior of Ti-6Al-4V ELI including mean stress effects. Int J Fatigue. 2017;99:87–100.

156. Baragetti S. Notch corrosion fatigue behavior of Ti-6Al-4V. Materials. 2014;7:4349–66.

157. Hosseini S, Limooei MB. Investigation of fatigue behaviour and notch sensitivity of Ti-6Al-4V. Applied Mechanics and Materials. 2011;80–81:7–12.

158. Yamashita Y, Ueda Y, Kuroki H, Shinozaki M. Fatigue life prediction of small notched Ti-6Al-4V specimens using critical distance. Eng Fract Mech. 2010;77:1439–53.

159. Lanning DB, Nicholas T, Palazotto A. The effect of notch geometry on critical distance high cycle fatigue predictions. In: International Journal of Fatigue. Elsevier; 2005. p. 1623–7.

160. Sivaraman K, Chopra A, Narayan AI, Balakrishnan D. Is zirconia a viable alternative to titanium for oral implant? A critical review. J Prosthodont Res. 2018;62:121–33.

161. Niinomi M. Fatigue characteristics of metallic biomaterials. Int J Fatigue. 2007;29:992–1000.

162. Gehrke SA, Poncio da Silva PM, Calvo Guirado JL, Delgado-Ruiz RA, Dedavid BA, Aline Nagasawa M, et al. Mechanical behavior of zirconia and titanium abutments before and after cyclic load application. Journal of Prosthetic Dentistry. 2016;116:529–35.

163. Prados-Privado M, Bea JA, Rojo R, Gehrke SA, Calvo-Guirado JL, Prados-Frutos JC. A New Model to Study Fatigue in Dental Implants Based on Probabilistic Finite Elements and Cumulative Damage Model. Appl Bionics Biomech. 2017;1–8.

164. Prados-Privado M, Prados-Frutos JC, Manchón Á, Rojo R, Felice P, Bea JA. Dental implants fatigue as a possible failure of implantologic treatment: The importance of randomness in fatigue behaviour. Biomed Res Int. 2015;Special Is:Article ID 825402.

165. Santiago Junior JF, Pellizzer EP, Verri FR, de Carvalho PSP. Stress analysis in bone tissue around single implants with different diameters and veneering materials: A 3-D finite element study. Materials Science and Engineering C. 2013;3:4700–14.

166. Chang SH, Lin CL, Hsue SS, Lin YS, Huang SR. Biomechanical analysis of the effects of implant diameter and bone quality in short implants placed in the atrophic posterior maxilla. Med Eng Phys. 2012;34:153–60.

167. Raaj G, Manimaran P, Kumar C, Sadan D, Abirami M. Comparative evaluation of implant designs: Influence of diameter, length, and taper on

stress and strain in the mandibular segment-A three-dimensional finite element analysis. J Pharm Bioallied Sci. 2019;16:486–94.

168. Langer B, Langer L, Herrmann I, Jorneus L. The wide fixture: a solution for special bone situations and a rescue for the compromised implant. Part 1. Int J Oral Maxillofac Implants. 1993;8:400–8.

169. Lee JH, Frias V, Lee KW, Wright RF. Effect of implant size and shape on implant success rates: A literature review. Journal of Prosthetic Dentistry. 2005;94:377–81.

170. Misch CE. Implant Design Considerations for the Posterior Regions of the Mouth. Implant Dent. 1999;8:376–86.

171. Himmlová L, Dostálová T, Kácovský A, Konvičková S. Influence of implant length and diameter on stress distribution: A finite element analysis. Journal of Prosthetic Dentistry. 2004;91(1):20–5.

172. Shemtov-Yona K, Rittel D, Machtei EE, Levin L, Machtei EE, Levin L, et al. Effect of dental implant diameter on fatigue performance. Part I: Mechanical behavior. Clin Implant Dent Relat Res. 2014;16:172–7.

173. Fan H, Gan X, Zhu Z. Evaluation of dental implant fatigue performance under loading conditions in two kinds of physiological environment. Int J Clin Exp Med. 2017;10:6369–77.

174. Anitua E, Piñas L, Orive G. Retrospective study of short and extra-short implants placed in posterior regions: Influence of crown-to-implant ratio on marginal bone loss. Clin Implant Dent Relat Res. 2015;17:102–10.

175. Anitua E, Piñas L, Begoña L, Orive G. Long-term retrospective evaluation of short implants in the posterior areas: Clinical results after 10-12 years. J Clin Periodontol. 2014;41:404–11.

176. Anitua E, Orive G. Short Implants in Maxillae and Mandibles: A Retrospective Study With 1 to 8 Years of Follow-Up. J Periodontol. 2010;81(6):819–26.

177. Anitua E, Alkhraisat MH. 15-year follow-up of short dental implants placed in the partially edentulous patient: Mandible Vs maxilla. Annals of Anatomy. 2019;222:88–93.

178. Topkaya H, Kaman MO. Effect of Dental Implant Dimensions on Fatigue Behaviour: A Numerical Approach. Uludag University Journal of the Faculty of Engineering. 2018;23:249–60.

179. Anitua E, Tapia R, Luzuriaga F, Orive G. Influence of implant length, diameter, and geometry on stress distribution: a finite element analysis. Int J Periodontics Restorative Dent. 2010;30:89–95.

180. Georgiopoulos B, Kalioras K, Provatidis C, Manda M, Koidis P. The effects of implant length and diameter prior to and after osseointegration: a 2-D finite element analysis. J Oral Implantol. 2007;33:243–56.

181. Lum LB. A biomechanical rationale for the use of short implants. J Oral Implantol. 1991;17:126–31.

182. Atieh MA, Ibrahim HM, Atieh AH. Platform Switching for Marginal Bone Preservation Around Dental Implants: A Systematic Review and Meta-Analysis. J Periodontol. 2010;81:1350–66.

183. Minatel L, Verri FR, Kudo GAH, de Faria Almeida DA, de Souza Batista VE, Lemos CAA, et al. Effect of different types of prosthetic platforms on stress-distribution in dental implant-supported prostheses. Materials Science and Engineering C. 2017;71:35–42.

184. Nicolas-Silvente AI, Velasco-Ortega E, Ortiz-Garcia I, Jimenez-Guerra A, Monsalve-Guil L, Ayuso-Montero R, et al. Influence of Connection Type and Platform Diameter on Titanium Dental Implants Fatigue: Non-Axial Loading Cyclic Test Analysis. Int J Environ Res Public Health. 2020;17:8988.

185. Mishra SK, Chowdhary R, Kumari S. Microleakage at the different implant abutment interface: A systematic review. Journal of Clinical and Diagnostic Research. 2017;11:ZE10–5.

186. Shafie HR, White BA. Different Implant–Abutment Connections. In: Shafie HR, editor. Clinical and Laboratory Manual of Dental Implant Abutments. New Jersey, USA: John Wiley & Sons, Inc; 2014. p. 33–46.

187. Dittmer S, Dittmer MP, Kohorst P, Jendras M, Borchers L, Stiesch M. Effect of implant-abutment connection design on load bearing capacity and failure mode of implants. Journal of Prosthodontics. 2011;20:510–6.

188. Khraisat A, Stegaroiu R, Nomura S, Miyakawa O. Fatigue resistance of two implant/abutment joint designs. Journal of Prosthetic Dentistry. 2002;88:604–10.

189. Fernández-Asián, Martínez-González, Torres-Lagares, Serrera-Figallo, Gutiérrez-Pérez. External Connection versus Internal Connection in Dental Implantology. A Mechanical in vitro Study. Metals (Basel). 2019;9:1106.

190. Yamaguchi S, Yamanishi Y, Machado LS, Matsumoto S, Tovar N, Coelho PG, et al. In vitro fatigue tests and in silico finite element analysis of dental implants with different fixture/abutment joint types using computer-aided design models. J Prosthodont Res. 2018;62(1):24–30.

191. Mericske-Stern R, Geering AH, Bürgin WB, Graf H. Three-dimensional force measurements on mandibular implants supporting overdentures. International Journal of Oral and Maxillofacial Implants. 1992;13:36–43.

192. Khraisat A, Abu-Hammad O, Dar-Odeh N, Al-Kayed AM. Abutment screw loosening and bending resistance of external hexagon implant system after lateral cyclic loading. Clin Implant Dent Relat Res. 2004;6:157–64.

193. Chaar MS, Att W, Strub JR. Prosthetic outcome of cement-retained implant-supported fixed dental restorations: A systematic review. J Oral Rehabil. 2011;38:697–711.

194. Jung RE, Pjetursson BE, Glauser R, Zembic A, Zwahlen M, Lang NP. A systematic review of the 5-year survival and complication rates of implant-supported single crowns. Clin Oral Implants Res. 2008;19:119–30.

195. Simon RL. Single implant-supported molar and premolar crowns: A ten-year retrospective clinical report. Journal of Prosthetic Dentistry. 2003;90:517–21.

196. Aboyoussef H, Weiner S, Ehrenberg D. Effect of an antirotation resistance form on screw loosening for single implant-supported crowns. Journal of Prosthetic Dentistry. 2000;83:450–5.

197. Cavazos E, Bell FA. Preventing loosening of implant abutment screws. Journal of Prosthetic Dentistry. 1996;75:566–9.

198. Kirov D, Stoichkov B. Factors affecting the abutment screw loosening. Journal of IMAB - Annual Proceeding (Scientific Papers). 2017;23:1505–9.

199. Arshad M, Shirani G, Refoua S, Yeganeh MR. Comparative study of abutment screw loosening with or without adhesive material. Journal of Advanced Prosthodontics. 2017;9:99–103.

200. Yeo IS, Lee JH, Kang TJ, Kim SK, Heo SJ, Koak JY, et al. The Effect of Abutment Screw Length on Screw Loosening in Dental Implants with External Abutment Connections After Thermocycling. Int J Oral Maxillofac Implants. 2014;29:59–62.

201. Wu T, Fan H, Ma R, Chen H, Li Z, Yu H. Effect of lubricant on the reliability of dental implant abutment screw joint: An in vitro laboratory and three-dimension finite element analysis. Materials Science and Engineering C. 2017;75:297–304.

202. Elias CN, Figueira DC, Rios PR. Influence of the coating material on the loosing of dental implant abutment screw joints. Materials Science and Engineering C. 2006;26:1361–6.

203. Park CI, Choe HC, Chung CH. Effects of surface coating on the screw loosening of dental abutment screws. Metals and Materials International. 2004;10:549.

204. Yao KT, Kao HC, Cheng CK, Fang HW, Yip SW, Hsu ML. The effect of clockwise and counterclockwise twisting moments on abutment screw loosening. Clin Oral Implants Res. 2012;23:1181–6.

205. Siamos G, Winkler S, Boberick KG. The relationship between implant preload and screw loosening on implant-supported prostheses. J Oral Implantol. 2002;28:67–73.

206. Fauroux MA, Anxionnat C, Biens C, Mechali M, Romieu O, Torres JH. Fuites de la connexion implantaire: comparaison de plusieurs types d'implants par la méthode de diffusion gazeuse. Rev Stomatol Chir Maxillofac Chir Orale. 2014;115(2):74–8.

207. Torres JH, Mechali M, Romieu O, Tramini P, Callas S, Cuisinier FJG, et al. Development of a new quantitative gas permeability method for dental

implant-abutment connection tightness assessment. Biomed Eng Online. 2011;10(1):28.

208. Harder S, Dimaczek B, Açil Y, Terheyden H, Freitag-Wolf S, Kern M. Molecular leakage at implant-abutment connection-in vitro investigation of tightness of internal conical implant-abutment connections against endotoxin penetration. Clin Oral Investig. 2010;14(4):427–32.

209. Black DL, Turkyilmaz I, Lien W, Chong CH. Evaluation of the sealing capability of the internal conical connections of implants with titanium and zirconia abutments. Journal of Contemporary Dental Practice. 2017;18:915–22.

210. Smith NA, Turkyilmaz I. Evaluation of the sealing capability of implants to titanium and zirconia abutments against Porphyromonas gingivalis, Prevotella intermedia, and Fusobacterium nucleatum under different screw torque values. Journal of Prosthetic Dentistry. 2014;112(3):561–7.

211. Baj A, Bolzoni A, Russillo A, Lauritano D, Palmieri A, Cura F, et al. Cone-morse implant connection system significantly reduces bacterial leakage between implant and abutment: An in vitro study. J Biol Regul Homeost Agents. 2017;31(2, Supplement 1).

212. da Silva-Neto JP, Prudente MS, Carneiro T de APN, Nóbilo MA de A, Penatti MPA, das Neves FD. Micro-leakage at the implant-abutment interface with different tightening torques in vitro. Journal of Applied Oral Science. 2012;20(5):581–7.

213. Faria R, May L, de Vasconcellos D, Maziero Volpato C, Bottino M. Evaluation of the bacterial leakage along the implant-abutment interface. Journal of Dental Implants. 2011;1(2):51.

214. Mohammadi F. Bacterial Leakage at Implant-Abutment Interface With Different Intermediate Materials. Journal of Oral Implantology. 2019;XLV(6):451–5.

215. de Chaves e Mello Dias ECL. Assessment of Bacterial Leakage at the Implant- Abutment Interface of Internal and External Connection Implants: An In Vitro Study. Dental Health: Current Research. 2016;2(2):2–5.

216. do Nascimento C, Barbosa RES, Issa JPM, Watanabe E, Ito IY, Albuquerque RF. Bacterial leakage along the implant-abutment interface of premachined or cast components. Int J Oral Maxillofac Surg. 2008;37(2):177–80.

217. Tripodi D, Vantaggiato G, Scarano A, Perrotti V, Piattelli A, Iezzi G, et al. An in vitro investigation concerning the bacterial leakage at implants with internal hexagon and morse taper implant-abutment connections. Implant Dent. 2012;21(4):335–9.

218. Gehrke P, Hartjen P, Smeets R, Gosau M, Peters U, Beikler T, et al. Marginal adaptation and microbial leakage at conometric prosthetic connections for implant-supported single crowns: An in vitro investigation. Int J Mol Sci. 2021;22(2).

219. Assenza B, Tripodi D, Scarano A, Perrotti V, Piattelli A, Iezzi G, et al. Bacterial Leakage in Implants With Different Implant–Abutment Connections: An In Vitro Study. J Periodontol. 2012;83(4):491–7.

220. D'Ercole S, Tripodi D, Ravera L, Perrotti V, Piattelli A, Iezzi G. Bacterial leakage in morse cone internal connection implants using different torque values: An in vitro study. Implant Dent. 2014;23(2):175–9.

221. de Chaves e Mello Dias ECL, Bisognin EDC, Harari ND, Machado SJ, da Silva CP, Soares GD de A, et al. Evaluation of implant-abutment micro gap and bacterial leakage in five External-hex implant systems: an in vitro study. Int J Oral Maxillofac Implants. 2012;27(2):346–51.

222. Lopes de Chaves e Mello Dias E, Sperandio M, Napimoga M. Association Between Implant-Abutment Microgap and Implant Circularity to Bacterial Leakage: An In Vitro Study Using Tapered Connection Implants. Int J Oral Maxillofac Implants. 2017;33:505–11.

223. Koutouzis T, Gadalla H, Lundgren T. Bacterial Colonization of the Implant-Abutment Interface (IAI) of Dental Implants with a Sloped Marginal Design: An in-vitro Study. Clin Implant Dent Relat Res. 2016;18(1).

224. Tesmer M, Wallet S, Koutouzis T, Lundgren T. Bacterial Colonization of the Dental Implant Fixture–Abutment Interface: An In Vitro Study. J Periodontol. 2009;80(12):1991–7.

225. Triveni VVS, Jagadeesh KN, Parihar AS, Alduwayhi S, Annapoorneshwari S, Khalid FM, et al. Evaluation of microleakage and microgap of two different internal implant-abutment connections: An in vitro study. Journal of Contemporary Dental Practice. 2020;21(6).

226. Koutouzis T, Mesia R, Calderon N, Wong F, Wallet S. The effect of dynamic loading on bacterial colonization of the dental implant fixture-abutment interface: An in vitro study. Journal of Oral Implantology. 2014;40:432–7.

227. Ricomini Filho AP, Fernandes FS de F, Straioto FG, da Silva WJ, del Bel Cury AA. Preload loss and bacterial penetration on different implant-abutment connection systems. Braz Dent J. 2010;21:123–9.

228. Nassar HI, Abdalla MF. Bacterial leakage of different internal implant/abutment connection. Future Dental Journal. 2015;1(1):1–5.

229. Smojver I, Vuletić M, Gerbl D, Budimir A, Sušić M, Gabrić D. Evaluation of antimicrobial efficacy and permeability of various sealing materials at the implant–abutment interface—a pilot in vitro study. Materials. 2021;14(2).

230. Zipprich H, Miatke S, Hmaidouch R, Lauer HC. A New Experimental Design for Bacterial Microleakage Investigation at the Implant-Abutment Interface: An In Vitro Study. Int J Oral Maxillofac Implants. 2016;31(1):37–44.

231. Akula SKJ, Ramakrishnan H, Sivaprakasam AN. Comparative evaluation of the microbial leakage at two different implant-abutment interfaces using a new sealant. Journal of Dental Implant Research. 2021;40(2):35–47.

232. Ranieri R, Ferreira A, Souza E, Arcoverde J, Dametto F, Gade-Neto C, et al. The Bacterial Sealing Capacity of Morse Taper Implant–Abutment Systems in Vitro. J Periodontol. 2015;86:696–702.

233. Berberi A, Tehini G, Rifai K, Bou Nasser Eddine F, el Zein N, Badran B, et al. In vitro evaluation of leakage at implant-abutment connection of three implant systems having the same prosthetic interface using rhodamine B. Int J Dent. 2014;2014.

234. Martin-Gili D, Molmeneu M, Fernandez M, Punset M, Giner L, Armengou J, et al. Determination of fluid leakages in the different screw-retained implant-abutment connections in a mechanical artificial mouth. J Mater Sci Mater Med. 2015;26(7).

235. Coelho PG, Sudack P, Suzuki M, Kurtz KS, Romanos GE, Silva NRFA. In vitro evaluation of the implant abutment connection sealing capability of different implant systems. J Oral Rehabil. 2008;35(12):917–24.

236. Rocha Ferreira J, Song N, Machado M, Machado L, Correia A, Reis A. Fatigue and microgap behaviour of a three-unit implant-fixed dental prosthesis combining conventional and dynamic abutments. J Med Eng Technol. 2018;42(5).

237. Kavadia V, Kourtis S, Zoidis P, Sarafianou A. The influence of impression coping splinting on the accuracy of the open-tray technique. Gen Dent. 2019;67(3).

238. Kano S, Binon P, Curtis D. A classification system to measure the implant-abutment microgap. Int J Oral Maxillofac Implants. 2007; 22(6):879-85.

239. Tiossi R, Gomes ÉA, Lapria Faria AC, Silveira Rodrigues RC, Ribeiro RF. Effect of cyclic loading on the vertical microgap of long-span zirconia frameworks supported by 4 or 6 implants. Journal of Prosthetic Dentistry. 2014;112(4).

240. Duraisamy R, Krishnan CS, Ramasubramanian H, Sampathkumar J, Mariappan S, Navarasampatti Sivaprakasam A. Compatibility of Nonoriginal Abutments with Implants: Evaluation of Microgap at the Implant-Abutment Interface, with Original and Nonoriginal Abutments. Implant Dent. 2019;28(3).

241. Molinero-Mourelle P, Cascos-Sanchez R, Yilmaz B, Lam WYH, Pow EHN, del Río Highsmith J, et al. Effect of fabrication technique on the microgap of CAD/CAM cobalt-chrome and zirconia abutments on a conical connection implant: An in vitro study. Materials. 2021;14(9).

242. Sui X, Wei H, Wang D, Han Y, Deng J, Wang Y, et al. Experimental research on the relationship between fit accuracy and fracture resistance of zirconia abutments. J Dent. 2014;42(10).

243. Katsoulis J, Mericske-Stern R, Enkling N, Katsoulis K, Blatz MB. In vitro precision of fit of computer-aided designed and computer-aided manufactured titanium screw-retained fixed dental prostheses before and after ceramic veneering. Clin Oral Implants Res. 2015;26(1).

244. Markarian R, Galles D, França F. Scanning Electron Microscopy Analysis of the Adaptation of Single-Unit Screw-Retained Computer-Aided Design/Computer-Aided Manufacture Abutments After Mechanical Cycling. Int J Oral Maxillofac Implants. 2018;33(1):127–36.

245. Gois Filho DM, Gois-Santos VT de, Silva RS, Marqueti AC, Cortes ARG, Trento CL. Evaluation of sealing between abutment and inner connection of cone morse dental implant. Clinical and Laboratorial Research in Dentistry. 2018; 1-6.

246. Vahey BR, Sordi MB, Stanley K, Magini RS, Novaes de Oliveira AP, Fredel MC, et al. Mechanical integrity of cement- and screw-retained zirconium-lithium silicate glass-ceramic crowns to Morse taper implants. J Prosthet Dent. 2018;120(5):721–31.

247. Spies BC, Fross A, Adolfsson E, Bagegni A, Doerken S, Kohal RJ. Stability and aging resistance of a zirconia oral implant using a carbon fiber-reinforced screw for implant-abutment connection. Dental Materials. 2018;34(10):1585–95.

248. Gil FJ, Herrero-Climent M, Lázaro P, Rios J v. Implant-abutment connections: Influence of the design on the microgap and their fatigue and fracture behavior of dental implants. J Mater Sci Mater Med. 2014;25:1825–30.

249. Pereira J, Morsch C, Henriques B, Nascimento R, Benfatti C, Silva F, et al. Removal Torque and Biofilm Accumulation at Two Dental Implant–Abutment Joints After Fatigue. Int J Oral Maxillofac Implants. 2016;31(4):813–9.

250. Wiest W, Rack A, Zabler S, Schaer A, Swain M, Nelson K. Validation of finite-element simulations with synchrotron radiography – A descriptive study of micromechanics in two-piece dental implants. Heliyon. 2018;4(2):e00524.

251. Bagegni A, Zabler S, Nelson K, Rack A, Spies BC, Vach K, et al. Synchrotron-based micro computed tomography investigation of the

implant-abutment fatigue-induced microgap changes. J Mech Behav Biomed Mater. 2021;116:104330.

252. Rack T, Zabler S, Rack A, Riesemeier H, Nelson K. An In Vitro Pilot Study of Abutment Stability During Loading in New and Fatigue-Loaded Conical Dental Implants Using Synchrotron-Based Radiography. Int J Oral Maxillofac Implants. 2013;28:44–50.

253. Rack A, Rack T, Stiller M, Riesemeier H, Zabler S, Nelson K. In vitro synchrotron-based radiography of micro-gap formation at the implant–abutment interface of two-piece dental implants. J Synchrotron Radiat. 2010;17:289–94.

254. Jörn D, Kohorst P, Besdo S, Borchers L, Stiesch M. Three-Dimensional Nonlinear Finite Element Analysis and Microcomputed Tomography Evaluation of Microgap Formation in a Dental Implant Under Oblique Loading. Int J Oral Maxillofac Implants. 2016;31:e32–42.

255. Wiest W, Zabler S, Rack A, Fella C, Balles A, Nelson K, et al. In situ microradioscopy and microtomography of fatigue-loaded dental two-piece implants. J Synchrotron Radiat. 2015;22.

256. Blum K, Wiest W, Fella C, Balles A, Dittmann J, Rack A, et al. Fatigue induced changes in conical implant-abutment connections. Dental Materials. 2015;31:1415–26.

257. Kapishnikov S, Gadyukov A, Chaushu G, Chaushu L. Micro-CT Analysis of Microgap at a Novel Two-Piece Dental Implant Comprising a Replaceable Sleeve In Vitro. Int J Oral Maxillofac Implants. 2021;36(3).

258. Scarano A, Valbonetti L, Degidi M, Pecci R, Piattelli A, de Oliveira PS, et al. Implant-Abutment Contact Surfaces and Microgap Measurements of Different Implant Connections under 3-Dimensional X-Ray Microtomography. Implant Dent. 2016;25(5):656–62.

259. Sahin C, Ayyildiz S. Correlation between microleakage and screw loosening at implant-abutment connection. Journal of Advanced Prosthodontics. 2014;6(1):35–8.

260. Sebastien B, Fauxpoint G, Arntz Y, Etienne O. Microgap Between Zirconia Abutments and Titanium Implants. Int J Oral Maxillofac Implants. 2010;25:455–60.

261. Koutouzis T, Wallet S, Calderon N, Lundgren T. Bacterial Colonization of the Implant–Abutment Interface Using an In Vitro Dynamic Loading Model. J Periodontol. 2011;82:613–8.

262. Queiroz DA, Hagee N, Lee DJ, Zheng F. The behavior of a zirconia or metal abutment on the implant-abutment interface during cyclic loading. J Prosthet Dent. 2020;124(2):211–6.

263. Farronato D, Pieroni S, Mangano FG, Briguglio F, Re D. Effects of different abutment material and surgical insertion torque on the marginal adaptation of an internal conical interface: An in vitro study. J Prosthodont Res. 2014;58(4):230–6.

264. Kofron MD, Carstens M, Fu C, Wen HB. In vitro assessment of connection strength and stability of internal implant-abutment connections. Clinical Biomechanics. 2019;65:92–9.

265. Lopes de Chaves e Mello Dias EC, Bisognin ED, Harari D, Machado SJ, Pereira da Silva C, Soares G de A, et al. Evaluation of Implant-Abutment Microgap and Bacterial Leakage in Five External-Hex Implant Systems: An In Vitro Study. Int J Oral Maxillofac Implants. 2012;27:346–51.

266. Gehrke SA, Shibli JA, Aramburú Junior JS, Sánchez de Val JEM, Calvo-Girardo JL, de David BA. Effects of different torque levels on the implant-abutment interface in a conical internal connection. Braz Oral Res. 2016;30:e40.

267. Honório Tonin BS, He Y, Ye N, Chew HP, Fok A. Effects of tightening torque on screw stress and formation of implant-abutment microgaps: A finite element analysis. Journal of Prosthetic Dentistry. 2021;S0022-3913:30749–6.

268. Biotechnology Institute BTI. https://bti-biotechnologyinstitute.com/es.

269. ISO 5832-2: Implants for surgery — Metallic materials — Part 2: Unalloyed titanium. 2018.

270. ASTM F67-13: Standard Specification for Unalloyed Titanium, for Surgical Implant Applications. 2017.

271. ISO 5832-3: Implants for surgery — Metallic materials — Part 3: Wrought titanium 6-aluminium 4-vanadium alloy. 2016.

272. ASTM F136: Standard Specification for Wrought Titanium-6Aluminum-4Vanadium ELI (Extra Low Interstitial) Alloy for Surgical Implant Applications. 2021.

273. Houpert L. An engineering approach to hertzian contact elasticity-part I. J Tribol. 2001;123:582–8.

274. Norton, RL. Cam Design and Manufacturing Handbook. Journal of Mechanical Design. 2004;126(2).

275. Abasolo M, Aguirrebeitia J, Coria I, Fernandez de Bustos I, Heras I. Dental Implant Test Bench and Methodology. Patent No.: P201830801, 2018.

276. Dowling NE, Calhoun CA, Arcari A. Mean stress effects in stress-life fatigue and the Walker equation. Fatigue Fract Eng Mater Struct. 2009;32:163–79.

277. Yamanaka S, Amiya K, Saotome Y. Effects of residual stress on elastic plastic behavior of metallic glass bolts formed by cold thread rolling. J Mater Process Technol. 2014;214:2593–9.

278. Chiapasco M, Casentini P, Zaniboni M, Corsi E, Anello T. Titanium-zirconium alloy narrow-diameter implants (Straumann Roxolid®) for the rehabilitation of horizontally deficient edentulous ridges: Prospective study on 18 consecutive patients. Clin Oral Implants Res. 2012;23:1136–41.

279. Klein M, Schiegnitz E, Al-Nawas B. Systematic Review on Success of Narrow-Diameter Dental Implants. Int J Oral Maxillofac Implants. 2014;29:43–54.

280. Domblesky JP, Feng F. A parametric study of process parameters in external thread rolling. J Mater Process Technol. 2002;121(2–3):341–9.

281. Saglam H, Kus R. Performance of internal thread rolling head and the mechanical properties of rolled thread. In: Proceedings of 6th International Advanced Technologies Symposium (IATS'11). 2011. p. 16–8.

282. Zhang DW, Zhao SD, Ou H. Analysis of motion between rolling die and workpiece in thread rolling process with round dies. Mech Mach Theory. 2016;105:471–94.

283. Janíček L, Petruška J, Maroš B, Rusz S. Cold forming of bolts without thermal treatment. J Mater Process Technol. 2002;125:341–6.

284. Zhelezkov OS, Malakanov SA, Semashko V v. Prediction of thread rolling tools wear resistance. Procedia Eng. 2017;206:630–5.

285. Furukawa A, Hagiwara M. Estimation of the residual stress on the thread root generated by thread rolling process. Mechanical Engineering Journal. 2015;2(4).

286. Lange K. Handbook of metal forming. 1st ed. New York: McGraw-Hill; 1985.

287. Khostikoev MZ, Mnatsakanyan VU, Temnikov VA, Maung WP. Quality control of rolled threads. Russian Engineering Research. 2015;35(2):143–6.

288. Kim W, Kawai K, Koyama H, Miyazaki D. Fatigue strength and residual stress of groove-rolled products. J Mater Process Technol. 2007;194(1–3):46–51.

289. Oberg E, Jones FD, Horton HL, Ryffel HH. Machinery's handbook: a reference book for the mechanical engineer, designer, manufacturing engineer, draftsman, toolmaker, and machinist. 29th ed. New York: Industrial Press; 2012.

290. Stephens RI, Bradley NJ, Horn NJ, Gradman JJ, Arkema JM, Borgwardt CS. Fatigue of high strength bolts rolled before or after heat treatment with five different preload levels. SAE Technical Papers. 2005;10.4271/2005-01–1321.

291. Cullity BD, Stock SR. Elements of X-ray diffraction, 3rd edition. Prentice Hall. 2001.

292. Fitzpatrick ME, Fry A, Holdway P, Kandil F a, Shackleton J, Suominen L. Measurement good practice guide No. 52. Determination of residual stresses by X-ray diffraction. Measurement Good Practice Guide. 2005.

293. Schajer GS. Practical residual stress measurement methods. Wiley; 2013.

294. Thread rolling. In: Machining. ASM International; 1989. p. 280–95.

295. Tschaetsch H, Koth A. Metal forming practise: Processes - Machines - Tools. 1st ed. Berlin: Springer; 2006. 1–405 p.

296. Ruiz-Hervias J, Atienza JM, Elices M. Synchrotron strain scanning for residual stress measurement in cold-drawn steel rods. Journal of Strain Analysis for Engineering Design. 2011;46(7):627–37.

297. Rotundo F, Korsunsky AM. Synchrotron XRD study of residual stress in a shot peened Al/SiC pcomposite. Procedia Eng. 2009;1(1):221–4.

298. Khan MK, Fitzpatrick ME, Hainsworth S v., Evans AD, Edwards L. Application of synchrotron X-ray diffraction and nanoindentation for the determination of residual stress fields around scratches. Acta Mater. 2011;59(20):7508–20.

299. Cui M, Zhao S, Chen C, Zhang D, Li Y. Finite element modeling and analysis for the integration-rolling-extrusion process of spline shaft. Advances in Mechanical Engineering. 2017;9(2):1–11.

300. Li Y, Zhao S. Study on the improvements of incremental rolling process for spline shaft with round tools based on finite element method. In: 2013 IEEE International Conference on Mechatronics and Automation, IEEE ICMA 2013. 2013.

301. Kim JK, Kim DS, Takeda N. Notched Strength and Fracture Criterion in Fabric Composite Plates Containing a Circular Hole. J Compos Mater. 1995;29(7):982–98.

302. Shen J, Fan H, Zhang G, Pan R, Wang J, Huang Z. Influence of the stress gradient at the notch on the critical distance and life prediction in HCF and VHCF. Int J Fatigue. 2022;162:107003.

303. Zhu SP, He JC, Liao D, Wang Q, Liu Y. The effect of notch size on critical distance and fatigue life predictions. Mater Des. 2020;196:109095.

304. Hu X, Jia X, Bao Z, Song Y. Effect of notch geometry on the fatigue strength and critical distance of TC4 titanium alloy. Journal of Mechanical Science and Technology. 2017;31(10):4727–37.

305. Yang X, Wang J, Liu J. High temperature LCF life prediction of notched DS Ni-based superalloy using critical distance concept. Int J Fatigue. 2011;33(11):1470–6.

306. Patterson EA, Johns RB. Theoretical analysis of the fatigue life of fixture screws in osseointegrated dental implants. Int J Oral Maxillofac Implants. 1992;7:26–33.

307. Horváth P, Tóth P. Nondestructive Bolt Preload Measurement. Athens Journal of Technology & Engineering. 2018;5:91–110.

308. Junker GH. Criteria for Self Loosening of Fasteners Under Vibration. Aircraft Engineering and Aerospace Technology. 1973;44:14–6.

309. Guda T, Ross TA, Lang LA, Millwater HR. Probabilistic analysis of preload in the abutment screw of a dental implant complex. Journal of Prosthetic Dentistry. 2008;100(3):183–93.

310. Kim SK, Lee JB, Koak JY, Heo SJ, Lee KR, Cho LR, et al. An abutment screw loosening study of a Diamond Like Carbon-coated CP titanium implant. J Oral Rehabil. 2005;32:346–50.

311. Sun F, Wang L, Li XC, Cheng W, Lin Z, Ba DC, et al. Effect of surface modification on the long-term stability of dental implant abutment screws by plasma nitriding treatment. Surf Coat Technol. 2020;399.

312. Bulaqi HA, Mousavi Mashhadi M, Geramipanah F, Safari H, Paknejad M. Effect of the coefficient of friction and tightening speed on the preload induced at the dental implant complex with the finite element method. Journal of Prosthetic Dentistry. 2015;113(5):405–11.

313. Yang X, Nassar SA, Wu Z. Criterion for preventing self-loosening of preloaded cap screws under transverse cyclic excitation. Journal of Vibration and Acoustics, Transactions of the ASME. 2011.